THE UNIVERSITY *of* EDINBURGH

Improving Rapid Pathogen Detection: Towards a Gram-Selective Lateral Flow Test

Doctorate of Philosophy

University of Edinburgh

2023

James Crossland

Lay Summary

The aim of my PhD was to develop a lateral flow test for the detection of Gram-negative bacteria using small molecules as ligands rather than conventional antibodies or aptamers. The small molecules targeted for this role were antibiotic-based because they have a known, good interaction, with the outer periphery of the target bacteria.

To make these molecules useable in a lateral flow test, extra functional groups were added to them. These additional functional groups allowed the molecules bind to both the bacteria and, to other parts required for the test. These parts included gold nanoparticles which provide the strong red colour that shows the results of the test and, the test strip that is made of the material nitrocellulose through which the bacteria flows.

A lateral flow test was designed and built to use the antibiotic-based molecules and a smartphone was used to image and analyse the test results. By optimising the design of the lateral flow test Gram-negative bacteria were successfully detected.

This is a promising development in the kinds of molecules that can be used in lateral flow tests and for simple bacterial detection. This work could be further developed to expand the range of antibiotics used and further the lateral flow test.

Abstract

The development of rapid detection assays, such as lateral flow tests, have been effective in helping to detect a range of biological targets, most recently in the COVID-19 pandemic. The effective detection and classification of bacteria, such as their Gram status using rapid low-cost lateral flow assay could help diagnose and target treatment of bacterial infections in medical and veterinary applications. This is important as over prescription of broad-spectrum antibiotics is a well-known contributor to the rise in antimicrobial resistance.

My work targeted the development of lateral flow assays to achieve the specific detection of Gram-negative bacteria. To make the assay Gram selective, targeting/binding ligands were synthesised based on Polymyxin B, a Gram-negative selective antibiotic.

A literature method of selective functionalisation of Polymyxin B was optimised to service material at the gram scale for the development of three Polymyxin conjugates: a Lipoic acid-Polymyxin conjugate and two Biotin-Polymyxin conjugates with and without a spacer. The most effective binding/labelling agent was determined to be a Biotin-Polymyxin conjugate with a six-carbon spacer, which allowed the fluorescently labelling of *E. coli* by the generation of a Bacteria-Polymyxin-Biotin-Streptavidin-fluorophore sandwich.

Most lateral flow tests use gold nanoparticles to label the target analyte as it provides an intense red colour that is easily detectable by eye, and this was replicated here by the attachment of Polymyxin to gold nanoparticles. Through testing a range of methods for the attachment of Polymyxin, a nanoparticle system that could be used

to selectively label the surface of bacteria was developed. This Polymyxin-nanoparticle labelling system was characterised via electron microscopy.

Nitrocellulose membranes were laser cut to shape and printed with reagents to give a strip assay platform that could analyse the behaviour of the synthesised gold nanoparticles and the Polymyxin targeting agents in flow. 3D printing was used to fabricate an imaging enclosure to enable repeatable imaging that allowed for smartphone capture of the assays and analysis with a custom Python-based image analysis script. This allowed high-throughput testing and optimisation of the assay and flow conditions.

Through the optimisation of the lateral flow assay design Gram-negative *E. coli* were able to be detected in flow, imaged, and analysed. My PhD work thus provides an example of a lateral flow assay functioning without antibodies or aptamers. This work could provide the foundation for further development, including other antibiotics to target different bacteria.

Contents

Declaration of Authorship

The research detailed within this thesis has been performed by the author in the duration of the PhD studentship between the dates of September 2019 and August 2023 under the supervision of Professor Mark Bradley, School of Chemistry, University of Edinburgh. The work, data, analysis, and interpretation presented here are those of the author unless explicitly stated otherwise. Where published work has been consulted or referred to in the text, the source has been clearly cited. This work has not been submitted for any other degrees or professional qualifications.

Signed

James Crossland

31/08/2023

Acknowledgements

I am immensely grateful to the many individuals who have contributed to the completion of this thesis. I extend my deepest gratitude to my supervisor, Professor Mark Bradley. Your dedication, expertise, and unyielding commitment to excellence have been the driving force behind the successful completion of this research.

I am indebted to my friends and colleagues Dr Maxime Klausen, Dr Richa Sharma and Dr John White. A PhD is fundamentally a training program, and you all were instrumental in teaching me the basics of being a researcher both in and out of the lab. I thank you all for your kindness and patience in dealing with me these last four years, it has truly been a pleasure to work with you.

To Sonia, Paige, Maria, Ewan, Tommy, Yuguo, Meltem, Zainab and the rest of the Bradley group you have supported me with camaraderie, encouragement, and humour that provided much-needed relief. Your presence has made this journey much more enjoyable and memorable, particularly through the exciting times and disruption we have all worked through.

The support of my family has always been vital. Thanks to my parents Jane and Tom, for instilling in me a love of science and providing unwavering encouragement through all too many years of higher education. Thanks to my siblings Matt and Alexandra for all the fun we had over the years, it certainly helped keep me sane through weeks of failed experiments.

The completion of this thesis would not have been possible without the collective support and encouragement of everyone. My gratitude knows no bounds.

Abbreviations

AFM: Atomic force microscopy

Ahx: 6-aminohexanoic acid

AmB: Amphotericin B

AMR: Antimicrobial resistance

AuNP: Gold nanoparticle

Boc: butyloxycarbonyl

Boc_2O: Di-tert-butyl dicarbonate

Boc-ON: [2-(tert-butoxycarbonyloxyimino)-2-phenylacetonitrile]

BSA: Bovine serum albumin

CFU: Colony-forming unit

Cy5: Cyanine-5

Dab: Diaminobutyric acid

DCM: Dichloromethane

DIPEA: N,N-Diisopropylethylamine

DLS: Dynamic light scattering

DMSO: Dimethyl sulfoxide

DoE: Design of Experiments

ELISA: Enzyme-linked immunosorbent assay

ESBL: Extended spectrum beta lactamase

GCMS: Gas chromatography mass spectrometry

HABA: 4'-hydroxyazobenzene-2-carboxylic acid

HPLC: High performance liquid chromatography

HRP: Horseradish peroxidase

HSPyU: Dipyrrolidino(N-succinimidyloxy)carbenium hexauorophosphate

LAMP: Loop-mediated isothermal amplification

LCMS: Liquid Chromatography Mass Spectrometry

LFIA: Lateral Flow Immunoassay

LOD: Limit of detection

LPS: Lipopolysaccharide

m/z: Mass to charge ratio

MALDI: Matrix assisted laser desorption ionisation

MWCO: Molecular weight cut off

NBD: Nitrobenzoxadiazole

NDH-2: NADH-menaquinone oxidoreductase

NHS: N-hydroxysuccinimide

NMR: Nuclear magnetic resonance

OD: Optical density

PBS: Phosphate buffered saline

PCR: Polymerase chain reaction

PEG: Polyethylene glycol

PMBN: Polymyxin B Nonapeptide

PMX: Polymyxin

POC: Point-of-Care

PVP: polyvinylpyrrolidone

RH: Hydrodynamic volume

SELEX: systematic evolution of ligands by exponential enrichment

SPPS: Solid phase peptide synthesis

SPR: Surface Plasmon Resonance

ssDNA: Single stranded DNA

TB: Tuberculosis

TEM: Transmission electron microscopy

TFA: Trifluoroacetic acid

TOF: Time of flight

UV-Vis: Ultraviolet-visible spectroscopy

Van: Vancomycin

VRE: Vancomycin resistant enterococcus

1 Point of Care Detection of Bacteria

Since the discovery of Penicillin by Fleming in 1929[1] the impact of bacterial infections on global mortality has greatly diminished.[2] The explosion in antibiotic development through the 1950s to 1980s helped lead to a reduction in mortality by communicable diseases and an increase in life expectancy in the developed world.[3] This has made the top global causes of death (in the wealthy part of the world) non-communicable diseases such as heart disease, stroke and cancer.[4] However, bacterial infection remains a danger primarily in less developed counties due to lack of access to diagnosis and treatment, with deaths from the five leading pathogens (*Staphylococcus aureus*, *Escherichia coli, Streptococcus pneumoniae, Klebsiella pneumoniae,* and *Pseudomonas aeruginosa*) causing 230 deaths per 100,000 people in the sub-Saharan Africa region compared to 52.2 deaths per 100,000 people in the highest income regions.[5–7]

However, the spectre of bacterial infections is returning to the developed world due to the rise of antimicrobial resistance (AMR)[8,9] and has been identified as a leading public health threat and requires urgent invention.[10,11] It has been estimated that there were 4.95 million deaths associated with bacterial AMR in 2019 alone (Figure 1).[12] These deaths are currently unevenly distributed towards the global south but this is a challenge that will impact all countries.

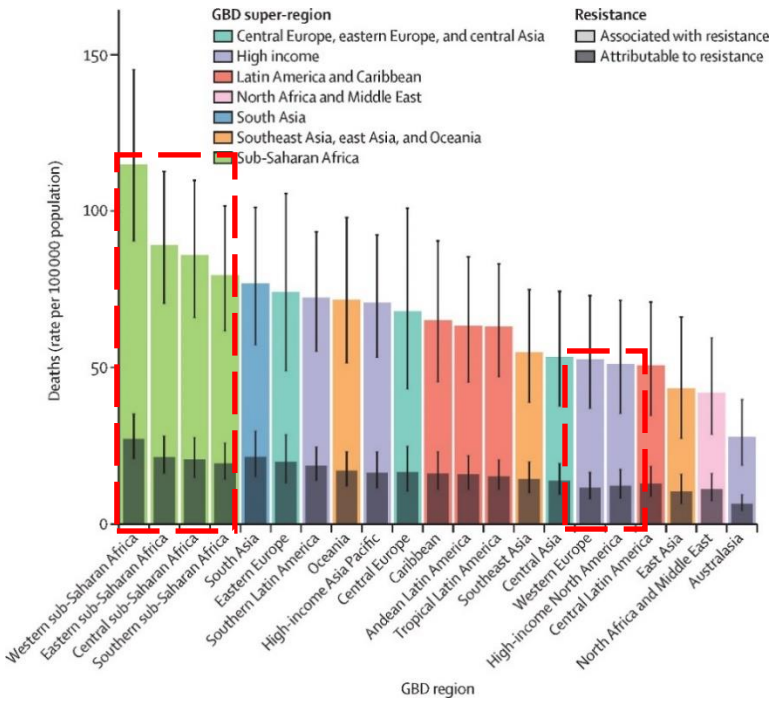

Figure 1: All-age rate of deaths attributable to (dark bars) and associated with (light bars) antimicrobial resistance by Global Burden of Diseases (GBD) regions. Vertical lines represent uncertainty in the values derived from statistical modelling applied to the data. Red highlighted sections highlight a particular disparity between outcomes in Africa compared to developed western countries. Reproduced from The Lancet, 2022, 399, 629–655, under the Creative Commons CC-BY license. Published by Elsevier Ltd.[12]

Tackling these issues requires a multi-pronged approach and significant investment.[13] One such approach is to improve the detection, diagnosis, and treatment of bacterial infections and identify their susceptibility to antimicrobials. Accurate, rapid detection and diagnosis can guide clinical treatment decisions, resulting in a lower overall disease burden and reducing antibiotic misuse, which is a key driver of AMR, through more targeted antibiotic selection. An area of research aimed specifically at improving the speed of bacteria detection is the development of Point-of-Care (POC) diagnostic assays and devices as an alternative to, or supplement of, traditional detection methods.[14–17]

1.1 Traditional Methods for the Detection of Bacteria

Before examining how POC methods can improve bacteria detection it is worth considering what traditional methods are available to understand how new POC tests can be positioned to improve on them.

The existing approach to clinical bacteria identification is centred on three key methods[18]:

1. **Culturing**, where bacteria are grown in a nutrient medium from a patient sample[19], is used to amplify bacteria in the sample for subsequent analysis and/or provide additional identifying details through the use of selective[20] assays such as antibacterial susceptibility[21]or chromogenic[22] substrates.
2. **Optical microscopy**, using either patient samples directly (e.g. blood smears[23]) or after culturing the sample to amplify the bacteria. Identification can be by direct identification by morphology[24] or in combination with stains (e.g. Gram stain[25], Auramine-Rhodamine TB stain[26,27], Wirtz-Conklin spore stain[28])
3. **Indirect methods**, such as biochemical function assays, (*e.g.* measurement of the activity of enzymes such as phosphatase[29], catalase[30] and , oxidase[31]) and serology, measuring the immune response in patient serum (i.e. the detection of antibodies and antigens which would be present during/after infection)

A combination of data from this constellation of tests can specifically determine the species of bacteria present in a sample and guide treatment.[32] While some of these tests, such as for enzyme activity, can provide rapid results (e.g. urine dipstick assays

with chromogenic reporters[30,31]) culture dependent methods are slow, requiring upwards of 24 hours for cultures to grow[33,34].

Recent developments aimed at improving clinical detection of bacteria have focused on a few key areas: improvements to existing method (e.g., culturing and microscopy stains), novel applications of analytical techniques such as mass spectrometry and, expansion of molecular biology methods.

1.1.1 Developments in Culturing

Culturing on solid agar has been available since it was developed by Louis Pasteur in 1860[20] and is often used where bacterial infection is suspected.[35] Improvements in the amount of data that can be gleaned from this method can aid in combined species/antimicrobial susceptibility identification (Figure 2) and optimise the downstream analysis by indicating the presence or absence of characteristic enzymes.

Chromogenic media typically function by dosing the culture media with a compound that can be turned over by an enzyme carried by the target bacteria. Once converted by the compound either generates a chromophore (i.e., gains a colour) or more commonly an existing chromophore is altered (i.e., changes colour). For media that is also species selective a combination of specific antibiotics and nutrients will be added[36] along with the chromogenic compound(s).

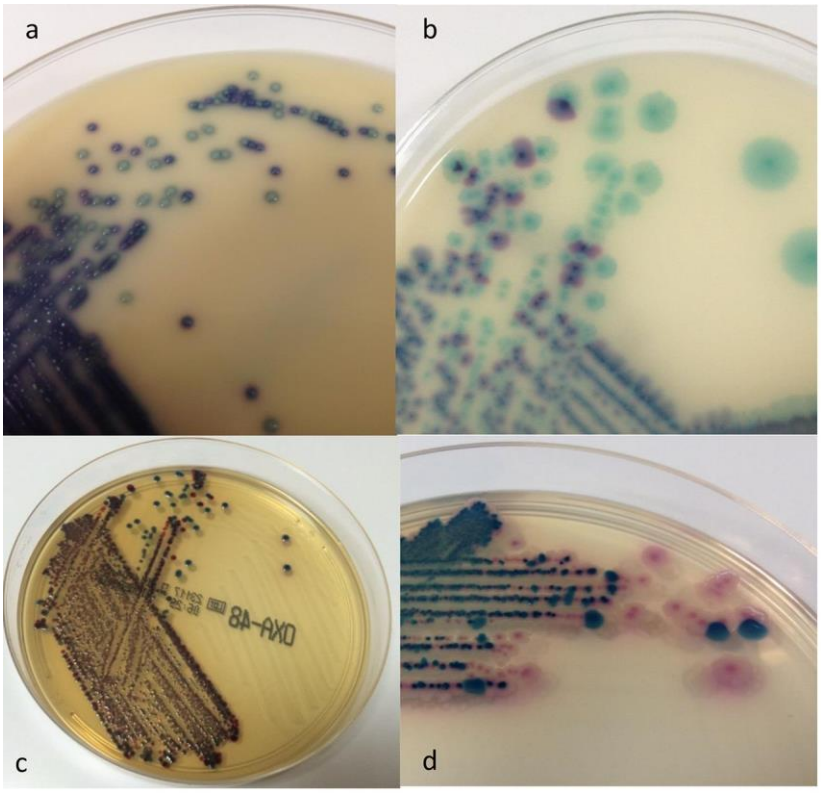

Figure 2: Examples of chromogenic media for detection of antimicrobial-resistant pathogens that have been reported in the last decade. (a) Purple colonies of *Enterococcus faecium* (carrying the vanB resistance gene) and blue-green colonies of *Enterococcus faecalis* (carrying the vanA resistance gene) on Brilliance VRE agar. (b) Extended spectrum beta-lactamase (ESBL) producing colonies of *K. pneumoniae* with SHV-36 and CTX-M-9 enzymes (green colonies) and *E. coli* with CTX-M-9 enzyme (pink/blue colonies) on Brilliance ESBL agar. (c) *K. pneumoniae* (green colonies) and *E. coli* (red colonies), both with OXA-48 carbapenemase, isolated on chromID OXA 48. (d) Carbapenemase-producing *K. pneumoniae* with OXA-48 enzyme (blue colonies) and *E. coli* with NDM-1 enzyme (pink colonies) isolated on Colorex mSuperCarba medium. Figure reprinted with permission Clin. Microbiol. Rev., 2017, **30**, 449–479 © Crown copyright 2017[22]

As an example of how selective, chromogenic media can be clinically useful Perry et al evaluated a prototype media (IDCd) for the identification of *Clostridium difficile* from stool samples (Figure 3).[37] *C. difficile* is a common cause of hospital acquired infectious diarrhoea[38] and known to be challenging to culture[39].

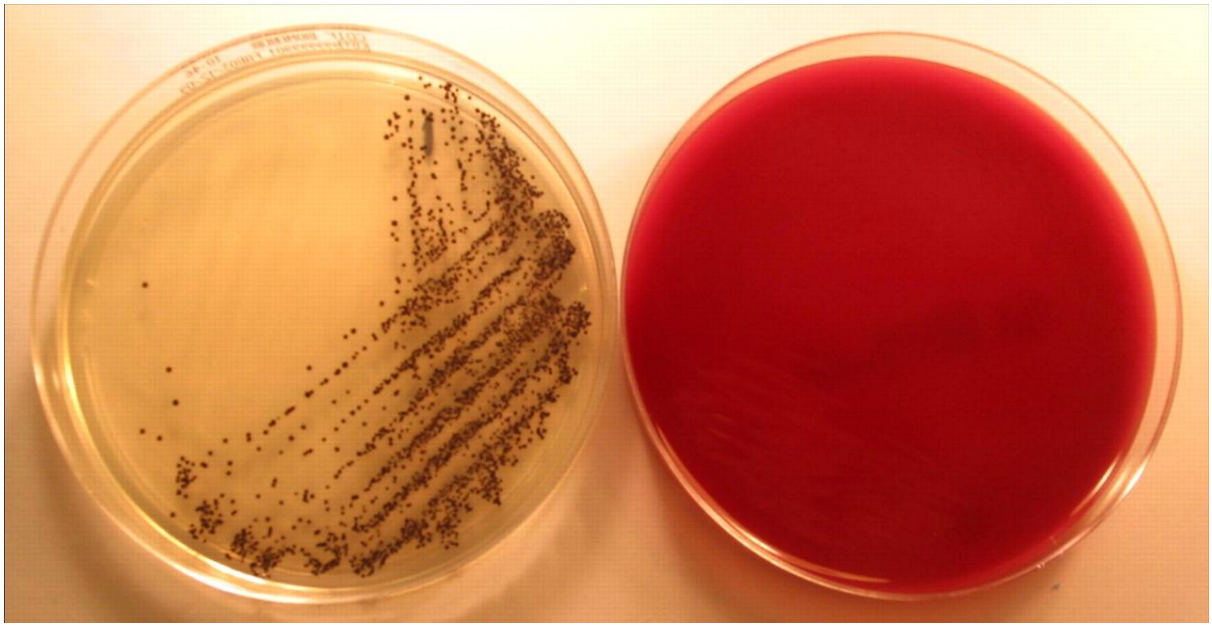

Figure 3: Culture of *C. difficile* from a stool sample after 24 h of incubation on IDCd prototype medium (left) and a non-chromogenic existing bioMérieux product, CLO medium (right). IDCd prototype media showed C. difficile formed black colonies, compared to CLO medium plate shows no growth.

This media enabled the successful selective growth of *C. difficile* and the inclusion of an enzyme substrate that, when hydrolysed, generated highly visible black colonies instead of the normal white colonies.

A novel, mechanistically distinct, method leveraging bacterial enzyme action via doped culture media was shown by Ramírez-Guízar et al that used two enzyme substrates, 2-amino-N-phenylpropanamide and 2-amino-N-(4-methylphenyl)propanamide doped into Tryptone Soya Agar that could be turned over by the enzyme L-alanine aminopeptidase, which is present in the cell wall of Gram-negative bacteria.[40] The product of the enzyme action generated the volatile compounds aniline and p-toluidine which were detected by gas-chromatography mass-spectrometry (GCMS). This was able to discriminate between Gram-positive and Gram-negative bacteria with high accuracy across 22 different species.

1.1.2 Developments in Microscope Identification of Bacteria

Traditional brightfield microscopy has been a mainstay of clinical microbiology since the work of Antonie van Leeuwenhoek in the late 1600s.[41] Subsequent improvements in the resolving power of microscopes in combination with early selective staining was fundamental in developing our understanding of bacteria and their role in infections.[42]

One of the earliest was the Gram stain developed in 1884 by Hans Christian Gram which involves staining a sample with Crystal Violet followed by a safranin or fuchsine counterstain.[43] This allowed the classification of bacteria as either Gram-positive or Gram-negative based on Crystal Violet binding to bacteria with a thick outer peptidoglycan layer staining them purple, thus defining 'Gram-Positive'. Conversely, Gram-Negative bacteria have a hydrophobic lipopolysaccharide outer membrane which inhibits this staining and are subsequently counterstained pink/red (Figure 4).

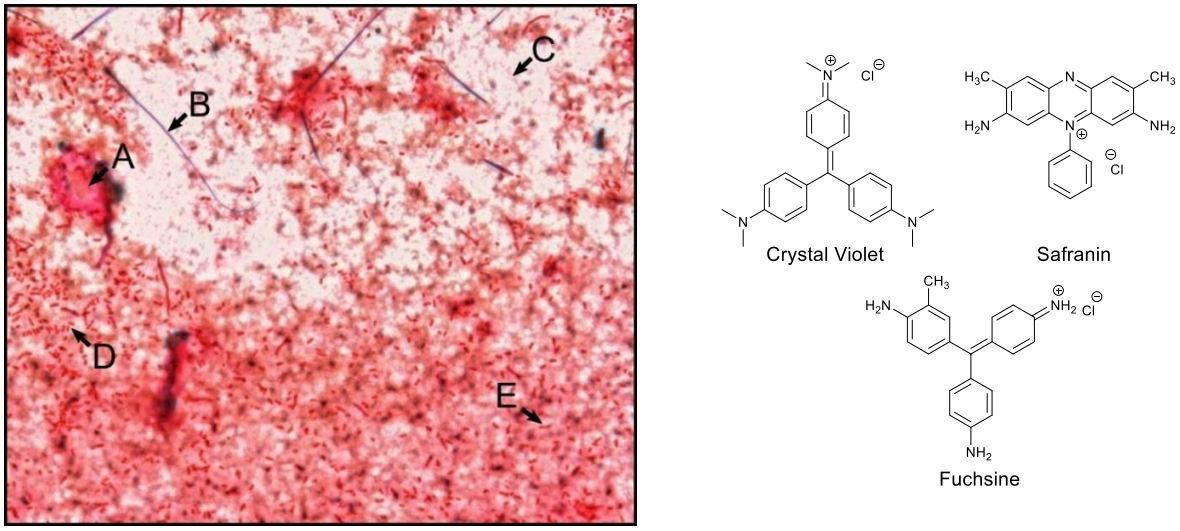

Figure 4: Representative image of a blood culture smear (Left). The structure of Gram-stain dyes (Right) The highlighted features are characteristic of blood culture Gram stains, including (A) an area of intense background staining, (B) an artefact from stain crystallization, (C) diffuse background staining, and (D and E) individually resolved Gram-negative rods with (D) high contrast and (E) low contrast compared to background. Reprinted with permission J. Clin. Microbiol., 2018, **56**. Copyright American Society For Microbiology [44]

While classical stains tend to operate on the basis of direct interaction of the dye compounds with biological structures interesting research developments focus on separating the targeting of a stain from the chromophore element (Figure 5).[45] This has enabled the variety of bacterial labelling probes to expand, adding new capabilities both in colours/wavelengths of the chemical optical labels (e.g. fluorescence or absorbance based) but also to include inorganic labels such as nanoparticles.[46] Equally expansion of the targeting agents through this approach enabled techniques such as: immunostaining[47] where antibodies are used for binding, molecular targeting[48] where small molecules such as antibiotics bind specific elements and, enzyme targeting[49] where the agent is a substrate for a specific enzyme.

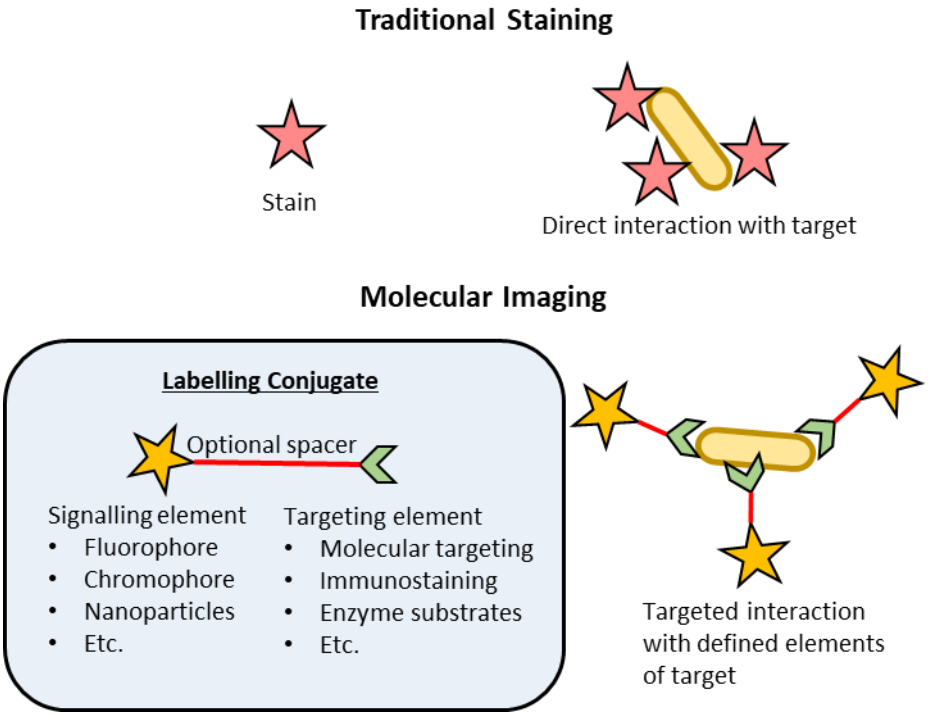

Figure 5: Diagram of traditional staining approach (Top) where the staining compounds interact directly with the target compared to the 'Molecular Imaging' approach (Bottom) were the targeting and labelling are separated, either conjugated together directly or through an optional spacer (e.g. short PEG chain). This combined labelling conjugate then binds to the target through the targeting element, localising the labelling element along with it.

There is a broad field of research focused on compounds using molecular targeting for fluorescent microscopy. For example, Baibek et al[50] used a combination of antibiotic-conjugated fluorophores to label Fungi, Gram-negative and, Gram-positive bacteria (based on the antibiotics amphotericin B (AmB), Polymyxin B (PMX) and Vancomycin (Van) respectively) that were co-cultured together (Figure 6). Confocal fluorescence imaging was able to use the three different fluorophores Cyanine-5 (Cy5), Nitrobenzoxadiazole (NBD) and, Merocyanine (MeroCy) respectively) to separately detect each microbe selectively.

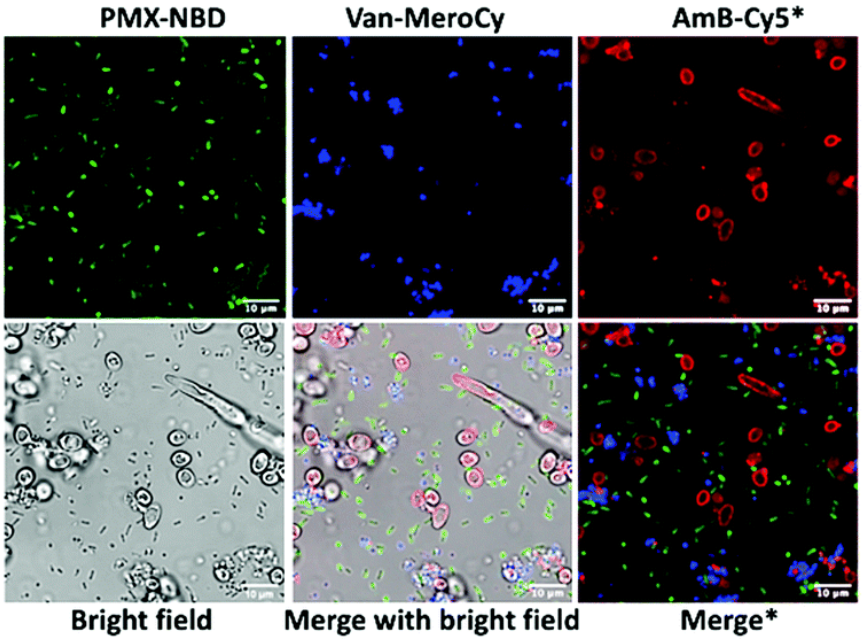

Figure 6: Multiplexed imaging of a fungi and bacteriaConfocal microscopy images of a live co-culture of fungi (*C. albicans*) with Gram-positive bacteria (*S. aureus* in blue) and Gram-negative bacteria (*E. coli* in green). The bacteria and fungi were co-incubated for 1 h at 37 °C with AmB-Cy5 (10 μM in red) and the Gram-positive bacteria probe Van-MeroCy (1 μM) and Gram-negative bacteria probe PMX-NBD (5 μM). Scale bar 10 μm. For imaging, the cells were simultaneously excited at 488 nm, 561 nm and 633 nm with emission detected in three channels. Reprinted from Chem. Commun., 2021, 57, 1899-1902 under the CC-BY-NC licence.[50]

The level of clarity in these images compared to a tradition stain such as Gram-staining highlights how molecular imaging is a powerful tool for microscopy-based detection of complex biological specimens.

1.1.3 Novel Method for Bacteria Detection – Mass Spectrometry

Mass spectrometry has become an increasingly powerful clinical tool with advancements in equipment and techniques in recent years allowing methods like matrix-assisted laser desorption ionisation (MALDI) mass spectrometry.[51] MALDI was developed in the mid-1980s[52] and uses organic compounds (commonly organic acids such as sinapinic acid) to form a matrix that strongly absorbs laser energy around large, hard to ionise analytes, such as proteins or even whole bacteria[53] (Figure 7). The ability to ionise components within clinical samples provides access to a large amount of complex mass data, which can be analysed for markers indicative of specific bacteria and metabolic by-products directly or through bioinformatic / proteomic analysis techniques.[54,55]

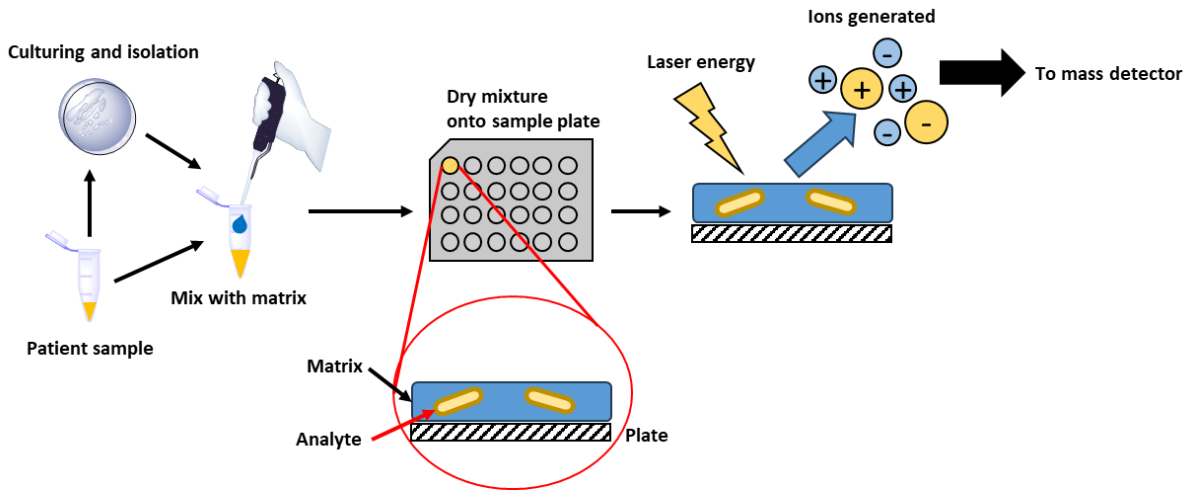

Figure 7: The process for MALDI-MS detection of a sample. Samples can either be sourced directly from patient samples or go through pre-treatment such as culturing to isolate a 'pure' sample. The sample is mixed with the matrix compound and dried onto a sample plate. This plate is loaded into the instrument and hit with a laser to ionise the matrix/sample. The ions are transferred to a mass detector such as a time-of-flight.

Lau et al investigated the application of mass spectrometry to the identification of clinically significant strains by analysing 67 clinically isolated bacteria that were 'difficult-to-identify' phenotypically.[56] The isolates were analysed using a 'direct

transfer method' where whole cells were deposited onto the sample plate and mixed with an HCCA (α-Cyano- 4-hydroxycinnamic acid) matrix solution. They showed that MALDI paired with time of flight (TOF) mass analysis was able classify 45% of isolates to the species level with 30% identified at the genus level. The remaining samples were either misidentified (6%) or could not be classified (19%). They concluded that MALDI-TOF was technically capable as an analytical technique for bacterial detection/classification and that with improvements in data analysis and comparative databases, accuracy could be improved even among less common species.

Mass spectrometry is most reliable when applied to 'pure' bacterial samples such as colonies isolated after culturing of a clinical sample as this excludes issues of contamination and simplifies data analysis. However, methods to analyse patient samples directly have also been developed as shown by Ferreira et al that performed direct detection of pathogens (*E. coli, E. faecalis,* and *P. aeruginosa*) from urine samples.[57] They were able to show reliable detection across 235 samples when bacteria concentration was $>10^5$ CFU/mL but below this concentration weak signal to noise resulted in incorrect or no identification.

When targeted at a specific strain of bacteria MALDI-TOF can also be used to provide detailed analysis beyond just species and genus. Reil et al used the commercial extended SARAMIS™ MALDI-TOF system in the analysis of *C. difficile* aiming to classify isolates based on their ribotype (a phylogenetic identifier based on the 16S ribosomal RNA) which can be useful in tracking the spread of strains of interest (i.e. strains with high virulence).[58] Their analysis of 355 *C. difficile* samples was able to be validated to correctly identify the three most common ribotypes encompassing 80% of all samples.

While mass spectrometry is a powerful technique it is not universally available. Currently the widespread application of mass spectrometry has been slowed by the high cost of equipment and the need to develop improved bioinformatics analysis techniques.

1.1.4 Nucleic Acid Amplification

Through direct analysis of a bacteria's genetic information, a wide variety of properties can be identified and characterised. The key challenge to successful analysis of genetic information was overcoming its low concentration which was resolved by the discovery of the Polymerase Chain Reaction (PCR) in 1985 which amplifies specific sections of the genetic information into detectable concentrations. While bacteria could be characterised on the basis of their whole genome, full genetic sequencing is slow and costly and not suitable in many application.[59,60] Targeting specific genes by PCR is sufficient for species identification or giving useful clinical information such as resistance profiles[61].

The techniques of PCR uses primers (20-30 bases long[62]), in combination with thermally stable DNA polymerases and free nucleoside triphosphates through a specific sequence of heating and cooling cycles to amplify the DNA (Figure 8).[63] Through careful selection of primers, specific characteristic genetic sequences, i.e. targeting a specific species of bacteria, can be identified and amplified.

Species identification can be done through targeting highly conserved areas of the genome such as 16S ribosomal RNA (part of cellular protein synthesis machinery) and early work by Radstrom et al was able to distinguish between 28 different species (133 strains) with high sensitivity and specificity [64] It can also detect markers

of antibiotic resistance as shown by Yengui et al. who detected the eight most frequent genes for beta-lactamase synthesis in *E. coli* and *K. pneumoniae* from urine samples from patients suffering from urinary tract infections.[65]

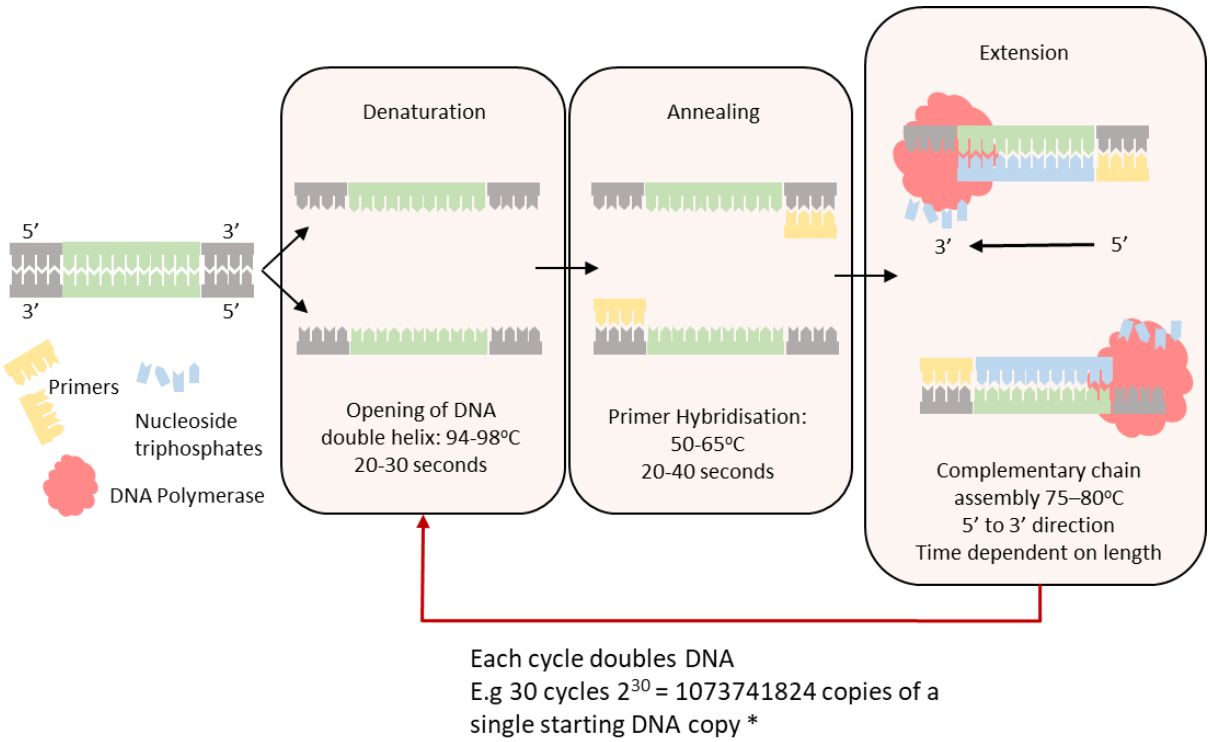

Figure 8: The classical steps involved in the PCR: Denaturation where heat is used to denature the double helix into two single strands, annealing is where primers attach to the single strands through complementary binding and, extension is where the DNA polymerase builds the new complementary strand from free nucleoside triphosphates. These steps are repeated depending on the desired amount of amplification and the starting concentration of reagents. * DNA doubling calculation is a theoretical maximum assuming 100% yield. Times and temperatures listed are for a generic method, using thermostable Taq polymerase.

The degree of amplification of PCR is based on the number of cycles, with each additional cycle resulting in a doubling of DNA content (assuming 100% yield). This makes it excellent for detecting the presence of very low amounts of bacteria in a sample. However, this amplification approach is sensitive to contamination as even a single contaminating fragment of DNA, could be amplified into a false positive result,[66] while in complex biological samples e.g. blood or urine, inhibitors to

amplification can interfere, resulting in false negatives.[67] Also the human body is well able to fight low levels of bacterial infection such that the results from amplification can be misleading, for example, low levels of Vibrio cholerae are readily dealt with by the innate human immune system, and only become a problem upon high levels of infection.[68]

While PCR alone only amplifies DNA it needs to be paired with a signalling system to measure the outcomes of amplification. In its simplest form gel electrophoresis is used to separate the fragments based on mass and successful amplification is determined through a band appearing. Other methods, such as real time quantitative PCR use fluorescently tagged primers or dyes that intercalate double stranded DNA, with an associated reader to provide rapid results.[69–71]

As described PCR is clearly a powerful technique but the equipment requirements and infrastructural overhead somewhat limits its reach outside of controlled laboratory settings. However, there is a significant body of work focused on solving these issues with a lab-on-a-chip / microfluidic approaches but currently these approaches still require the involvement of external heating blocks and/or reader.[72–74] Park provides a comprehensive overview of developments in this area.[75]

1.2 Point-of-Care Diagnostics

As powerful as the developments in the discussed 'traditional' methods are, they remain quite limited to laboratory-based diagnosis and in many cases specifically to labs in highly developed countries. This limitation is the area in which point-of-care assays can provide the maximum utility[76], providing diagnostic information in settings where either laboratory methods take too much time (i.e., acute care) or in settings where laboratory testing is not available at all either due to the cost of testing or general inaccessibility (i.e., rural areas and/or less developed countries). [77]

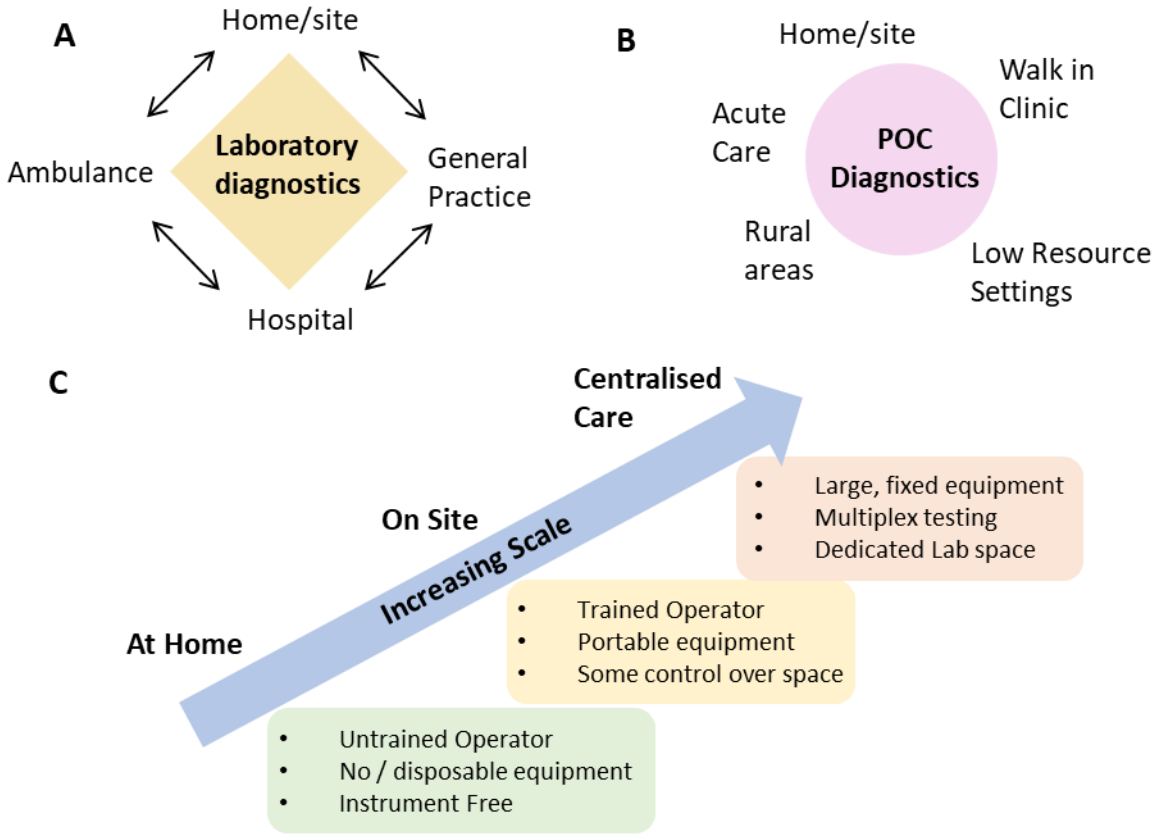

Figure 9: An overview of the way that POC diagnostics can fit within the broader diagnostic landscape. A) The applications of Lab-based diagnostics impacts a range of healthcare settings where samples can be taken and submitted centrally for analysis. These settings can be interlinked but require an advanced healthcare system and well equipped/funded laboratories. B) The settings for POC diagnostics are significantly different to Lab-based settings and may or may not be performed by a healthcare professional. C) Different healthcare setting can be categorised based on the scale and thus the availability of equipment and personnel. POC diagnostics focuses mostly on the At Home scale. Figure adapted from Anal. Chem. 2022, 94, 1, 26-40[76]

POC as a term is sometimes applied quite broadly in the literature and is not strictly defined. However, in 2003 the WHO published a set of criteria to describe ideal POC tests - known by the acronym ASSURED (affordable, sensitive, specific, user-friendly, rapid, equipment-free, delivered).[5,78] In the time since the publication of these criteria there has been a driving force in increasing interest, both research and commercial, on the challenge of creating POC tests. This ideally should encompass an entire system/method that runs from taking a sample from a patient all the way through to a diagnosis/result.

However, many methods that are labelled as POC do not fit the ASSURED criteria fully and only hit a subsection of the requirements. For example, the GeneXpert system (endorsed by the WHO for the rapid detection of tuberculosis)[79] which is based on nucleic acid amplification, is frequently included in POC categorisations but incurs significant costs (Instrument cost $17500 and between $2500-7000 just for installation)[80], requires trained personnel, and dedicated propriety instrumentation to effectively use. While on a per-test basis ($10)[79] it may be considered cheap in western, developed, healthcare systems the additional overhead costs and infrastructural requirements such as consistent electricity exclude it from the affordable and user-friendly requirements.

Currently the most viable approach to POC tests that best fit the ASSURED criteria is the lateral flow assay. These devices have already made a significant impact in low-resource environments where lab-based health infrastructure is inaccessible due to location, lack of infrastructure or cost.[81] They have provided benefit in the diagnosis of a range of notable diseases such as: COVID-19[82–84], HIV[85], Tuberculosis[86], Maleria[87], Syphilis[88].

A benefit of POC assays that are cheap and portable, which allow at-home diagnosis of infection, is that they minimise societal stigma associated with getting tested. [89,90]

1.3 Lateral Flow Tests

The type of assay that best meets the ASSURED criteria is the lateral flow test. It offers rapid results with acceptable sensitivity, detecting a range of biologically relevant analytes. It requires no additional equipment and is generally cheap, costing $0.10–$3.00 each.[91] It saw widespread use as a first line of testing against the COVID-19 pandemic, enabling at-home testing which made quarantine measures based on real diagnosis easier.[83]

While the basic physical structure of a lateral flow assay requires only a separation element (typically a nitrocellulose membrane) and a labelling and capture element (most commonly antibodies and antibody-gold nanoparticle conjugates),[92] in a commercial design additional elements are added to improve performance (Figure 10). This includes a sample dosing pad, a conjugate pad, and an absorbent pad.[93] A plastic housing case is used to contain the device and to apply pressure around the strip to ensure efficient flow.

The assay ‘runs’ by adding a fluid to the sample pad, followed by a running buffer if required. This is drawn up the device by capillary action, bringing the analyte through the conjugate pad and into the testing area. In the testing area, made of a test and control line, the analyte is bound by a labelling conjugate and captured onto the test line. Additional, unbound labelling conjugate continues to flow through the strip and is captured at the control line. The testing area generates a result which is either interpreted visually or spectroscopically.[94–96]

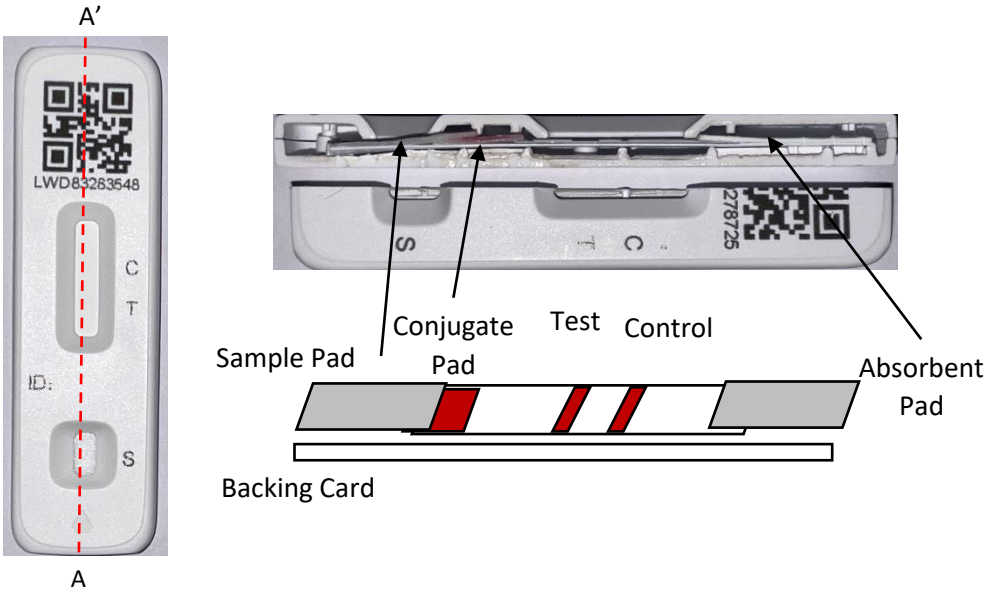

Figure 10: The make-up of a typical commercial lateral flow testing device encased in a moulded plastic housing (left).[93] Each of the components is laminated together onto a backing card with each section overlapping the next to allow fluid transfer up the device. Splitting the device in half (A – A') shows each component and its position in the device (top) and a diagrammatic representation for clarity (bottom) Mass produced testing strips can be manufactured for between $0.10–$3.00 each.[91]

The sample pad: serves two main purposes: to increase the volume of fluid that can be analysed in the test and, to ensure even transport of the sample to the conjugate pad. Typically, the sample pad is made from cellulose filters or a glass fibre mesh with the option of doping in surfactants, buffers, or proteins. The sample pad can serve a significant role in reducing the needs for sample pre-treatment. These modifications are highly dependent on the specifications of the device and the fluids intended to be sampled (e.g. blood, urine, nasopharyngeal swabs) and in many cases there are commercially available sample pad options designed to handle most common sample types.[97]

The conjugate pad: contains a labelling conjugate made from the combination of a signalling element (i.e., gold nanoparticles, quantum dots, latex beads) and a targeting element (most commonly an antibody) and allows the analyte to mix

uniformly with this conjugate before traveling through the nitrocellulose membrane. The binding to, and thus labelling of the analyte with the labelling conjugate happens at this stage. The conjugate pad is made of similar material to the sample pad with greater focus on good flow properties so that the analyte is labelled and is released to the nitrocellulose membrane consistently. Normally, the only major optimisation concerning the conjugate pad is the concentration of the labelling conjugate dosed onto it.[92]

Detection on nitrocellulose: As the labelled analyte flows from the conjugate pad it must travel along the nitrocellulose membrane where it meets the test and control lines. This is where the labelled analyte is captured and immobilised, concentrating the labelling in a single position creating a visible result. The choice of nitrocellulose as the membrane material is because antibodies (which are the most common targeting element) are readily immobilised, while the exact binding mechanism is not clear it appears to be primarily driven through strong hydrophobic interactions between hydrophobic sections of the protein and the nitrate ester groups.[98]

While labelled analyte should be captured and concentrated at the test line, excess unbound labelling conjugate flows over the test line and encounters another capture element that binds the labelling conjugate creating the control line. The control line acts as a check on the correct running of the test, showing both that the reagents correctly ran through the test and that the test was stored/manufactured properly. Incorrect storage could lead to a breakdown of reagents, especially when stored at high temperature where proteins could de-nature, meaning the validity of the test is called into question.[99]

The absorbent pad: manages the flow through the device and absorbs any waste fluid, indeed when using biofluids care must be taken to ensure that waste is managed carefully, especially in the case when infectious material may be present. Fluid from the absorbent pad will eventually diffuse back into the testing area, therefore a design requirement is to determine for how long the test remains readable.[100]

1.3.1 Signal Detection / Enhancement

In lateral flow assays the labelling conjugate allows the specific recognition of the analyte to become a detectable signal. Colorimetric signals are the simplest to detect by eye as changes in colour are straightforward to interpret without any expert knowledge. This is why the most common approach used in lateral flow tests it to use gold nanoparticles (AuNPs) to provide a clear response as a red line. This is discussed in greater detail in Chapter 4.

Whilst simple determination by eye and sensitivity increased through enhancement is sufficient for a test where a simple pass/fail result is required there are a variety of approaches to measure colorimetric responses quantitatively. Park provides a detailed review of a range of readers both commercially available and research, covering colourimetric, fluorescence, magnetic, photothermal and electrochemistry. [101] These readers enable new detection methods and can offer highly sensitive quantitative analysis; however, this generally comes with significant additional cost or equipment overhead.

Colorimetric results with AuNPs can be enhanced by the addition of sliver nitrate and hydroquinone/citrate buffer to the test area, precipitating a layer of silver on the

nanoparticles increasing contrast. This was shown by Bazsefidpar et al. who developed a test for *E. coli* O157:H7 which achieved a limit of detection (LOD) of 2 × 10^6 CFU/ mL with standard AuNPs which was improved to 2 × 10^3 CFU/mL after the silver enhancement procedure.[102]

A key focus for the quantitative analysis of lateral flow assays in low-resource environments has been the development of cheap smartphone-based detection systems instead of more costly commercial detectors.[103,104] Jung et al developed a 3D printed holder and app for smartphone-based quantification of a commercial lateral flow test for E.*coli* O157:H7.[105] While the LOD was not improved compared to standard tests (10^4-10^5 CFU/ml) the advantage was that it was able to provide quantitative results between 10^4 CFU/ml to 10^6 CFU/ml rather than only qualitative.

This approach can be expanded to include more advanced detection with Rajendran et al. showing the smartphone detection of methicillin resistant *S. aureus* using PCR with fluorescent primers on a lateral flow assay.[106] Their 3D printed smartphone holder included a cheap LED for excitation, with the total cost of the reader $26 and achieving a LOD of 4.7 × 10^3 copies of DNA.

Binding Strategies: Sandwich vs Competitive

There are two binding formats that a lateral flow assay usually involves based on the arrangements of binding elements at the test line: a so-called sandwich assay or, a competitive binding assay.

Sandwich assays: more common in the analysis of larger molecules and proteins[107] and works by having a pair of targeting elements binding an analyte ‘sandwiching’ it. On one side the labelling conjugate (AuNP-antibody conjugates for example) and

on the other side is a second binding element fixed to the test area to capture the analyte at the test line. (Figure 11).

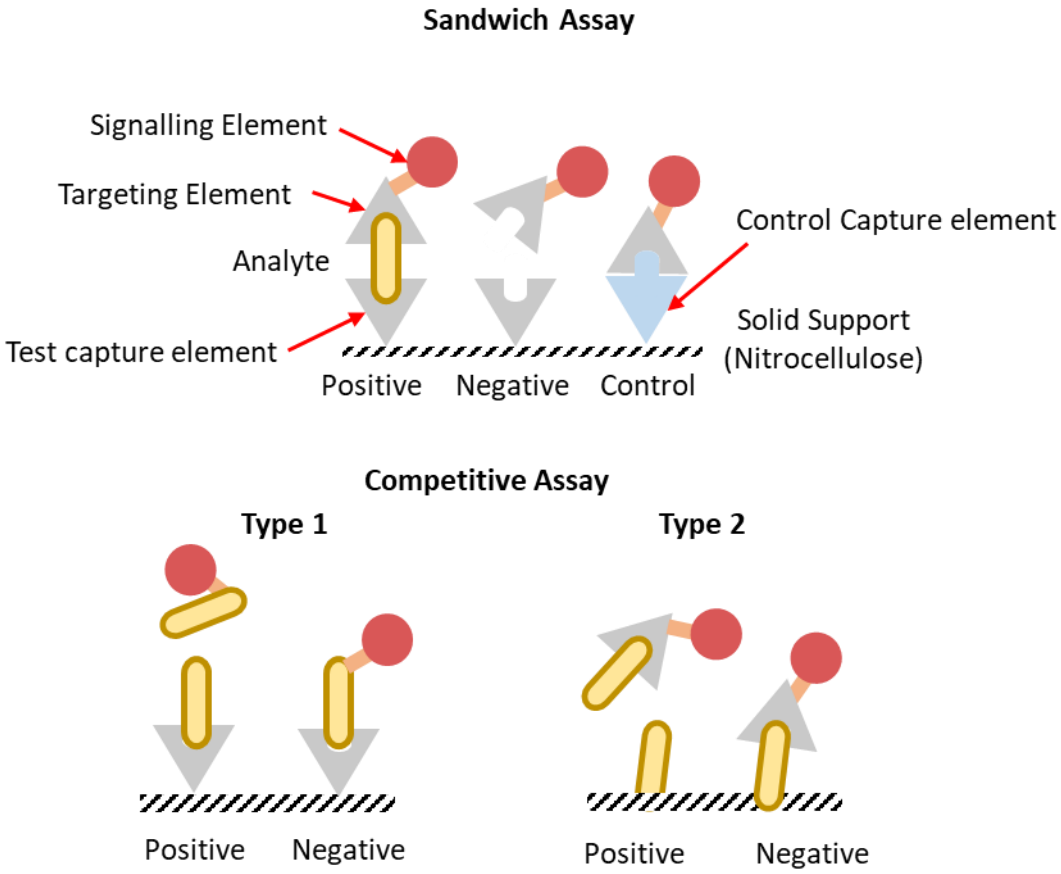

Figure 11: The possible layouts for a sandwich assay (top) and for competitive assays (bottom) as used in lateral flow tests. The sandwich assay uses a labelled targeting element and a targeting element to capture the analyte to the test line. Positive results yield a coloured test line. Competitive assays can be classified into two types based on the positioning of the signalling element. Type 1 shows a competitive assay where pre-labelled analyte is present thus showing no colour when the test analyte is present. Type 2 shows an assay where the bio receptor is labelled but the test line is made from the target analyte.

Competitive assays: can be designed in two ways depending on whether the analyte or antibody is labelled (Figure 11). They only require a single antibody to bind to the analyte which allows the sensing of small molecules. In a type-1 competitive assay, a pre-tagged analyte is synthesised and loaded onto the test prior to the sample addition. An antibody or aptamer is typically immobilised in the testing area. When

the sample is run there is a competition between the tagged and untagged analyte for the available binding sites. In a type-2 competitive assay the antibody is tagged with the visualising agent and loaded into the conjugate pad and the target epitope is fixed to the test line. This means there is competition for the antibody between the fixed analyte and the sample analyte. In both cases the signal generated from a competition assay is the reverse of a sandwich assay with the intensity of colour on the test strip decreasing with increasing analyte concentration.[107]

For comparison Frohnmeyer et al. used both a type 1 and 2 competitive assay format assay for the aptamer based detection of cholera toxin, an 83 kDa protein produced by the bacterium *Vibrio cholera*.[108] However, for detection of the comparatively larger whole bacteria Yu et al. used a sandwich style lateral flow assay using antibodies against the serogroups O1 and O139. [109] (Figure 12)

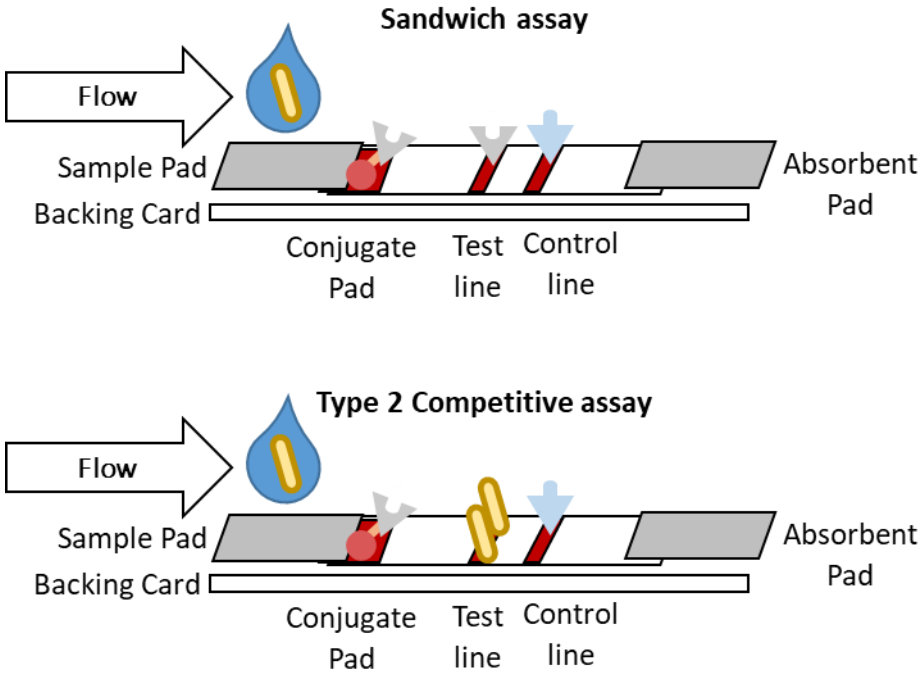

Figure 12: The generalised layout of components on a sandwich assay (top) and type 2 competitive assay (bottom) design lateral flow test. The analyte is added in solution to the sample pad and flows

through the test. The conjugate pad contains a labelled targeting element which binds to the analyte. In a sandwich assay, the labelled targeting element – analyte complex is trapped at the test line providing visible results while any excess labelled targeting element flows to the control line or is washed into the absorbent pad. In a type 2 competitive assay, the test line contains the analyte and will only trap the labelling conjugate when no analyte is present in the sample.

One disadvantage of sandwich assays comes from the 'high dose hook effect'.[110] This is an effect seen when a sandwich assay is over saturated with the target analyte in excess of available targeting conjugate. This means that the untagged analyte is free to flow ahead of the bulkier tagged analyte. The free analyte then saturates the binding capacity of the testing area, blocking the tagged analyte from binding. This results in a drop off in signal intensity at extremely high concentrations, a concern when trying to design quantitative assays. Validation of sandwich type lateral flow assays requires that an upper limit on concentration is determined, beyond which the test is no longer valid.[111]

Each of the main components described above are laminated onto a card backing strip with a small overlap between them to allow flow along the assay from component to component. The test and control lines made of the appropriate targeting elements are printed onto the nitrocellulose and the labelling conjugate dried onto the conjugate pad. The exact size and position of each of these elements can vary based on the test and its optimisation. An interesting area of research and development is the expansion of binders used in lateral flow tests to include aptamers or novel, rationally designed compounds.

1.3.2 Targeting Elements

Antibodies

The most commonly used targeting element in lateral flow tests are antibodies, which are symmetrical Y-shaped glycoproteins with a molecular weight of approximately 150 kDa generated by the immune system to bind a specific site on an antigen (Figure 13). A single antigen can have many different such sites, known as epitopes, which can be targeted by antibodies. They bind to an epitope through highly specific non-covalent interactions at the antigen binding site. With a high binding affinity between the epitope and the antibody they can be treated as highly specific ligands for an analyte.

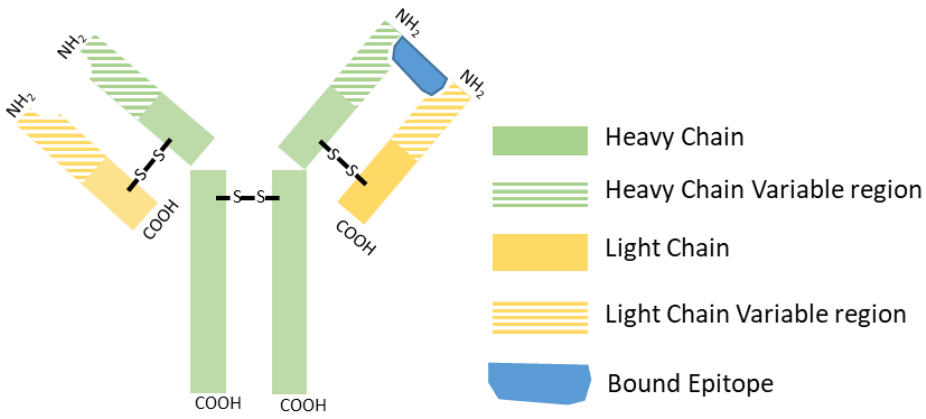

Figure 13: A general structure for an antibody which is comprised of two principal areas, a heavy chain (green) and a light chain (yellow). The variable regions (striped green and yellow) that bind to an epitope.

As an antigen can have many different epitopes that antibodies can target, a collection of antibodies is created in an immune response. These are known as polyclonal antibodies, which all act against the antigen but can have varying strengths of binding due to the differences in epitopes and the antibodies generated. For research and development applications monoclonal antibodies are frequently

used instead. These are antibodies for a single specific epitope, and therefore have a single site binding affinity. This creates more consistent binding behaviour which is useful for reliability and control of the process.

Antibodies are the most common targeting element for lateral flow tests with a range of useful properties such as simple conjugation to nanoparticles, binding to nitrocellulose membranes through hydrophobic interactions and their availability to a range of bacteria.

Simple antibody-based lateral flow tests have been applied in the detection of important bacterial strains such as: *E. coli*[112], *Yersinia pestis* [113] and, *Mycobacterium tuberculosis*[114]. These assays achieve sensitivities in the 10^4 - 10^5 CFU/mL range which can be sufficient for clinical use in many situations.

As antibodies are highly selective, lateral flow tests using them can be multiplexed to simultaneously test for a number of bacteria at the same time. Zhao et al developed an assay to detect 10 foodborne pathogens simultaneously using 10 parallel lateral flow tests all fed from a common sample pad.[115]

An interesting use case of antibody-based assays is in the development of tests directed at measuring the immune response to a disease. For example, Huang et al. describe the development of a competitive lateral flow assay testing for the presence of human IgM antibodies against SARS-CoV-2 nucleoprotein in patient serum samples.[116] This assay used anti-human antibodies conjugated to AuNPs and achieved a sensitivity and specificity 100% and 93% respectively only requiring 10-20 µL of serum for each test.

Nanobodies

An alternative to using entire antibodies is the application of nanobodies. These can be considered to be ‘just’ the variable region of a heavy-chain only antibody (approximately 15 kDa fragments) isolated primarily from Camelids.

Nanobodies provide the same highly selective binding but also exhibit resistance to heat and detergents. A particularly useful feature due to their smaller size compared to ‘full’ antibodies is that they can be efficiently produced through recombinant methods.

For example, Maher et al developed a lateral flow test for the SARS-CoV-2 S1 antigen and compared the effectiveness of gold conjugates made with anti-S1 nanobodies to anti-S1 monoclonal antibodies.[117] They used the same assay design and manufacture, with the substitution able to improve the limit of detection by 4 fold across 320 patient samples.

Pinto Torres et al. specifically chose nanobodies over antibodies for their lateral flow assay to detect active *Trypanosoma congolense* (a parasite that causes Animal African trypanosomiasis) infections due to the lower non-specific binding compared to host antbodies.[118] As their aim was to identify animals with an active infection, interference from the hosts own immune system could cause false negatives. They were able to show that a nanobody based lateral flow test could achieve sensitive and specific detection for the active infection and could also serve as a ‘test-of-cure’ assay.

Aptamers

The most common alternative to antibodies are aptamers. These are short (40 mers) single-stranded DNA (ssDNA) or RNA sequences which bind to target analytes like an antibody. Aptamer sequences are identified through the 'systematic evolution of ligands by exponential enrichment' known as the SELEX (Figure 14).[119]

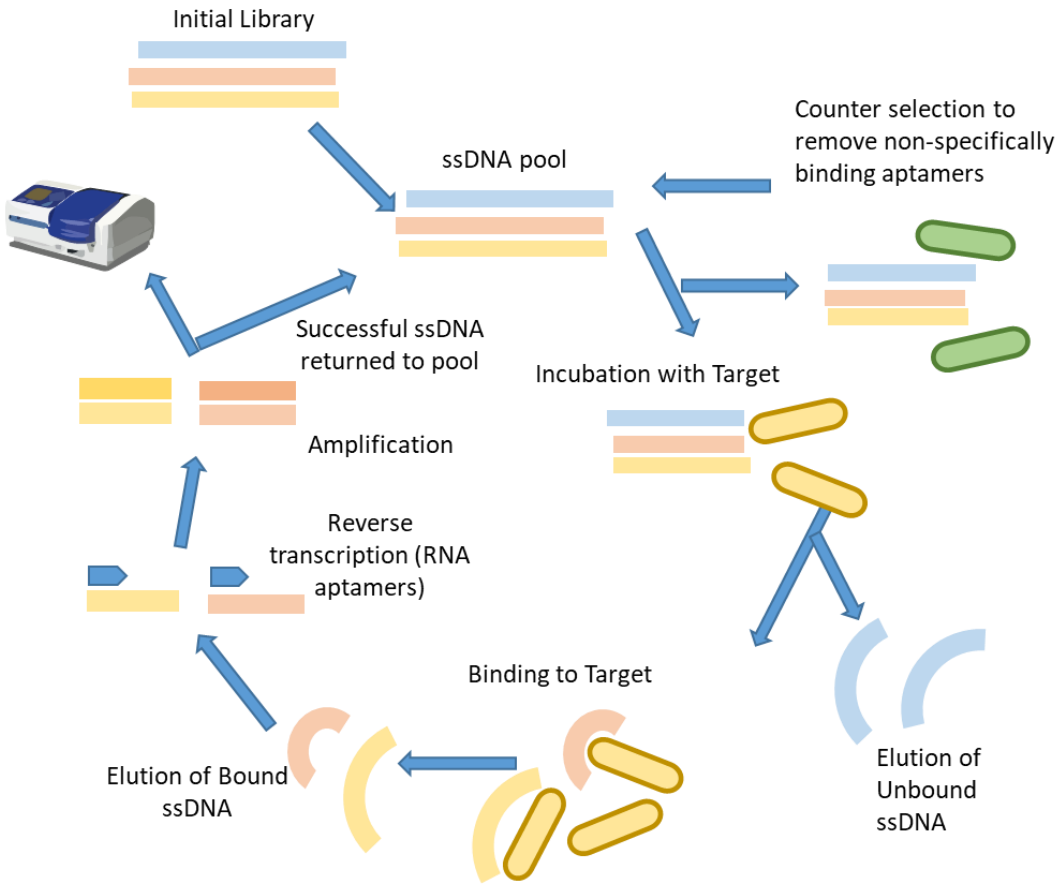

Figure 14: The standard SELEX process for the production of aptamers against a specific analyte. Additional steps such as a counter selection against non-specific binding can be added to further refine the process. Successive selection cycles refine the ssDNA pool down from the initial library to identify the best overall binders. Total number of cycles and the size of the initial ssDNA library can vary depending on the application. Adapted from Biotechnology Advances, 33, 6, 2015, 1141-1161[120]

They have particular advantages over antibodies when applied in lateral flow tests. They are synthesised, allowing targeting of non-immunogenic analytes, and can have a broader range of stabilities to temperature and pH. Bauer et al comment on the

advantage of the highly reproducible nature of synthetic aptamers when compared to polyclonal antibodies that can frequently have poor batch-to-batch reproducibility or experience genetic drift after multiple passages of the antibody producing cells.[121]

They can be paired with the same signalling techniques as antibodies such as conjugation to nanoparticles and are readily conjugated to a variety of chemistries.[122] Aptamers have been used in POC bacteria detection assays across a range of species with a high sensitivity.[123] However, while aptamers can replace the binding ability of antibodies in assays, they do not always interact with the nitrocellulose membrane of a lateral flow test in the same way as they are much smaller and do not experience the same hydrophobic interactions to bind them to the membrane. Often this issue is circumvented by pairing an aptamer labelling conjugate with an antibody capture element.

Ellipilli et al developed an aptamer based lateral flow test for SARS-CoV-2 targeting the spike proteins, comparing AuNP-aptamer conjugates produced through direct thiol attachment vs a streptavidin-biotin system.[124] They paired these aptamer labelling conjugates with an anti-SARS-CoV-2-S2 antibody as the capture element. They showed that this combination of aptamers and antibodies within the same test was able to achieve highly sensitive detection and potentially allow the rapid iteration of labelling aptamers to respond to mutations in the virus while keeping a more broadly binding capture element.

Lu et al developed an aptamer-based lateral flow test for the combined detection of *S. typhimurium*, *E. coli* and *S. aureus* with LOD of 10^3 CFU/mL, 10^4 CFU/mL, and 10^4 CFU/mL respectively.[125] This used 6 aptamers, three with terminal thiol groups for addition to AuNPs and three with terminal biotin groups. These terminal biotin

molecules were used to attach the aptamers to the nitrocellulose through a Streptavidin-Biotin interaction, using the hydrophobic interaction of Streptavidin (a 66kDa protein with high affinity for biotin[126]) to anchor onto the strip..

Aptamers can also be paired with a range of reporters as shown by Bruno who used aptamers against *E. coli*, *L. monocytogenes*, and *S. enterica* and compared AuNPs with fluorescent quantum dots to achieve LODs of 10^4 CFU/mL and 10^3 CFU/mL respectively.[127] The aptamers were bound to the AuNPs and quantum dots through Streptavidin-Biotin interactions and fixed to the nitrocellulose by UV crosslinking.[128]

1.4 Application of bacteria testing in healthcare

Understanding how these bacteria detection methods can be applied in the context of healthcare in the United Kingdom specifically can be done with reference to the National Institute for Health and Care Excellence (NICE) guidelines. These guidelines provide decision flow-charts to doctors that can aid in the clinical evaluation of disease and the prescription of antibiotics (Figure 15).[35] For example, when treating a patient presenting with a sore throat a flow chart can be used to select between a range of outcomes between doing nothing all the way up to referral to hospital.

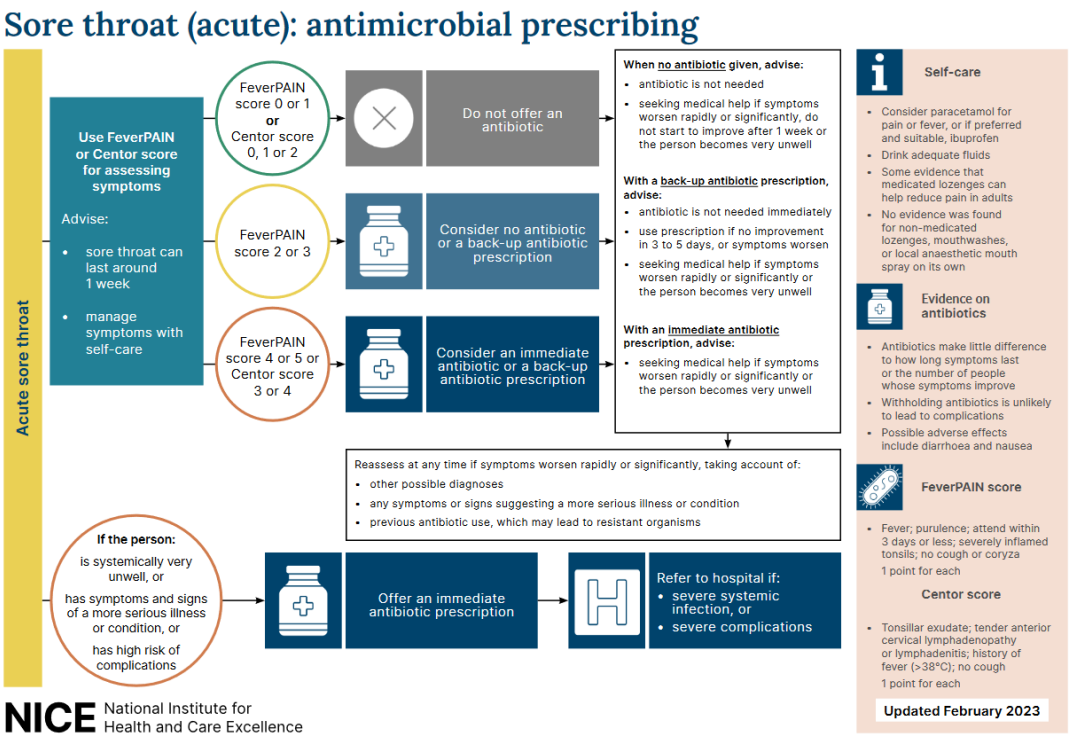

Figure 15: NICE flow chart for the treatment of patients presenting with sore throats highlighting the different antibiotic outcomes that are possible. Reproduced from NICE guideline [NG84] under the NICE UK Open Content Licence.[129]

A key feature of this particular guidance is that for a relatively low-risk issue such as a sore throat, antibiotics are often prescribed on the basis of signs and symptoms without any bacterial testing at all. At this level, simply identifying if the infection is bacterial or viral would be clinically useful, with the identification of exact bacterial species becoming more relevant in hospital settings and more severe infections. Introducing any level of testing here could help support clinical decision making and reduce the over prescription of antibiotics for non-bacterial diseases.

With this in mind, each of the discussed detection methods (Lateral flow, Mass Spec, PCR and, Culturing) can be loosely categorised based on four key properties (cost, speed, sensitivity and, selectivity) that could influence their application in such a situation (Figure 16).

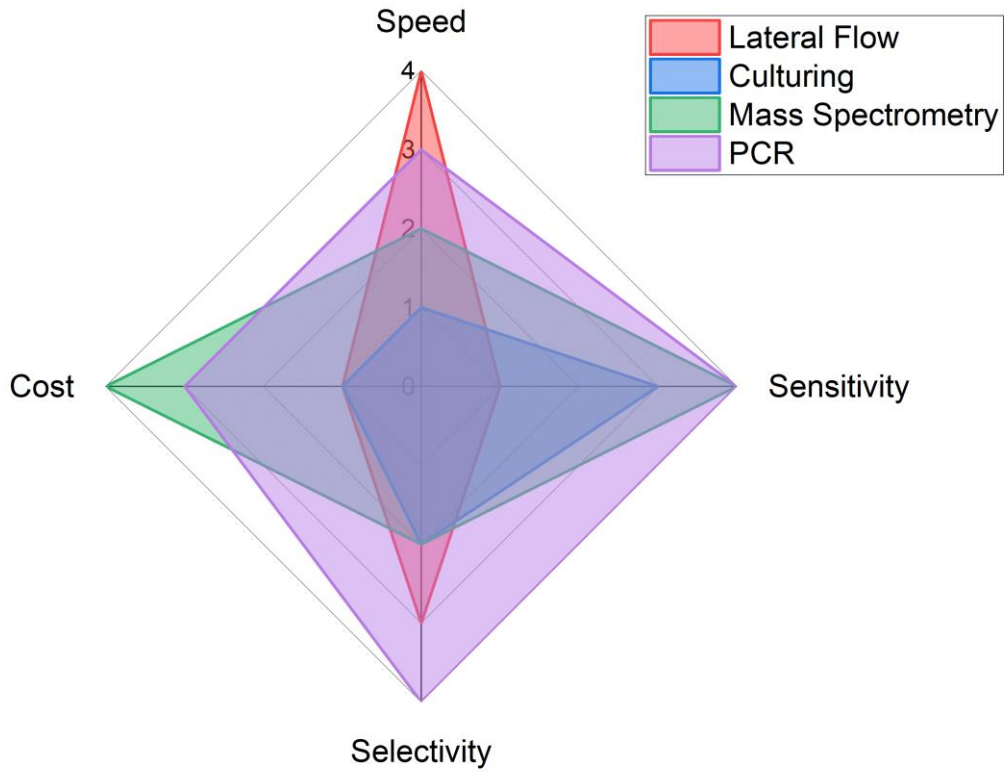

Figure 16: Comparison of four bacterial testing methods on the basis of four categories that can influence their application in healthcare settings. Cost refers to the overall cost of implementing the technique (including equipment) not just the per test cost. Speed refers to the time to result from taking a sample from the patient. Sensitivity refers to the limit of detection that the technique can achieve, and selectivity refers to the technique's ability to discriminate between species of bacteria.

Each of techniques offers a different range of characteristics but of particular interest for this project was the low cost and high speed of lateral flow tests. While traditional lateral flow immunoassays offer a moderate degree of discrimination between bacterial species, for an application such as seen in the 'sore throat scenario' a less selective (i.e. more broad) test could be used to rapidly determine if an infection was bacterial in nature.

2 Aims and Objectives

The aim of my PhD thesis was to develop a small molecule-based sandwich assay style lateral flow test that can detect Gram-negative bacteria. To achieve this the component parts of a lateral flow test: a recognition element that selectively binds Gram-negative bacteria a signalling element (based on AuNP's) and a capture element were developed.

A chemical probe based on the Gram-negative selective antibiotic Polymyxin was utilised. For detection, the aim was to modify Polymyxin to allow functionalisation of AuNPs while additional functionality was developed to fix Polymyxin to the nitrocellulose membrane to allow for the capture of bacteria through streptavidin-biotin anchoring.

These elements were then combined into the lateral flow format, paired with a 3D printed, low cost, smartphone-based imaging system for characterisation/ optimisation.

3 Synthesis of Bacterial Binding Ligands

Antibodies and aptamers currently used in lateral flow systems for bacterial detection tend to be highly selective for specific strains of bacteria.[125,130–132] This is a product of their selection that directs the identification of ligands with target elements (often undefined) on the bacteria.[133–135] These highly selective ligands are useful when designing an assay for a known pathogen, but in many cases it would be useful to have an assay that is more general; such as Gram status determination, or bacterial/fungi differentiation to direct immediate therapy.[136,137]

The design of ligands for a novel lateral flow test can be based on compounds that have known binding affinities for bacteria. Antibiotics such as Polymyxin B are relatively low cost, manufactured at scale and offer a scaffold for a range of potential assays. Here, a range of ligands targeting Gram-negative bacteria were prepared based on the antibiotic Polymyxin B.[138,139]

3.1 Polymyxin

Polymyxins (Figure 17) are a class of antibiotics isolated from *Paenibacillus polymxa* that were discovered in the 1940s and introduced into the clinic in the late 1950s and 60s. Thirty-seven naturally derived variations of the polymyxin structure are known and Polymyxin B and E were identified as the least nephrotoxic.[140,141] Clinical use declined from the 1970s as cases of neuro- and nephrotoxicity became widely reported.[142] However, there has been revived interest in them over the last 20 years as increasing cases of multi-drug resistant *P. aeruginosa*, *A. baumannii* and *K. pneumonia* have needed to be treated despite the associated risks.[143]

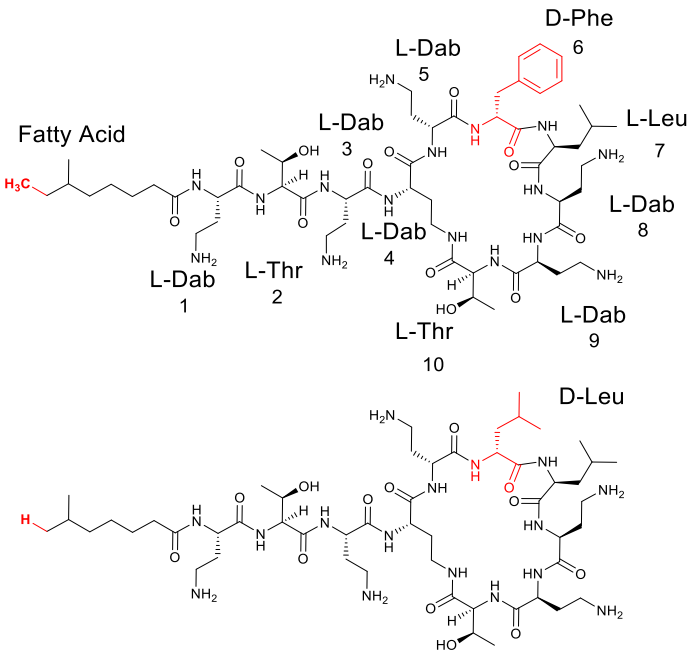

Figure 17: Structure of two clinically relevant polymyxins B1 (top) and E2 (bottom) showing the structural similarities and differences in the aliphatic tail and the substitution of a Phe residue with Leu. From the numbered amino acid positions, the main variable positions across the polymyxin types are 3, 6, 7 and 10. The most conserved amino acids are primarily L-Dab residues which provide the charges required for the electrostatic interaction between polymyxins and Lipid A. At physiological pH the amines will be largely protonated.

Polymyxins specifically interact with Lipid A (Figure 18), a constituent part of the lipopolysaccharide (LPS), present in the outer membrane of Gram-negative bacteria.

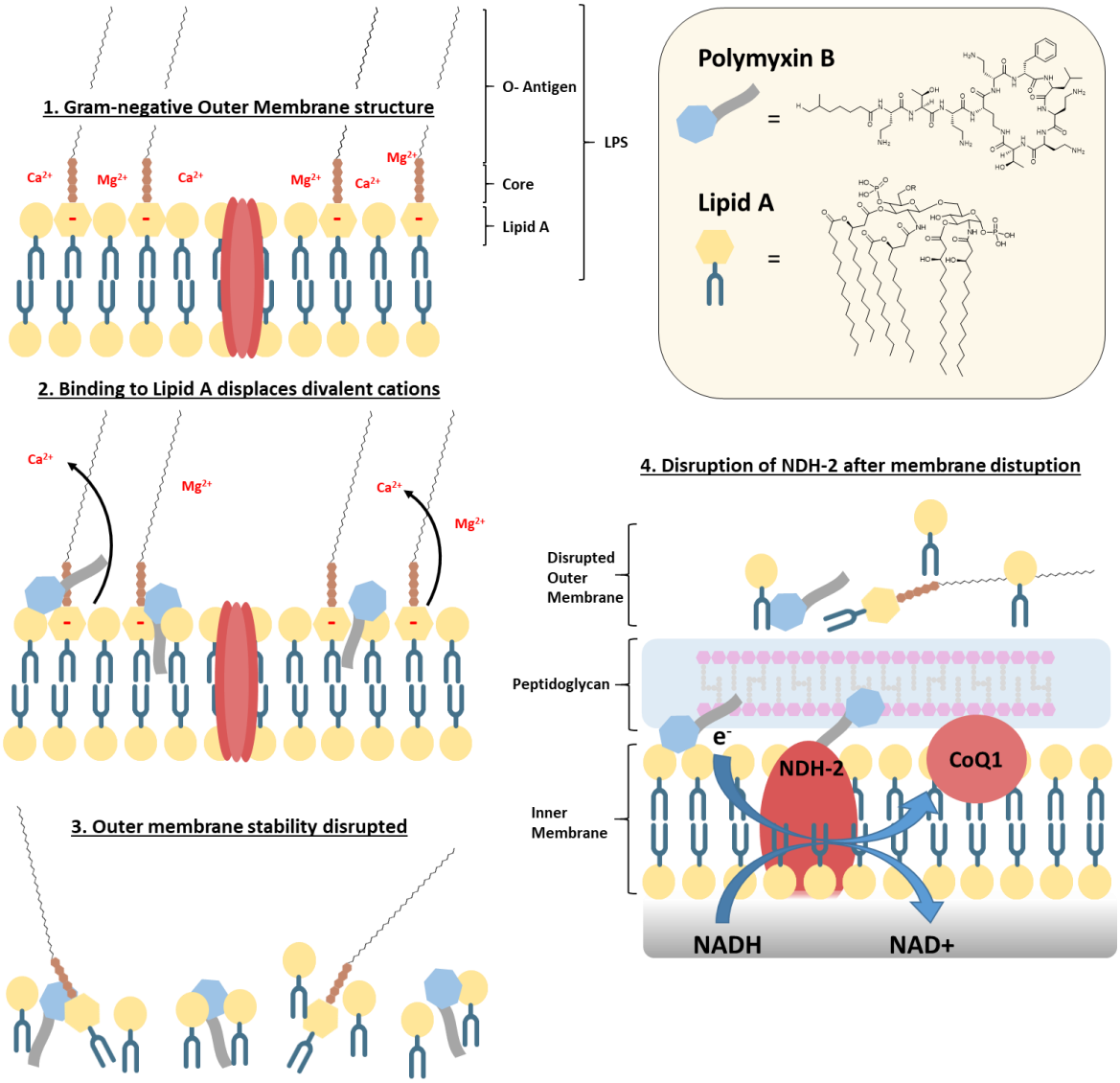

Figure 18: The mechanism by which Polymyxin's interaction with the outer membrane of Gram-negative bacteria results in the disruption of cell integrity and inhibition of NDH-2. 1) The structure of an unmodified Gram-negative outer membrane. 2) The binding of Polymyxin to Lipid A displaces the Ca^{2+} and Mg^{2+} ions and the aliphatic tail intercalates with the hydrophobic areas of the membrane. 3) Stability of the membrane is disrupted and structurally fails. 4) The failed outer membrane allows access to the inner membrane where NDH-2 action is disrupted. Adapted from 'Polymyxin Antibiotics: From Laboratory Bench to Bedside' by Li et al. Springer Cham 2019 [144]

Permeabilizing this outer membrane causes the collapse of bacterial integrity and is the primary mode by which polymyxins kill bacteria.[144] There is also evidence that polymyxins might also act on bacterial respiration by inhibiting the action of NADH-menaquinone oxidoreductase (NDH-2) present in the inner membrane of Gram-negative bacteria.[145]

Studies have shown that two key structural motifs are conserved across the different Polymyxin structures that drive their mode of action:

- Initial long-range interactions with the LPS and displacement of divalent cations are mediated through the 5 x diaminobutyric acid (Dab) residues (the free $-NH_3^+$ groups binding to the phosphates in Lipid A).
- Shorter range hydrophobic interactions with the acyl chains of Lipid A are controlled by the residues in positions 6 and 7 paired with the hydrophobic chain on the amino terminus.[146]

The key importance of these hydrophobic interactions is shown by the removal the hydrophobic tail from Polymyxin B (Figure 19).[147]

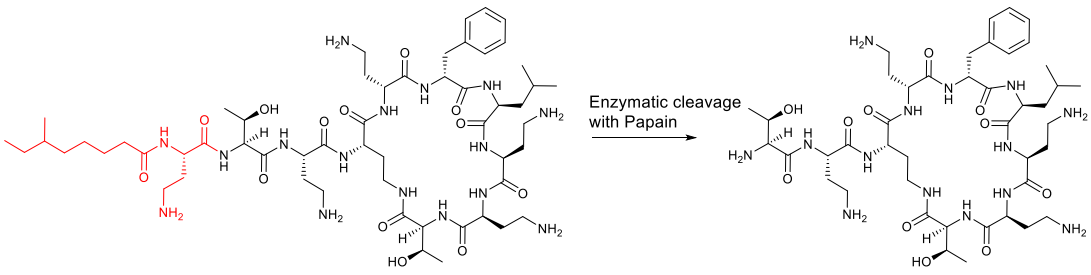

Figure 19: Cleaving the hydrophobic tail and terminal Dab residue (red) of Polymyxin B1 to produce Polymyxin B nonapeptide (PMBN) with papain in aqueous conditions.

The in vitro activity of this truncated Polymyxin B was reduced 64 fold against *E. coli* and *P. aeruginosa* and 32 fold against *K. pneumonia.*[148] Interestingly, despite reduced antibacterial activity, binding still increased the permeability of the outer membrane[149], sensitizing bacteria to combination therapy with other antibiotics.[150] The truncated cyclic peptide also showed minimal nephrotoxicity indicating that the hydrophobic tail is a key promoter of renal toxicity. [151]

Mechanistic understanding of the structure-function relationship has been further explored by the synthesis and analysis of analogues of Polymyxin. Reviews provide

a comprehensive overview of Polymyxin derivatives covering substitutions, modifications and deletions of amino acids.[146,152] Many modifications result in inactive compounds, largely because the focus has been on modification of the Dab residues and substitution of the hydrophobic tail, key functional elements in the mode of action. However, some modifications are able to improve activity such as those shown by Cooper *et al.* who investigated a range modifications and showed that altering the residues at positions 6/7 (Figure 15) to give increased hydrophobicity, increased activity against resistant bacteria but at the expense of increased nephrotoxicity.[153]

Li *et al.* explored modification and replacement of the hydrophobic tail, Thr-2 and Thr-10 residues through solid-phase peptide synthesis (SPPS) and semisynthetic methods. Their modifications showed that analogues that replaced the Thr residues with more hydrophobic ones improved the MIC and altered the selectivity of the antibiotic towards different bacterial species depending on the substitution pattern (Figure 20). [154]

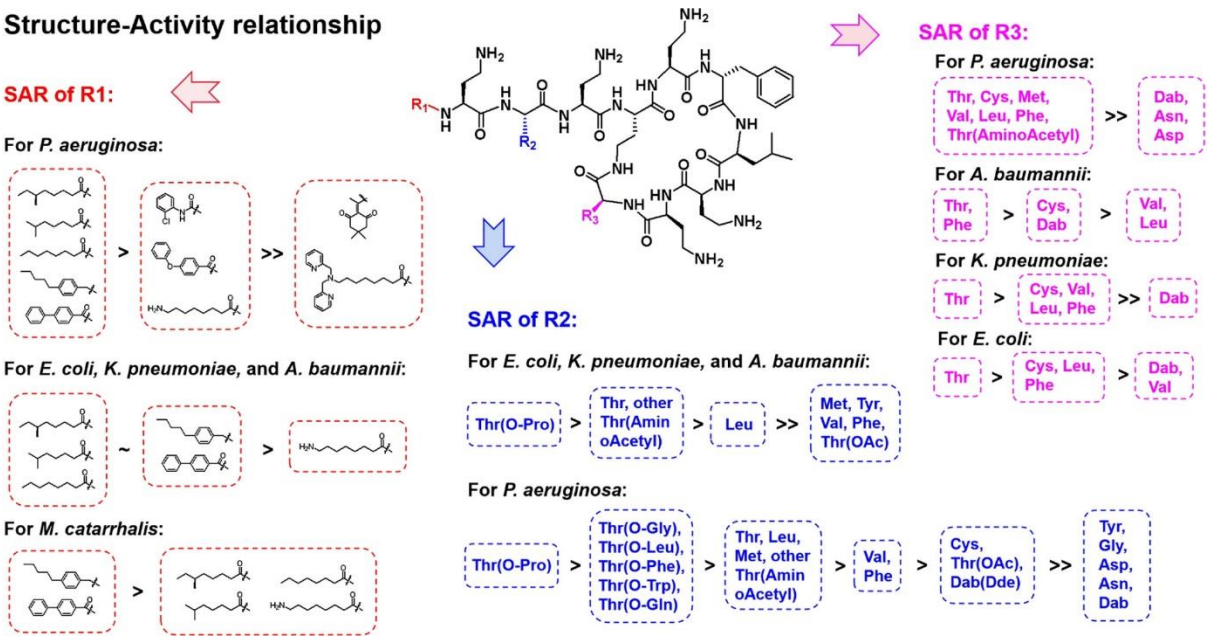

Figure 20: Structure-activity relationship explored through modification of the hydrophobic tails (R1), Thr-2 (R2) and Thr-10 (R3) residues. Reprinted with permission from Li et al. *J. Med. Chem.* 2021, 64, 9, 5746–5765. Copyright 2021 American Chemical Society.

Beyond investigations aiming to improve Polymyxin's abilities as an antibiotic, there have been a range of applications of Polymyxin as bacterial targeting/detection probes. Early work by Schindler *et al.* used Dansyl chloride to randomly functionalise Polymyxin B for subsequent fluorescent microscopy studies[155] but resulted in a complex mixture of isomers all with different binding abilities.

As the understanding of polymyxin has grown, functional applications of polymyxin have been expanded to include selective fluorophore addition[138,156,157], incorporation into polymers[158,159] and addition onto nanoparticles.[160] These applications have often followed semi-synthetic approaches, involving modification of the tail rather than addition/modification of the Dab residues.

As mentioned above, Polymyxin has been used in bacterial labelling applications through direct functionalisation with a fluorophore.[138] A different approach is to separate the labelling and binding processes, and perform a secondary labelling

similar to the use of secondary antibody-enzyme conjugates in enzyme-linked immunosorbent assay(s) (ELISA).[161] Among the most commonly used pairs for secondary labelling approaches is the use of streptavidin-biotin[126] and the following section describes the nature of this interaction and the modification of polymyxin with biotin.

3.2 Streptavidin – Biotin

Streptavidin and Avidin are proteins with an extremely high binding affinity for the small molecule biotin (vitamin B7) with a dissociation constant (K_D) on the order of 10^{-15} M and this interaction is highly resistant to temperature, pH and detergents/surfactants. [162]

Equation 1 $$Streptavidin + Biotin \underset{k_{off}}{\overset{k_{on}}{\rightleftharpoons}} [Streptavidin - biotin\ complex]$$

Equation 2 $$K_D = \frac{k_{off}}{k_{on}} = \frac{[Strep][Biotin]}{[Strep{-}biotin\ complex]}$$

The kinetic constants of protein binding for the streptavidin-biotin pair are reported in literature, with the dissociation constant (K_D) being a measure of the ratio of the backwards and forward rate constants for the binding event or the ratio of [X][Y]/[X-Y].

This high binding affinity was originally measured through a radiolabelled biotin assay by Green giving $a\ K_D$ of 10^{-15} M for a single binding site with a k_{on} of 10^7 M^{-1} s^{-1} and a k_{off} of 10^{-8} s^{-1} between pH 5 and 7.[163] These kinetic parameters have since been investigated with a variety of methods such as Reed *et al.* measuring the

kinetics on a silicon nanowire biosensor and reporting similar values with a k_{on} = 5.50 ± 0.08 × 10^8 M^{-1} s^{-1} and a k_{off} = 3.10 ± 0.07 × 10^{-5} s^{-1} resulting in a K_D of 5.6 × 10^{-14} M.[164] Edel *et al.* used a FRET based microfluidic system and reported a k_{on} in the range of 3.0 × 10^6 − 4.5 × 10^7 M^{-1} s^{-1}.[165] Harris *et al.* used a single-molecule imaging system and reported values of: k_{on} of 2.1 ± 0.5 × 10^8 M^{-1} $s^{-1}$and a k_{off} 3.8 ± 0.5 × 10^{-4} s^{-1} resulting $in\ a$ K_D of 1.8 × 10^{-12} M.[166]

These properties have meant that the pair are widely used for tagging and labelling targets of interest.[167] Kulomaa *et al.* provided a comprehensive review of the properties of a range of (strept)avidins and genetically modified variants for specific applications.[168]

Applications of the binding pair have spanned a wide range of fields such as: ELISA[169], self-assembled monolayer surface bound sensors [170–172] and as part of a detection method in lateral flow tests. For example, Zhao *et al.* developed a lateral flow assay using an *E. coli* O157:H7 targeting antibody functionalised with biotin, captured by streptavidin immobilised on the test line (Figure 21).[173]

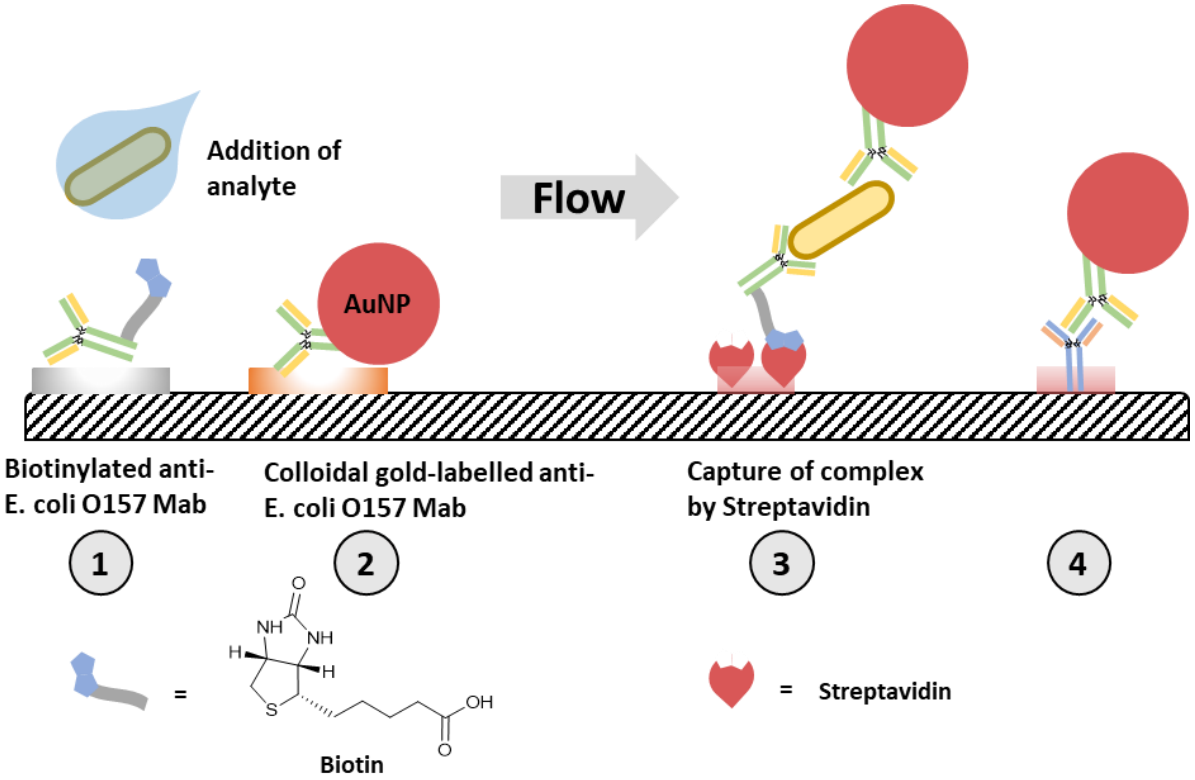

Figure 21: Design of an *E. coli* detecting lateral flow test from Zhao *et al.* 1) A biotinylated antibody was added to the sample pad and bound to the *E. coli*. 2) Gold nanoparticles labelled with anti-*E. coli* O157 Mab were also added to the conjugate pad and attach to the *E. coli* complex from 1. 3) The complete *E. coli*-complex is captured by streptavidin in the test line area through the pendant biotin. 4) A second antibody complementary to anti-*E. coli* O157 Mab captures the AuNP complex from 2 to provide a test line.

A different application of the streptavidin-biotin system was shown by Cho *et al.* using a combined biotin-AuNP-antibody conjugate as the detection agent and adding streptavidin conjugated with horseradish peroxidase (HRP) as a secondary detection conjugate (Figure 22). On the addition of a 3,3′,5,5′-tetramethylbenzidine (a substrate for HRP), enzymatic turnover generates a blue colour that enhances the detectable signal from 10^5 CFU/mL to 10^2 CFU/mL.[174]

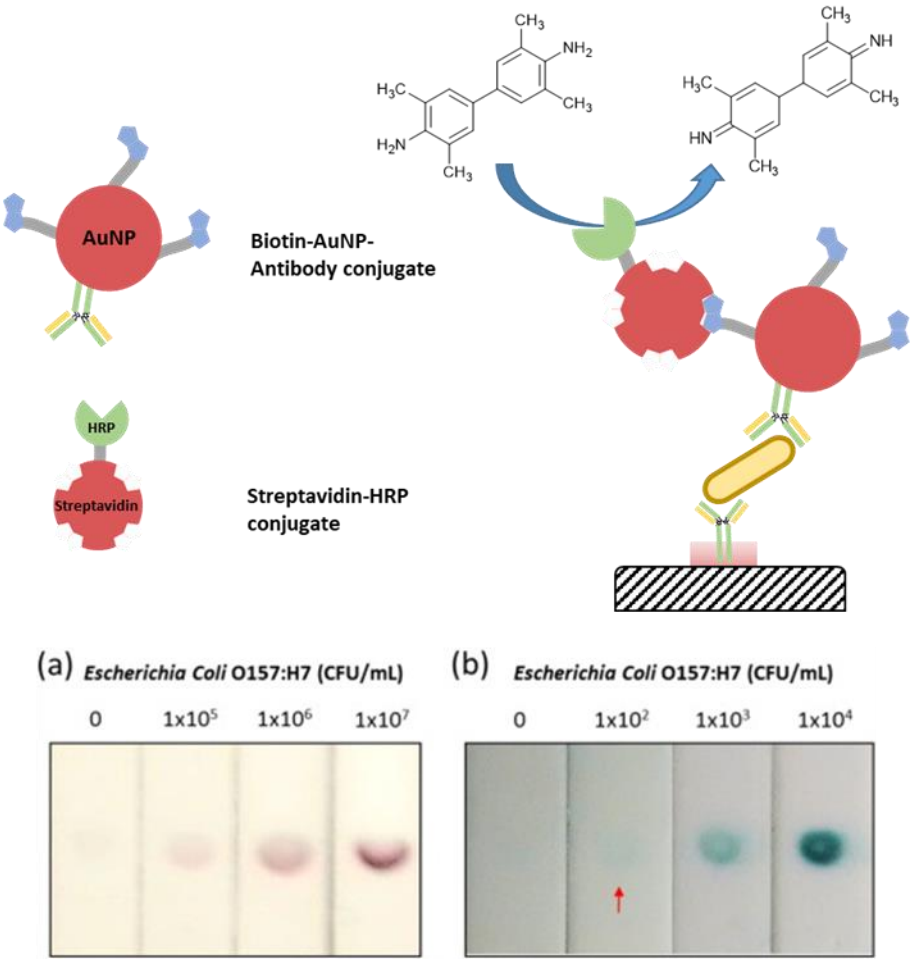

Figure 22: Design of the signal amplification strategy used by Cho *et al.* based on the binding of streptavidin-biotin allowing the capture of HRP to the test line and turnover of TMB. Images of strips:(a) detection with biotin-AuNP conjugate (b) detection with secondary streptavidin-HRP conjugate reproduced from Int. J. Food Microbiol., 2015, 206, 60–66 with permission from Elsevier[174]

While streptavidin-biotin is typically treated as a near-covalent binding system Holmberg *et al.* showed that the interaction can be broken through heating at 70 °C in water, theoretically allowing the reuse of assays based on streptavidin coated surfaces.[175]

Many commercially available biotinylation kits provide biotin with a range of spacer lengths and moieties, but there is not a general optimal spacer length for the streptavidin-biotin interaction. Hamblett *et al.* showed, using a polyethylene glycol (PEG) spacer system, that increasing the spacer length from 29 Å to 40 Å improved

binding of biotin dimers to streptavidin because of greater distance between biotins and increased flexibility of the spacer.[176] Anastasiadis *et al.* used aminocaproyl spacers when optimising binding between biotinylated non-ribosomal peptides Gramicidin A and Avidin and showed that increasing the spacer length improved binding specifically by reducing steric hindrance.[177] However, maximising spacer length was not always optimal as Rosenthal *et al.* showed that a biotinylated poly(N-isopropylacrylamide) functionalised surface performed better using a PEG_3 spacer rather than a PEG_{23} spacer.[178]

Aims

The aim of this part of my PhD was to carry out the selective functionalisation of polymyxin B to create compounds that could both bind to Gram-negative bacteria and to a labelling element such as gold nanoparticles. To achieve this, synthesis of selectively protected Polymyxin B nonapeptide on a suitable scale to provide a core building block was required (Figure 23). Each target compound needed to be bi-functional, with the Polymyxin B nonapeptide providing specific binding towards Gram-negative bacteria and, extending from the N-terminus, functionality for the addition of a labelling element such as biotin for binding to streptavidin or thiols for gold attachment.

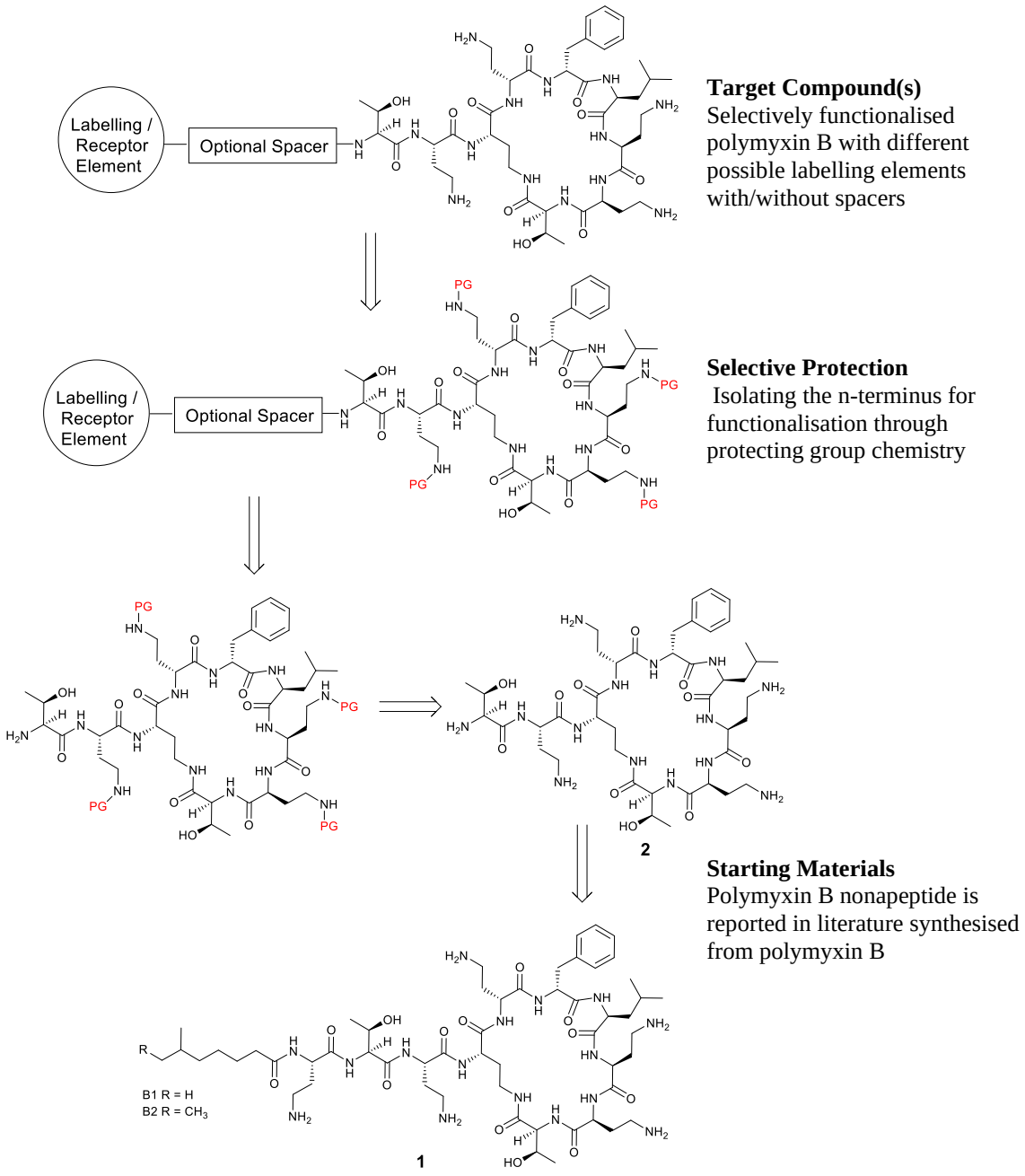

Figure 23: Retrosynthetic scheme for the synthesis of selectively functionalised polymyxin B with the option to explore a number of different 'labelling elements' from the same building block of a selectively protected polymyxin B nonapeptide.

3.3 Synthesis of the Boc_4 Protected Polymyxin B Nonapeptide

The synthesis of a Boc_4 protected derivative of PMBN (**2**) over two synthetic steps[179] is reported in literature. In the first step the hydrophobic tail of Polymyxin B is cleaved through the action of the cysteine protease papain (Scheme 1). The enzyme is known to cleave after residues such as arginine and lysine that are preceded by a hydrophobic residue.[180] In this application, the aliphatic tail directs the enzyme to cleave after the terminal Dab residue resulting in **2** and the cleaved 'Tail-Dab-OH' fragments (**CF1** / **CF2** due to the Polymyxin mixture used).

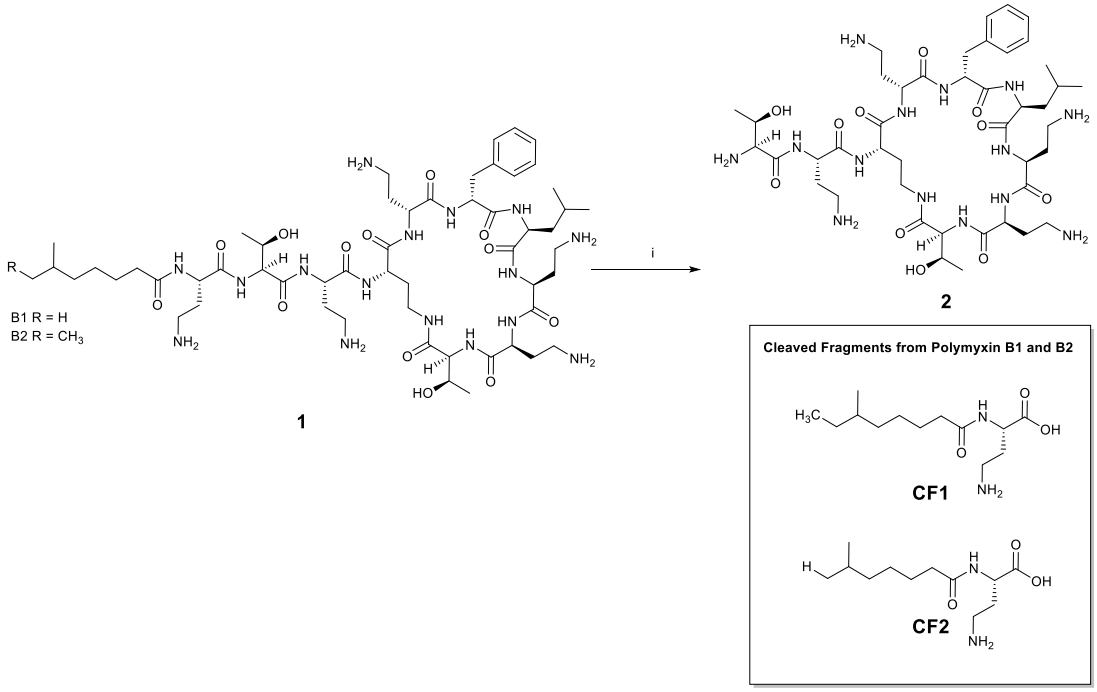

Scheme 1: Synthesis of PMBN **2** through the enzymatic cleavage of a mixture of Polymyxin B1 and B2 (**1**) i) Papain, H_2O/toluene, 55 °C 18 h.

The enzymatic action of papain proceeds optimally at slightly elevated temperatures and, under the conditions previously reported,[138] conversion to PMBN was confirmed by liquid-chromatography mass-spectroscopy (LCMS) (Figure 24). Due to its high solubility in water, there was poor separation between Polymyxin B and **2**

under standard reverse phase high performance liquid-chromatography (RP-HPLC) elution conditions but the disappearance of the mass corresponding to Polymyxin B mass and the loss of the 'tail' in the LCMS was used to confirm cleavage.

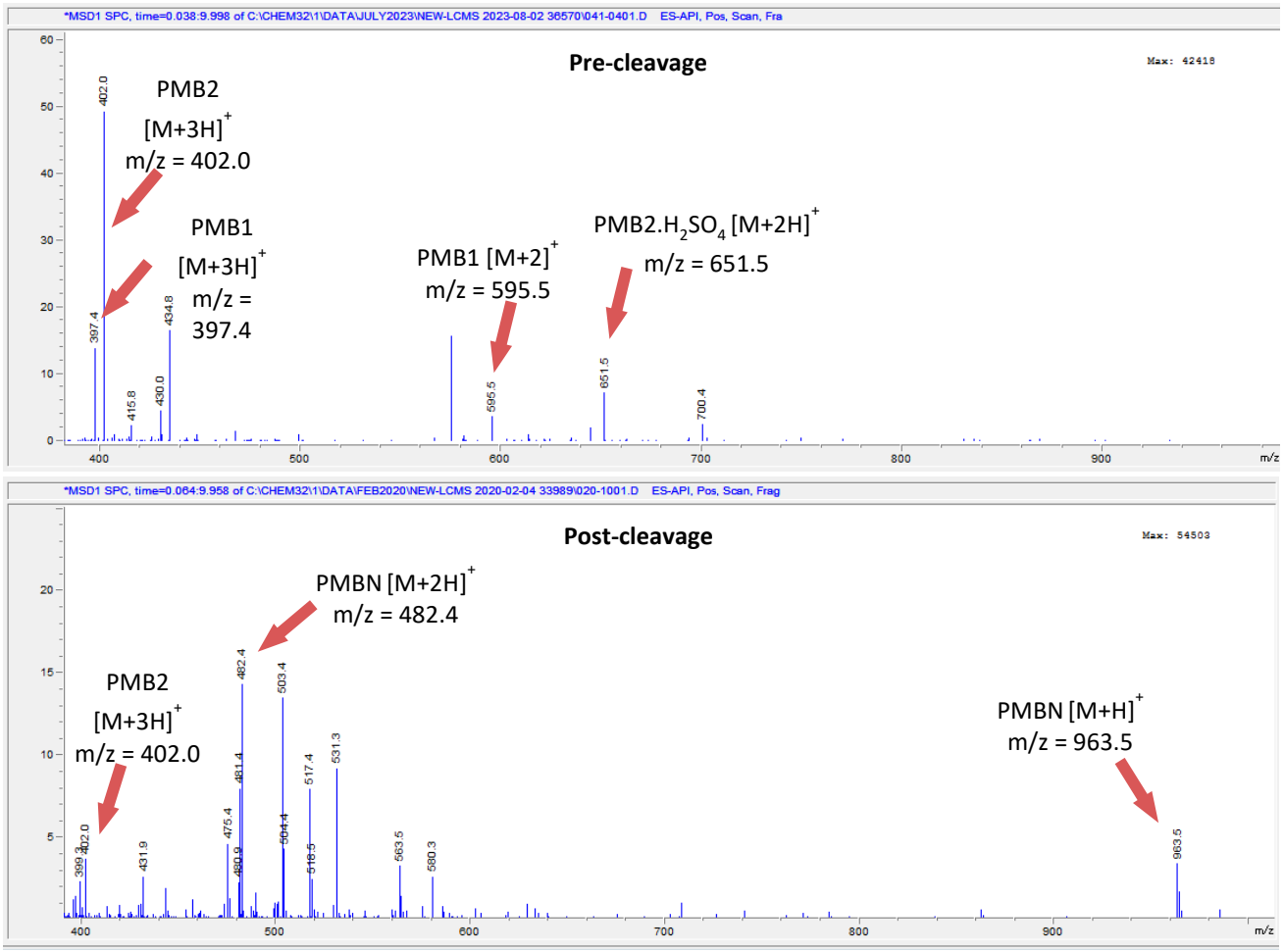

Figure 24: Mass spectrometry before (top) and after (bottom) Papain enzymatic cleavage of **1**. Disappearance/reduction of mass peaks at 595.5 / 651.5 m/z and at 397.4 / 402.0 m/z (corresponding to the B1 and B2 isomers) and the appearance of **2** at 963.5 m/z indicated a successful reaction. A residual peak of polymyxin B2 was still present.

The literature reports Boc protection using 1-(Boc-oxyimino)-2-phenylacetonitrile (Boc-ON)[181] to provide selective protection of the Dab residues over the amino terminus (Scheme 2), the rationale being due to the greater steric hindrance of, and lower electron density at, the terminal Threonine amine residue.[182]

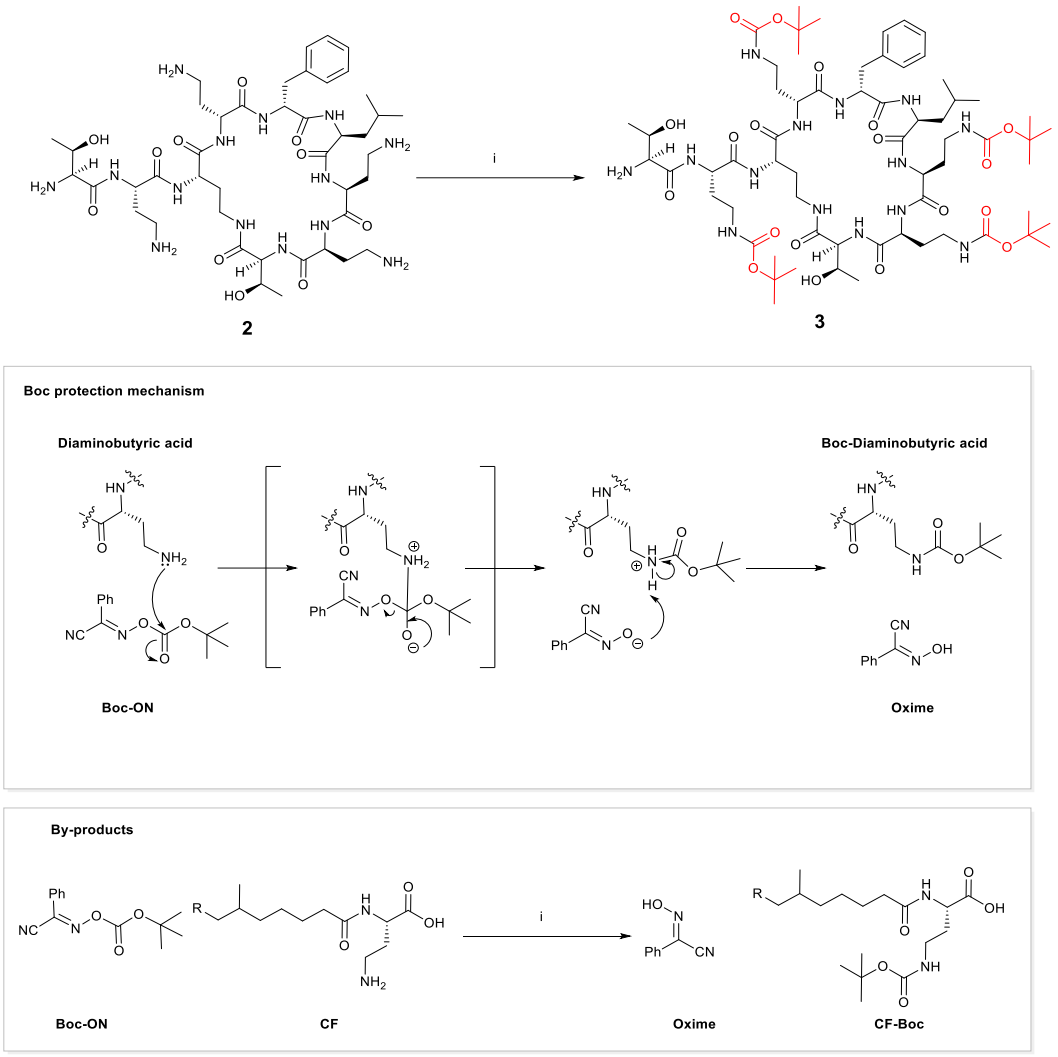

Scheme 2: Synthesis of PMBN-Boc$_4$ (**3**) after the enzymatic cleavage of the hydrophobic tail with papain. i) Boc-ON, Et_3N/H_2O/Dioxane 1:1:1 ratio, 23 °C 4 h, 1-47% yields.

Within the literature, yields from this reaction vary from 22 %[138] to 64 %[183] however, replicating this reaction proved challenging. The literature method used 5 equivalents of Boc-ON and then quenched the Boc addition reaction with ammonia after 20 minutes stopping the reaction after the addition of 4 Boc groups, yielding the desired PMBN-Boc$_4$ (**3**), and before the addition of the final 5th Boc group, resulting in fully protected PMBN-Boc$_5$. The oxime by-product being mostly removed during the precipitation step with Diethyl ether. The result of this reaction was initially a complex mixture of PMBN-Boc$_n$ with different levels of protection. It should be

noted that, assuming that the amine of the terminal Threonine does not react, the product of the first Boc addition (PMBN-Boc_1) corresponds to four products different regio-isomers, while the product of the second addition (PMBN-Boc_2) similarly corresponds to six products.

Multiple attempts at this reaction resulted in crude reaction mixtures that showed a >80% conversion to the desired PMBN-Boc_4 by evaporative light scattering detection (ELSD)-HPLC but with a significant proportion of the four possible PMBN-Boc_3 isomers and some unreacted starting material. The structural similarity of the multiple PMBN-Boc_3 products and the desired PMBN-Boc_4 resulted in poor separation under a range of column chromatography conditions. This included:

- Screening stationary phase media
    - Normal phase Silica
    - C-18 Silica
    - Basic Alumina
    - Neutral Alumina
- Solvent Conditions
    - Variable Gradient Elution
    - Isocratic Elution
    - Amine solvent additives

Elution under reverse phase HPLC conditions showed the polymyxin products in order of increasing protection level (Figure 25-1), with each of the Boc additions identified by LCMS (see Experimental). The sharp peak at 4.9 minutes (Peak C) was identified to be the desired PMBN-Boc_4 product however, this peak overlapped with the by-product 2-(Hydroxyimino)-2-phenylacetonitrile (Oxime) which had a strong absorbance at 254 nm (all the polymyxin derivatives have little absorption at this wavelength).

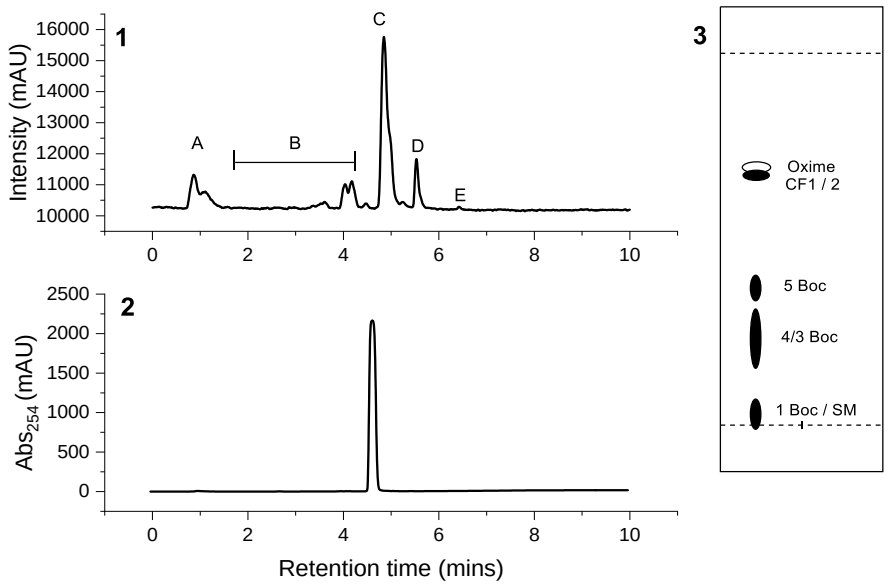

Figure 25: Analysis of the reaction (5 equiv. of Boc-ON) after quenching the reaction after 20 minutes with methanolic ammonia and the resulting analysis by RP-HPLC (ELSD) (1). The same reaction analysed by RP-HPLC (254nm) (2). TLC analysis eluting 10% MeOH/DCM (3).

1) Elution order via RP-HPLC A) Overlapping starting material and PMBN-Boc_1; B) Multiple PMBN-Boc_{1-3} isomers occur over the marked region; C) The majority of this peak is the desired PMBN-Boc_4 overlapping with residual Oxime by-product (see 2); D) Boc-protected cleaved fragments; E) Fully protected PMBN-Boc_5.
2) RP-HPLC signal detected at 254 nm showing a single intense peak of the residual Oxime by-product (the difference in retention time between the ELSD and UV detector is due to instrument lag time).
3) TLC analysis: The Oxime is visible under 254 nm illumination, while all other spots required staining/heating with ninhydrin.

Normal phase TLC separation showed the Oxime by-product (highest Rf) followed by the Boc-protected cleaved fragments (CF-Boc) eluting, (distinguishable by UV / ninhydrin staining) followed by the most to least protected PMBNs. However, while separation between the totally protected PMBN-Boc_5 and PMBN-$Boc_{3/4}$ was clear, there was a lack of separation between PMBN-Boc_3 and PMBN-Boc_4 with these compounds giving a long streak on the TLC plate. The least protected PMBN compounds were mostly retained at the baseline even when significant amounts of methanol were used in the eluent (4:1 DCM/MeOH).

To tackle these issues, a gradient elution was used to try and increase separation. The conditions are reported in Table 1 focusing on a 2-10% gradient. Increasing the

gradient to 15% (Purification B) resulted in a small increase in recovery but with a noticeable contamination with the oxime by-product). At high column loadings (in combination with higher polarity elution), the Oxime was prone to streaking throughout the column.

Table 1: Column conditions used for the purification of the PMBN Boc protection products following the literature method of synthesis (and the yields of pure PMBN-Boc_4 isolated). *Column purification was performed on Biotage Isolera system. Yield determined by the mass of pure **3** isolated from column fractions.

Purification	Column Conditions	PMBN-Boc_4 Yield (%)
A	2-10% DCM/MeOH	9
B	2-15% DCM/MeOH	10
C	2-10% DCM/MeOH	7
D*	2-12% DCM/MeOH	2
E	2-10% DCM/MeOH (1 %Et_3N)	3
F	15% DCM/MeOH	0
G	2-10% DCM/MeOH	6

Across a number of repeated purifications (Table 1) of the literature synthesis crude reaction mixture, the isolated yields of PMBN-Boc_4 were not improved significantly.

Modifications such as purification on an automated column chromatography system (Purification D), isocratic elution with a higher polarity solvent system (Purification F) or the addition of 1% Et_3N in the eluent mixture (Purification E), all resulted in extremely low isolated recoveries. The mean average yield from these methods was 8 % which was insufficient for the project.

After the poor yields seen in reactions D-F, the column from Reaction G was flushed with 100% methanol confirming that there was no degradation or capture of compounds on the silica. The primary issue related to streaking/mixing of PMBN-$Boc_{3/4}$ yielding a large proportion of mixed fractions, and this led to different stationary phase media being investigated.

Table 2: Alternative column stationary phase media explored to try and improve the yield of **3**. †Reverse phase separation in H was performed on a Biotage Isolera system. *Yield calculated after a subsequent normal phase separation to fully remove the oxime contamination (DCM/MeOH 2-10%)

Purification	Column Type	Column Conditions	PMBN-Boc$_4$ Yield / %
H	C-18 Silica†	95-5% H_2O/MeCN	13*
I	Alumina Basic	2-10% DCM/MeOH	0
J	Alumina Neutral	2-10% DCM/MeOH	0
K	Alumina Basic	0-2% DCM/MeOH	0

Reverse phase separation (C-18 Silica) was explored due to the good separation of PMBN-Boc$_{3/4}$ fractions under analytical RP-HPLC methods. Due to the scale, this was performed on a Biotage Sfär C18 60g column. While the isolated yields were higher than on normal phase silica, co-elution of the oxime and PMBN-Boc$_4$ (Figure 23) was particularly noticeable. However, a final yield of 13% was achieved after a subsequent normal phase column (65 mg).

Alumina showed an interesting effect wherein the order of elution reversed with respect to normal phase silica. However, with similar elution conditions to the silica columns (Purifications I, J) the compounds eluted off the column so rapidly that there was little to no separation between them. Elution at low percentages of methanol (Purification K, 0-2%) resulted in a slower elution and still resulted in large overlap between each compound.

In summary, exploration of different purification conditions was not able to bring yields in line with published methods. The key issue was the poor separation between PMBN-Boc$_4$ and the multiple PMBN-Boc$_3$ isomers. This prompted further exploration of the synthesis method to see if control over the crude reaction mixture could be improved. Specifically, as the separation between PMBN-Boc$_4$ and PMBN-Boc$_5$ was significantly cleaner than between PMBN-Boc$_4$ and the 4x PMBN-Boc$_3$

isomers, the aim was to push the reaction as far as possible to completely remove PMBN-Boc_3 while minimising loss of yield to over protection to PMBN-Boc_5.

3.3.1 Optimisation of Reaction Conditions

Two experiments were designed to help provide more data on how the Boc protection reaction worked and thus select more optimal conditions for the reaction. These reactions compared the reactivity and selectivity of Boc-ON and Boc Anhydride (Boc_2O) as reagents and the reactions were tracked by RP-HPLC over time.

3.3.2 Analysis of Boc-ON

To investigate the progression of the reaction over time a total of 6 equivalents of Boc-ON as a 1.3 M solution in dioxane was dosed via syringe pump at a rate of 1.5 equivalents/hour into the reaction. To track progress, 100 µL aliquots were taken for HPLC analysis every 30 minutes over 4 hours. Each aliquot was subjected to the work up as per the original method, (quenched with methanolic ammonia and the product precipitated with diethyl ether).

The slow dosing of Boc-ON was chosen because it lowered the effective concentration of Boc-ON in the reaction solution, with the aim of improving the preference to attach to the less sterically hindered Dab amines.

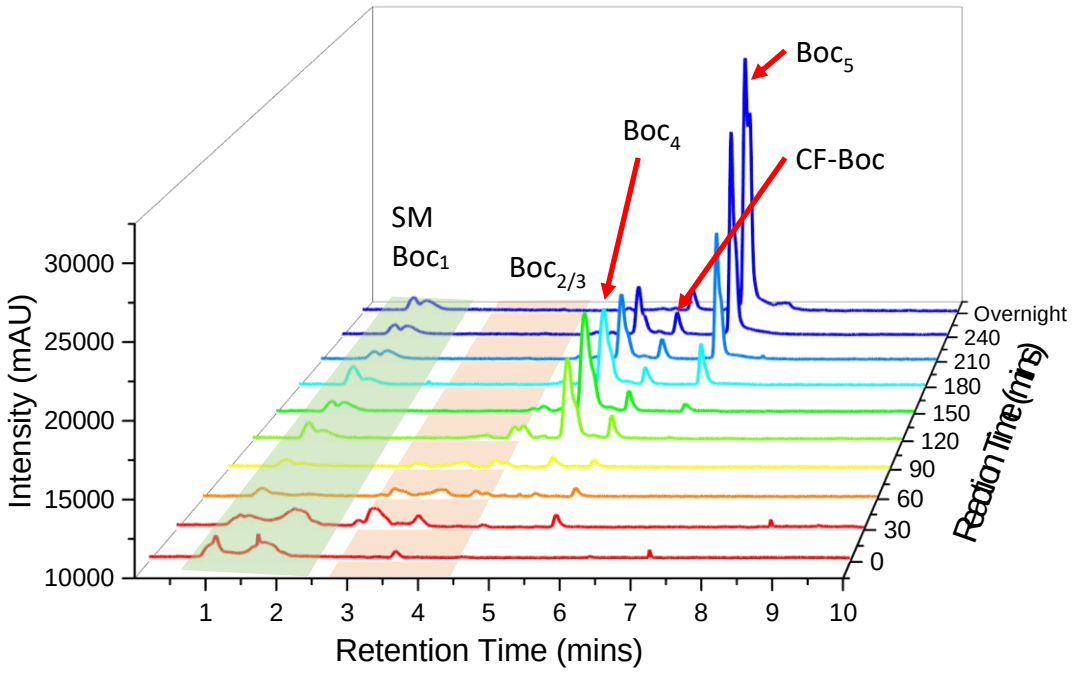

Figure 26: RP-HPLC analysis (ELSD) of the evolution of PMBN Boc protection reaction over time as Boc-ON was dosed via a syringe pump. The HPLC shows starting material peaks (green shading). The region showing PMBN-Boc_{2-3} is shown in orange shading. The evolution of PMBN-Boc_4 and PMBN-Boc_5 is seen in the highlighted peaks at 4.9 and 6.5 minutes, respectively. The peak corresponding to the Boc protected cleavage fragments (CF-Boc) is highlighted at 5.6 minutes. To track progress, 100 µL aliquots were taken and subjected to a mini-work up (quenched with methanolic ammonia (4.0 M solution, 500 µL), evaporated to dryness then re-dissolved in 200 µL methanol before precipitation with cold Et2O (500 µL). The collected precipitate was dissolved in 300 µL of 1:1 H_2O:Acetonitrile.

From the stacked HPLC traces (Figure 26) it can be seen that the reaction proceeds almost sequentially with starting material and PMBN-Boc_1 peaks in the 1–2-minute elution region, then further converted PMBN-Boc_{2-3}, shown in the 3–4-minute elution region. This appears as a range of overlapping peaks, probably due to the different possible structural isomers. As the reaction proceeds, the major product peak of PMBN-Boc_4 can be seen rapidly forming at 120 minutes, with a maximum at 150 minutes before decreasing in size in favour of a peak at 6.5 minutes corresponding to PMBN-Boc_5.

Each peak in the HPLC spectrum (with ELSD) (Figure 26) was manually integrated to track the changing composition of the reaction mixture over time (Figure 27).

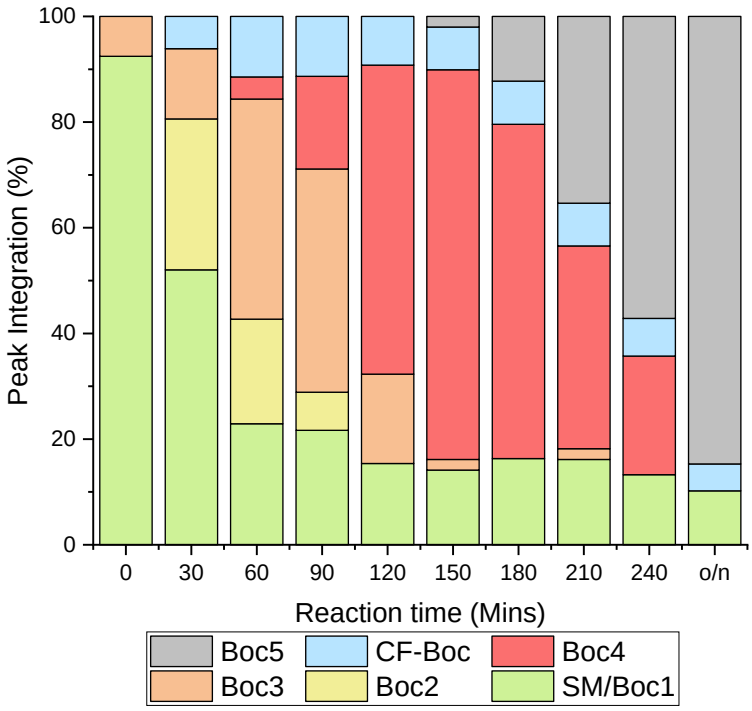

Figure 27: Comparison of changing composition of the reaction mixture (Boc-ON/Syringe pump reaction) over the course of the reaction as Boc-ON was added. Selection of the HPLC peaks for integration was performed manually and plotted as a percentage all the peaks in the trace. Peak integrations at < 2% (i.e. PMBN-Boc_3 at 150/210 minutes) were close to background indicating that complete reaction of PMBN-Boc_3 may not have been able to be determined under these measurement conditions. The integration of peaks assigned to the PMBN-Boc_3 isomers were combined for clarity. Peaks were assigned based on LCMS analysis.

From this analysis it was calculated that the formation of PMBN-Boc_4 was 73% after 150 minutes when 3.75 equivalents of Boc-ON had been added under these syringe pump conditions. Only a minimal degree of over-protection had occurred at this stage (2% PMBN-Boc_5). There was some remaining PMBN-Boc_3 present, but this was completely removed/reacted after the 180 minute (4.5 equivalents of Boc-ON added) although this led to incurring an increase in PMBN-Boc_5 (2 to 12%). The crude reaction mixture yielded by the published method (5 equivalents and

quenching at 20 minutes) was most similar to the 120 – 150 time point analysis from this study.

3.3.3 Analysis of Boc Anhydride

The Boc protection of PMBN with Boc anhydride was also investigated under the same conditions for comparison. The primary aim being to see if selectivity could be matched and, the issue of the Oxime by-product avoided. The reaction showed a similar initial evolution of compounds with rapid conversion of starting materials to the PMBN-Boc_1 and PMBN-Boc_2 isomers and protected cleaved fragments at 5.5 minutes.

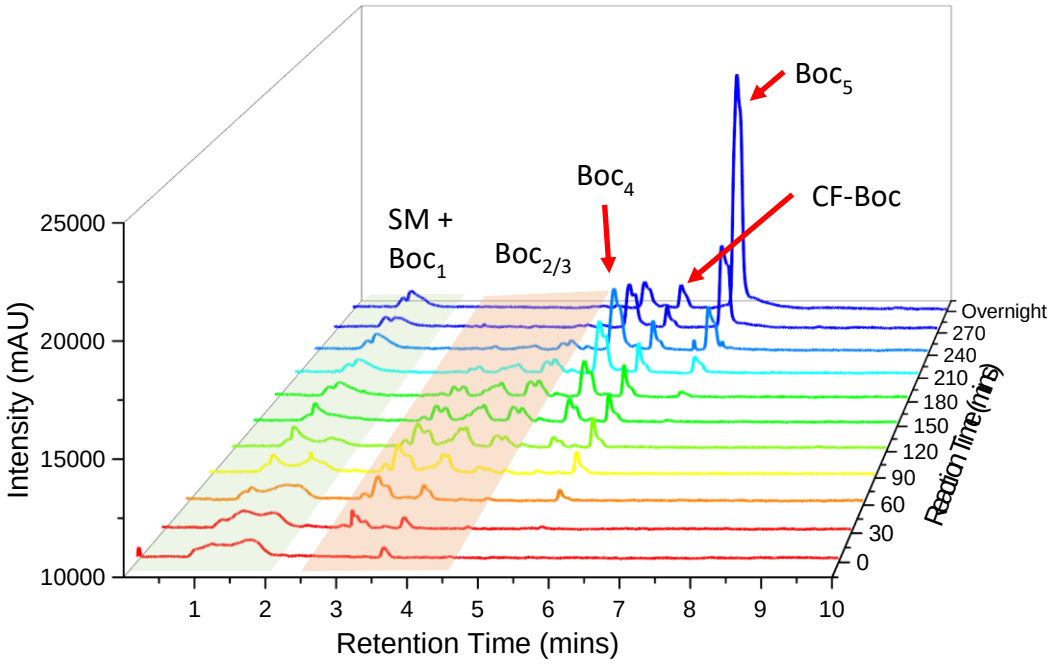

Figure 28: RP-HPLC analysis with ELSD of the evolution of the PMBN Boc protection reaction over time as Boc_2O (5 eq) was dosed via a syringe pump. The HPLC regions showing starting material and PMBN-Boc_1 isomer peaks are shown in green shading. The region showing PMBN-$Boc_{2\text{-}3}$ is shown in orange shading.

After 120 minutes it can be seen that conversion to each of the PMBN-Boc_X isomers occurred in parallel rather than sequentially (Figure 28). It was also noted that the

peak shape for each PMBN-Boc species appeared to be split into more peaks than seen on the Boc-ON time study, possibly suggesting that there may be more isomers of each species forming.

Conversion to PMBN-Boc_4 peaked at 45% (Figure 29) after at minutes, although there was still 24% of the PMBN-Boc_{1-3} isomers and the Boc_4 peak was split. As the reaction proceeded the proportion of PMBN-Boc_4 decreased, increasing the proportion of PMBN-Boc_5.

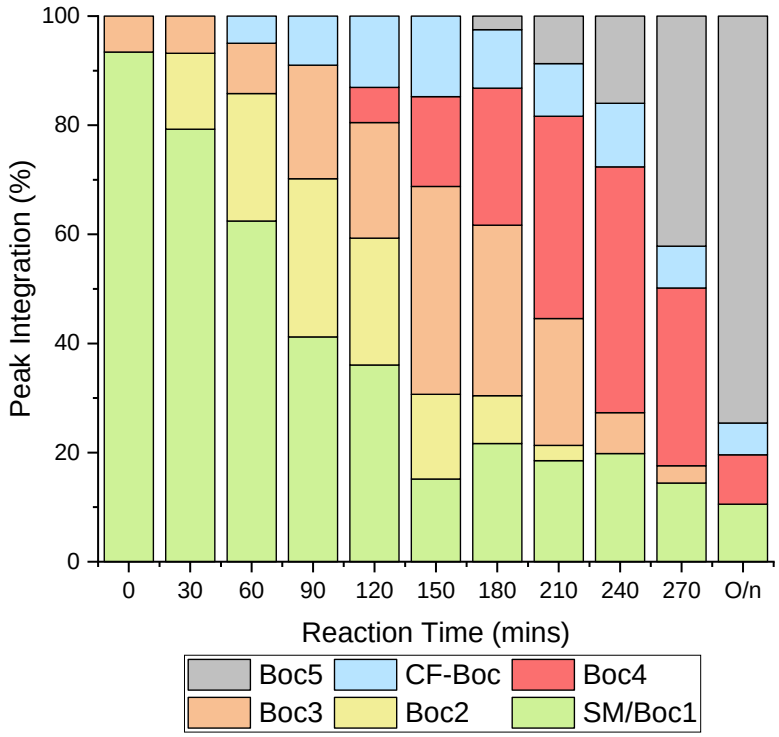

Figure 29: Comparison of changing composition of the crude reaction mixture over the course of the reaction as Boc_2O was added. Integration of HPLC peaks was performed manually and plotted as a percentage of all the peaks in the spectrum. The integration of peaks assigned to the PMBN-Boc_3 and PMBN-Boc_4 isomers were combined for clarity. Peaks were assigned based on LCMS analysis.

Ultimately this showed that even with slow dosing of Boc_2O to try and control the selectivity of the Boc protection of PMBN, Boc-ON yielded a greater proportion of the desired PMBN-Boc_4.

The outcome of these two time-dose studies suggested that an optimal reaction mixture for purification would be achieved by dosing a total of between 4 and 4.5 equivalents of Boc-ON into the reaction, with the final dose being controlled by monitoring the disappearance of PMBN-Boc_3 by RP-HPLC with ELSD.

3.3.4 Optimisation of Column Purification Conditions

With this additional control over the crude reaction mixture, silica gel purification of PMBN-Boc_4 was revisited. The addition of a base to the elution solvent was explored to improve separation between PMBN-Boc_4 and PMBN-Boc_5 now that the proportion of PMBN-Boc_3 in the reaction crude was suppressed by altering the reaction procedure. Therefore, the column conditions used included 1% trimethylamine or ammonia. Ammonia (in methanol) made TLC visualisation simpler due to its lower boiling point permitting staining with ninhydrin.

Table 3: Column conditions for the purification of the modified PMBN Boc protection reaction (Reactions B-G). Reaction A used the original literature method and is included for comparison. All separations were run on a Biotage Isolera automatic column system except where indicated (*). ** In reactions E – G, the column size was 100 g with an 8 g dry load. In the case of E, the purification was split into two runs of 5 g each and the products combined afterwards.

Reaction	Scale / g	Column Conditions	PMBN-Boc_4 Yield / %
A *	1	2-10% DCM/MeOH (1% Et_3N)	3
B	0.5	12% DCM/MeOH (1% Et_3N)	14
C	0.5	2-20% DCM/MeOH (1% NH_3)	44
D	5	2-20% DCM/MeOH (1% NH_3)	29
E	10	2-10% DCM/MeOH (1% NH_3)	37
F**	5	2-10% DCM/MeOH (1% NH_3)	47
G**	5	2-10% DCM/MeOH (1% NH_3)	39

Comparing these reactions to Reaction A (the original literature method) large improvements in yield were found. Starting with small scale tests of the modified method (Reaction B and C), an isocratic elution was compared to a gradient elution

with a yield improvement of 30 percentage points primarily due to a reduction in the oxime streaking into later fractions.

Scaling the reaction up to 5 g of **2** resulted in a reduced yield. Due to the columns being run on the Isolera system the column sizes and diameters were fixed, both 0.5 g reactions were columned using a 2 g dry load on a 25 g column resulting in a 1:50 ratio of crude reaction mixture to column silica. Increasing to 5 g scale (Reaction D), the column size was only increased to 50 g with a 4 g dry loading which resulted in streaking and poorer separation.

3.3.5 Optimised PMBN Boc Protection Reaction

The combined optimisation of the reaction and purification conditions resulted in a robust/practical method that allowed the production of the required PMBN-Boc_4 core on scale.

Key was that the addition of an excess of Boc-ON (5 equiv.) was reduced to between 4-4.5 equiv. with HPLC monitored addition until the proportion of PMBN-Boc_3 was at a minimum. The major modification was the addition of ammonia to the column eluent to reduce streaking. These optimisations improved the consistency of the reaction and increased isolated yields of pure PMBN-Boc_4 giving an average of 39% over 5 independent reactions (Reactions C-G, Table 3, total combined mass obtained was 9.4 g).

3.4 Synthesis of Polymyxin-conjugates

3.4.1 Lipoic acid-PMBN

The rationale behind this compound was to allow binding of polymyxin onto the surface of gold nanoparticles due to the high Au-S affinity (see Chapter 3), while maintaining its bacterial binding affinity. Lipoic acid coated gold nanoparticles have been reported in literature and here Lipoic acid was chosen to introduce a sulfur containing moiety into the compound.

Firstly, (R)-(+)-α-Lipoic acid was activated with *N*-Hydroxysuccinimide (NHS) using EDC as the coupling agent to synthesise the Lipoic acid NHS ester (**4**) according to a literature procedure.[184] This activated carboxylic acid was readily reacted with the free amine of PMBN-Boc_4 under basic conditions yielding the Boc-protected Lipoic acid functionalised polymyxin (**5**) (Scheme 3).

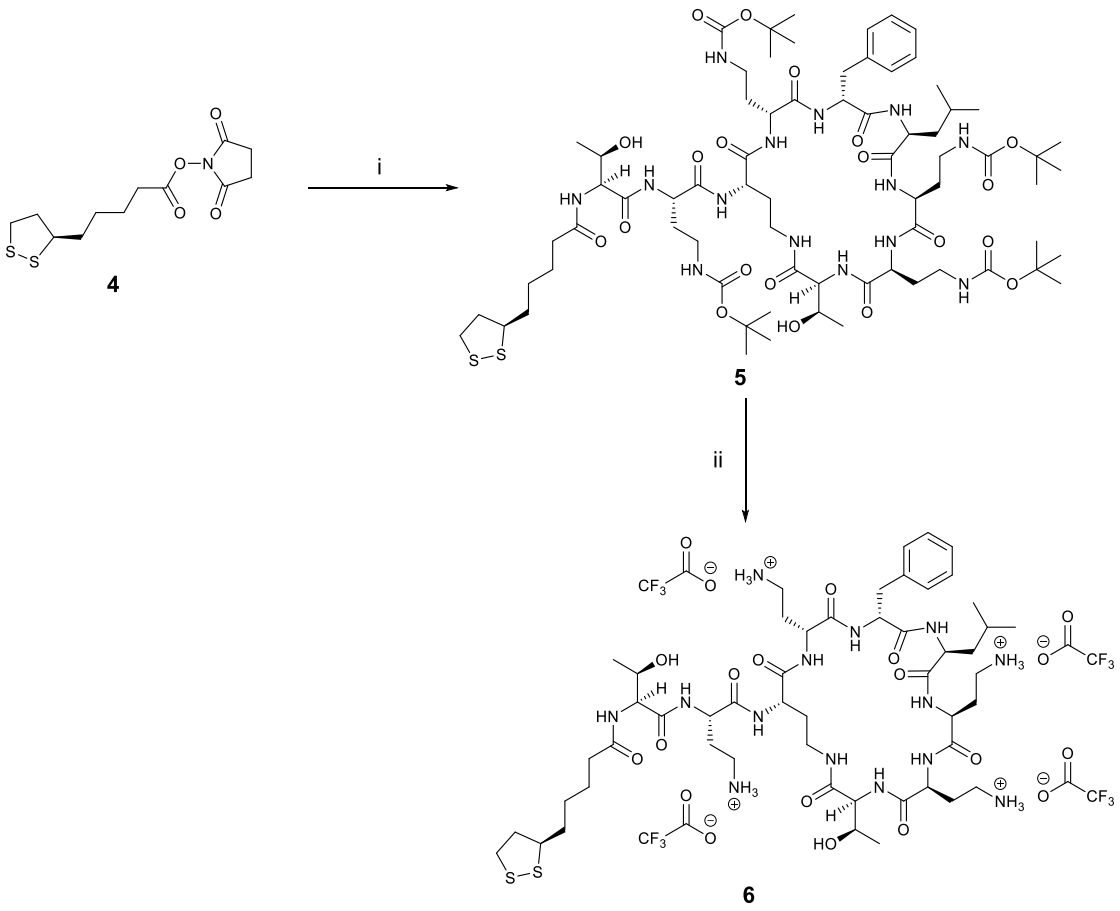

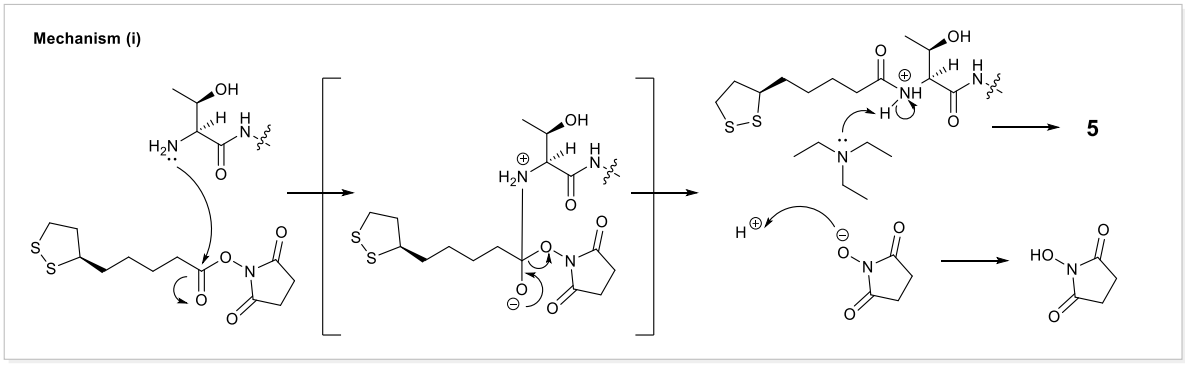

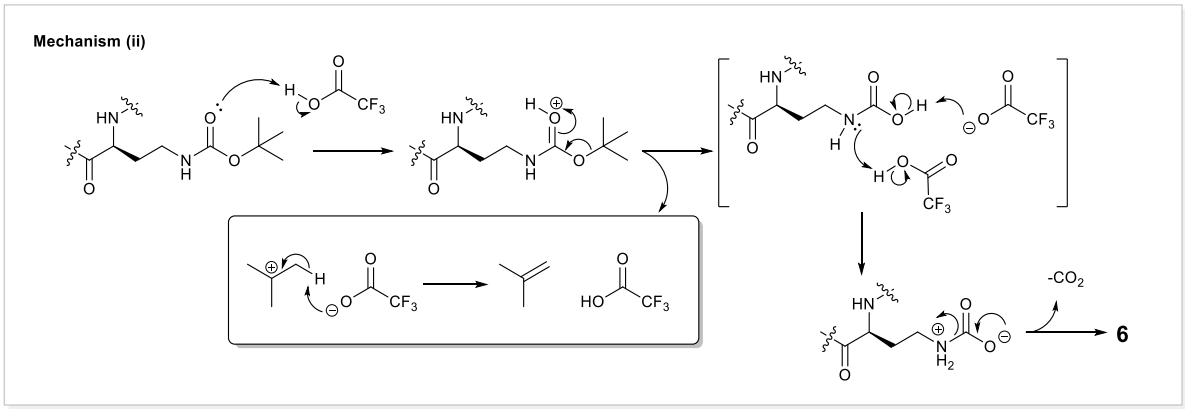

Scheme 3: Amide coupling between Lipoic acid and Boc-protected polymyxin, and its subsequent deprotection. i) PMBN-Boc_4 0.9 eq, DIPEA, DCM, 4 hours, 81%. ii) 20% TFA in DCM, 30 minutes, quantitative.

The Boc-protected intermediate **5** was purified using normal phase column chromatography with the final deprotection step, using a 20% solution of TFA in DCM, giving a quantitative yield of compound **6**. The deprotection led to a sticky oil of the final compound **6** as a TFA salt. High resolution mass spectrometry of **6** showed that the disulfide bond of Lipoic acid had remained intact during the synthesis (as anticipated). The application of **6** to AuNP binding was investigated in detail in the following chapter (see Chapter 4).

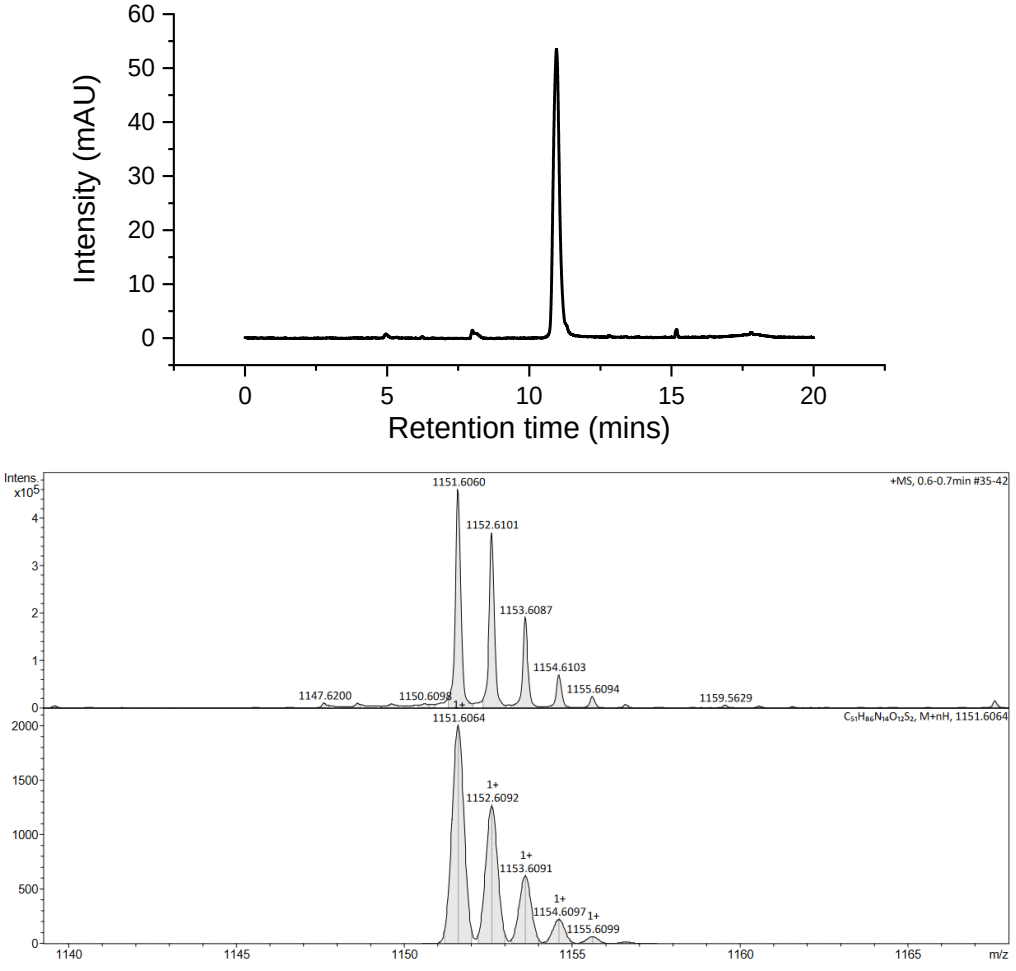

Figure 30: Analysis of compound 6 by RP-HPLC (ELSD) and HRMS. HRMS (ESI+) calc. $C_{51}H_{86}N_{14}O_{12}S_2$ m/z = 1151.6064, found m/z = 1151.6060 $[M+H]^+$ confirming the Lipoic acid disulfide bond remained intact.

3.4.2 Biotin-Polymyxin Conjugates

A polymyxin-biotin conjugate (Biotin-PMBN, **9**) was generated through amide bond formation using a biotin *N*-hydroxysuccinimide active ester.

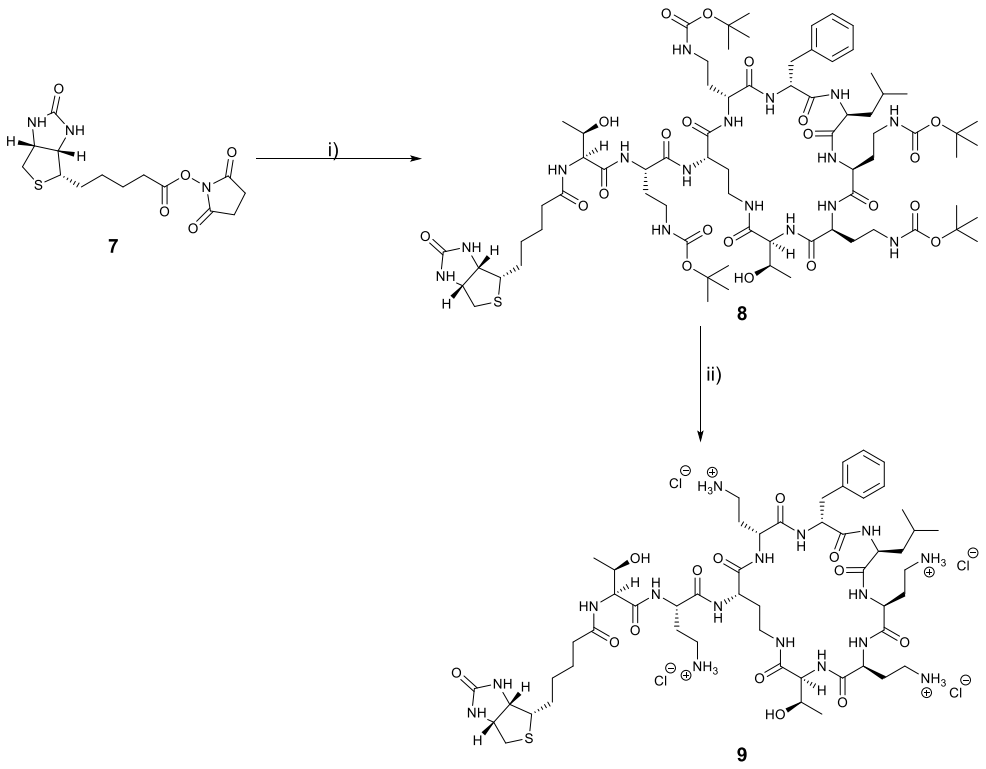

Scheme 4: Synthesis of biotinylated PMBN using Biotin-NHS. i) DCM, DIPEA, 18 h, 55% ii) 4M HCl, Et_2O, quantitative yield

The Boc-protected intermediate **8** was isolated in 55% yield after normal phase column chromatography and deprotected with either a solution of TFA in DCM, or with a 4M solution of HCl in dioxane. Both methods resulted in complete deprotection of **8**. However, TFA deprotection yielded a sticky viscous oil of **9** while during the HCl deprotection **9** precipitated out of solution as a white solid. As the choice of deprotection method impacted neither the yield nor the purity of the final compound deprotections were performed with HCl in dioxane. This would change the counter ion present in the final product but was deemed unlikely to affect the final application(s).[185]

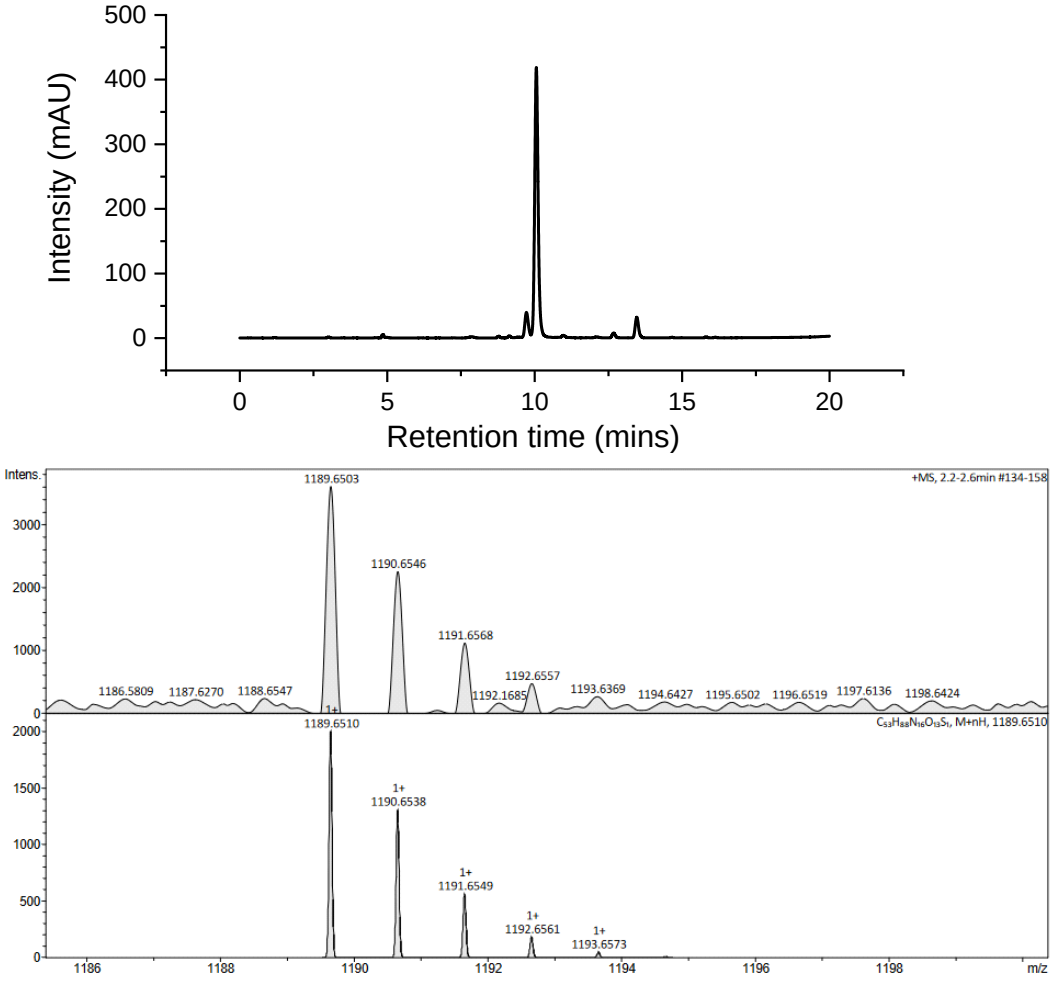

Figure 31: Analysis of compound **9** by RP-HPLC with ELSD and HRMS analysis. LCMS showed a minor peak at 9.9 minutes which was identical to the major peak at 10 minutes. HRMS (ESI+) calc. $C_{53}H_{88}N_{16}O_{13}S_1$ m/z = 1189.6510, found m/z = 1189.6503 [M+H]+.

3.5 Testing and Validation of Biotin Conjugated PMBN

3.5.1 Labelling *E. coli* with Fluorescent Streptavidin and Biotin-PMBN (**9**)

The dual binding of **9** to bacteria and streptavidin was investigated. *E. coli* were labelled through sequential incubation with **9** (giving a biotinylated outer membrane surface (Expanded view Inset Figure 32)) and, then the iFluor 555-streptavidin conjugate (henceforth ‘streptavidin-555’).

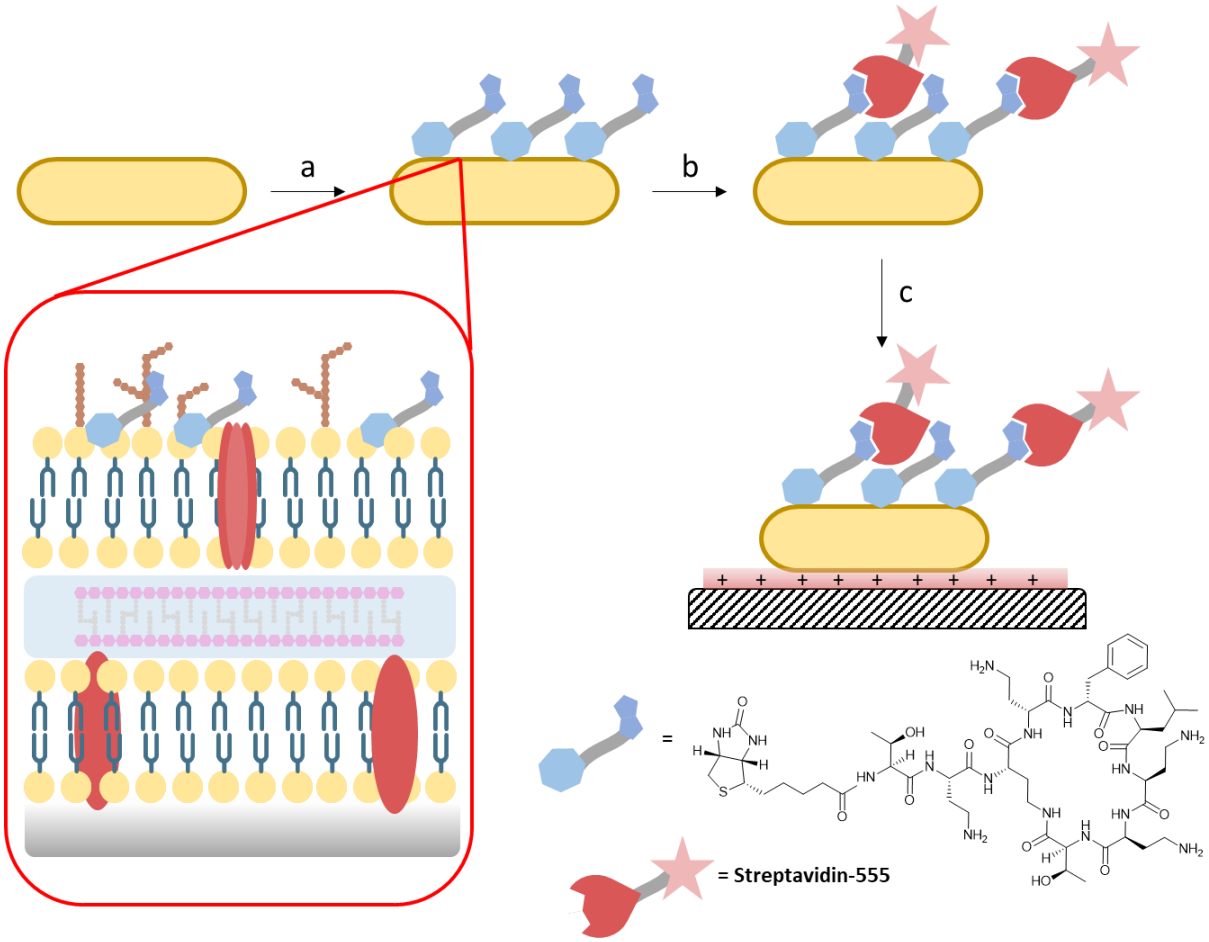

Figure 32: Overview of the method used to label bacteria with a combination of the Biotin-PMBN conjugate and fluorescently labelled streptavidin. Insert shows probe binding onto the bacterial surface. a) Bacteria were incubated with **9**. b) Incubation with streptavidin-555 c) Attachment onto poly-D-lysine coated microscope well plate for confocal imaging

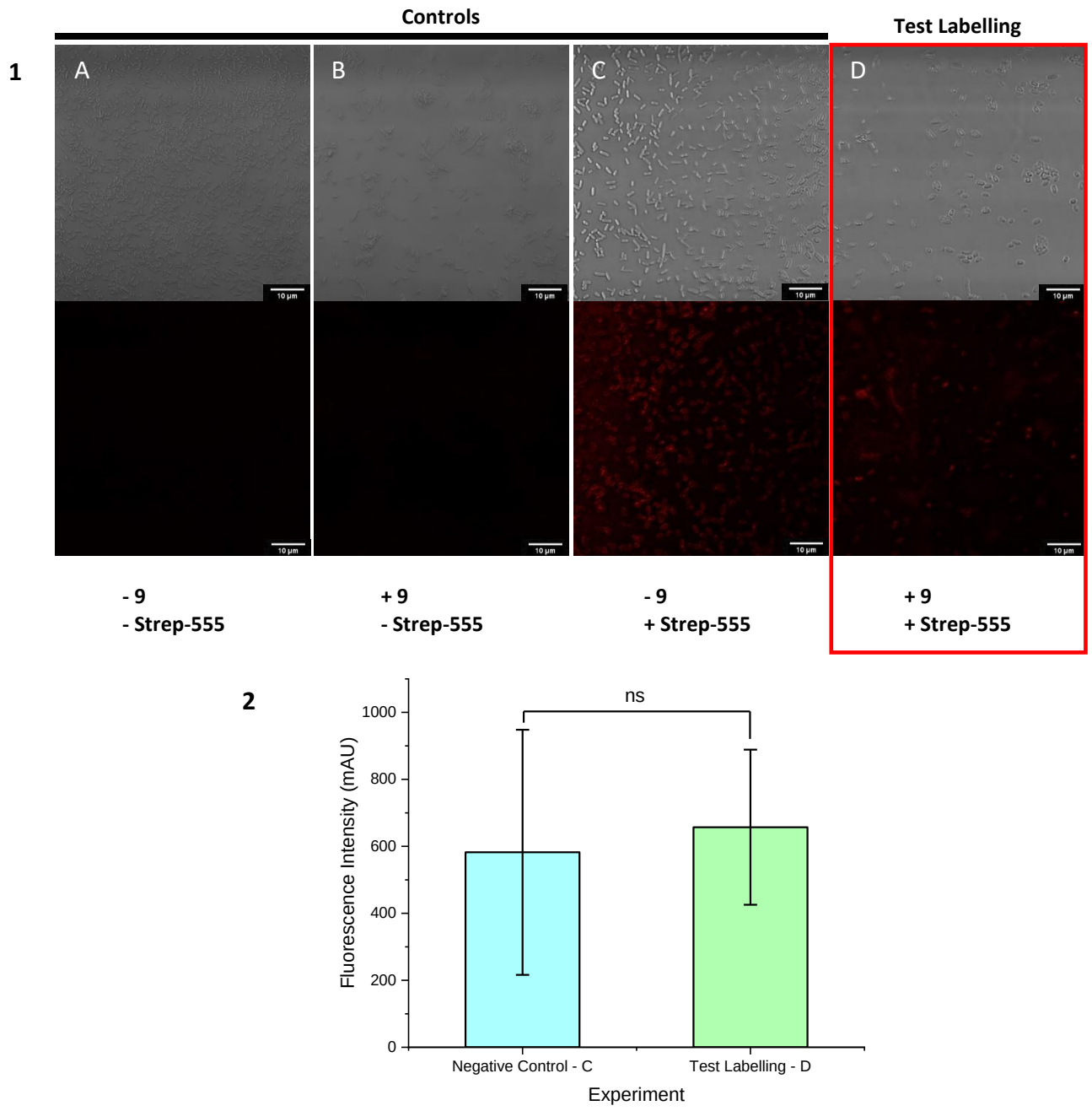

Figure 33: 1) Confocal laser scanning microscopy images of *E. coli*: Top bright field; Bottom: fluorescence. A) *E. coli* untreated and imaged;). B) Labelling of *E. coli* with **9** (50 µM) for 1 hour, washed and imaged; C) Labelling of *E. coli* with Streptavidin-555 (20 µg/mL) for 30 minutes then washed and imaged; D) Labelling of *E. coli* with **9** (50 µM) for 1 hour. Bacteria were then washed and treated with Streptavidin-555 (20 µg/mL) for 30 minutes. Bacteria were washed again and imaged. Scale bar 10 µm. Excitation λ_{ex} = 561 nm; Emission λ_{em}= 570 - 600 nm.

2) A comparison of bacteria fluorescence intensity in images C and D as calculated by ImageJ, Fiji. A total of 15 area samples were taken for bacteria and background to provide averages for analysis. Error bars were calculated from the standard deviation in the signal intensity. Significance tested with Bonferroni's Multiple Comparison Test to a confidence of $p < 0.05$

Image analysis of the control labelling experiment (Figure 33 - 1C) showed a fluorescent signal from streptavidin-555 non-specifically binding to both the *E. coli* and the polylysine coating on the microscope slide wells. The addition of Biotin-PMBN **9** to bacteria followed by the addition of streptavidin-555 (Figure 33 - 1D) did not show any significant fluorescence above background control seen in C (Figure 33 – 2). While optimisation of the labelling process, such as the inclusion of additional blocking steps could have been performed, the low overall fluorescence and the lack of distinction between the test and control experiments prompted a re-examination of the ligand binding.

Validation of Streptavidin-Biotin-PMBN Binding

The lack of labelling suggested that the dual binding (*E. coli* – [PMBN – Biotin] – Streptavidin-555) was not functioning so the binding between **9** and streptavidin was investigated.

A colorimetric binding assay based on 4'-hydroxyazobenzene-2-carboxylic acid (HABA) was performed. In this assay,[186] HABA weakly binds to the binding pocket of streptavidin, with tautomerisation (Figure 34) leading to the generation of a peak in the absorbance spectrum at 500 nm. This tautomerisation was confirmed in literature by Strzelczyk *et al.* using X-ray crystallography to show the binding geometry in the avidin binding pocket.[187]

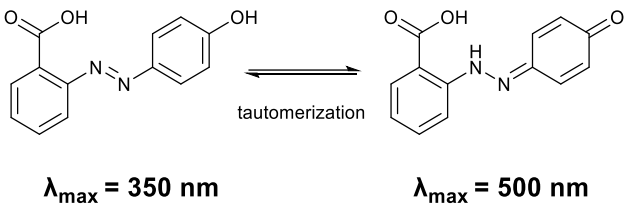

Figure 34: Tautomerisation of HABA triggered by the binding to Strept(avidin) which manifests as a change in the UV-Vis absorbance spectra.

When HABA is displaced from the binding pocket the absorbance at 500 nm is reduced. The relative weak binding ($K_D = 12.2 \pm 0.3 \times 10^{-6}$ M) of this dye allows it to be completely displaced by biotinylated compounds[188] and by monitoring the reduction in absorbance at 500 nm, the degree of HABA displacement and thereby biotin binding, can be quantified.

The aim was to determine if **9** could access the streptavidin binding sites without the cyclic heptapeptide sterically interfering with the binding (Figure 35).

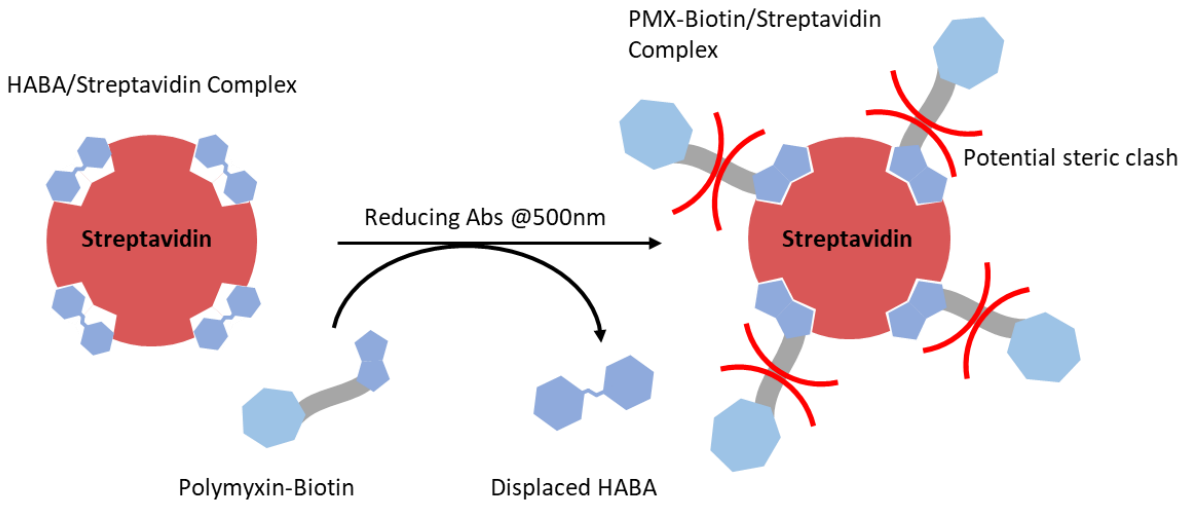

Figure 35: Representation of the streptavidin binding assay with the bound HABA being displaced by Biotin. This displacement is characterised through the reduction in absorbance at 500 nm. This assay allowed the determination of whether a potential steric clash between the PMBN and streptavidin would interfere with the displacement of HABA by the biotin in **9**.

To a test solution of the streptavidin-HABA complex (7.4 µM streptavidin, 0.3 mM HABA) **9** (50 µM) was added and equilibrated (and compared to the same assay

performed with unmodified Biotin at the same concentration (50 µM) for reference). The resulting colour change was measured, and the reaction quantified through the change in absorbance at 500 nm (Figure 36).

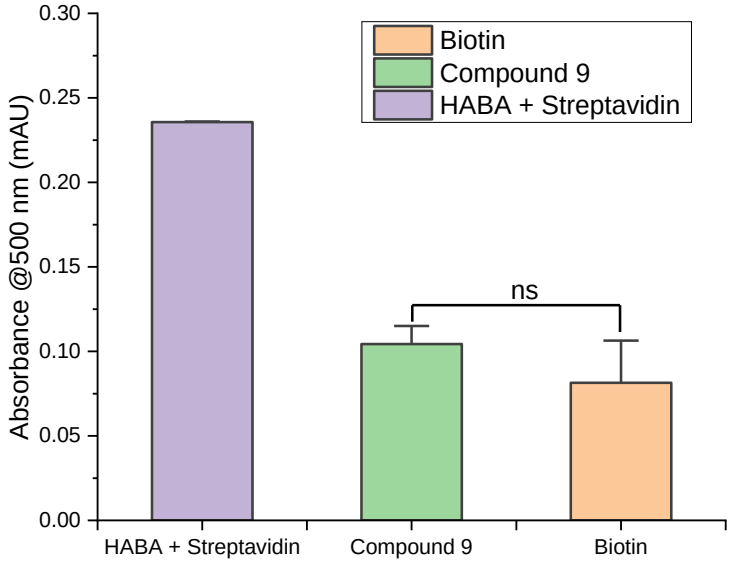

Figure 36: Comparison of the absorbance at 500 nm of the HABA-Streptavidin complex before and after the displacement of HABA with Compound **9** or Biotin. There was no statistically significant difference between Compound **9** and Biotin (n =3). Significance tested with Bonferroni's Multiple Comparison Test to a confidence of $p < 0.05$.

Both displacement experiments (**9** and Biotin) showed near instantaneous colour changes from orange to yellow, that were confirmed through UV-Vis measurements. This showed that the binding between **9** and streptavidin was possible and that the lack of binding seen in the bacterial labelling experiment was not caused by steric hindrance blocking access to the streptavidin binding site.

The most likely explanation was that while binding between **9** and streptavidin was possible in solution, the two binding events were rendered mutually exclusive when on the bacterial surface, perhaps due to steric issues introduced by the bacterial surface chemistry.

3.6 Synthesis Biotin-Ahx-PMBN

Since literature supports the introduction of spacers to address steric hindrance, this approach was explored to provide additional steric clearance between the two binding events. The initial investigation focused on introducing a 6-aminohexanoic acid (Ahx) C_6 spacer to give **12** in three steps.

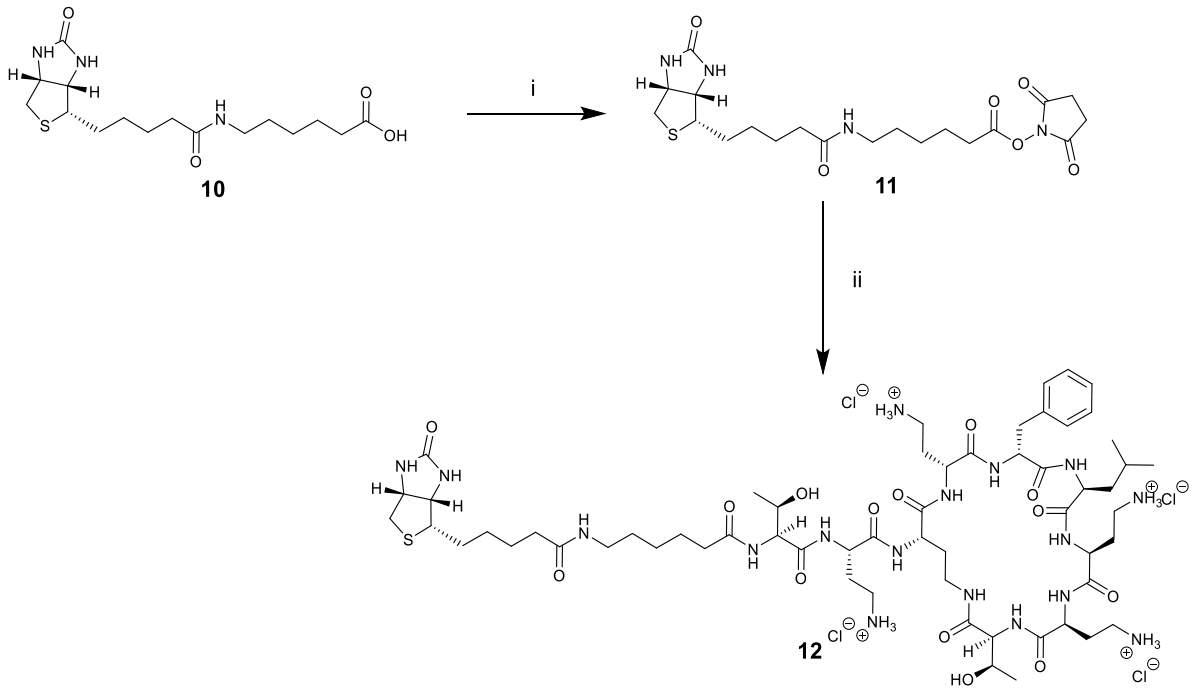

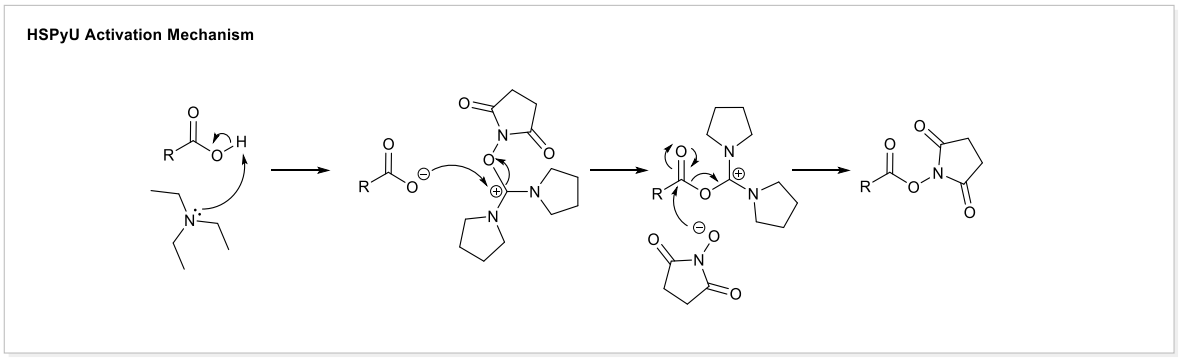

Scheme 5: Synthesis of PMBN-C_6-Biotin. i) HSPyU, DMF, DIPEA, 4 hours, RT. ii) PMBN-Boc_4 (0.9 equiv.), microwave heating 80 °C, 3 hours. iii) HCl 4M, Dioxane, 4 hours, 10% yield over 3 steps.

Biotin-C_6 (**10**) was converted to the NHS ester using HSPyU with the formation of the NHS ester confirmed by HPLC. Following this, PMBN-Boc_4 was added, with the reaction completed in one-pot. **3** and **10** were soluble in DMF at elevated temperatures, so the reaction was carried out with microwave heating (80 °C) until conversion was complete. The temperature was constrained due to the lability of Boc groups above 100 °C.[189]

Poor solubility impacted the purification of the product and as such the Boc-protected compound was not isolated. As with **9** it was found that HCl deprotection was preferable to TFA deprotection as the resulting hydrochloride salt was easier to handle. After deprotection, **12** became water soluble allowing separation by preparative RP-HPLC**.**

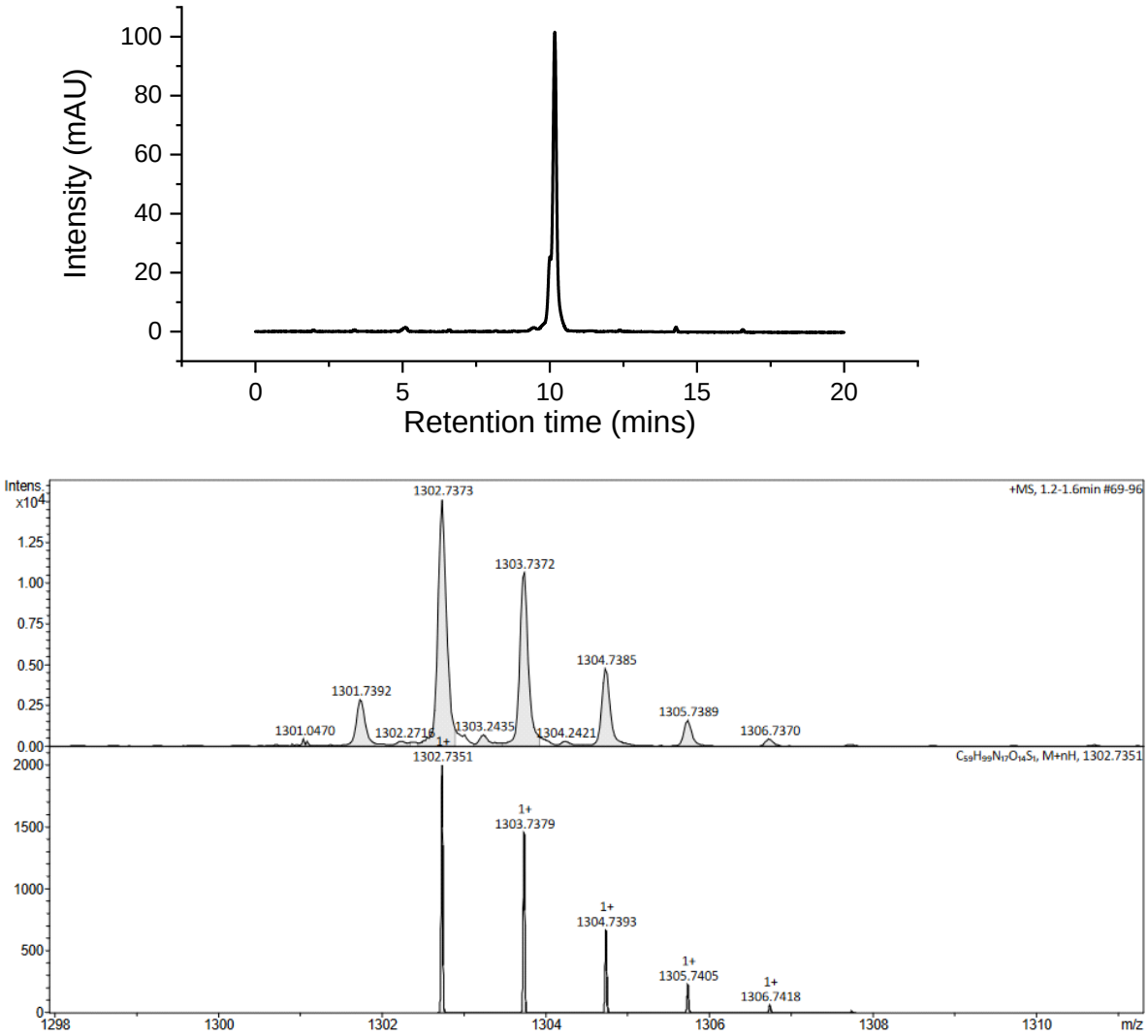

Figure 37: Analysis of compound **12** by RP-HPLC with ELSD (top) and HRMS (bottom). HRMS(ESI+) Calculated m/z = $C_{59}H_{100}N_{17}O_{14}S_1$ = 1302.7351, Found m/z = 1302.7373

3.6.1 Comparison of *E. coli* Labelling Between **9** and **12**

To investigate if the addition of a C_6 linker improved the labelling of bacteria, fluorescent labelling of *E. coli* was repeated comparing **9** and **12**. Labelling concentrations were maintained but the streptavidin-555 concentration was reduced to try and lower the background signal.

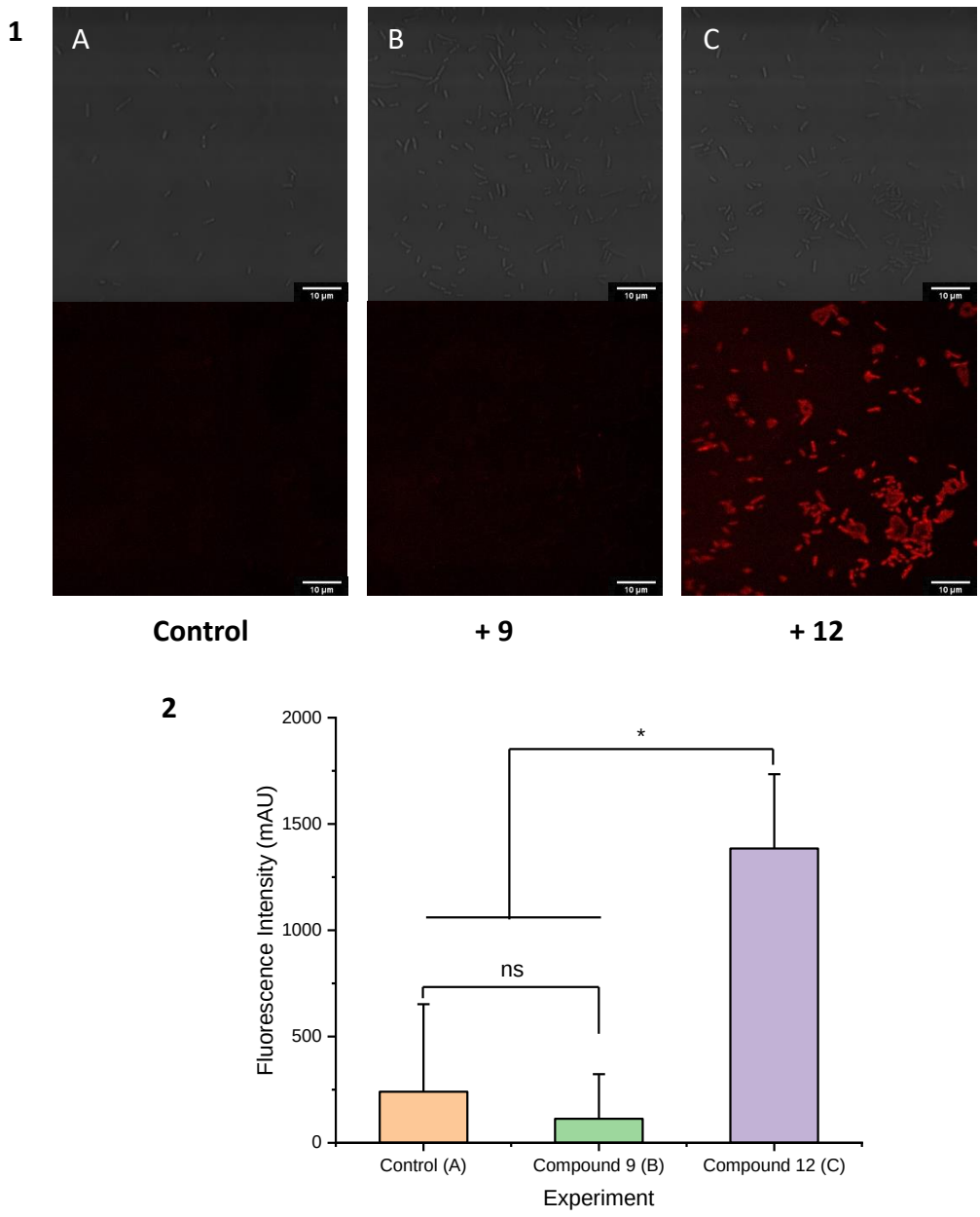

Figure 38: 1) Confocal laser scanning microscopy images of *E. coli*, bright field (top) fluorescence (bottom). A) *E. coli* treated with Streptavidin-555 (10 µg/mL for 30 minutes); B) Labelling of *E. coli* with **9** at 50 µM for 1 hour, followed by the addition of Streptavidin-555 (10 µg/mL for 30 minutes).; C) Labelling of *E. coli with* **12** at 50 µM for 1 hour, followed by the addition of Streptavidin-555 (10 µg/mL for 30 minutes). Scale bar 10 µm. Excitation λ_{ex} = 561 nm, Emission λ_{em}= 570 - 600 nm. 2) Bacteria fluorescence intensity comparison showing the improved labelling effectiveness **12** as calculated by ImageJ, Fiji. A representative sample of 15 areas were taken for bacteria and background to provide average intensities. Error bars were the standard deviation in the signal intensity. *P < 0.05 between A-B and C. There was no significant difference between A-B (significance tested with Bonferroni's Multiple Comparison Test).

Confocal fluorescence microscopy showed that the additional steric clearance in **12** allowed specific labelling with streptavidin-555. The fluorescence signal from the *E. coli* control and *E. coli* incubated with **9** (Figure 38 – 1 A/B) were close to

background, *whereas E. coli* labelled with **12** (Figure 38 – 1 C) showed 5 times greater corrected total cell fluorescence over the *E. coli* control and 12 times increase over bacteria incubated with **9 (**Figure 38 -2).

Overall, this showed that there was a significant increase in labelling efficacy through the addition of the spacer, suggesting that a steric clash between the PMBN binding and the streptavidin-biotin binding was the issue with **9**.

3.6.2 Labelling Concentration Effect on Off-Target Labelling

With a view towards the adaption of the polymyxin-biotin binding assay towards a lateral flow test, the concentration dependence of the labelling was investigated. Additionally, an aim of this probe was to be able to distinguish between Gram-negative and Gram-positive bacteria, hence limiting off-target labelling was important.

The concentration of **12** was varied between 0 and 50 μM with Gram-negative *E. coli* and non-target Gram-positive *B. subtilis.*

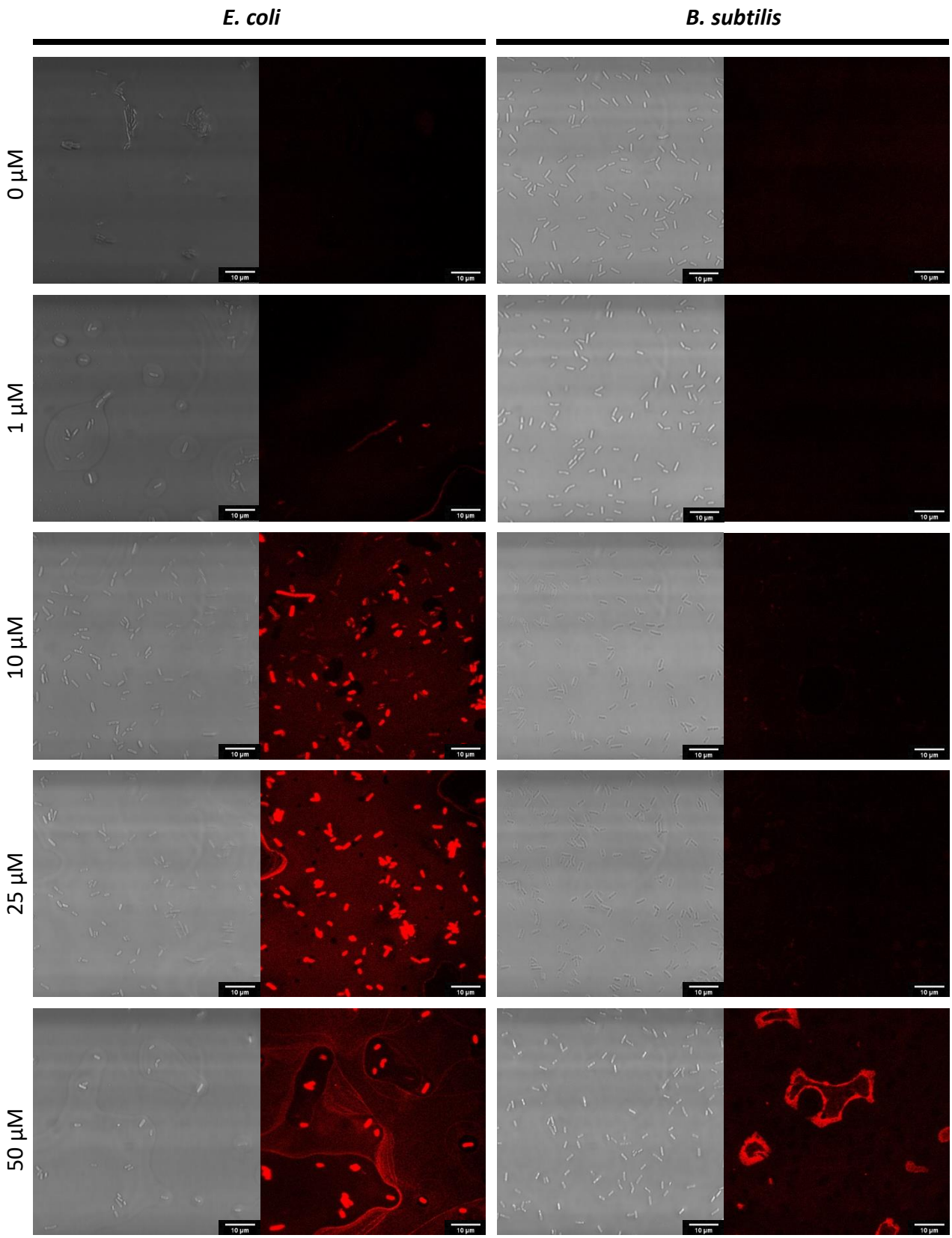

Figure 39: Confocal laser scanning microscopy images of *E. coli* (left) and *B. subtilis* (right), bright field (left) fluorescence (right). *E. coli* and *B. subtilis* were prepared in PBS at 0.5 OD from overnight cultures. Labelling with **12** (0 - 50 µM for 1 hour) was followed by the addition of Streptavidin-555 (10 µg/mL for 30 minutes) – with washing via centrifugation after each incubation step. Scale bar 10 µm. Excitation λ_{ex} = 561 nm Emission λ_{em}= 570 - 600 nm. The background (*B. subtilis*, 50 µM) is due to residual Streptavidin-555 bound to the poly-D-lysine plate and does not correspond to bacteria.

Fluorescence images showed increasing signal with concentration, though the difference between 10 and 50 µM was small and with an increased background (Figure 40). The background labelling was not necessarily an issue for the lateral flow application however, and it is worth noting that there were diminishing returns beyond 10 µM. At all concentrations there was essentially no off-target-labelling of *B. subtilis* which was in line with the imaging seen with the fluorescent probe NBD-PMX [138] At 50 µM there was some additional binding of residual streptavidin-555 to the poly-D-lysine plate, but this did not correspond to labelled bacteria.

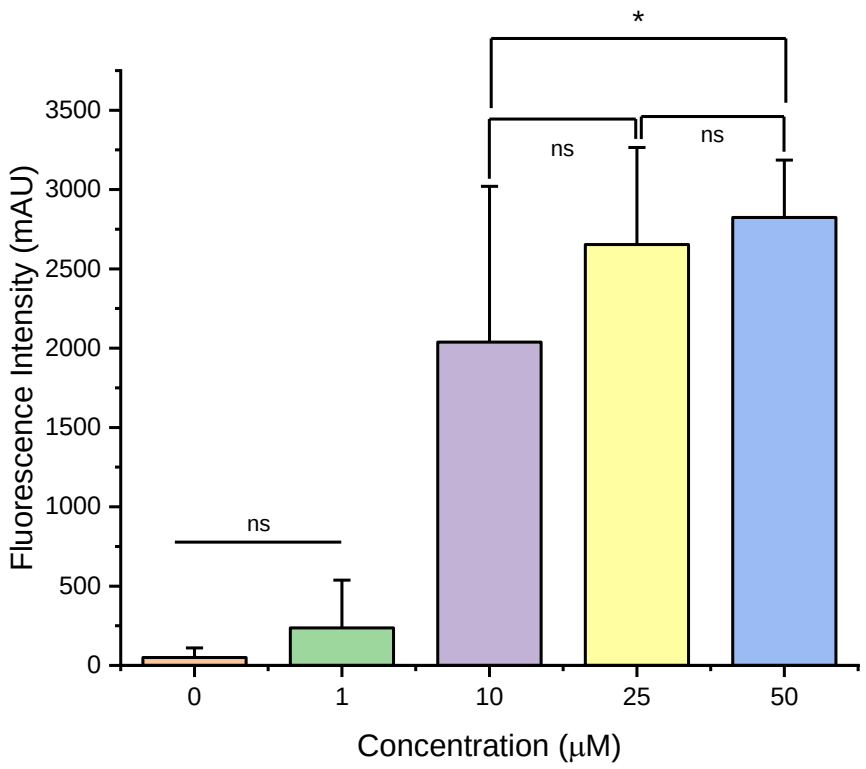

Figure 40: A comparison of *E. coli* fluorescence labelling intensity across the concentration range shown in figure 37 as calculated by ImageJ, Fiji. A representative sample of 15 bacteria and 15 areas of background were taken in each fluorescence image to provide averages for analysis. Error bars calculated from the standard deviation in the signal intensity. *P < 0.05 between 50-10 µM. No significant difference between 10-25 µM and 25-50 µM was observed. Significance was tested with Bonferroni's Multiple Comparison Test.

Results showed that strong labelling was possible at 10 µM and background was lower than 25 or 50 µM. The variance in signal strength of bacteria at 10 µM warranted further investigation to see if labelling at this concentration was time dependant, this was also important as the planned application of the probe is in lateral flow test where speed of detection is vital.

3.6.3 Incubation Time Optimisation Biotin-Ahx-PMBN (**12**)

E. coli was initially incubated with **12** for different times (1 – 60 mins) before being washed and the streptavidin-555 added for 5 minutes before another washing step. The washing steps (pelleting bacteria via centrifuge and replacement of supernatant) resulted in a minimum contact time of 1 minute between **12** and the bacteria. Confocal images (Figure 39) showed labelling of *E. coli* across all time points and, the reduced incubation time with streptavidin appeared not to strongly effect the final labelling of the bacteria.

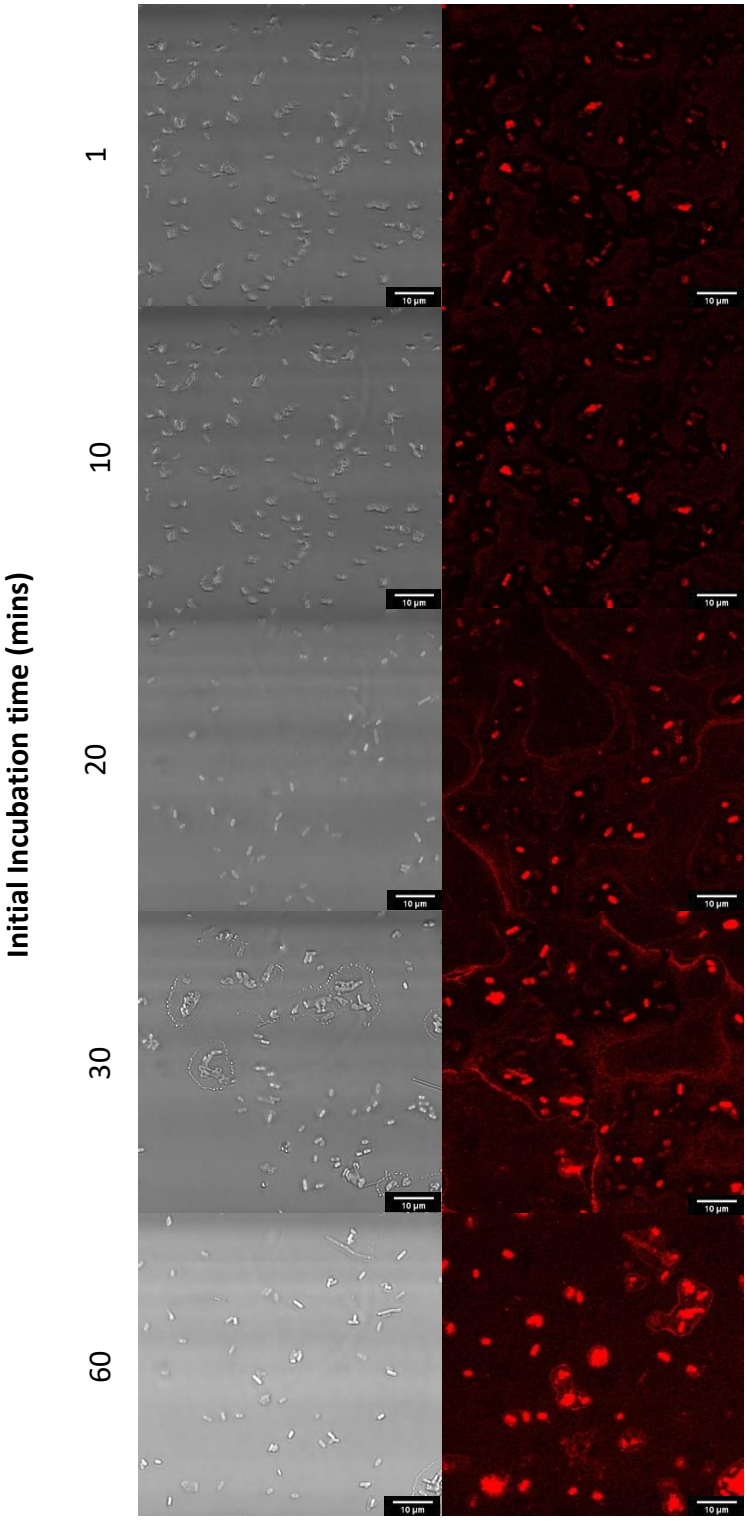

Figure 41: Confocal laser scanning microscopy images of *E. coli* which was prepared in PBS at 0.5 OD from an overnight culture. Labelling with **12** at 10 µM for the indicated time prior to washing via centrifuge pelleting resulting in a consistent 1 minutes of contact time between **12** and the bacteria for all samples, Streptavidin-555 (10 µg/mL for 5 minutes). Scale bar 10 µm. Excitation λ_{ex} = 561 nm, Emission λ_{em} = 570 - 600 nm

The labelling of the bacteria appeared to be strong, and even rapid labelling (i.e. 1 minute incubation time), however the proportion of bacteria in the imaging area that were strongly labelled was low (compare bright field and fluorescence). As the incubation time increased the maximum fluorescence of an individual bacterium increased slightly but the key feature was that the overall proportion of stained bacteria increased.

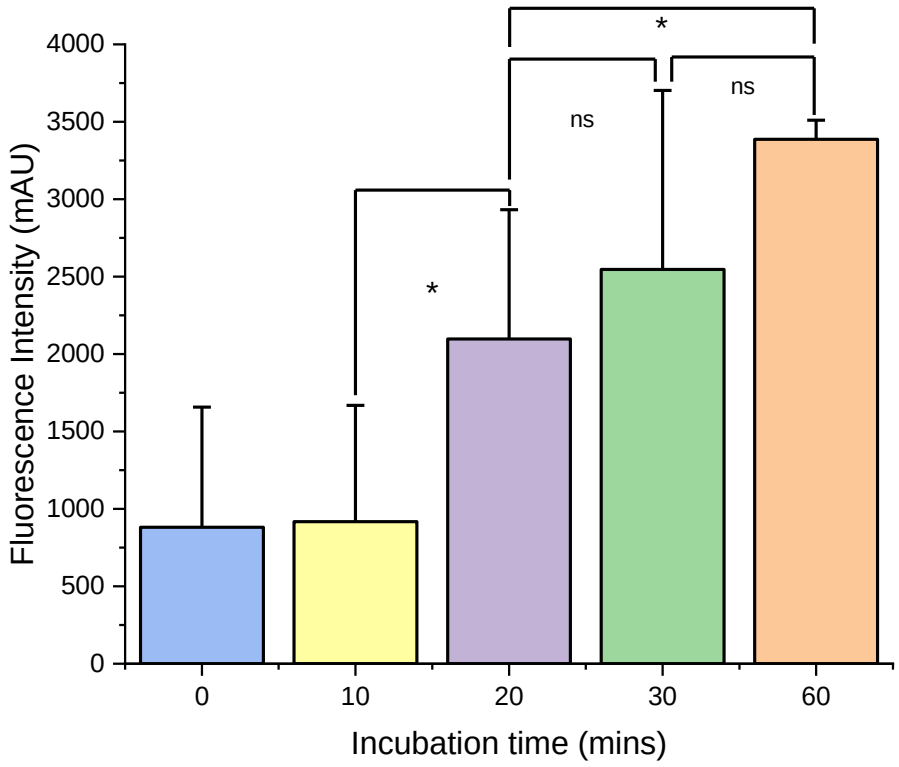

Figure 42: A comparison of *E. coli* fluorescence intensity across the incubation time range shown in figure 41 as calculated by ImageJ, Fiji. A total of 15 area samples were taken for bacteria and background in each fluorescence image to provide averages for analysis. Error bars calculated from the standard deviation in the signal intensity. *P < 0.05 between time intervals. Significance tested with Bonferroni's Multiple Comparison Test.

The total fluorescence increased 2-fold as incubation increased from 0 - 60 mins. However, the standard deviation highlights the variability between bacteria, some of which are strongly labelled and some weakly labelled at incubation time <30

minutes. At 60 minutes all the bacteria present in the field of view were strongly labelled showing a greatly reduced standard deviation.

The combination of microscopy experiments showed that probe **12** with streptavidin-555 selectively labelled Gram-negative bacteria rapidly at 10 μM but that labelling is more intense and with lower standard deviation with increased concentration and increased incubation time. This labelling essentially biotinylates the surface of the bacteria which would be used in the development of a lateral flow assay.

4 Functionalised Gold Nanoparticles for Lateral Flow Assays

Colloidal gold nanoparticles (AuNPs) have been used in a wide range of biological applications taking advantage of the many unique properties seen at the nanoscale that are not seen in the bulk material. This includes their strong absorbance of specific wavelengths of light, tuneable by controlling particle shape and size (including aggregation) which gives the particles a strong absorbance/colour which has been applied in a range of sensors (such as lateral flow[190] assays). This absorbance has also be used for photothermal therapy where the absorbed energy results in highly localised heating and has been explored as a possible treatment for tumours (thermal ablation).[191]

An important property of AuNPs is their ability to bind thiol containing molecules due to the nature of the Au-S bond. This enables the facile attachment of biologically relevant compounds to their surface, as seen in their application as drug delivery vehicles[192] where proteins[193], DNA[194] and, chemotherapy agents[195] are attached to the AuNPs to facilitate increased uptake of these drugs to the diseased tissue.

In my PhD I applied the properties of AuNPs to allow the attachment of polymyxin-based compounds to AuNPs to allow bacterial targeting and then use their strong colour for sensing/reporting on a lateral flow test.

4.1 Optical Properties of AuNPs

The strong absorbance of visible light by gold nanoparticles arises from the surface plasmon reasonace (SPR) phenomenon.[196] SPR occurs due to the interaction of

electrons on the nanoparticle collectively interacting with electromagnetic radiation and oscillating (Figure 43). This collective movement of a cloud of electrons is similar to a plasma which, when described in terms of a single quantum of movement, is the basis for the name plasmon (i.e. 'plasmon' is a portmanteau of 'plasma oscillation').[197]

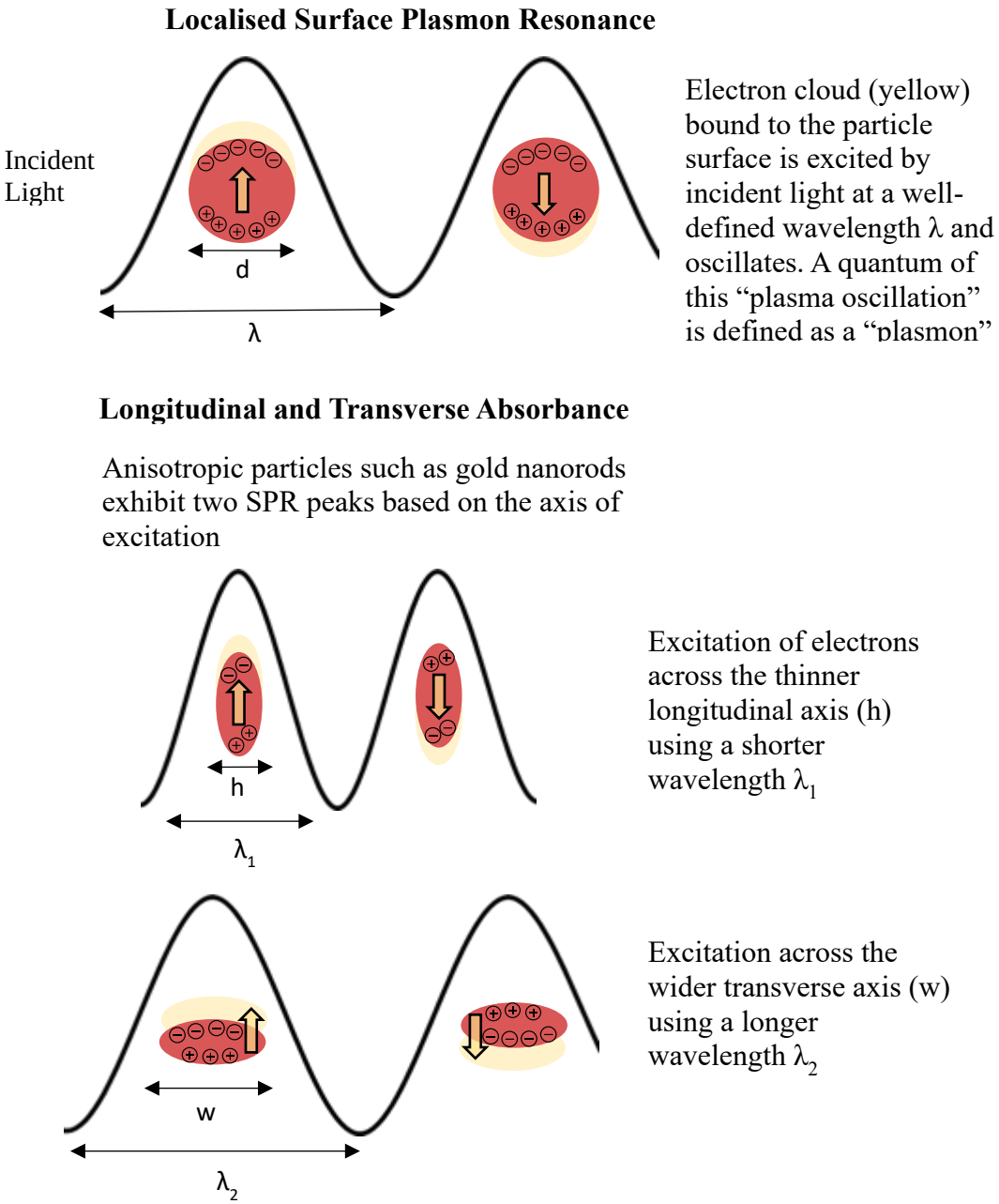

Figure 43: The interaction of light with the localised surface plasmon of gold nanoparticles gives rise to strong absorbance relative to the particles shape and size. The anisotropic nature of nanorods gives rise to separate transverse and longitudinal resonances.

This effect is not seen in bulk material as the electromagnetic radiation can only excite electrons at the surface and at the nano-scale the radiation can polarise the electrons across the entire particle.

As this effect is based on an osciallation of the electron cloud it behaves in a similar fashion to the oscillation of a spring. The effect is therefore highly specific to defined wavelengths of light with a frequency in resonance with the osciallation. This means that the exact wavelengths of light that resonate with the electron cloud depends on the shape and size of the particle (Figure 44). Larger particles experience a larger oscillation and therefore absorb strongly at longer wavelengths.[198] Anisotropic particles such as gold nanorods show two SPR peaks depending on the direction of the oscillation.[199,200] This effect can also be influenced to a degree by the surface coating of the particle which alters the dielectric environment at the surface.[201]

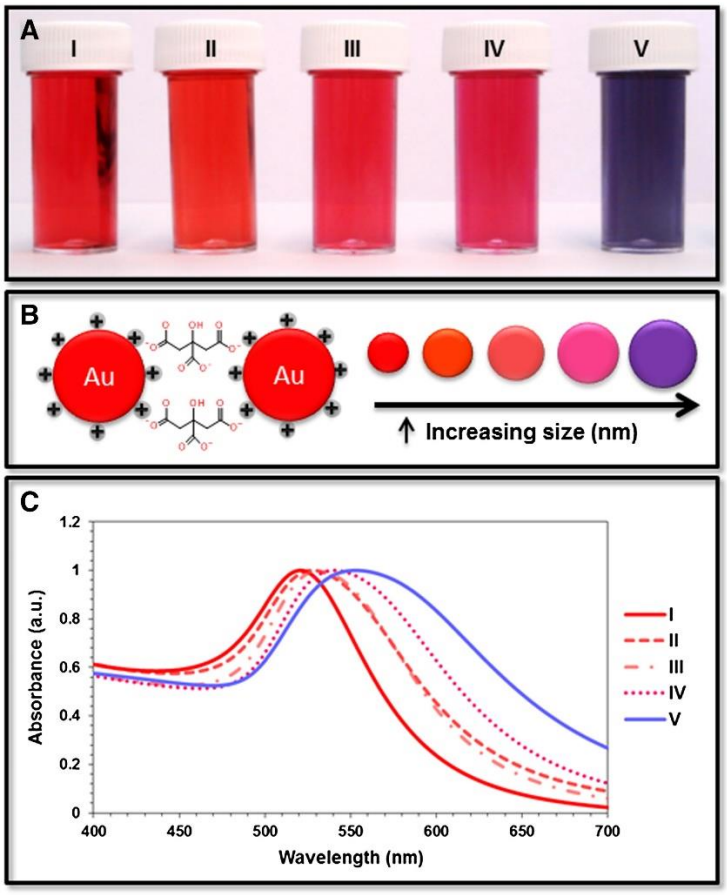

Figure 44: Overview of the change in AuNP absorbance properties caused by shifts in the SPR with increasing size. A) Image of citrate stabilised gold nanoparticle solutions with particles sizes of: I – 12 nm, II – 28 nm, III – 45 nm, IV – 63 nm V- 85 nm as determined by TEM. B) Representation of the relationship between increasing particle size and change in colour. C) UV-Vis measurement of the SPR peak normalised to 1 OD. Reproduced from Nanomedicine Nanotechnol. Biol. Med., 2017, 13, 1531–1542 Creative Commons CC-BY license – Elsevier [202]

4.2 Functionalisation of Gold Nanoparticles

As mentioned before, another key property of gold nanoparticles that makes them well suited to many biological applications is their compatibility with surface functionalisation. If the nanoparticles are made with a weakly binding stabilising agent such as sodium citrate, a substitution reaction can be used to add functionality to the particle relying on the greater binding affinity of the target ligand for the gold surface.

Attachment of ligands, both small molecules and large biomolecules, is classically achieved through a thiol-group which has a high affinity for the gold surface.[203] While the exact nature and strength of the Au-S bond on AuNPs is somewhat debated[204] it is generally understood to be a strong (i.e. near covalent) interaction.[205] Inkpen et al. recently showed, using a scanning tunnelling microscope 'break-junction' method, that the Au-S bonds seen in self-assembled monolayers, particularly when derived from dithiol precursors, are physisorbed in nature rather than chemisorbed.[206]

A common alternative method specifically for the attachment of large biomolecules and polymers is to rely on the broadly non-specific electrostatic/hydrophobic interactions between biomolecules and the nanoparticle surface. One concern with this non-specific addition is the lack of orientation control, relevant to biomolecules such as antibodies where there are specific regions like the antigen binding site that need to remain accessible to maintain their function. If orientation is not controlled a percentage of the attached antibodies would have their binding sites 'face-down' on the surface of the AuNP instead of facing out into the solution.

An example of this orientation control was carried out by Oliveira *et al.* (Figure 45).[207] They attached an antibody to AuNP's with controlled orientation via covalent coupling to a mercaptoundecanoic acid spacer and compared it with the non-controlled physisorbtion addition to nanoparticles and analysed the amount and orientation of the attached antibodies.

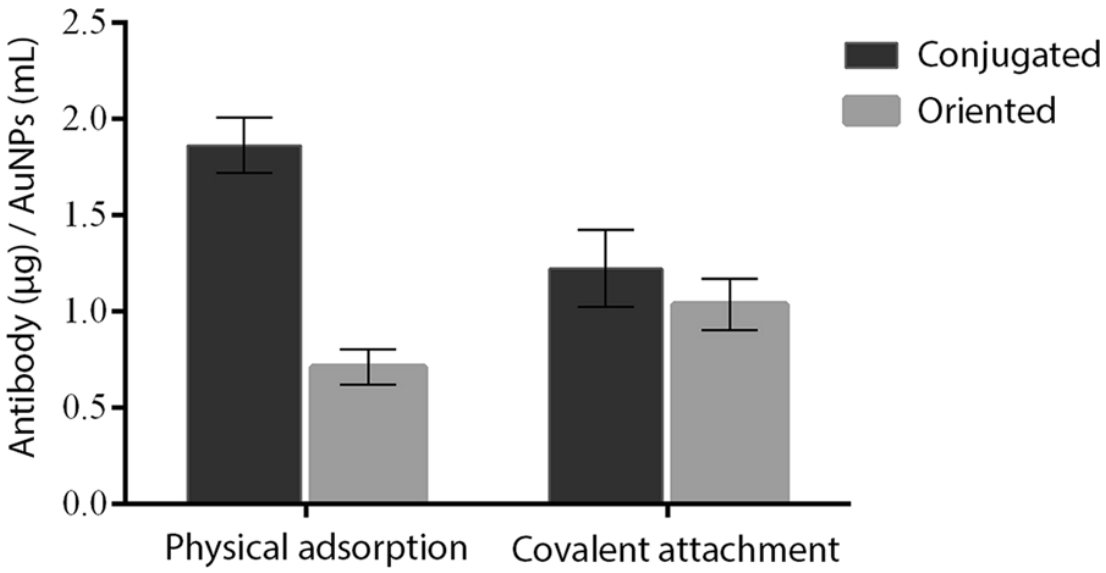

Figure 45: A comparison of conjugation techniques for the addition of antibodies to a gold nanoparticle. Physical absorption resulted in a higher loading of antibodies, but a lower proportion were correctly oriented for binding – as determined by complementary antibody binding. Image reproduced from Sci Rep **9**, 13859 (2019). Creative Commons CC BY license. [207]

They characterised the binding through the addition of an anti-Fab Alexa Fluor 750 secondary antibody. They showed that while a higher total loading could be achieved through physisorbtion, controlled covalent attachment resulted in a higher proportion of the attached antibodies being in the correct (binding) orientation.

4.3 Synthesis

There are a range of common and robust synthesis methods for colloidal gold nanoparticles, the key method relavent for this project being that of Turkevich (1951)[208] which was later refined by Frens (1973)[209].

This method uses a precursor gold salt ($HAuCl_4$) as the source of gold ions and a chemical reducing agent to convert the Au^{III} down to Au^0 atoms which start to gather together to form particles. A capping agent coats the surface of the newly forming

particles stopping their continued growth. The Turkevich/Frens method uses trisodium citrate as both the reducing and capping agent.

4.3.1 Turkevich / Frens Method

The standard experimental procedure for this synthesis involves heating an aqueous solution of $HAuCl_4$ (typically 0.1 – 0.5 mM) to boiling point before the rapid addition of an aqueous trisodium citrate solution (typically 2 – 4 mM).[209] The addition of the trisodium citrate triggers the formation of the nanoparticles and the solution's colour transitions in a characteristic pattern from the light yellow (of the $HAuCl_4$ solution) to grey/blue before turning red.[210]

The process of Au^{III} reduction with trisodium citrate to stable citrate capped AuNPs in the Turkevich / Frens method happens over a number of steps and the exact mechanism has been the subject of debate since Turkevich's first publication. An overview of the current best understanding of the mechanism is provided by Wuithschick et al[211] based on real-time x-ray scattering spectroscopy methods.[212,213]

The proposed mechanism occurs in four steps (Figure 46):

1. Reduction / formation of clusters
2. Formation of seed particles
3. Slow growth on seed particles
4. Fast growth on seed particles

In the first step, the introduction of a reducing agent (trisodium citrate) triggers the formation of clusters of Au^0 from Au^{III}. These clusters continue to grow and clusters themselves can join together, to give seed particles (>1.5 nm). The remaining remaining Au^{III} ions are attracted to the electric double layer that is formed at the

surface of the seed particles and remain there as co-ions. These co-ions are reduced and incorporate onto the surface of the existing seed particles in two stages, first slowly then in a final rapid stage.

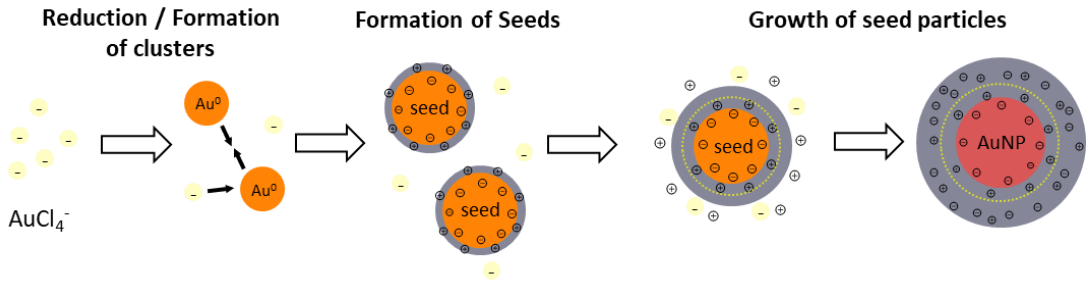

Figure 46: Illustration of the formation of gold nanoparticles via citrate mediated chemical reduction showing the stages of seed formation, seed growth and stabilisation of full particles. Figure adapted from reference ACS Nano 2015, 9, *7*, 7052–7071[211] Copyright © 2015 American Chemical Society

Control of the particle size is based on the ratio of Au precursor to trisodium citrate as this controls the number of seed particles that are formed in step 2. During this initial seed formation reduction of the reactive $[AuCl_4]^-$ species is fast but is terminated by conversion of the remaining $[AuCl_4]^-$ to a less reactive $[AuCl_{3-x}(OH)_{1+x}]^-$ species.

While the stability of the final particles arises from the capping of the surfaces by trisodium citrate the overall particle size is controlled solely by seed particle formation, not the rate of capping. The final growth stages result in nanosphere formation, as the final reduction of $[AuCl_{3-x}(OH)_{1+x}]^-$ species occurs preferentially on the surface of the existing seed particles evenly across the surface.

Work by Dong et al showed the range of particles produced through the Turkevich method and the effect of alterations of the molar ratio between trisodium citrate and $HAuCl_4$ (Figure 47).[214]

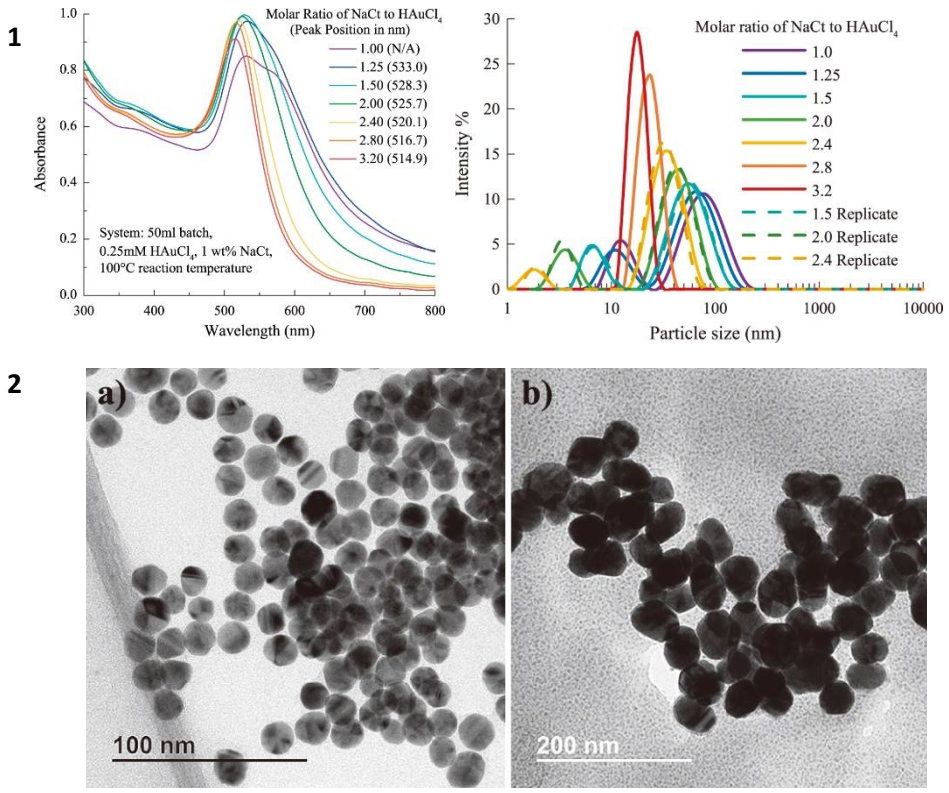

Figure 47: 1) UV-Vis analysis (left) showing the shift in SPR peak with increasing size and the associated DLS (right) measurement of particle size. 2) TEM imaging of as-synthesized AuNPs a) MR = 2.80, mean size = 15 nm, batch size = 1.5 L; b) MR = 1.50, mean size = 50 nm, batch size = 1.5 L. Reproduced from KONA Powder Part. J., 2020, 37, 224–232[214] Creative Commons CC-BY license

They showed a large range of particle sizes are technically accessible through the Turkevich/Frens method but that particles in the range of 15 – 30 nm were the most monodisperse (PDI < 0.2) across a range of synthesis scales (50 mL – 1.5 L).

4.3.2 Seed-Growth method

A method which has seen significant interest recently, the seed-growth method, can be thought of as a combination of the Turkevich and Brust[203] methods. In this method typically small (< 2 nm) seed particles (i.e. Figure 46 parts 1 and 2) are first generated and isolated using $NaBH_4$ reduction of $HAuCl_4$ in the presence of trisodium citrate .[215] The starting size of the seed particle controls the minimum size acessible from the method so standard Turkevich synthesis (i.e. reduction with

trisodium citrate) can be reliably used to create the seed particles if the target size is >10 nm.[216]

The method progresses to use these seed particles as the basis for the controlled addition of an Au^{III} containing 'growth solution', slowly increasing their diameters. Zeigler et al. showed a seed-growth synthesis method that provides stepwise control over the size of the resulting particles to between 15 – 300 nm (Figure 48).[216] The growth solution consisted of two parts: an $HAuCl_4$ solution to act as the Au^{III} - feedstock and, a gentle reducing solution of trisodium citrate and ascorbic acid.

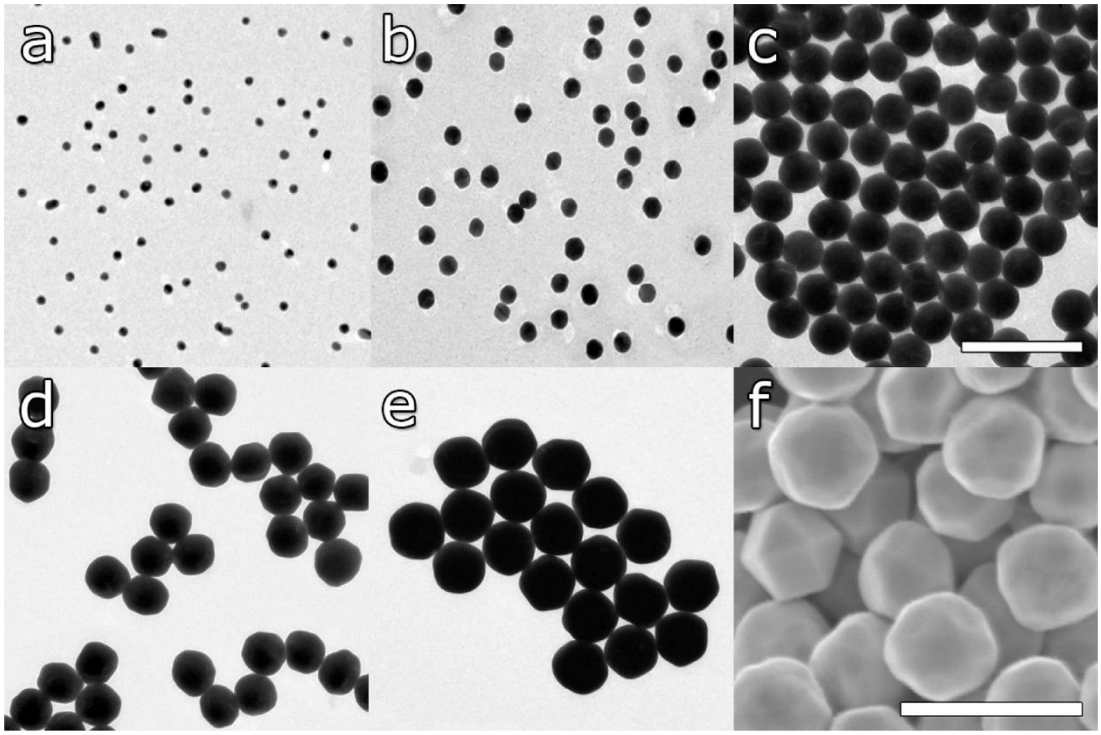

Figure 48: Particles produced using the seed-growth synthesis by Zeigler et al. . TEM images of (a) 15 ± 2 nm (seeds), (b) 31 ± 3 nm, (c) 69 ± 3 nm, (d) 121 ± 10 nm, and (e) 151 ± 8 nm and SEM image of (f) 294 ± 17 nm gold nanoparticles. Scale bars are 200 nm for parts a−c and 500 nm for parts d−f. Reprinted with permission from J. Phys. Chem. C 2011, 115, *11*, 4502–4506. Copyright 2011 American Chemical Society.[216]

This method enables access to citrate coated gold nanoparticles with a broad range of diameters with significantly improved control over the resulting monodispersity. While the Turkevich method maintained good dispersity in the 10 – 30 nm range this

method is particularly useful for accessing larger sizes (> 60 nm up to 300 nm) while still maintaining an easily substitutable surface coating such as trisodium citrate.

4.4 Characterisation

Through understanding how the SPR changes with shape, size, and concentration these properties can be estimated for an unknown sample. Specifically, through an application of Mie theory in combination with experimental measurements Haiss et al. showed that for citrate coated gold nanospheres with diameters between 15 – 130 nm), concentrations of nanoparticle could be accurately calculated from the absorbance spectrum.[217]

They derive two key equations from a modified Mie theory method in combination with experimental data to determine fit parameters (accounting for variations in theory due to surface coatings). The first equation determines the size of particles based on a ratio of absorbance at the SPR peak and at 450 nm, where scattering does not contribute significantly to the absorbance measured.

Equation 3 $$d = exp\left(B_1 \frac{A_{SPR}}{A_{450}} - B_2\right)$$

Where d is the diameter of the particle, A_{SPR} is the absorbance measured at the SPR peak, A_{450} is the absorbance measured at 450 nm. B_1 and B_2 are experimentally derived fit parameters based on measured $\frac{A_{SPR}}{A_{450}}$ values of particles of known size and determined to be 3.00 and 2.20 respectively.

Based on the same method of fitting derived equations to experimental data they showed a second equation could be used to calculate the concentration of a gold nanoparticle solution.

Equation 4

$$N = \frac{A_{450} \times 10^{14}}{d^2\left[-0.295+1.36\exp\left(-\left(\frac{d-96.8}{78.2}\right)^2\right)\right]}$$

Where N is the number of particles in the solution per millilitre, A_{450} is the absorbance measured at 450 nm and d is the diameter either derived experimentally or through the previous equation. The fitting factors were derived from a Gaussian fit of experimentally determined data of the extinction coefficient of nanoparticles of known diameters at 450 nm.

The equations shown are explicitly limited to monodisperse citrate coated nanospheres and other characterisation techniques such as dynamic light scattering (DLS) and transmission electron microscopy (TEM) are key for a more detailed understanding of the shape and size of nanoparticles.

DLS is an analytical technique from colloid chemistry which uses the scattering properties nanoparticles in a colloidal system to give their hydrodynamic radii (R_H) through measurement of scattered light from an incident laser (Figure 49). In the context of gold nanoparticles this means DLS is measuring the size of the [particle+corona] built up from solvent, ligands or proteins attached to the surface which can lead to significant deviation between[218] DLS and TEM measurements.[219]

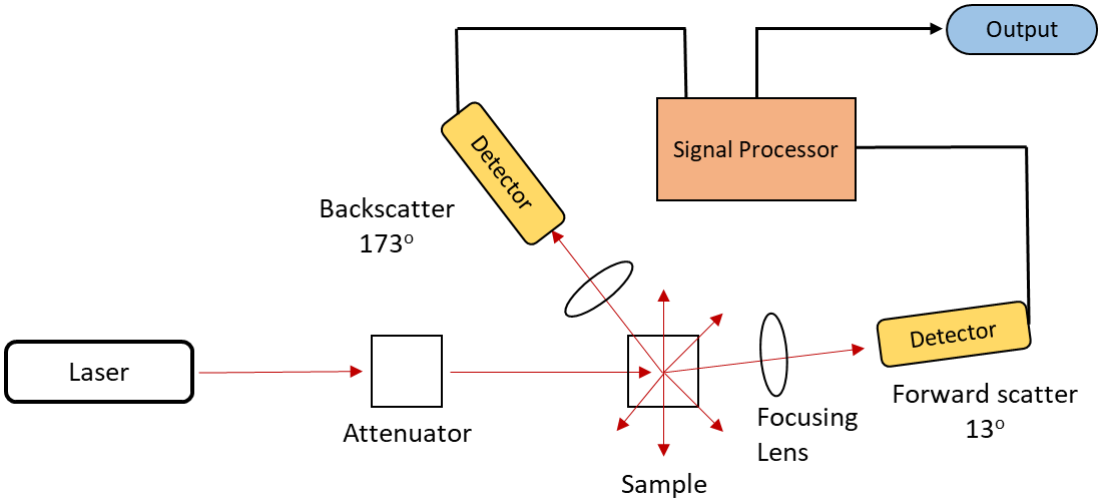

Figure 49: Overview of a DLS system. The laser is fired at the sample with its power controlled by a variable attenuator. Light scattered from particles in the sample scatter in all directions but are detected at two angles, either/both non-invasive backscatter (173°) or forward scatter (13°). Some instruments will also collect at scattering data 90° from the sample. Figure adapted from JCR 235, 2016, 337-351 © 2016 Elsevier B.V. All rights reserved.[220]

The intensity of scattering is proportional to the particles radius raised to the power of six.[221] In a disperse colloid this scattering is altered by the phasing in and out of scattered light as the particles move with Brownian motion. The variation in the intensity of scattered light is measured and fit to an autocorrelation function automatically by the instrument's software with key parameters of solvent viscosity, refractive index, and temperature part of the analysis. This yields 'Intensity' based measurement of particle size distribution.

As 'Intensity' measurement is highly sensitive to even a small number of larger debris or aggregates, it can lead to 'erroneous' results where particles are reported to be significantly larger than seen in TEM measurements. Additionally as DLS assumes particles to be spherical, impossibly small measurements (< 1 nm) can be erroneously reported from off-axis scattering of anisotropic particles.[222] Weighted measurements can be derived from the 'Intensity' data to account for the proportion

of the signal arising from particles by number or by volume (i.e. to account for the r^6 proportionality by size).[223]

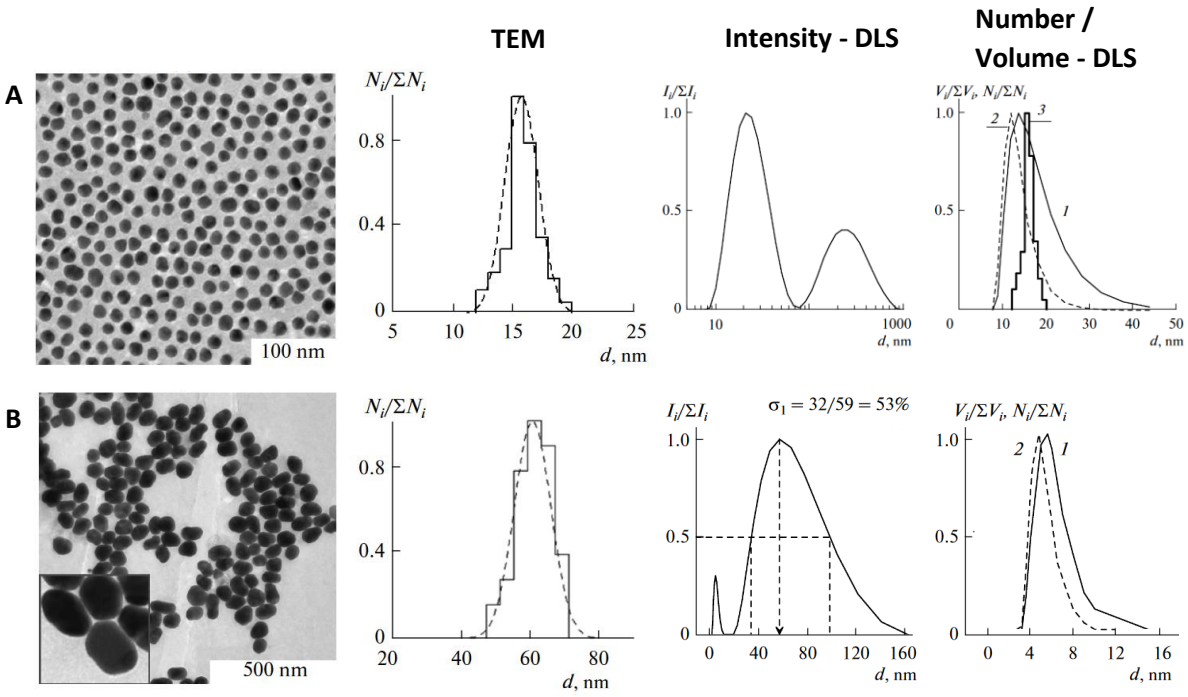

Figure 50: Characterisation of gold nanoparticles by TEM and DLS. A) 16 nm diameter particles (from TEM imaging) showing an erroneous peak at 400 nm under DLS analysis based on intensity which is not present on the Volume or Number derived measurements (labelled 1 and 2 respectively, 3 – overlaid TEM data). B) 60 nm diameter particles (from TEM imaging) showing an erroneous peak at 1 nm via DLS analysis based on intensity which is not present on the Volume or Number derived measurements (labelled 1 and 2 respectively). Reproduced with permission Colloid Journal volume 73, pages 118–127. 2011 Copyright Pleiades Publishing, Ltd.[222]

The measurement inconsistencies with DLS as shown by Khlebtsov et al. (Figure 50) show the different weighting of the measurements and how it can be challenging to interpret DLS values. While number and volume weighted measurements tend to emphasise smaller particles methods such as z-averaging combines the measurements, resulting in a final reported size closer to TEM measurements, at the expense of losing information about size distribution.[224] There is little consistency with which DLS values are reported in literature, an issue that has been commented on[220], yet 'Intensity' values are generally regarded as the primary measurement.

For measurement of the core particles (i.e. without the influence of the coating), TEM is the standard technique as metals are highly diffracted by an electron beam and give excellent contrast in the image. This, in combination with the high magnification achievable with TEM (with resolution down to < 50 Å depending on beam power and aberration correction)[225] means that individual nanoparticles can be imaged. Commonly, image(s) of a collection of nanoparticles are taken and image processing software is used to measure the size of the particles and plot size distribution. [226]

Other methods such as laser diffraction, differential centrifugal sedimentation, atomic force microscopy (AFM), inductively coupled plasma mass spectrometry (ICP-MS), and nanoparticle tracking analysis have all been used to characterise various nanoparticle properties.[227] For this project, a combination of DLS, UV-Vis and TEM was used to characterise of the size of the core metal particle, the resulting R_H and the concentration of the particles in solution. However, to get a good understanding of surface functionality different techniques must be used.

Measuring the zeta potential of gold nanoparticles can provide characterisation of the surface charge of a particle. Changes in the surface coating with differently charged, or completely uncharged, ligands can identify successful functionalisation of a nanoparticle and analyse its important functional characteristics.

Zeta potential is a measurement of the electric potential of the slipping plane of a colloidal particle when exposed to an electric field (Figure 51). The slipping plane is the theoretical boundary where ions held beyond the particles electrical double layer (surface charge + stern layer) interface with the mobile ions held in the bulk solvent. This measurement can be performed by applying a voltage across a sample and using

a light scattering measurement to quantify the resulting particle movement. Through the particle's direction and speed of travel the charge of the particle can be determined.

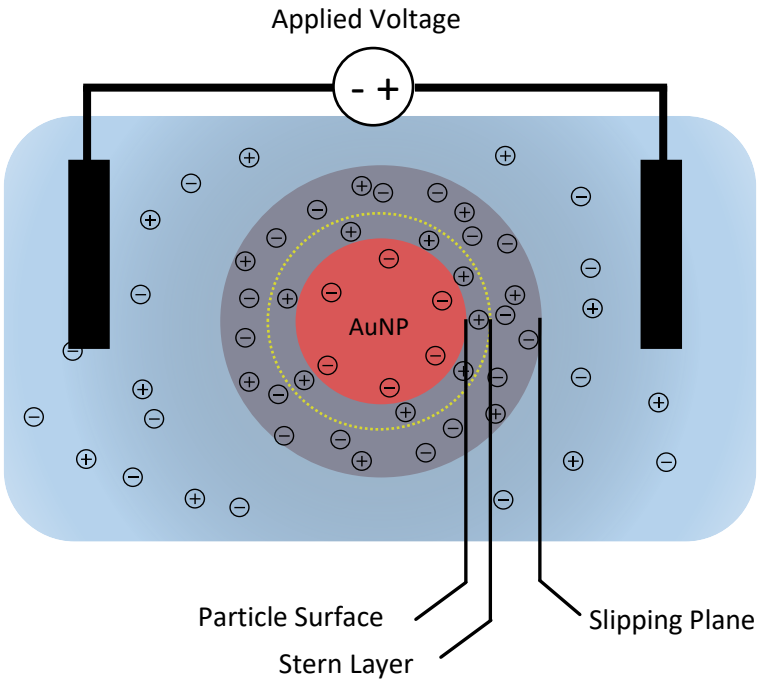

Figure 51: Illustration of the make-up of surface charges on a gold nanoparticle. Zeta potential measures the charge at the slipping plane by applying a voltage to a suspension of nanoparticles and monitoring their movement direction and speed via the same instrumentation as DLS measurements. Adapted from reference Journal of Controlled Release Volume 235, 10 August 2016, 337-351 © 2016 Elsevier B.V. All rights reserved.[220]

For functionalised gold nanoparticles it is this charge which can determine the interactions between the particle and biological targets. Additionally, it is this surface charge which helps stabilise the nanoparticles against aggregation.

Aggregation in a nanoparticle system is the irreversible agglomeration of particles (as opposed to reversible agglomeration) however, these terms are used somewhat interchangeably in literature.[228] As particles aggregate, the optical properties change and as aggregates continue to grow the size becomes greater than can be suspended in solution. This can be detected in gold nanoparticle solutions through each of the

analytical methods discussed above but is most obvious through the red shifting of the absorbance. Additionally, the increase in size increases the scattering of particles which results in a large increase in the absorbance around 600 nm. If the degree of aggregation is severe, the entire suspension collapses and no useful analysis (other than TEM) can be performed as most if not all of the characterisation methods rely on characteristics that are only present while the particles are suspended.

The colour change upon aggregation can be extremely noticeable and has been applied in a number of gold nanoparticle-based sensors with the target analyte disrupting the stabilisation of the nanoparticle. For example Chang et al. developed a sensor for mercury ions based on the aggregation of gold nanoparticles functionalised with mercaptopropionic acid (Figure 52).[229] This was able to selectively sense Hg^{2+} with minimal interface from other di-cations in the presence of 1 mM Dipicolinic acid, with a limit of detection of 100 nM. There are a number of similar assays reviewed by Chang et al. for detecting mercury, lead and copper ions with aggregation induced colour change.[230]

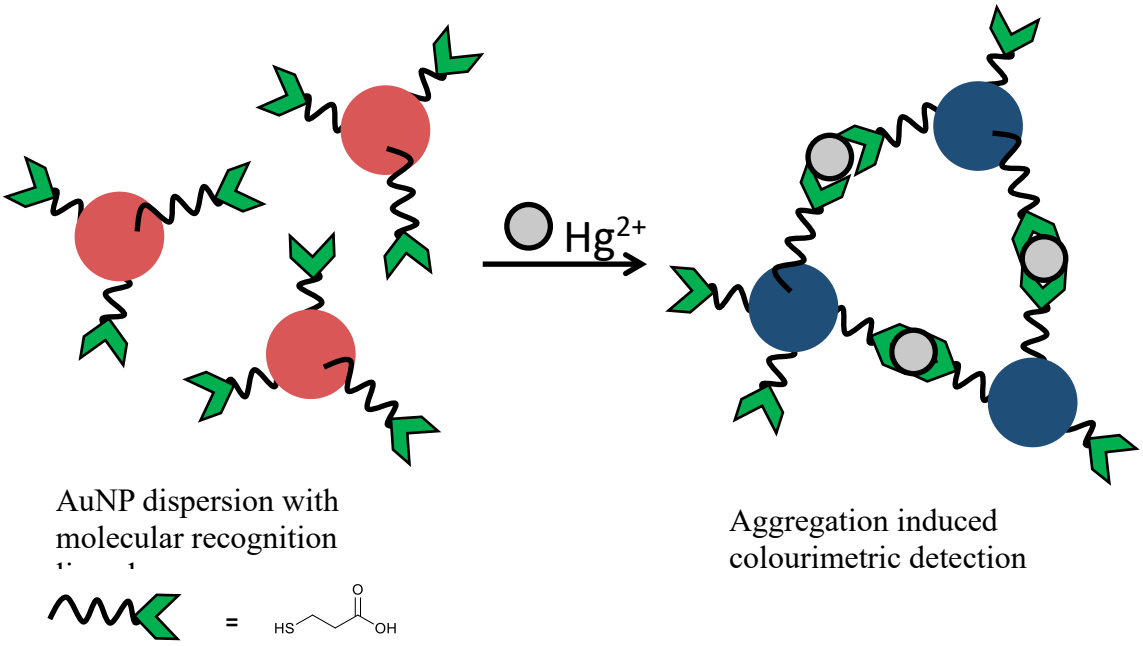

Figure 52: Illustration of the aggregation induced colour change of gold nanoparticle solutions on specific detection of mercury ions.

An interesting application of the effect is seen in the addition of aptamers to gold nanoparticles that in isolation stabilise the particles but, in the presence of their binding target (and NaCl) lose their stabilising effect and an aggregation induced colour change is observed. This was used by Song *et al.* to detect kanamycin (an aminoglycoside antibiotic) using a DNA aptamer.[231]

Even though the core structure of the nanoparticle is not affected, if Au-nanoparticles are brought close enough together, they can act as a larger particle and show the red shift of aggregation. This effect is tied to the average size of the particles and is not consistently seen in all sensors, possibly due to particles not being able to get close enough together due to surface coatings, especially when the original diameter was small.[232]

4.5 Stability

For a colloidal suspension to remain stable in the long term the dispersed particles must be able to resist the attractive forces attempting to bring the particles together to form aggregates.[233] The forces involved in colloidal stability include:

- Electrostatic interactions
- Van der Waals forces
- Steric Forces

Derjaquin–Landau–Verway–Overbeek (DLVO) theory has been used as a theoretical framework to understand and investigate aggregation in colloidal systems.[234] It describes the forces between two particles of radius α each having a charge Z separated by a distance r in a fluid, combining electrostatic interactions and van der Waals forces.

Equation 5 $$\beta U(r) = Z^2 \lambda_B \left(\frac{e^{\kappa\alpha}}{1+\kappa\alpha}\right)^2 \frac{e^{-\kappa r}}{r}$$

Where λ_β is the Bjerrum length, describing the length at which the electrostatic interaction between two charges equivalent to $k_B T \,.\, \kappa^{-1}$ Is the Debye–Hückel screening length and $\beta^{-1} = k_B T$ describing the thermal energy of the system at temperature T where k_B is the Boltzmann constant and U is the potential energy.

While the DVLO theory can help to understand the forces between two charged particles, many of the methods for stabilising colloids rely heavily on increasing the steric bulk of the particles by coating them with large polymers such as polyvinylpyrrolidone (PVP) or proteins such as BSA that keep the metallic core of the nanoparticles physically separate from each other, preventing aggregation.[235,236]

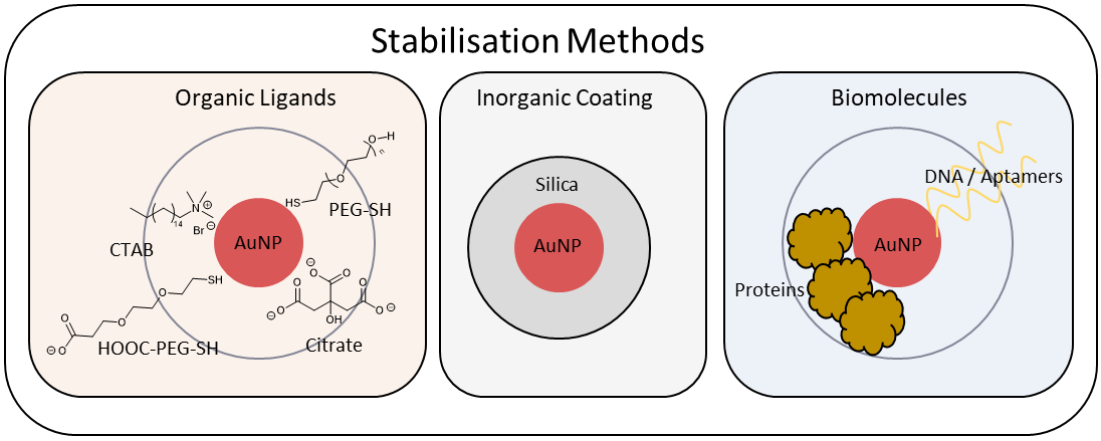

Figure 53: Types of stabilisation methods used in various AuNP applications. Figure adapted from Chem. Rev. 2019, 119, 1, 664–699. [237]

A range of strategies can be employed for the stabilisation of nanoparticles: charge and/or steric stabilisation through the addition of organic ligands, coating the particle with an inorganic shell such as mesoporous silica or coating with biomolecules such as aptamers/ antibodies (Figure 53).[237] In many cases the addition of functional ligands to a nanoparticle also provides the stabilisation required. However, in some applications a mixed monolayer structure is used to add a combination of a non-functional ligand that provides stability and a functional ligand that does not.[238]

Aims

The aims of this part of my PhD were to generate stable gold nanoparticle conjugates that could selectively label Gram-negative bacteria using a polymyxin targeting ligand for use in a lateral flow test (Chapter 4). This required the synthesis of gold nanoparticles with clearly defined optical properties with a well characterised surface functionalisation to enable bacteria ligand attachment. The nanoparticle conjugates needed to demonstrate long term stability and have a reliable synthesis for use in developing a lateral flow assay.

4.6 Results and Discussion

The first approach to making functional gold nanoparticles was to attach a ligand that would label bacteria via a substitution method. This required the synthesis of gold nanoparticles with a weakly bound surface coating that could be replaced with the ligands of choice containing thiols. For the purposes of this work, nanoparticles in the size range of 20-60 nm were appropriate as they have high extinction coefficients which would provide good sensitivity in lateral flow tests.

4.7 Citrate Coated Nanoparticles (Au@Citrate)

Citrate coated nanoparticles were synthesised with two different procedures. For small scale synthesis (1 – 20 mL) $HAuCl_4$ and trisodium citrate were added to sealable glass vials and microwave heated to 100^{o}C for 10 minutes. For larger batch synthesis (50 – 400 mL) a more traditional Frens synthesis was performed with the $HAuCl_4$ solution being brought to boiling before the rapid addition of the trisodium citrate solution. Heating time varied with volume and was maintained until a deep red colour of colloidal gold was observed. Each of these methods were able to reliably produce particles within the desired size range with low polydispersity (Figure 54).

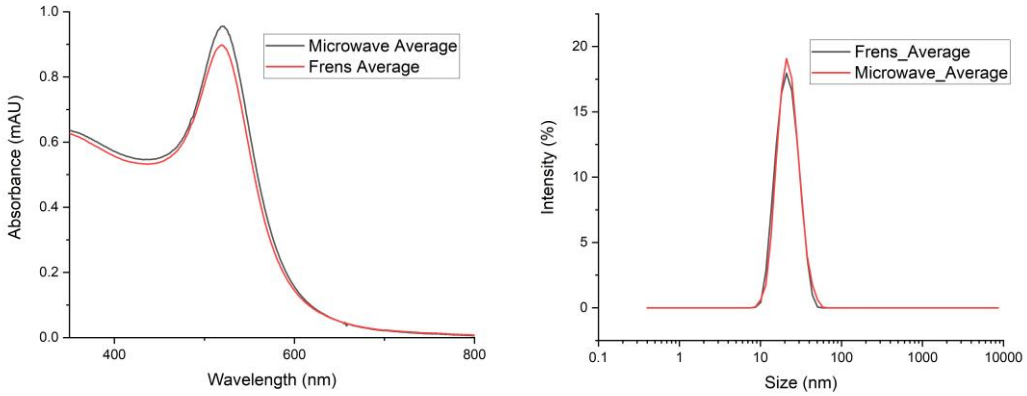

Nanoparticles	λ_{max}	UV-Vis Size	Intensity DLS / nm	PDI	Zeta / mV	SD / mV
Microwave	521	20.2	21.2	0.14	-27.8	7.32
Frens	519	16.7	22.4	0.12	-33.5	3.73

Figure 54: Absorbance spectra (Left) and DLS analysis (Right) for Au@Citrate synthesised through the microwave or the traditional method. Data for Frens method was averaged from 4 separate syntheses. Microwave method data averaged from 3 separate synthesise. The table summarises key characterisation data. *UV-Vis Size refers to diameter calculated using values from the absorbance spectra processed with equation 3

Analysis of the absorbance spectra using the equations from Haiss et al.[217] (Equation 3/4) provided a size measurement and yielded an average concentration of 1.7 nM (i.e. $1x10^{15}$ nanoparticles / L) for Au@Citrate synthesised through either of these methods.

4.7.1 Au@Citrate TEM Characterisation

The citrate particles from the Frens synthesis were characterised with TEM imaging and showed an average size of 18 ± 2 nm which is consistent with literature reports[219] that a citrate coating on the surface of gold nanoparticles adds approximately 2 nm in DLS measurements due to the hydrodynamic volume (Figure 55).[224,239]

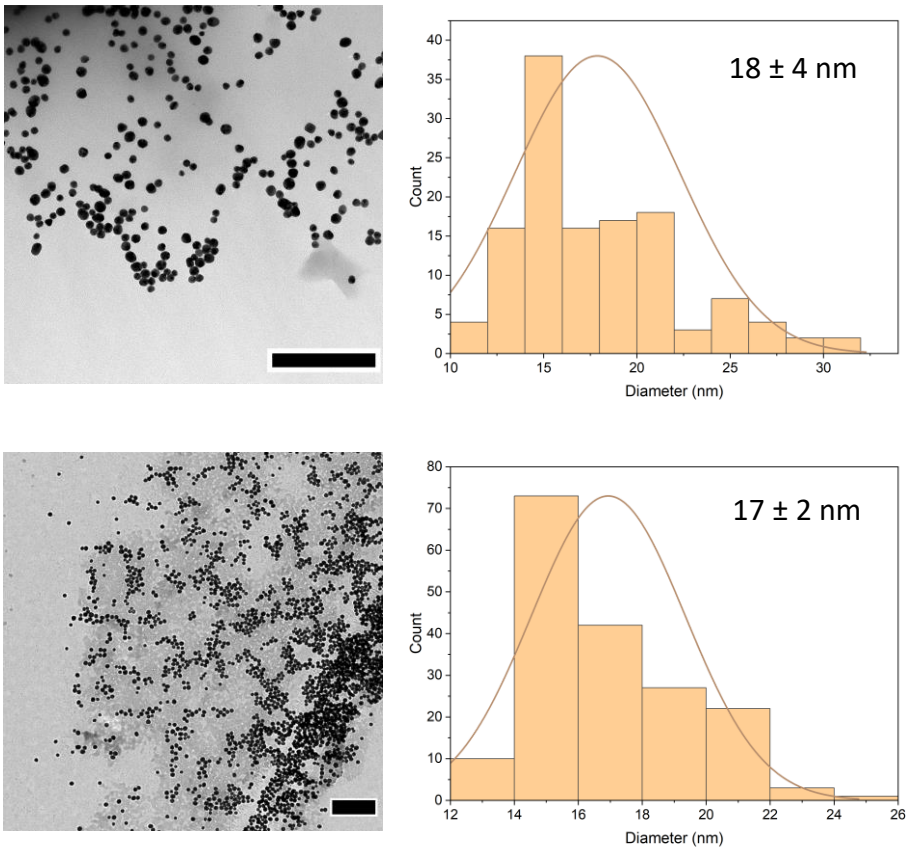

Figure 55: TEM images of synthesised gold nanoparticles with the corresponding particle diameters. Scale bar 200 nm. Sizes were extracted using ImageJ particle analysis plugin with area cut offs of 72 - 1256 nm^2 and a circularity parameter of 0.7.

These Au@Citrate particles were used for substitution experiments where the surface coating was replaced with functional compounds.

4.8 Au@**6** Particles

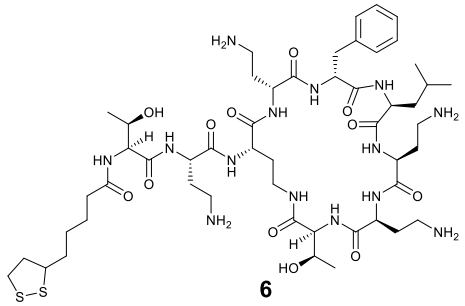

Figure 56: Structure of Lipoic Acid-PMBN (6). The sulfur atoms from the Lipoic acid provide the anchor for its attachment to Au@Citrate

Liu *et al* provide a comprehensive tutorial for the preparation of nanoparticles with thiol-terminated aptamers, describing their addition at 1 mM to a 13 nM Au@Citrate solution.[240] For small molecules, examples such as the preparation of carbapenem loaded gold nanoparticles by Shaker *et al.* describe the addition of the antibiotic at 2.5 mM (1 mg/mL) to Au@Citrate (0.1 mg/mL).[241] The differential binding strength of the thiol ligand over the citrate coating allows for the fairly rapid substitution of the surface coating.[242,243] These examples were used as the basis for the substitution of **6** onto Au@Citrate.

4.8.1 Au@Citrate Ligand Substitution

A preliminary experiment was performed to see the effect of the addition of **6** at three concentrations (0.1, 0.5 and 1 mM) to an Au@Citrate solution (1.7 nM). Upon the addition of **6** to the nanoparticle solution a rapid colour change from red, through purple to a dark blue colour occurred indicating that the nanoparticles had formed aggregates (Figure 57).

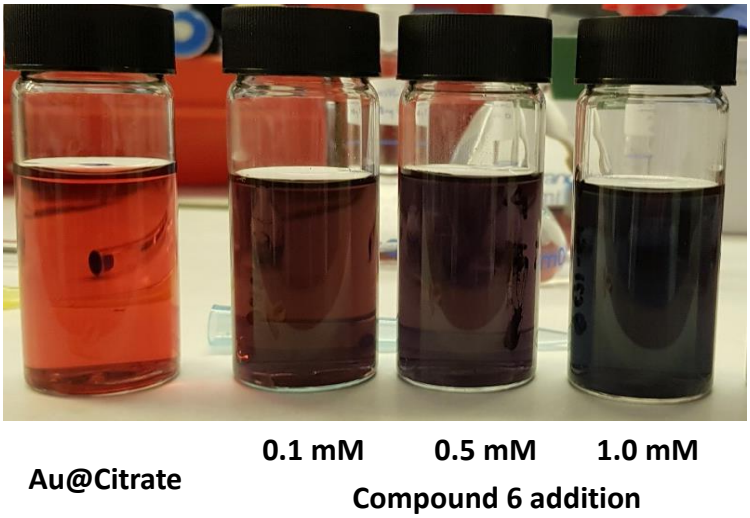

Figure 57: Obvious colour changes seen through visual inspection of nanoparticle solutions on the addition of **6** at 0.1, 0.5 and 1 mM from left to right to an Au@Citrate solution used as synthesised. Leftmost vial shows unmodified Au@Citrate for reference.

The nanoparticles that aggregated and were unrecoverable via sonication (to break apart aggregates), or filtration (to remove aggregates). To investigate this aggregation behaviour the concentration of **6** was reduced by several orders of magnitude (Table 4). Aggregation was assessed by eye, observing any colour change, pre and post purification. Purification involved centrifuging the nanoparticle solution into a pellet, removing the supernatant and redispersing them in water at the original concentration.

Table 4: Screening the addition of **6** (at different concentrations) to Au@Citrate at 1 OD_{SPR} 1.7 nM. The aggregation status was observed pre and post purification. Aggregated samples (+), non-aggregated samples (-). * For these initial screening experiments the nanoparticles were used 'as synthesised' with a starting pH of 5.2 ± 0.3.

		Aggregation	
Reaction*	**6** / nM	Pre-purification	Post- Purification
A	1.8	-	-
B	18	-	-
C	45	-	-
D	84	-	+
E	168	+	+
F	1680	+	+

At the lower concentrations (Reactions A-C) aggregation was not observed but, higher concentrations (Reactions E-F) showed obvious aggregation pre-purification. A replication of Reaction E was followed via absorbance spectroscopy to characterise the aggregation process (Figure 58) and showed the rapid loss of colloidal stability.

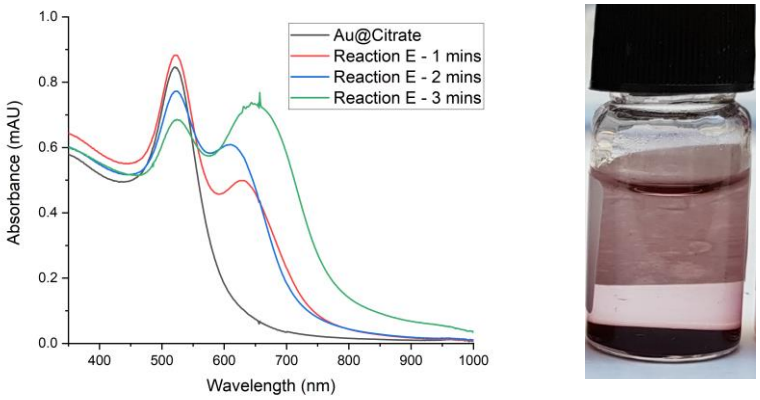

Figure 58: Absorbance spectra (Left) of Reaction E pre-purification after the addition of 168 nM **6** to Au@Citrate (1.7 nM) with absorbance spectra taken at 1 minute time intervals. After three minutes sample colour reduced in intensity and large black particles of Au^0 aggregates that settled to the bottom of the cuvette were observed (Right).

When 84 nM **6** was used (Reaction D) there was no colour change to indicate aggregation during the initial reaction, but upon purification via centrifugation the resulting pellet would not resuspend. Sonication of the pellet only served to disperse large black particles through a mostly clear solution indicating complete aggregation of the nanoparticles. Reactions A-C showed no observable aggregation pre or post purification which was confirmed with absorbance spectroscopy (Figure 59).

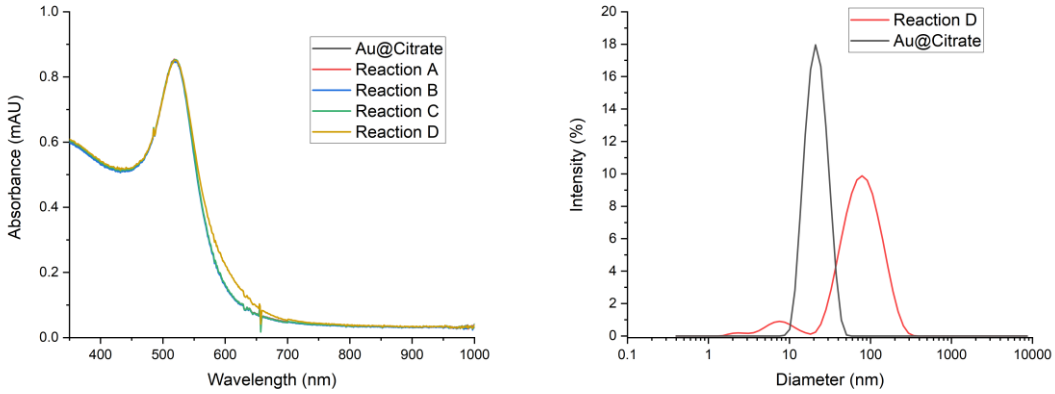

Particles	λ_{max}	Intensity DLS / nm	PDI	Zeta / mV	SD / mV
Reaction D pre-purification	519	83.2	0.35	-33.3	11.6
Au@Citrate	519	22.4	0.12	-33.5	3.73

Figure 59: (Left) UV-Vis spectrum of reactions A-D pre-purification showing no change in the SPR peak at 519 nm from the reference Au@Citrate spectrum. Aggregation in Reaction D was observed in DLS analysis (right). The highest stable loading reaction (D) was compared to the reference Au@Citrate with summarised results tabulated.

The analysis of Reactions A-C post purification showed no change from the starting Au@Citrate particles. This was not unexpected as, assuming complete substitution, the ratio of ligands:particles was extremely low, Reaction A only providing a 1:1 ratio (i.e., 1 molecule of ligand per nano particle). Reaction D (pre-purification) did not show a change in the SPR absorbance peak, which would be indicative of a change at the surface of the nanoparticle, but there was a small increase around 600 nm which is diagnostic of the start of aggregation.[244] Additionally, DLS analysis showed a 4x increase in average size with a bi-modal distribution showing small, partially stable, aggregates had formed.

While it was possible to measure solutions that were actively aggregating via UV-Vis spectroscopy and DLS, instability meant that measurements would change over time. For unstable particles, zeta potential measurements were omitted as is common

with poorly stabilised particles, the applied voltage resulted in fouling of the electrodes both invalidating the measurements and damaging the cuvette.

Au@Citrate Stabilisation Through pH Adjustment

The instability seen in Reactions D-F was believed to either be due to a crossing over point where the nanoparticles had lost their charge stabilisation from the citrate coating but were insufficiently coated with **6** to remain stable or that the ligand acted as a glue and bridged between multiple nanoparticles causing aggregation (Figure 60).

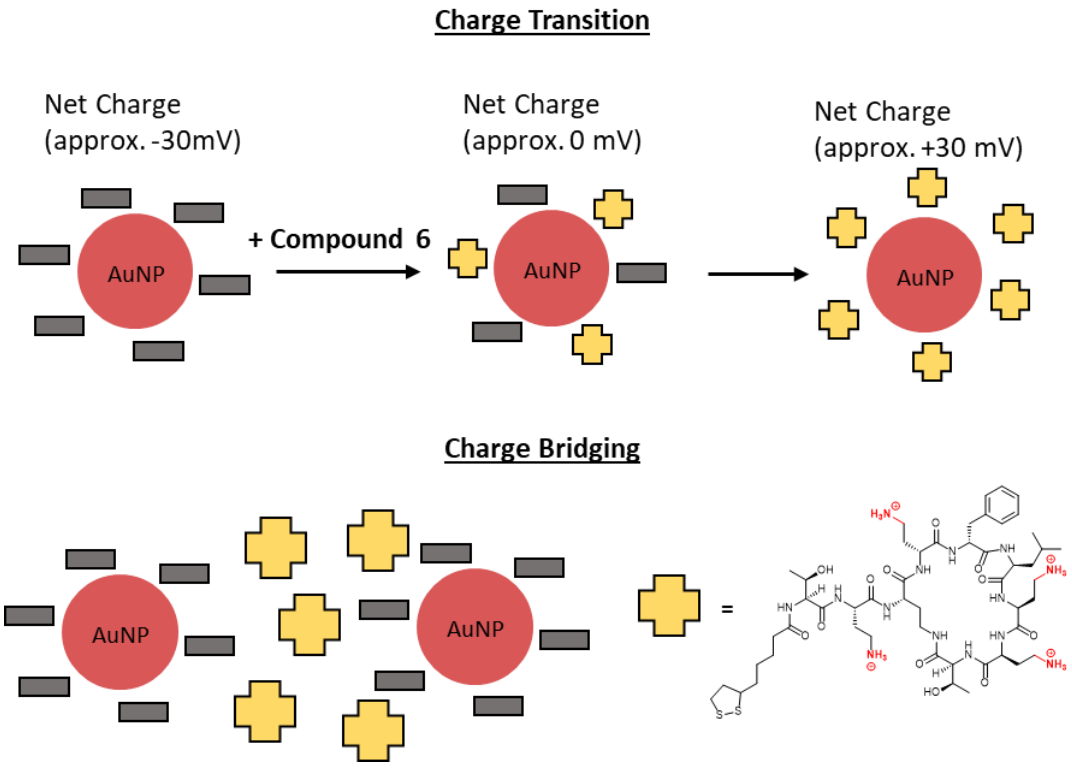

Figure 60: Illustration of the charge transition hypothesis (Top) where a combination of negative and positively charge ligands result in a net neutral charge. The alternative charge bridging hypothesis (Bottom) where **6** acts to 'glue' particles together by sitting in between anionic particles.

The aim therefore became to provide sufficient stabilisation to allow complete substitution of the citrate ligands by **6** to generate a highly positively charged, and

therefore stable, nanoparticle. To maintain stability while substitution took place, a method to reduce/remove the positive charge from the reaction was investigated (Table 5). To do this, the substitution reaction was performed while pH was maintained above 10 such that the $-NH_3^+$ amine groups on **6** would be predominantly formally neutral. Thus, the pH of an Au@Citrate solution was adjusted to 11.2 with NaOH (10 mM) prior to the addition of **6**.

Table 5: Results of the addition of compound **6** to an Au@Citrate solution (1.7 nM) with the pH adjusted to 11 and the resulting shift in the absorbance peak pre-purification.

		Aggregation		
Reaction	**6** / nM	Pre-Purification	Post- Purification	λ_{max}
G	84	-	+	520
H	168	-	+	525
I	1680	-	+	525
J	3360	+	+	561

In this case, even with higher concentrations of **6** the nanoparticle solutions were not observed to immediately aggregate (by visual inspection). Absorbance analysis showed increases in absorbance intensity for Reaction G-I and also a minor red shift for Reactions H and I which suggested that there may have been some surface modification occurring. Reaction J exhibited signification aggregation but remained stable long enough to measure an absorbance spectrum before collapse of the suspension.

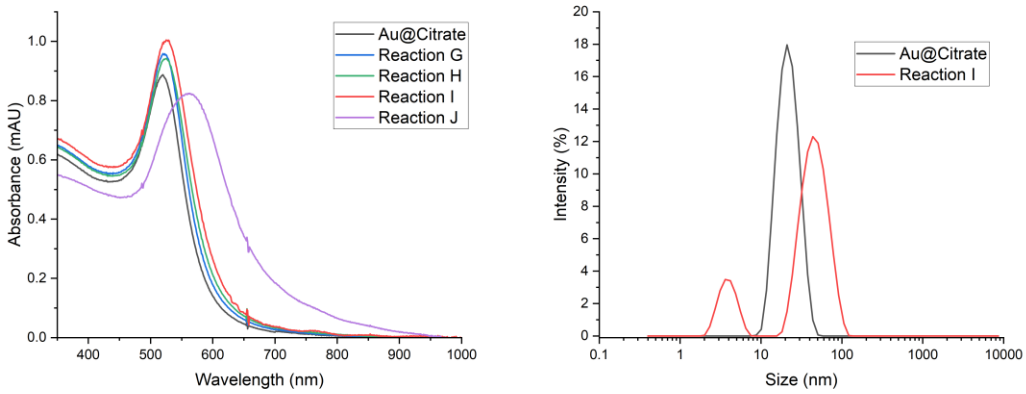

	λ_{max}	Intensity DLS / nm	PDI	Zeta / mV	SD / mV
Au@Citrate	519	22.4	0.12	-33.5	3.73
Reaction I	525	41.03	0.65	-22.4	17.1

Figure 61: (Left) UV-Vis spectrum of reactions G-K pre-purification showing SPR peak changes relative to the reference. Aggregation in Reaction I was observed via DLS analysis (right).

The reaction with the highest stable loading (Reaction I) was further analysed with DLS and Zeta potential measurements which showed an increase in size and a more positive surface charge, all of which indicated successful addition of **6** (Figure 61).

However, during the purification process of repeated centrifugation and resuspension in water, there was noticeable aggregation which increased after each cycle. After the first cycle of purification the pH of each reaction had reduced to 9-10 (as monitored by pH paper) with the extent of aggregation approximately proportional to the amount of **6** present in the reaction. Reaction I specifically aggregated after only a single centrifugation purification, while Reaction G and H aggregated after the second, where the pH was further reduced to 7-8.

Purification was also attempted with molecular weight cut off (MWCO) filters. While four purification cycles were required to lower the pH of the solution to 7,

aggregation was again observed. Additionally, simply dropping the pH to 7 with a buffer such as PBS (0.1x) or HCl (0.2 M) all resulted in irreversible aggregation.

This aggregation on reversion of pH back to 7 may have been due to incomplete substitution of the nanoparticle surface. This would mean that only some of the particles surface was covered and therefore protected with **6**. In literature, Ojea-Jiménez *et al.* suggest that there is a fundamental instability when trying to synthesise cationic biocongugated AuNPs from Au@Citrate due to the charge bridging effect from residual citrate in the solution (Figure 60).[245]

Due to the aforementioned stability issues an alternate approach was required. The streptavidin-biotin binding system was being explored for the bio-recognition aspect of the test because of the additional flexibility that it provided, both in its application in fluorescent imaging (Chapter 2) and as a method for anchoring the PMBN to nitrocellulose (Chapter 4). A literature investigation revealed that Au@Streptavidin presented a much more straightforward method to generate a stable nanoparticle-conjugate[246] that, in combination with **12** could specifically bind to Gram-negative bacteria. Hence, this was deemed to be the optimal path forward for this project and the Au@Citrate substitution with **6** was not explored further.

4.9 Au@Streptavidin

To attach biotinylated compounds such **12** to gold nanoparticles Au@Streptavidin was required. Streptavidin is well reported as a functional surface on gold nanoparticles[246] and the resulting Au@Streptavidin has been applied widely in lateral flow tests.[190].

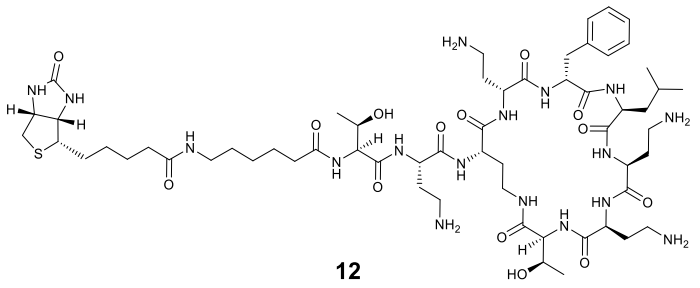

12

Attachment was performed according to a literature procedure[246] through the substitution of Au@Citrate with a streptavidin solution (0.8 µM) in a mildly basic solution (pH 9). Particles were purified via centrifugation with the substitution confirmed via DLS and optical characterisation (Figure 62).

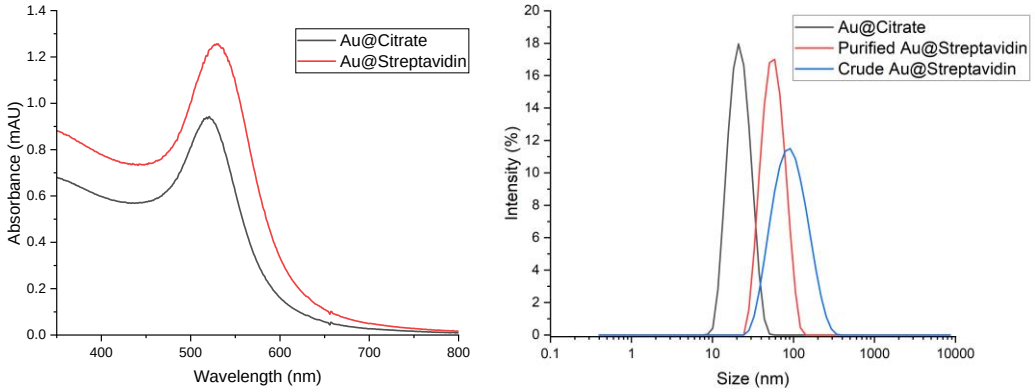

Particles	λ_{max}	Intensity DLS / nm	PDI	Zeta / mV	SD
Au@Citrate	521	21.2	0.14	-27.8	7.3
Au@Streptavidin pre-purification	529	99.8	0.21	-38.8	9.1
Au@Streptavidin post-purification	529	56.7	0.09	-18.8	17.2

Figure 62: Characterisation of Au@Streptavidin synthesis pre-purification (crude reaction mixture) via UV-Vis spectroscopy (left) and DLS (right). Key data tabulated to show comparison to starting Au@Citrate particles.

The addition of the Streptavidin to Au@Citrate showed a redshift in the SPR peak and an increase in absorbance in the UV-Vis spectrum, caused by the change in dielectric environment at the particle surface after protein coating[201], which was also

mirrored by the increase in DLS size to 100 nm. This large R_H increase was expected, primarily due to the large, well hydrated corona from protein absorption. Post purification the UV-Vis spectrum was unchanged, but the DLS size showed a slight reduction in overall size but a lower PDI suggesting that excess, loosely bound streptavidin had been removed leaving only more tightly bound streptavidin attached to the nanoparticle surface. Zeta potential measurements showed a slight reduction in negative charge.

For application and storage, the Au@Streptavidin particles were treated with 0.1% BSA in 0.1x PBS which provided additional steric bulk to the nanoparticles that aimed to reduce aggregation or non-specific binding to the container during storage.

4.10 TEM Characterisation of the Au@Streptavidin Binding Properties

For the purposes of using the nanoparticles in a lateral flow strip the particles were prepared in a running buffer solution with 0.1% Tween 20 and 0.1% BSA in PBS (a common running buffer composition for lateral flow tests in literature)[247]. The nanoparticles were imaged with TEM to characterise the shape and size of the particles (Figure 63).

To test and image the binding of Au@Streptavidin to bacteria with and without **12**, a range of labelling experiments with *E. coli* and *B. subtilis* were performed. The bacteria solutions were both prepared to 1 OD_{600} concentrations for all experiments as a relatively high concentration was required to achieve sufficient coverage of the TEM grid for imaging. To prepare the TEM grids, 10 µL of the bacteria solutions were added, allowed to settle/dry for 10 minutes before excess was removed. Labelling experiments with Au@Streptavidin used a labelling concentration of 1

OD_{SPR} (approximately 1.4 nM based on the post-functionalisation absorbance intensity of Au@Citrate).

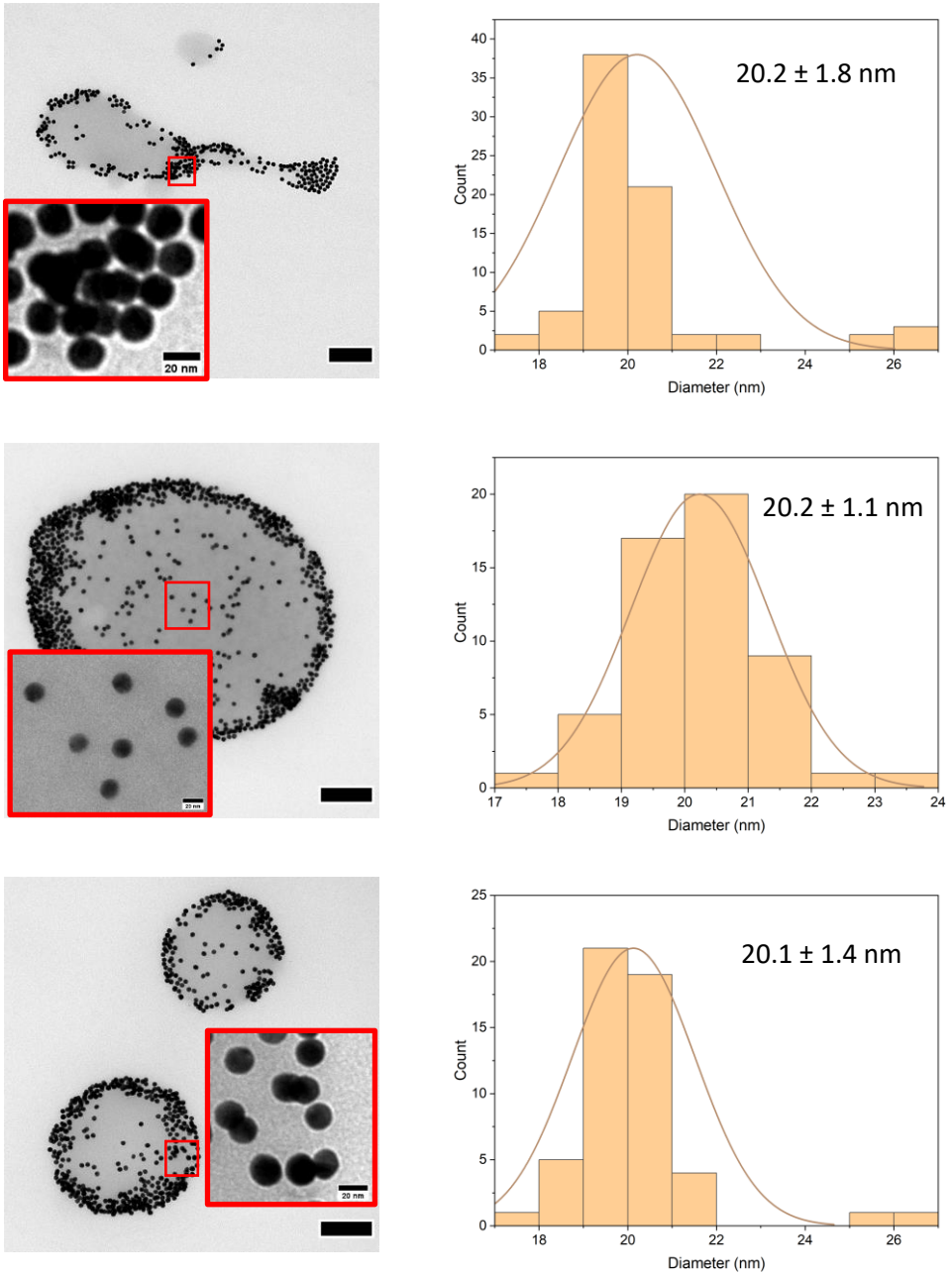

Figure 63: TEM images taken of the Au@Streptavidin particles Histogram plots of nanoparticle diameter were extracted through the ImageJ particle analysis tool and calculation from the particle area. Circularity of particles was set to between 0.7 – 1. Scale Bar 200 nm. Zoom of particles inset scale bar 20 nm.

It was seen that the shape and size of the particles was consistent with the Au@Citrate particles previously imaged. Interestingly as the nanoparticles were applied to the copper grids in the running buffer solution the particles formed droplets, likely due to the surfactant Tween 20.

4.10.1 Testing for Non-Specific Binding of Au@Streptavidin to *E. coli*

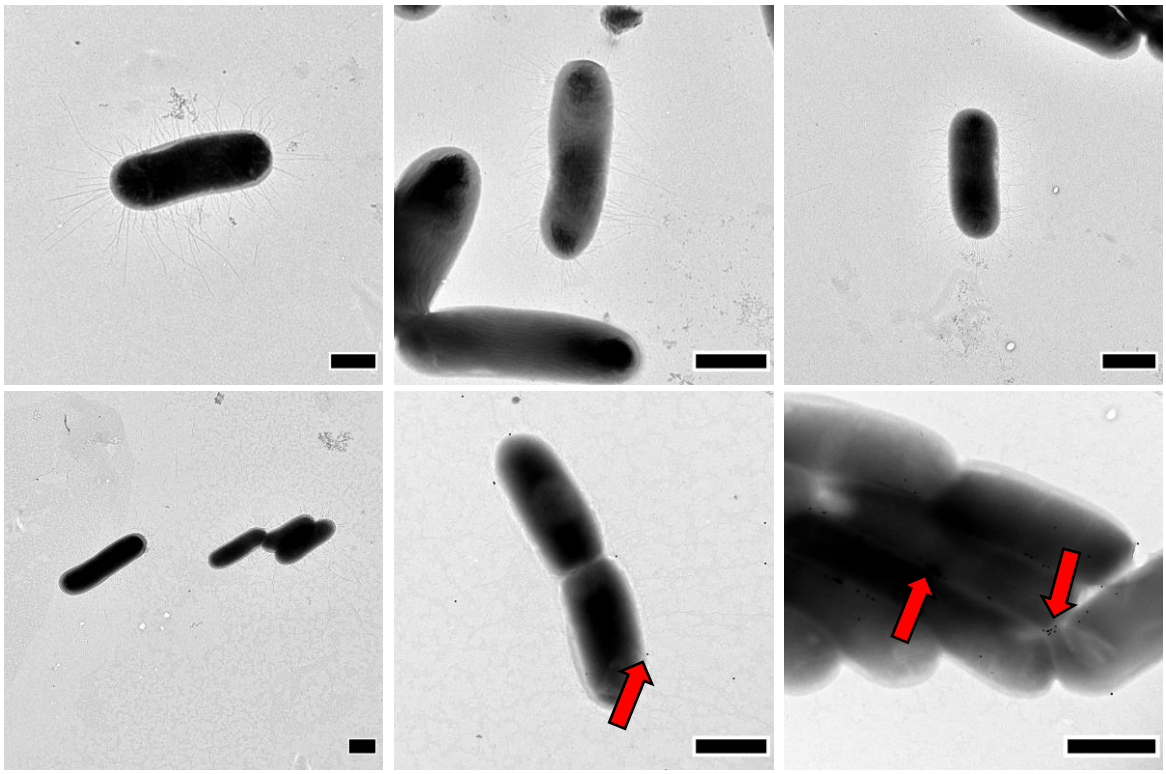

Figure 64: TEM images of *E. coli* treated with Au@Streptavidin showing limited non-specifically bound nanoparticles (indicated by red arrows). Bacteria were grown overnight and adjusted to 1 OD with PBS and incubated in PBS for 1 hour at 37 ºC before the addition of 1 OD Au@Streptavidin nanoparticles. The Bacteria+Au@Streptavidin solution was washed via centrifugation before fixing to copper grids with no staining. Scale Bar = 1 µm

TEM imaging of *E. coli* showed that there was limited non-specific binding of the Au@Streptavidin (Figure 64). This was also demonstrated when *E. coli* were centrifuged to remove unbound Au@Streptavidin giving a red solution and a white pellet of bacteria.

4.10.2 Outer-Membrane Binding and Disruption of *E. coli* Treated with **12**

As polymyxin is known to bind to the outer membrane of Gram-negative bacteria and increase its permeability *E. coli* was imaged after treatment with **12** (Figure 65).

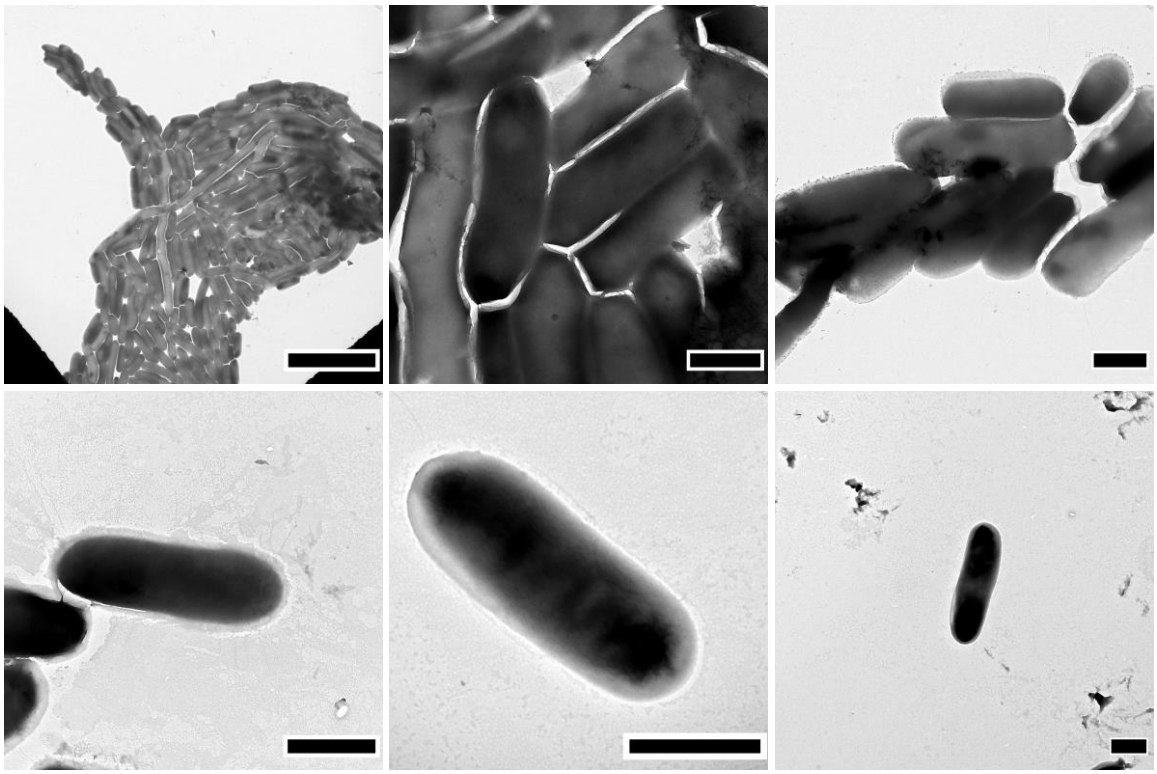

Figure 65: A representative selection of TEM images of *E. coli* treated with **12** (10 µM, 1hr) showing that for a large proportion of the bacteria there was no noticeable impact of the treatment with bacterial shape and size consistent with the control. Bacteria+**12** solution was washed via centrifugation before fixing to the copper grid with no staining. Zoomed out image (top left) scale bar = 5 µm. Other Scale Bars = 1 µm.

A small number of bacteria did show signs of damage/disruption to the outer membrane, but this was minor compared to the whole sample. A representative sample of images is displayed to illustrate the observed behaviour (Figure 66).

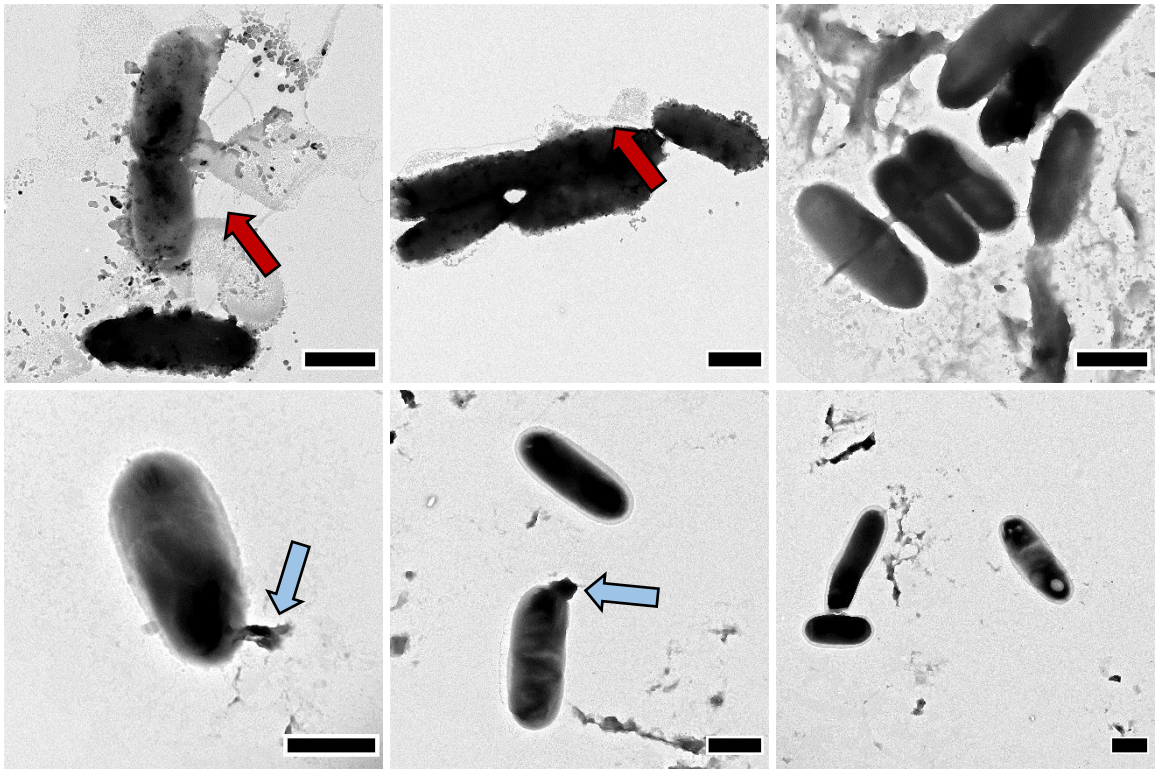

Figure 66: A selection of TEM images to show that on treatment there was a small number of bacteria that were damaged as indicated by evidence of material around the bacterial that appears to have been ejected from the bacteria as the structural integrity failed. Bacteria+**12** solution was washed via centrifugation before fixing to copper grid with no staining Scale Bar = 1 µm.

From this selection of images, bacteria can be seen at various stages of breakdown between single ruptures (blue arrows) and complete breakdown (red arrows) of the outer membrane. This possibly suggests an ongoing breakdown process which would be in line with the action of polymyxin B derivatives of which a single snapshot is represented by this experiment.

4.10.3 Imaging *E. coli* Labelling with **12** and Au@Streptavidin

The labelling procedure of *E. coli* with both **12** and Au@Streptavidin resulted in a noticeable red pellet of bacteria post-centrifugation (Figure 67) suggesting good binding between Au@Streptavidin and the *E. coli* labelled with **12.**

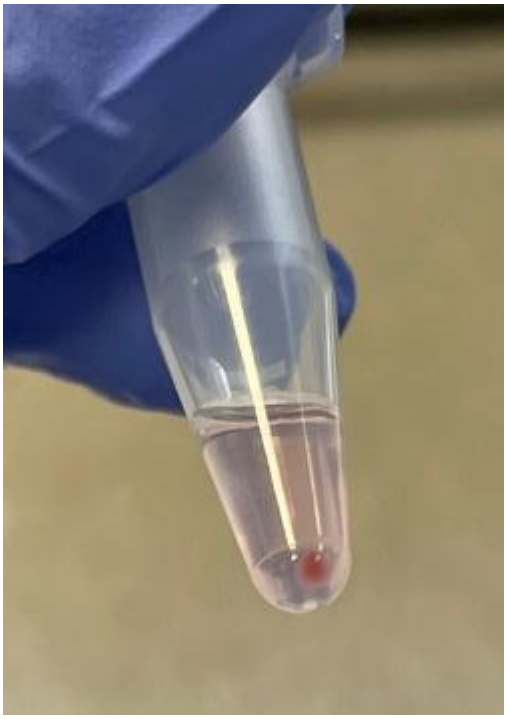

Figure 67: Image of *E. coli* labelled with **12** (10 µM) for 1 hour and incubated with Au@Streptavidin (1 OD) for 5 minutes. The solution was centrifuged to form a pellet which showing a red colour. Unbound nanoparticles still present giving the supernatant a light red tint.

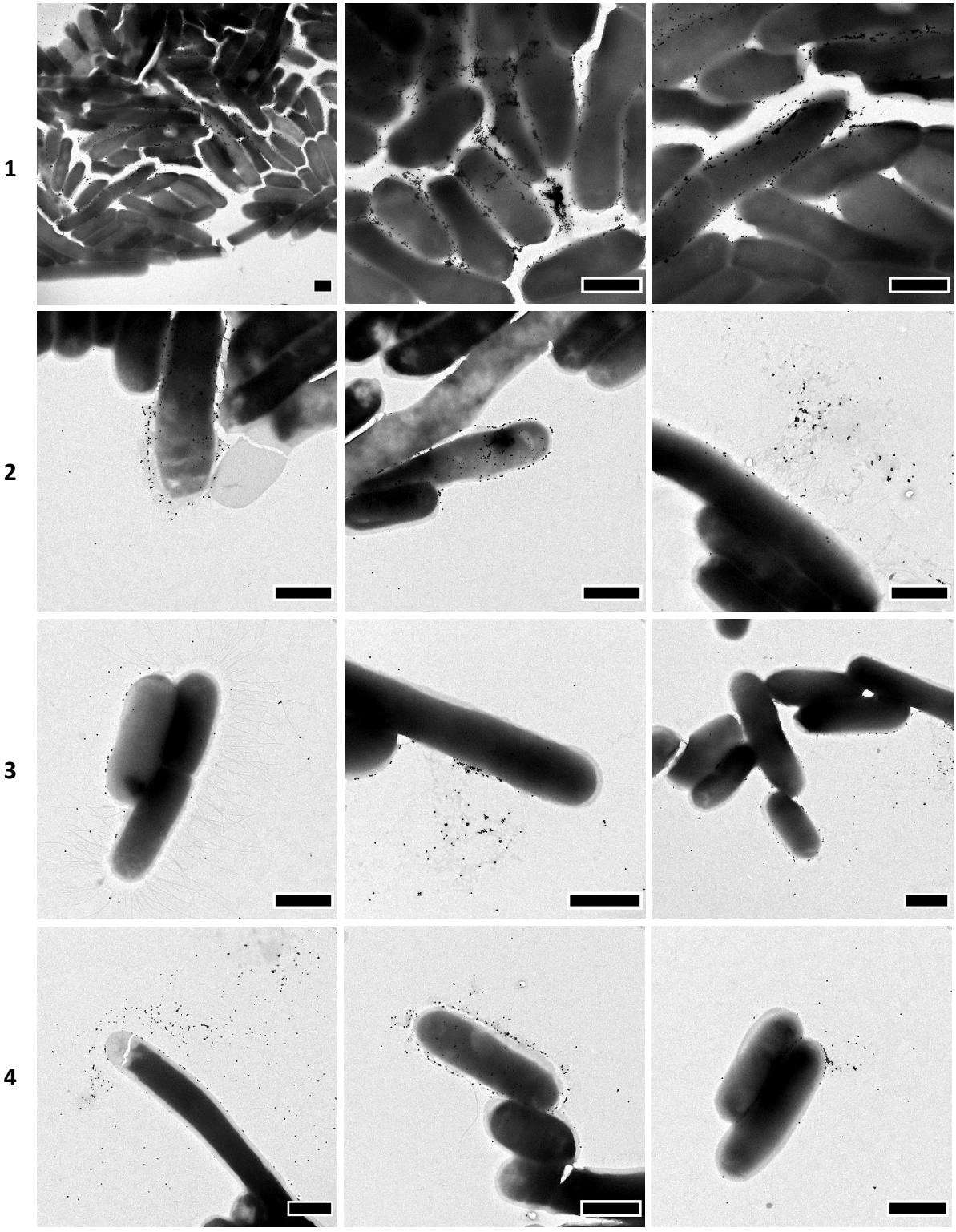

Figure 68: TEM images of *E. coli* treated **12** before adding Au@Streptavidin. A range of fields were chosen 1) large groups of bacteria showing particularly strong labelling at the interface between bacteria. 2-3) smaller groupings of bacteria showing consistent labelling of the outer membrane 4) individual bacteria showing non-uniform labelling both at an individual bacterium level and between adjacent bacteria. Bacteria were grown overnight adjusted to 1 OD with PBS and incubated with **12** (10 µM) for 1 hour at 37ºC before the addition of 1 OD Au@Streptavidin. The Bacteria+Au@Streptavidin solution was washed via centrifugation before fixing to a copper grid. Scale Bar = 1 µm,

Different regions of interest in the sample field were imaged to best represent the full picture of *E. coli* successfully being labelled with Au@Streptavidin via the bi-functional ligand **12** (Figure 68). Labelling was achieved both, in large clumps of bacteria and, individual cells. The degree of uniformity of the labelling varied from heavy coverage of the entire outer membrane of some bacteria to sparsely present nanoparticles on other cells. This labelling experiment also showed some of the same outer membrane disruption as noted previously.

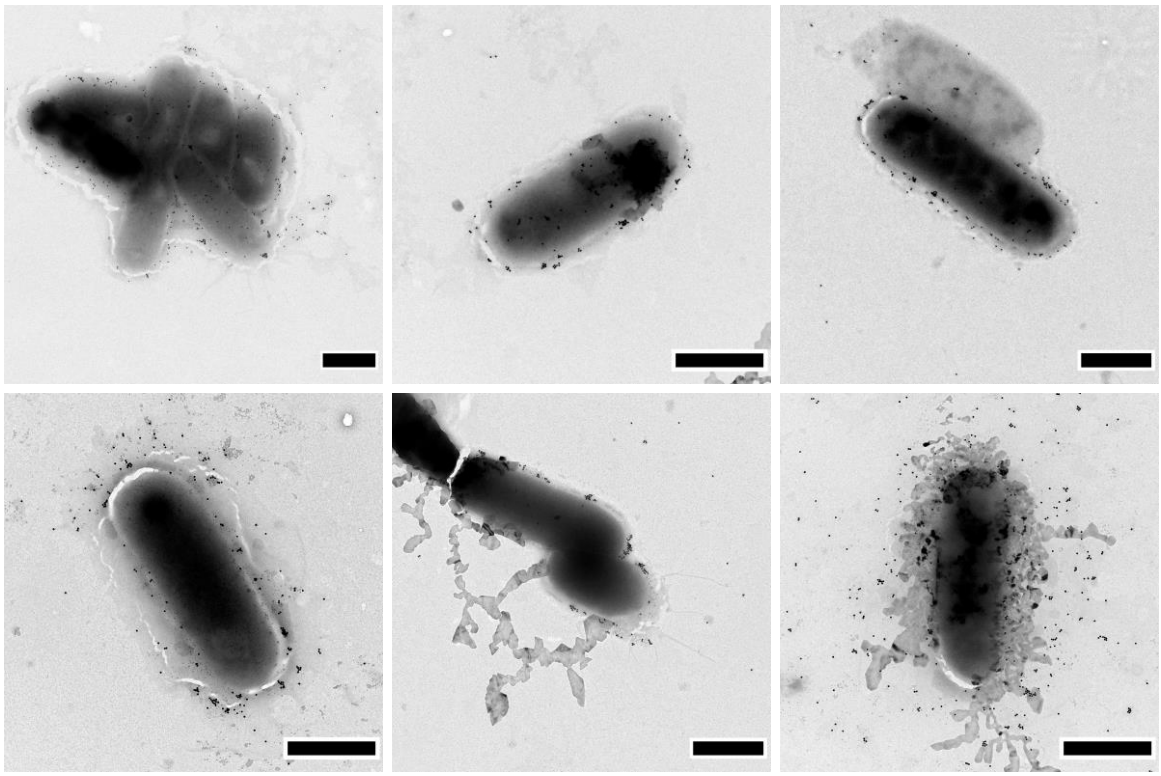

Figure 69: TEM images of *E. coli* incubated with **12** and treated with Au@Streptavidin highlighting different degrees of disruption of the outer membrane and bacterial labelling. Scale bar = 1 µm

The binding to the outer membrane was evident, as in many images ‘rafts’ of outer membrane material had been sloughed off the bacteria and was strongly labelled via **12** and Au@Streptavidin (Figure 69). Across the series of bacteria imaged, a selection highlighting some of the patterns of labelling such as well dispersed surface labelling and larger aggregates of Au@Streptavidin was collated (Figure 70).

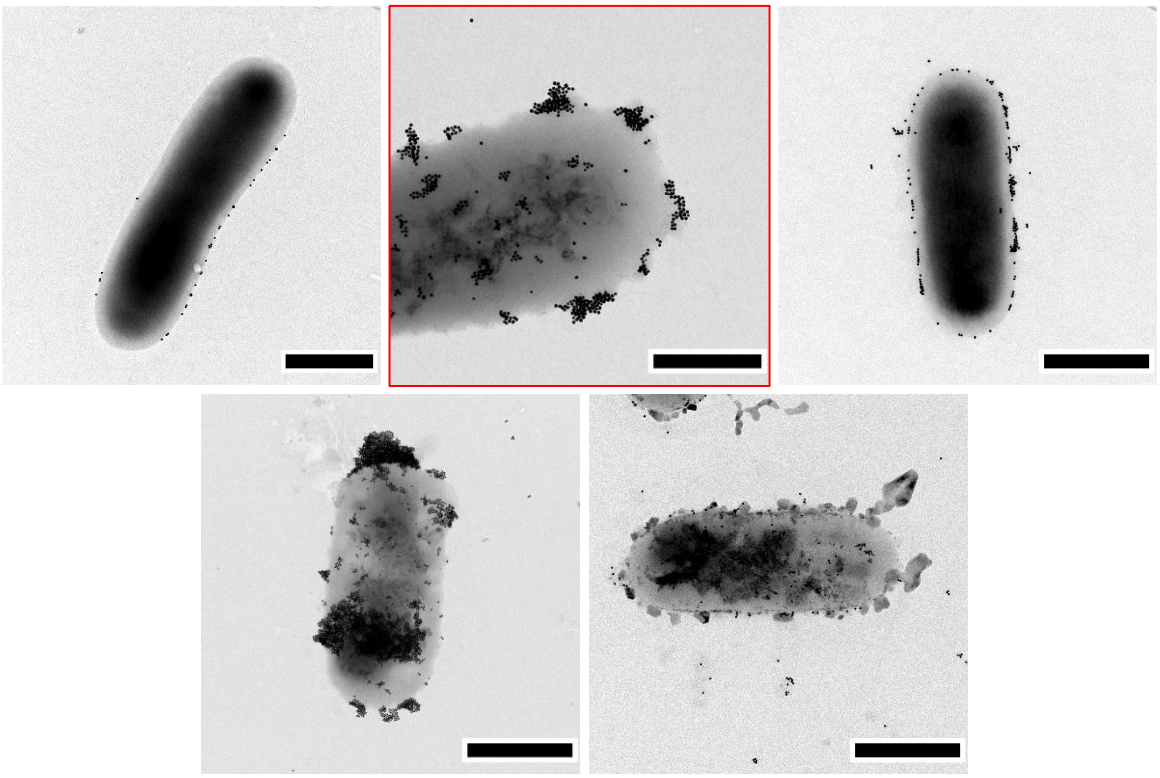

Figure 70: TEM images of single *E. coli* bacterium incubated with **12** and treated with Au@Streptavidin with a variety of labelling patterns identified e.g. larger aggregates of nanoparticles forming on the surface. Scale bar = 1 µm. Zoomed highlighted image (top centre) Scale bar = 500 nm

4.10.4 Non-Specific Binding of *B. subtilis* by Au@Streptavidin

B. subtilis was incubated with Au@Streptavidin to monitor for non-specific binding without the presence of **12.** The control images of *B. subtilis* (Figure 71) showed little non-specific labelling with Au@Streptavidin. The bacteria appeared to be more prone to forming clumps compared to *E. coli*. A thick 'outer grey area' surrounded each bacterium which is consistent with the much thicker peptidoglycan layer present in Gram-positive bacteria as well as long flagella (also seen in light grey).

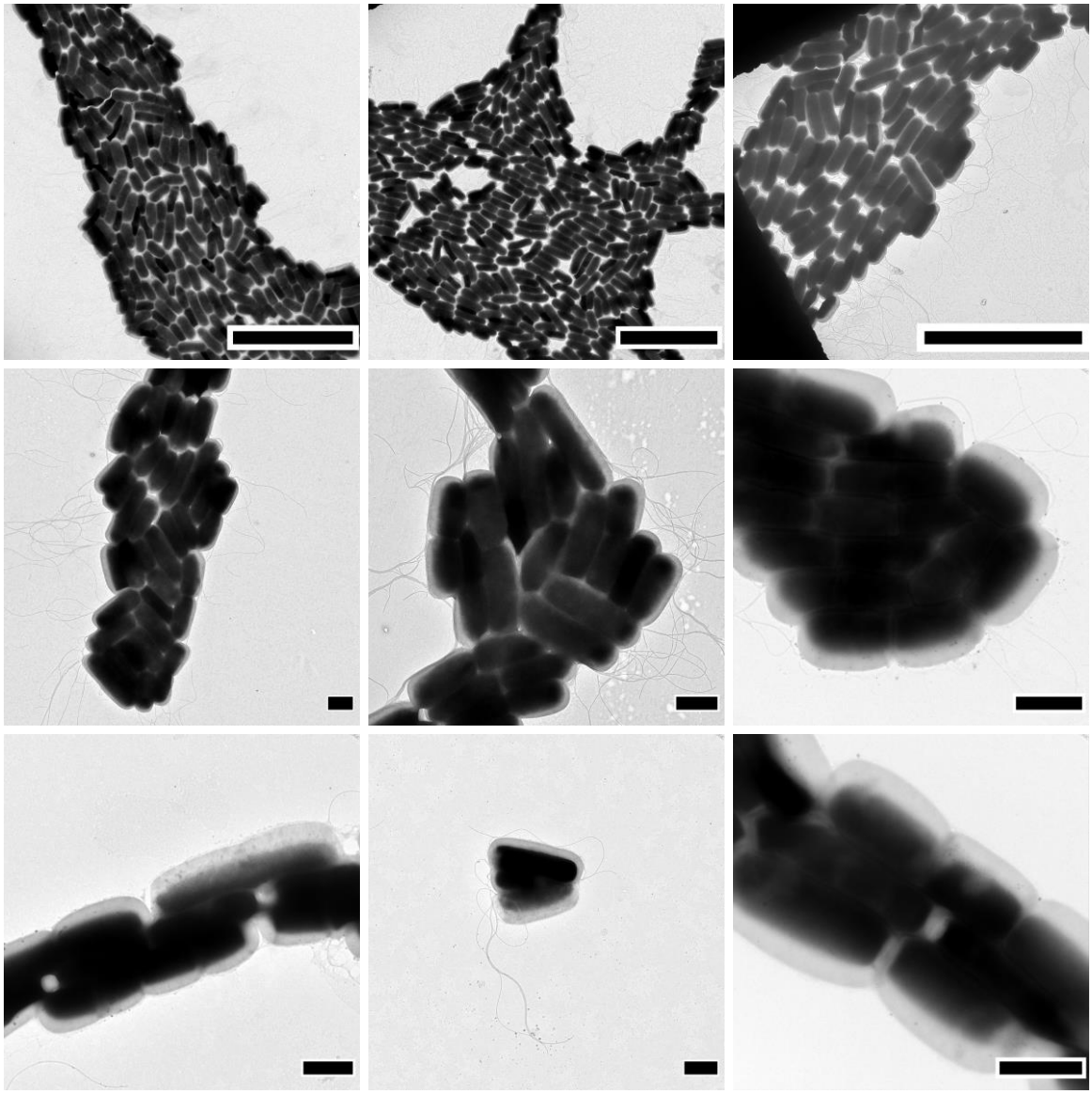

Figure 71: TEM images of *B. subtilis* treated with Au@Streptavidin showing that there are no/few non-specifically bound nanoparticles. Bacteria were grown overnight adjusted to 1 OD in PBS and incubated for 1 hour at 37^{o}C before the addition of 1 OD Au@Streptavidin. Bacteria+Au@Streptavidin solution was washed via centrifugation before fixing to copper grid without staining. Scale Bar = 1 μm

4.10.5 Outer-Membrane Disruption of *B. subtilis* Treated with **12**

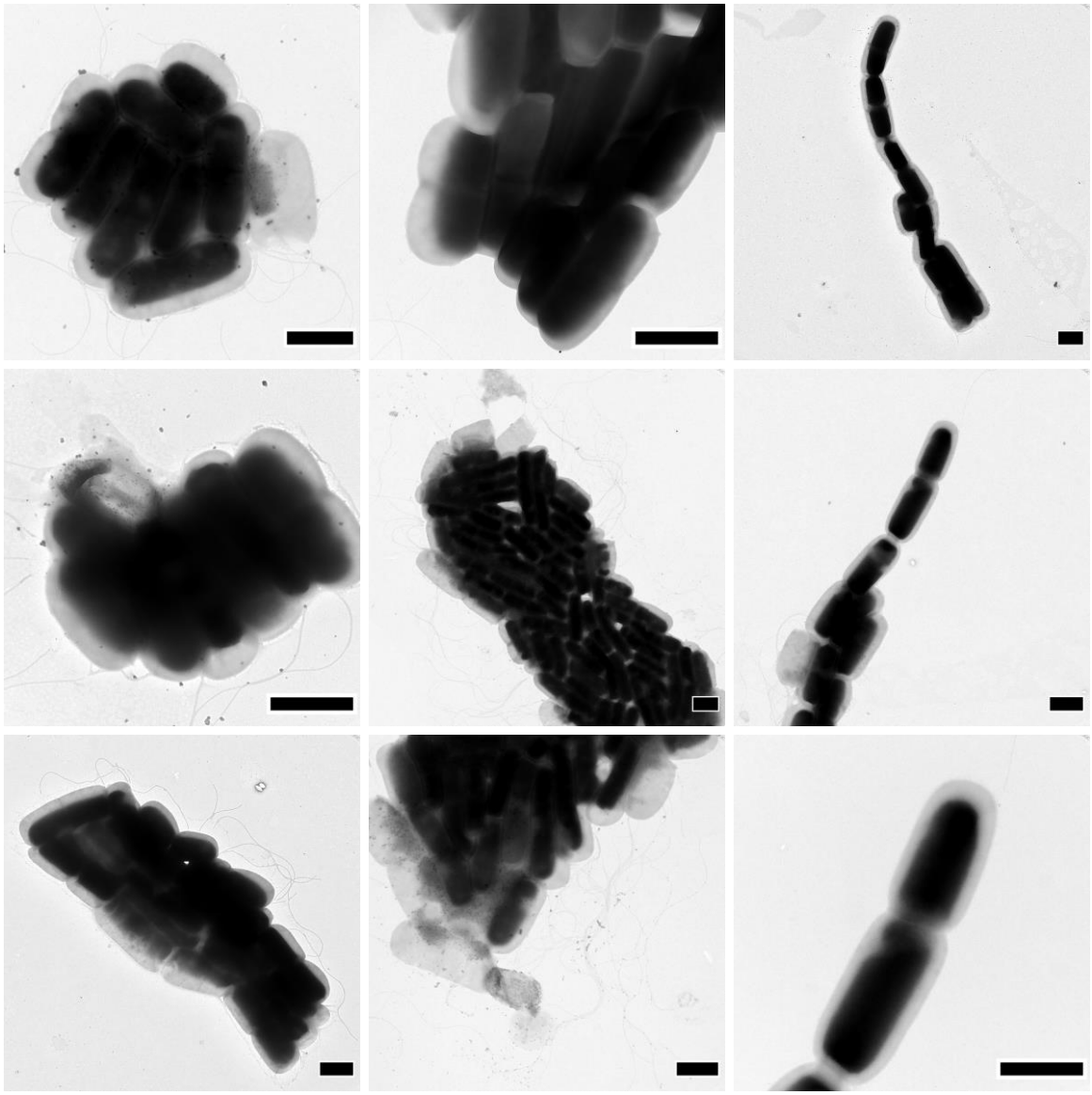

Figure 72: TEM images of *B. subtilis* treated with **12** showing that there was no/minimal outer membrane disruption. Bacteria were grown overnight adjusted to 1 OD with PBS and incubated with PBS for 1 hour at 37°C before the addition of 1 OD Au@Streptavidin. Bacteria+Au@Streptavidin solution was washed via centrifugation before fixing to the copper grid. Scale Bar = 1 µm

While the Gram-positive *B. subtilis* should not be targeted by the polymyxin based **12** there was some evidence of outer membrane damage. This was, in general, much more disperse and less severe than that seen in *E. coli* experiments. Small blebs on the bacteria surface or evidence of dead bacteria / broken outer membranes were possible to find on the TEM grid but only on a minority of bacteria (Figure 72).

4.10.6 Analysis of *B. subtilis* Labelled with **12** and Au@Streptavidin

The loading/labelling procedure resulted in red or white pellets of bacteria (Figure 73) suggesting good differential between the binding of Au@Streptavidin to *E. coli* and *B. subtilis* loaded/treated with **12.**

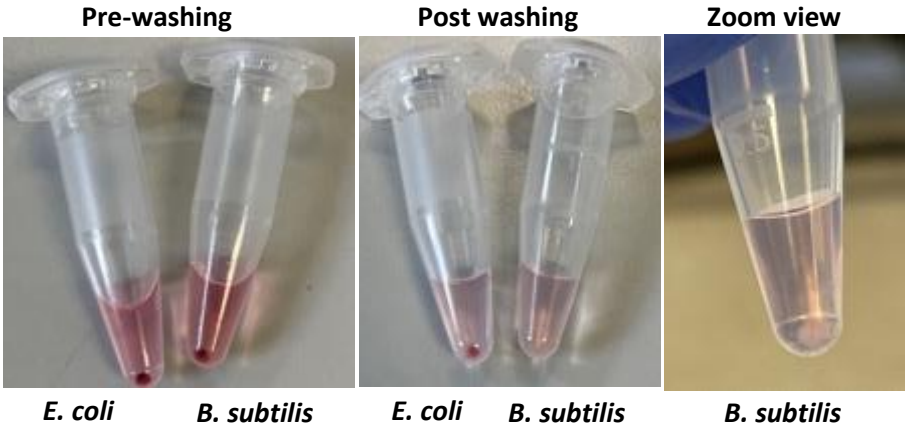

Figure 73: Images of *E. coli* and *B. subtilis* loaded with **12** (10 µM) for 1 hour and incubated with Au@Streptavidin (1 OD) for 5 minutes. The solution was centrifuged to form a pellet which was white (*B. subtilis*) or light red colour (*E. coli*). Unbound nanoparticles were still present giving the supernatant a light pink colour.

The *B. subtilis* did experience some binding of the Au@Streptavidin after the full labelling procedure but this seemed to be primarily isolated to locations where intracellular material that leaked out. The proportion of labelling was significantly lower than seen with *E. coli* and confirms the Gram-selective labelling of bacteria with a combination of compound **12** and Au@Streptavidin particles and is clearly demonstrated in Figure 74.

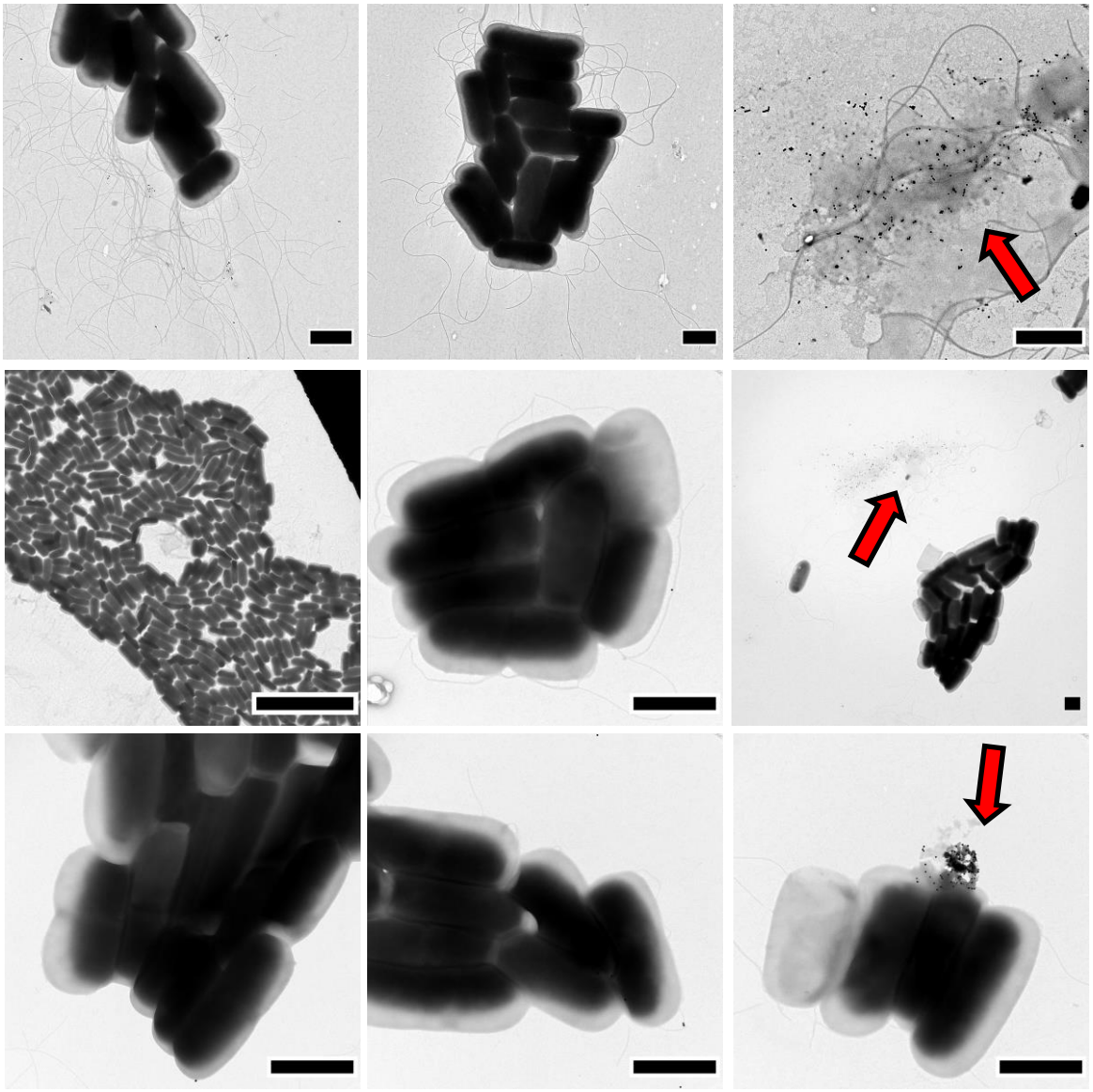

Figure 74: TEM images of *B. subtilis* loaded with **12** and then treated with Au@Streptavidin showing nanoparticles on extracellular material (red arrows). Bacteria were grown overnight adjusted to 1 OD in PBS and incubated with **12** (10 µM) for 1 hour at 37 °C before the addition of 1 OD Au@Streptavidin. The solution was washed before fixing to copper grid. Scale Bar = 1 µm.

Based on the TEM imaging which showed specific binding to *E. coli* with minimal non-specific or off target binding the development of this labelling system to a lateral flow design was pushed forward.

5 Development of a Lateral Flow assay for Gram-Negative bacteria

Having shown that a combination of Au@Streptavidin and **12** was able to effectively label Gram-negative bacteria in solution, their validation in a lateral flow assay was required. The elements that needed to be explored were the nitrocellulose membrane, the test line and the control line. As the aim was to build a test using a sandwich style assay design (Figure 75), the capture reagents also needed to be validated.

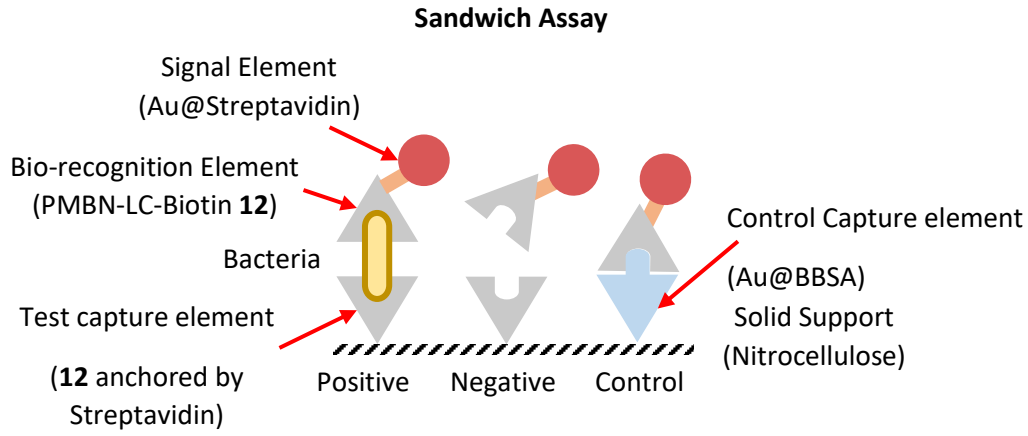

Figure 75: Target assay design. The test capture element utilising streptavidin -**12** binding, with a control line using Biotinylated-BSA as a capture element.

5.1.1 Nitrocellulose Membrane Selection and Solvent Flow

At the core of a lateral flow assay is a nitrocellulose membrane where the capture of the analyte and the visualisation of binding occur[248] (Figure 76).

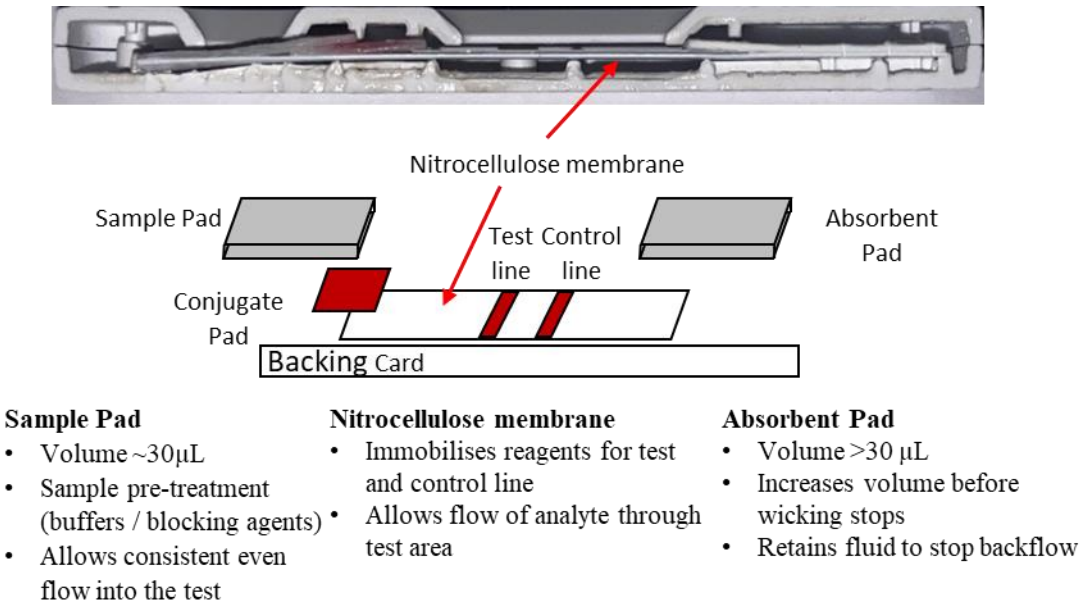

Figure 76: A cross section of a commercial COVID-19 lateral flow assay (top) and an expanded view (bottom) of the component parts. The central element is the nitrocellulose (highlighted by red arrows) in both a diagram. The main three elements that control flow through the assay (Nitrocellulose, Sample and Absorbent Pads) are briefly described. The volumes 'held' of each of these components is proportional to their dimensions and approximate values listed are based on commercially available COVID-19 lateral flow tests.

The primary consideration, in the selection of nitrocellulose membranes for lateral flow, is the rate of flow through the strip and as such, nitrocellulose membranes are supplied on the basis of number of seconds it takes for solutions to flow 4 cm along the strip[248] The slower the flow through the strip, the greater the contact time there is between reagents/analyte at the test area and therefore the sensitivity of the test is improved, however, slower flowing strips take longer to show results.[249]

Flow rates are controlled by properties of the nitrocellulose matrix such as: pore sizes[250], overall thickness (Figure 77)[251], addition of any patterning[252,253]. The dimensions of the membrane also play a role in flow speed or rate (e.g. wide strips flow more slowly) while also controlling the total bed volume of the strip.[254]

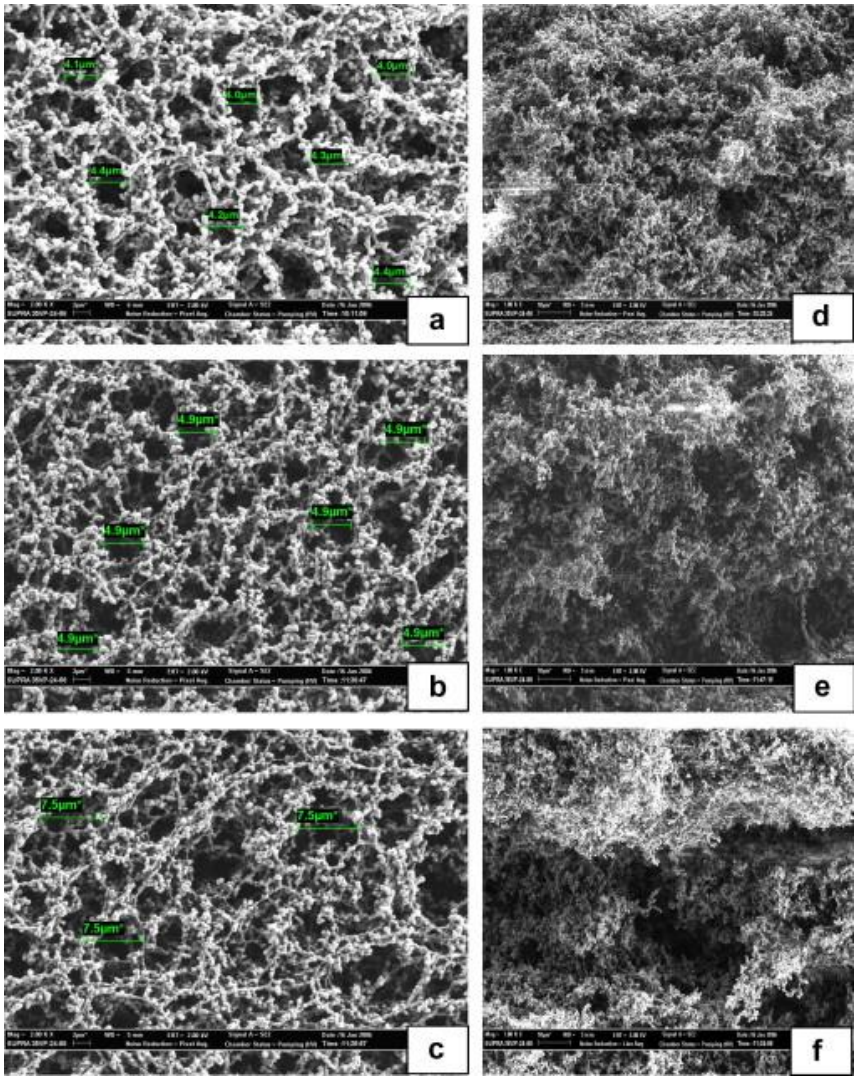

Figure 77: SEM micrographs for the surfaces (a–c) (2000×) and cross-sections (d–f) (1000×) of nitrocellulose membranes, prepared with cast thickness of (a, d) 600 μm, (b, e) 700 μm, and (c, f) 800 μm. Reprinted with permission Scr. Mater. 57, 8, 2007, 743-746 Copyright © 2007 Acta Materialia Inc. Published by Elsevier Ltd.[251] Average pore size measurements (green text): a – 4.2 μm, b - 4.9 μm, c - 7.5 μm

As well as controlling the flow of reagents along the test, the nitrocellulose acts as a solid support to hold the reagents making up the test and control line. In a sandwich assay lateral flow test, these reagents capture the labelled analyte and the labelling conjugate respectively and concentrate them into a tightly defined area, resulting in a visible line.

5.1.2 Developing a Test and Control Line System

One of the reasons for using a streptavidin-biotin system for labelling in the previous chapters was the ease of developing a test and control line for lateral flow. A standard lateral flow system uses hydrophobic interaction to bind antibodies directly to both a nanoparticle and nitrocellulose. Due to a combination of a small size, limited hydrophobicity and high water solubility meant that polymyxin would elute off nitrocellulose.

However, the biotinylation of PMBN to generate **12** allowed the use of streptavidin as an anchor to immobilise capture reagents as a test line and is well reported in the literature.[190,255–257]

Biotinylated BSA has been used in the validation of streptavidin-biotin lateral flow systems in literature.[258,259] The use of a streptavidin-based test line can be validated through the capture of Au@BBSA and equally the use of Au@Streptavidin enables the use of BBSA as a control line.

The next stage of test production required that reagent solutions for the test and control lines were placed onto the strip with fine control over their volume and position. There are several possible methods to achieve this, and the choice of method influences the consistency of the resulting assay, inconsistent application of reagents would result in strip-to-strip variability.

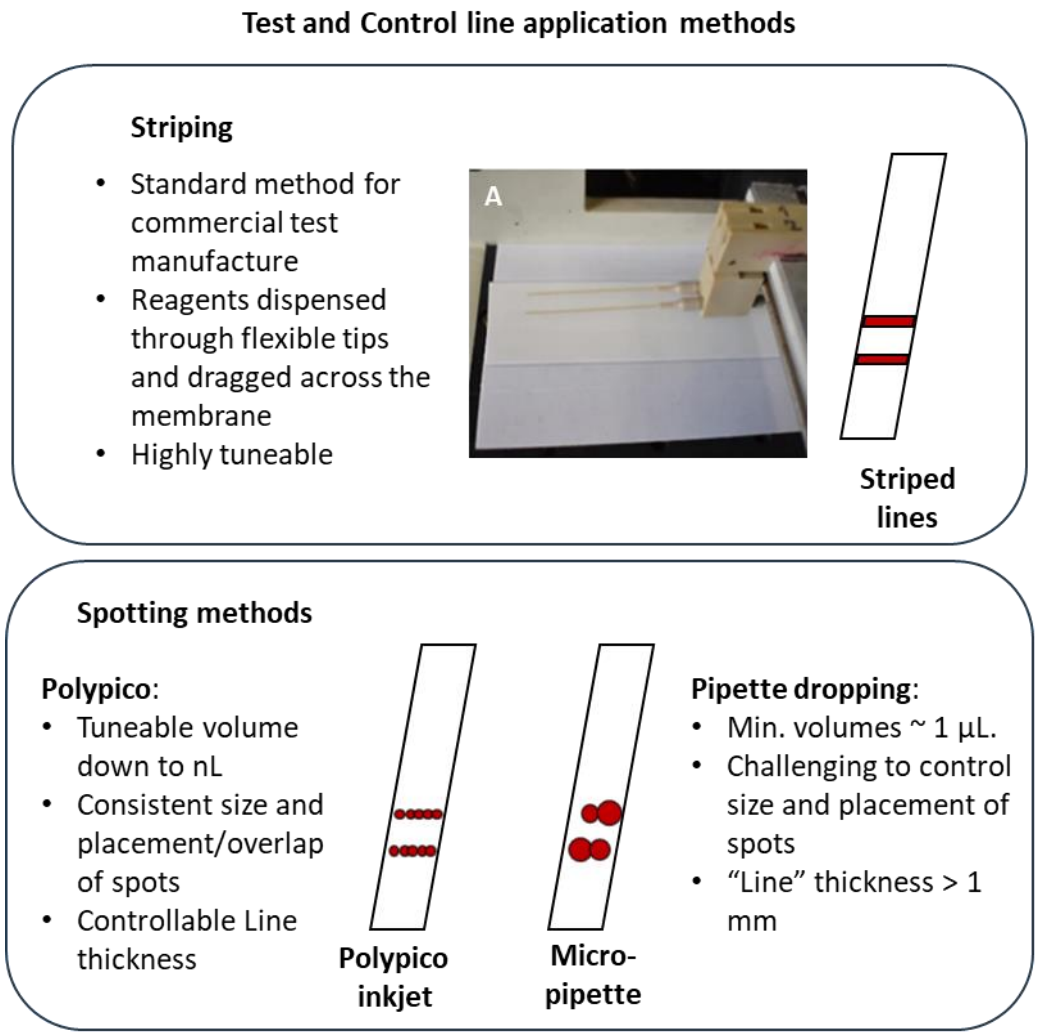

Figure 78: Comparison of different methods to apply the test and control line reagents to the nitrocellulose membrane in the production of a lateral flow test. The resulting test and control lines from these techniques are illustrated. A) Image of instrument used to simultaneously deposit 'strip' test and control lines. Image reprinted with permission. Nat Protoc **15**, 3788–3816 (2020). Copyright Springer Nature[260]

Commercially, application of the test and control line reagents is performed with specialised instruments that apply a thin line of reagents to a continuous strip of nitrocellulose (Figure 78). Here, a Polypico inkjet style printer was used to apply reagents onto the strips. Spotting the nitrocellulose strips with a micropipette yielded inconsistent test and control lines.

5.1.3 Image Analysis

Another part of developing the assay is determining how the results from the test would be measured, interpreted, and quantified. In the literature there are several approaches that are viable. The simplest version is a pass/fail assay were the presence or absence of a red colouration in the test line area is determined visually.[261] This provides quite a simple view of the outcome of a test and would make it challenging to optimise the test conditions to determine if changes to the test made a positive or negative difference to the assay.

An alternative approach is the development of a bespoke test strip reader. These are standalone devices that can measure the intensity of the colouration at the test line.[262] This information can then be used to quantify the outcome of the test which, in a complete assay, can be used to determine the concentration of the analyte detected. More recently there has been interest in developing more accessible low-cost methods for the quantification of lateral flow tests.[104] The combination of 3D printing and smartphones can replicate the majority of the function of a dedicated reader which reduces costs and increases the flexibility of the system.

5.2 Aims

The aim of this section of the PhD was to design and validated of a lateral flow test to detect Gram-negative bacteria. This required each separate component to be validated in isolation before assembling the full test. Firstly, a test platform was needed, comprising of a nitrocellulose strip printed with the test reagents and a method to image and analyse results. Secondly, the flow parameters needed to be optimised and control tests validating the binding of streptavidin-biotin components.

Thirdly, testing with *E. coli* was performed, initially keeping the bacteria stationary to bind the Au@Streptavidin+**12** labelling conjugate. Finally, all of the components could be brought together, and a full sandwich assay lateral flow test implemented.

5.3 Strip Engineering

The first challenge to be tackled for this part of the project was the development of the testing platform to see **12** and Au@Streptavidin functioning in flow. This required the selection of a nitrocellulose membrane, that was cut down into the appropriate strip geometry. With the nitrocellulose strips in hand, the challenge of printing the designed compounds onto the strips was approached. Once strips were printed with compounds, control tests could be performed to develop the image analysis platform.

5.3.1 Nitrocellulose Membrane Preparation

The slowest flowing membrane was selected (Whatman FF170 HP) with a flow of 140-200 seconds over 4 cm (on a 10 mm wide membrane). This membrane was supplied pre-attached to a flexible plastic backing card for support.

It was particularly important to prevent contamination of the nitrocellulose surface, so all handling steps were performed with gloves or with a paper coating on the exposed nitrocellulose surface. Oils from the hand bind to the surface and were visible in the flow of the running buffer through the strip.

While modifications to the flow geometry on lateral flow strips is something that has been investigated in the literature[253] for the purposes of this assay, a simple rectangular shape was used. The nitrocellulose membrane (85 mm x 126 mm) was

cut into 4.5 x 42.5 mm rectangular strips in a 2 x 28 pattern by laser cutter, producing 56 total strips at a time (Figure 79).

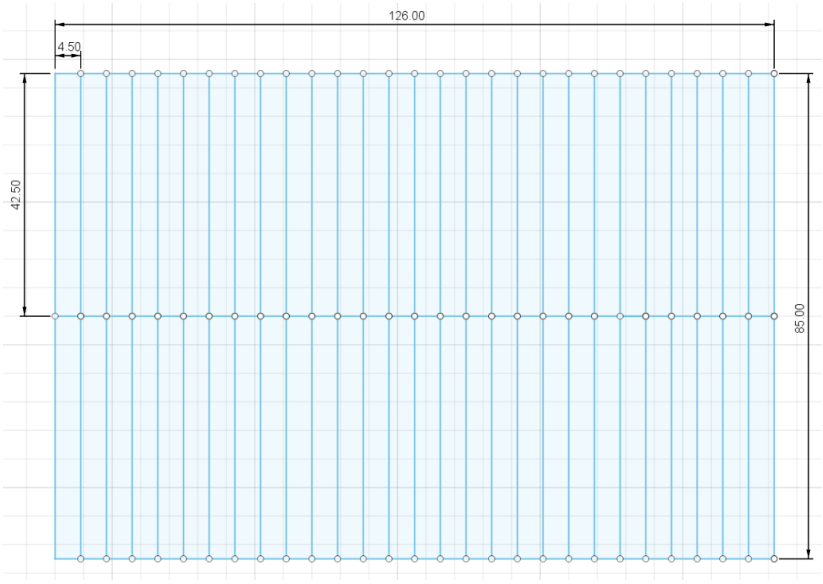

Figure 79: Sketch of the dimensions used to laser cut the A4 sheet of nitrocellulose membrane into a batch of 56 strips. Up to 4 batches could be cut from each sheet. (Sketch from Fusion 360, with units shown in mm).

The addition of sample and absorbent pads to the nitrocellulose membrane was initially trialled with prototype strips but, good and consistent contact between the pads and the strips would have required additional housing elements to provide downward clamping pressure and so was not used at this early validation stage.

5.3.2 Printing

With strips cut into an appropriate shape and size, the test and control lines were added. The main considerations were to control the line position on the strip and the thickness of the line with high strip-to-strip consistency. To achieve this, a PolyPico liquid handling system was used to apply the compound (Figure 80). This system uses disposable plastic print cartridges which could be filled with the solution to print. These ‘print cartridges’ were then fitted into the main print head that uses

controlled vibrations to eject individual droplets from the cartridge aperture. A built-in strobe and camera system calibrates the volume of the droplet, controlled through altering the parameters of the vibration motor.

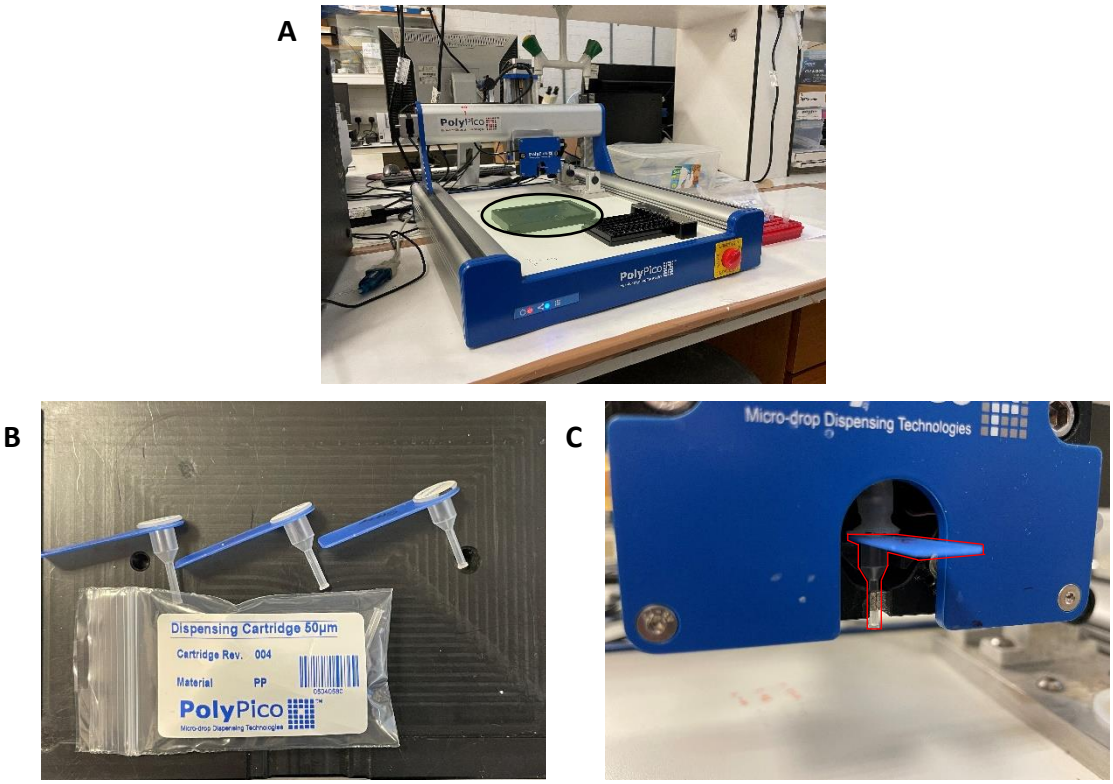

Figure 80: Images of the Picospotter inkjet system used to print the test and control lines for the assay. A) The whole Picospotter system showing the print head (centre blue) and the print area. The 96 well plate (highlighted green) was used to fill the print cartridges. B) Disposable print cartridges with variable aperture sizes (30 – 120 µm) (the cartridges are 15 mm high). A 50 µm aperture was used throughout this project. C) Enlarged view of the print head with the print cartridge fitted (highlighted in red).

The print head was programmed to print a pattern of drops of fixed volume and defined location. Here, a test line was printed 1 cm from the bottom of the strip and the control line was printed 0.5 cm above the test line. There was a built-in mounting area (Figure 80) designed to fit a 96 well plate that was used as a repeatable reference area for the printing of the nitrocellulose. This controlled the overall size of the laser cut nitrocellulose strips so that a batch of 56 strips could be printed

simultaneously. A new print cartridge was used for each solution and the droplet size was recalibrated immediately prior to each printing run.

The concentration of the print solutions were chosen based on the tutorial review by Parolo et al.[260] that suggested that a starting concentration for many lateral flow assay antibody-based test and control lines is 1 mg/mL. Higher protein concentrations printed inconsistently and occasionally blocked the print head, therefore, for all strips described in this work a concentration of 1 mg/mL was used.

Lines were printed using overlapping 15 nL spots that together would produce lines that were consistently 1 mm wide (Figure 81). To achieve a continuous line the spots had a 0.3 mm step over across the width of the test and to achieve the desired 1 mm thickness this was replicated three times. Each of the three print 'lines' had a 0.1 mm step over across the length of the strip. This resulted in a total of 42 total spots per test and control line with a volume of 0.63 µL. The test line was printed 1 cm up from the bottom of the strip and the control line 5 mm above the test line. These parameters were maintained on a per-strip basis for all strips presented here.

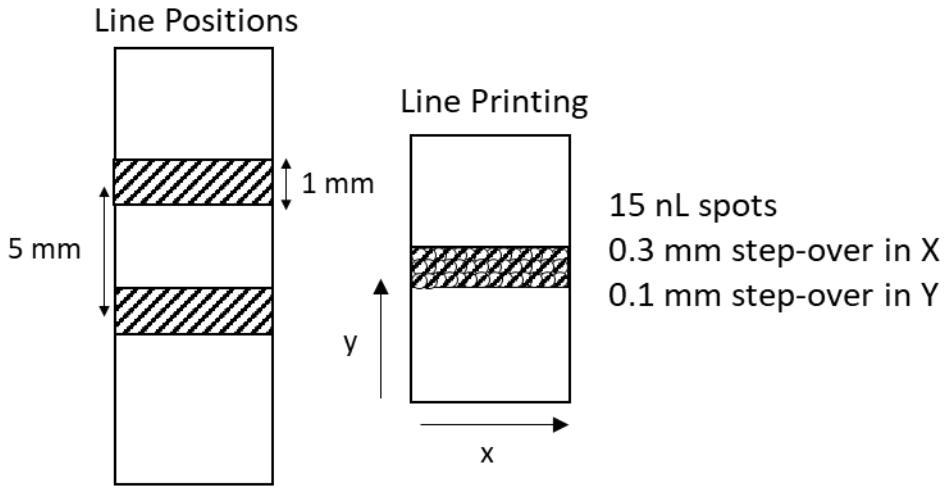

Figure 81: Positioning of test and control line printing using the PolyPico printer. Line printing was consistent on a per-strip basis. The parameters of the print were modified depending on the total batch of strips being printed (i.e. when printing 10 strips together a print line comprising of 140 spots was used to print all strips simultaneously).

Where possible, batch printing of strips was performed, and the print cartridges refilled with solutions as necessary (fill volumes of 100 – 150 µL was used) with volume calibration repeated between each line. Each line would be printed across the X axis of the batch of strips before returning to the start and advanced in the Y axis to allow for each line to partially dry before the next application. This reduced the spreading of spots due to saturation of the nitrocellulose with liquid, maintaining a consistent line width of 1 mm.

5.3.3 Image analysis

To quantify the results during optimisation a system for imaging the test and control lines was developed. A range of commercial strip readers are available along with other imaging methods such as the use of a consumer grade document scanner.[263] There are a number of well described smartphone-based imaging systems in literature[104,105] using the powerful cameras in modern smartphones in combination with the computational power on hand, results in the ability to achieve ultra-fast quantification of the signal intensity on a strip assay.

In order to standardise the images captured from the strips a repeatable imaging stage was required. This needed to position the strips consistently from experiment to experiment and allow for multiple strips to be imaged at the same time. Additionally, it needed to uniformly light the strips every time to ensure that the relative intensity of the signals was not skewed by differences in changes in lighting.

Imaging 3D Print Enclosure

A 3D printable imaging enclosure (Figure 82) designed for smartphone-based fluorescent imaging of lateral flow strips was described by Mahmoud et al.[264] A modified smartphone adapter plate was made to fit an iPhone 12 which was used to take images of the loaded strips. An additional cover for the lamp adaptor was printed to exclude external light and images were taken without zoom and with the flash always on. Each of the parts of the enclosure was made on an Ultimaker 3 Extended printer using black and blue PLA with 0.1 mm layer height. The main enclosure was printed with a 40% infill with a gyroid pattern to ensure that external light was appropriately excluded. Other components were printed with a 20% infill to reduce overall print time.

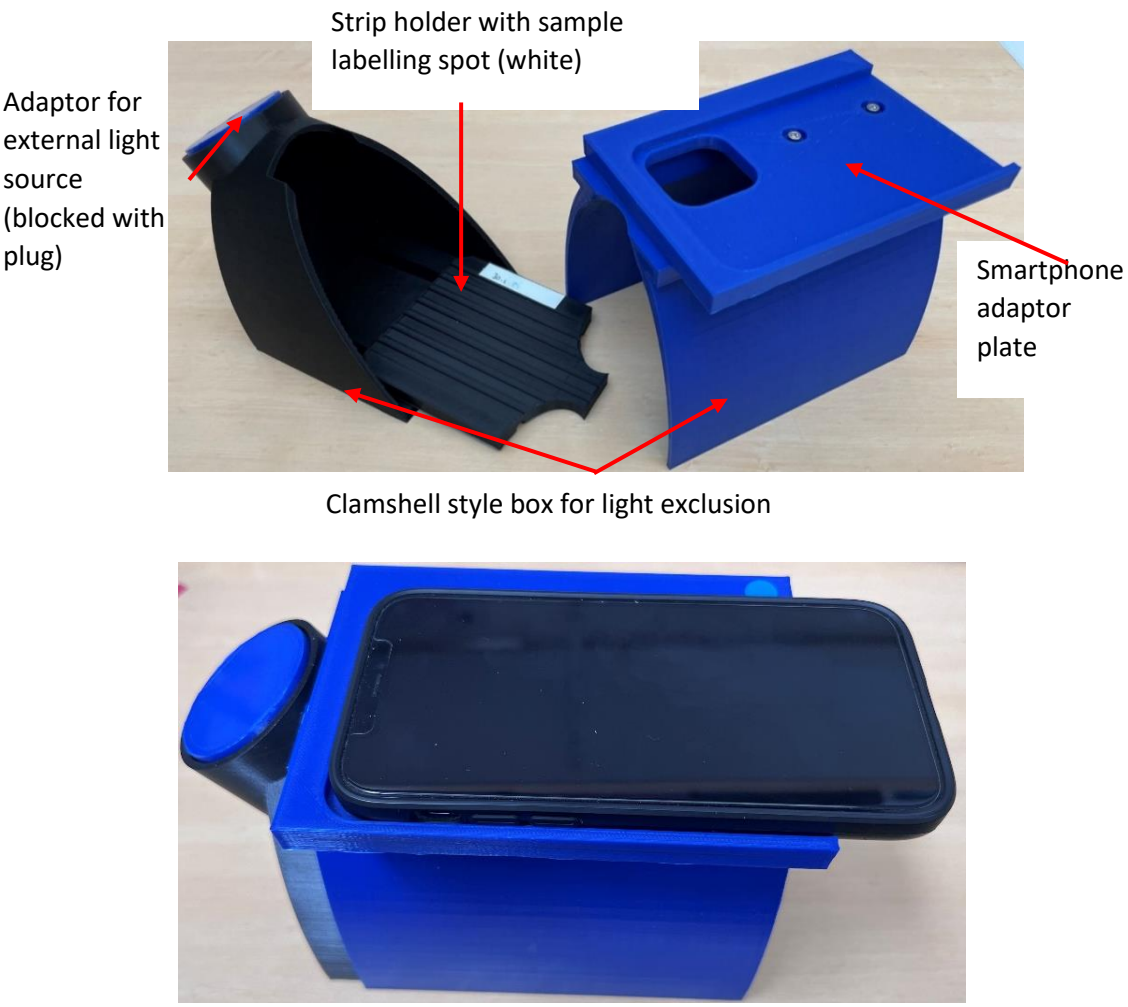

Figure 82: 3D printed enclosure customised for this project based on the work from Mahmoud et al. with a top adaptor plate designed for an iPhone 12. Separated view (top) shows each of the component pieces and assembled view (bottom) shows how the components fit together for imaging. The bottom half of the housing was printed in black to reduce blue reflections in the images.

The enclosure was made of upper and lower sections that together would hold the smartphone in a 'fixed' position above the lateral flow strips while allowing the enclosure to be opened and closed by separating the two halves. A separate carrier for the lateral flow strips held a maximum of 7 strips parallel to each other, which through interfacing rails, printed into the base of the lower half of the enclosure, would hold the strips in a repeatable position within the enclosure (see Figure 83 below)

Python Script for Automated Analysis

With a repeatable way of imaging a large number of lateral flow test strips, a method for analysing the images was required. A manual approach to lateral flow image analysis using ImageJ is reported in literature.[260] This provided a set of steps to follow to take an image of the strip and extract the intensity of the test and control lines. However, this manual approach had two key factors to consider:

1. Reliable image analysis requires that the images are taken under the same conditions every time. Differences in lighting or capture settings between images could alter the analysis results.
2. Manual processing of images limits the total throughput of the system and introduces variability in steps such as selecting the area of the strip to analyse.

The use of the imaging enclosure allowed for highly repeatable imaging with good consistency run to run, and software automation could be used to process the images.

To do this a python script (Appendix 1) was developed to take the full smartphone images and slice the image into seven individual images centred on the region over the test and control lines. This was done through referencing the x and y position of the top strip in the image (Figure 83). This position was held consistently throughout, ensuring that each strip was flush against the wall of the enclosure. This was another advantage of using a laser cutter to produce the strips as it provided confidence that every strip would have straight edges that were square to each other.

Figure 83: Image of lateral flow strips held in the 3D printed imaging enclosure. X and Y positions for image analysis were referenced from the top left-hand corner of the image. The yellow box shows an area that was ‘sliced’ from each strip and used to provide the individual images across the test and control lines. The orange line shows the reference edge that was used to ensure the strips were repeatable in the x direction.

With an image of the test and control lines isolated for each strip available it was converted to greyscale then the 3D data (x, y, pixel intensity) was compressed to 2D by averaging the pixel intensity over the y axis. This yielded data that could be plotted to show the changing pixel intensity over the length of the strip. The averaging over the y axis also aided in evening out any irregularities in the printing of the test and control lines (Figure 84).

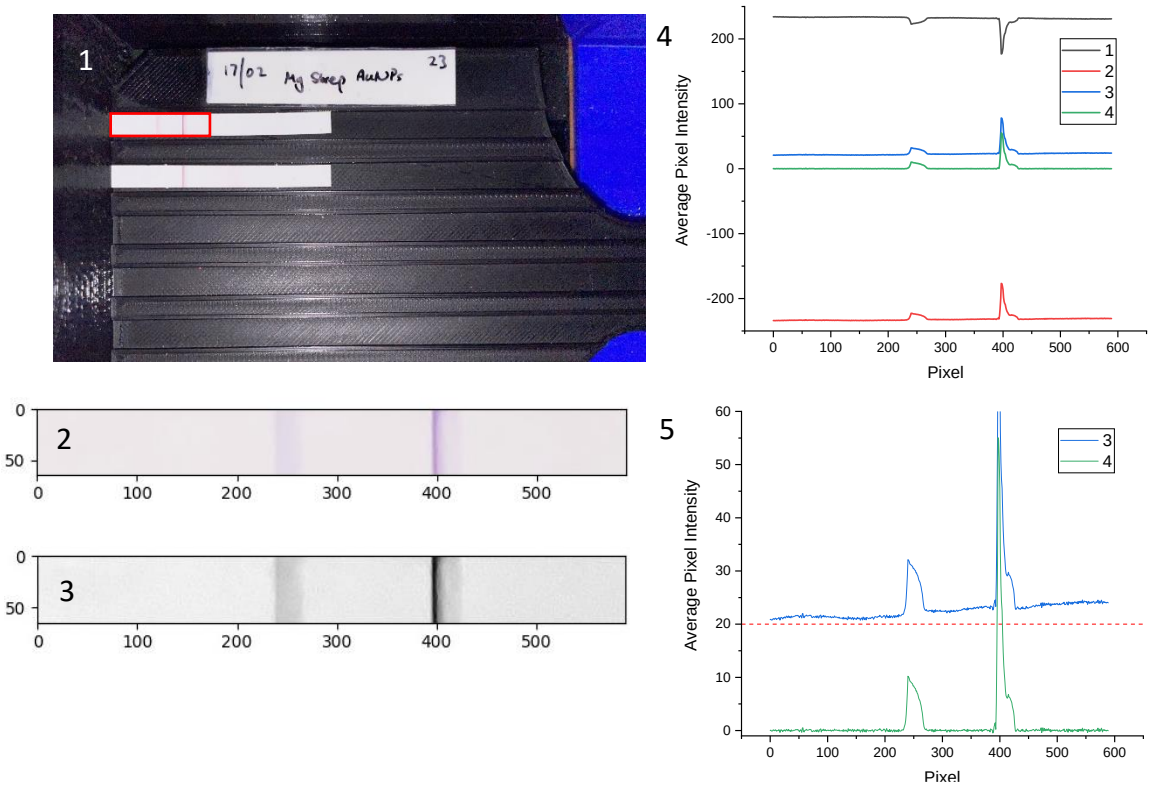

Figure 84: Illustration of the steps taken by the image analysis program to convert a smartphone image to a plot-able intensity graph and integrate the peaks.

1) Full image taken showing two strips under analysis; the top strip is highlighted showing the region isolated for analysis.
2) The highlighted strip area is sliced into a new image shown in colour.
3) The colour strip image is converted to greyscale using the Python OpenCV library. Greyscale gives pixels a value between 0 (completely black) and 255 (Completely white).
4) The pixel intensity data from 3 is averaged across the y axis giving average pixel intensity. 4-1) raw average pixel intensity plotted shows inverse peaks. 4-2) These inverted peaks are flipped by converting the sign of the data. 4-3) The inversion of the peaks is completed by adding 255 (maximum value in greyscale). 4-4) Baseline correction is applied, flattening and bringing the baseline to zero.
5) The difference before and after baseline correction is applied. A reference line (red) at 20 has been added to show the deviation more clearly in the baseline over the distance of the strip.

From this image, an automatic baseline correction system developed by Baek et al, originally reported for correction of Raman spectra, was applied.[265] This correction was to allow for automatic peak detection and integration, which was the primary method for quantifying the results of each strip assay.

Peak detection was implemented using the SciPy signal analysis library to find peaks based on prominence and with a maximum peak width of 60 pixels. Once the peaks

were detected, integration was done with Simpson's rule.[266] Peak height was also calculated to understand the maximum intensity, as a very broad peak may have a large integration but less visibility than a sharper peak.

The automation of image analysis increased the throughput of assay development and opened the option of applying high throughput experimental techniques such as design of experiments (DoE) to the problem.[267]With the production and analysis of the strips developed, the assays themselves could be run and experimental conditions optimised. Initial experiments aimed to verify the basic experimental conditions of the flow and the capture of gold nanoparticles.

5.4 Strip Testing

The main interaction being leveraged by the assay was the streptavidin-biotin interaction, so this was the first thing to be investigated.

The general approach used here to run a lateral flow assay was with the AuNPs solutions at 1 OD in the running buffer added to a well of a 96 well plate and the end of the nitrocellulose strip placed into the well (Figure 85) to allow flow up the strip by capillary action.

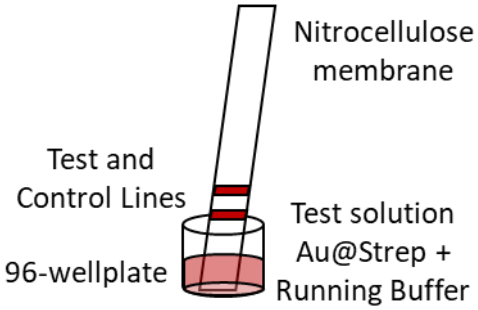

Figure 85: Positioning of the strip assay in a well of a 96 well plate with the test solution.

The total volume of nanoparticle solution being allowed to wick into the strip before a wash buffer would be added. Once the wash buffer had run into the strip, the strip would be removed from the plate and allowed to fully dry before loading into the imaging enclosure and analysed.

5.4.1 Control Tests

Blocking is the addition of non-reactive compounds to the assay to saturate non-specific binding sites to ensure target binding only happens in defined locations. Common blocking approaches in lateral flow are the addition of proteins such as BSA, Casein and non-fat skimmed milk powder or detergents to either the running buffer, nitrocellulose membrane or, both.[268]

Biotinylated BSA (BBSA) was used to verify the binding of my Au@Streptavidin nanoparticles to a biotin capture element. For a non-specific binding control, a test line of BSA (non-biotinylated) was printed (Figure 86).

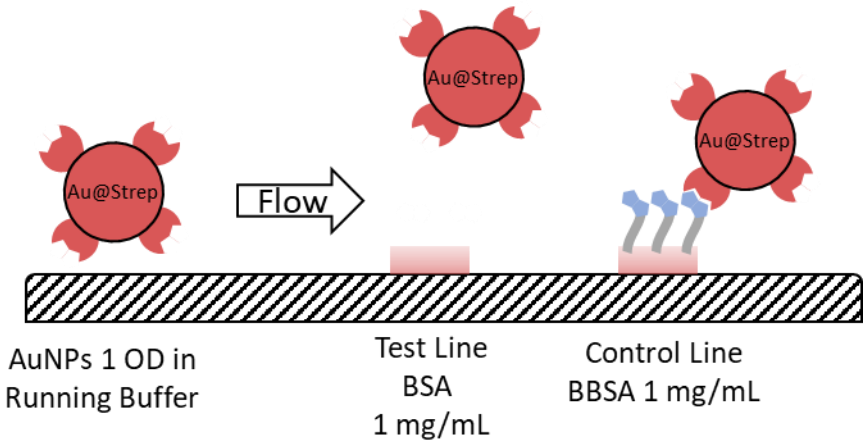

Figure 86: Illustration of the strip assay used to validate the binding of Au@Streptavidin in flow and to optimise the flow conditions.

Initial blocking conditions were taken from literature and used 0.1% Tween 20 in PBS as the running buffer. Tween 20 is (also known as polysorbate 20) is a non-ionic surfactant used in lateral flow tests as a wetting agents to allow the nanoparticles to flow into the strip.

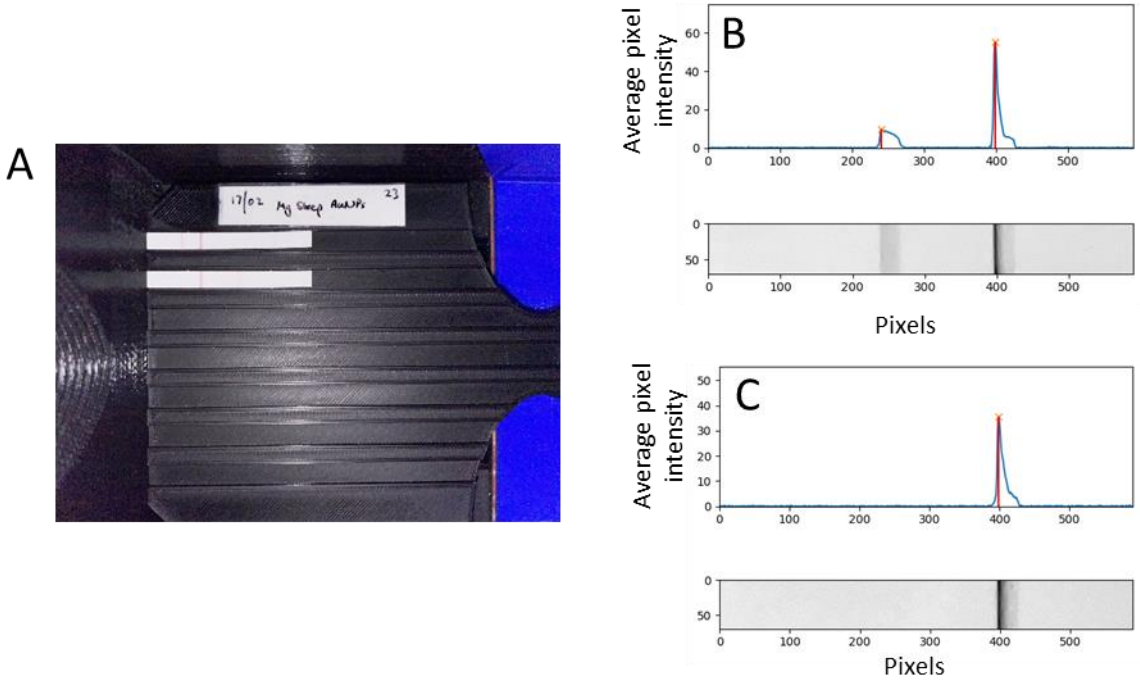

Figure 87: A) Image of a control experiment and strip imaging; B) strip 1 run with 0.2% Tween 20; C) strip 2 run with 0.2% Tween with 0.1% BSA

The image (Figure 87) shows two strips run with and without 0.1% BSA in the running buffer, both with 0.2% Tween. The BSA-free strip (B) showed a signal at both the test and control lines indicating that there was non-specific binding of Au@Streptavidin to BSA. The control line showed much stronger binding than the test line and both showed a similar peak shape indicating that the majority of the binding occurred on the leading edge of the printed line.

Upon addition of 0.1% BSA the non-specific binding to the BSA line was suppressed but this also coincided with a 35% reduction in the peak intensity of the

control line. This showed that optimisation of the running buffer would be vital to maintaining as strong of a signal as possible while suppressing non-specific binding. The complexity of these interactions is often difficult to unpick with a standard one-by-one experimental methods, so here a Design of Experiments (DoE) approach was applied.

Au@Streptavidin Biotinylated BSA capture

A four level, two factor full factorial design was chosen to screen the full range of BSA and Tween 20 concentrations seen commonly in the literature.

Table 6: Factors and their levels used to generate the DoE for the optimisation of the running buffer. Levels were the percentage of the reagents (Tween 20 / BSA) in a 1x PBS solution.

Factors	Levels (% w/w)			
Tween 20	0.01	0.1	1	10
BSA	0.01	0.1	1	10

The streptavidin-biotin binding pair is well known to be resistant to surfactants and has been shown to tolerate high percentages of Tween in a running buffer.[190] The percentages of BSA were chosen to match the range of Tween and screen the widest useable space for the running buffer.

Table 7: Experimental design of 24 full factorial DoE as generated by Minitab with a run order assigned from random ordering of the standard order. Line Intensity was measured from peak integrations after removing the influence of any non-specific binding to a BSA 'test' line.

Standard Order	Run Order	Tween 20 %	BSA %	Line Intensity (BBSA-BSA)
12	1	1	10	0
14	2	10	0.1	219
13	3	10	0.01	180
10	4	1	0.1	148
2	5	0.01	0.1	90
9	6	1	0.01	113
11	7	1	1	0
16	8	10	10	0
1	9	0.01	0.01	0
8	10	0.1	10	0
5	11	0.1	0.01	86
15	12	10	1	182
7	13	0.1	1	37
6	14	0.1	0.1	131
3	15	0.01	1	0
4	16	0.01	10	0

This experimental design resulted in 16 experiments that were run simultaneously (Table 7). Analysis of these experiments (Figure 88) showed the strong benefit of maximising the amount of Tween while minimising the BSA percentage.

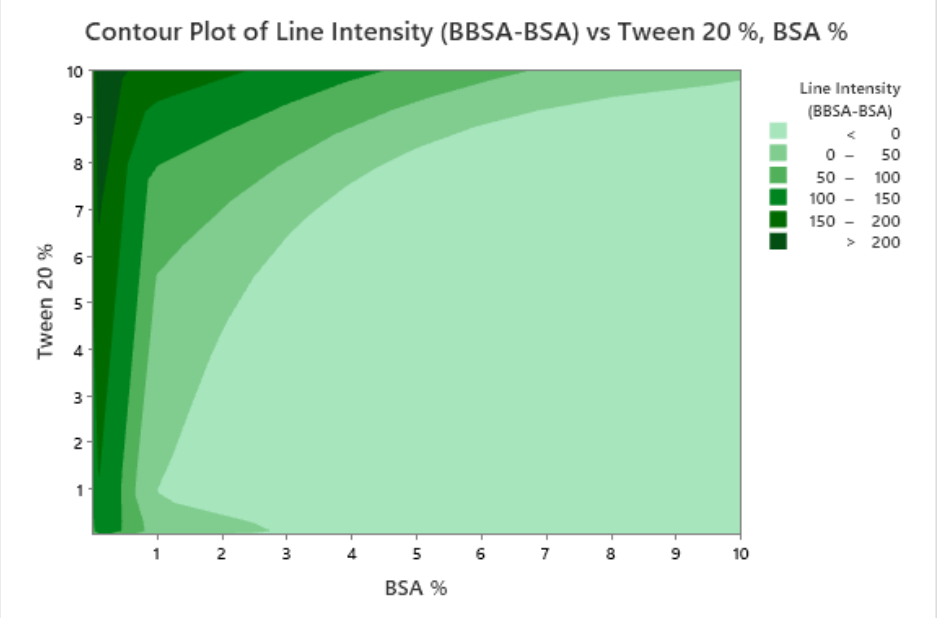

Figure 88: Contour plot of the DoE optimisation of signal intensity resulting from a screening of Tween and BSA percentage in the assay running buffer. The corrected line intensity (BBSA-BSA) was found to be improved by maximising the Tween 20 and minimising BSA levels.

There were several experiments that were worth highlighting as part of this optimisation study. At the two extremes of the experiment different behaviours were observed. At the lowest concentrations (0.01% Tween, 0.01% BSA) the nanoparticles would not flow through the strip at all, with the nanoparticles stuck at the meniscus line from where the strip was immersed in the nanoparticle solution (Figure 89).

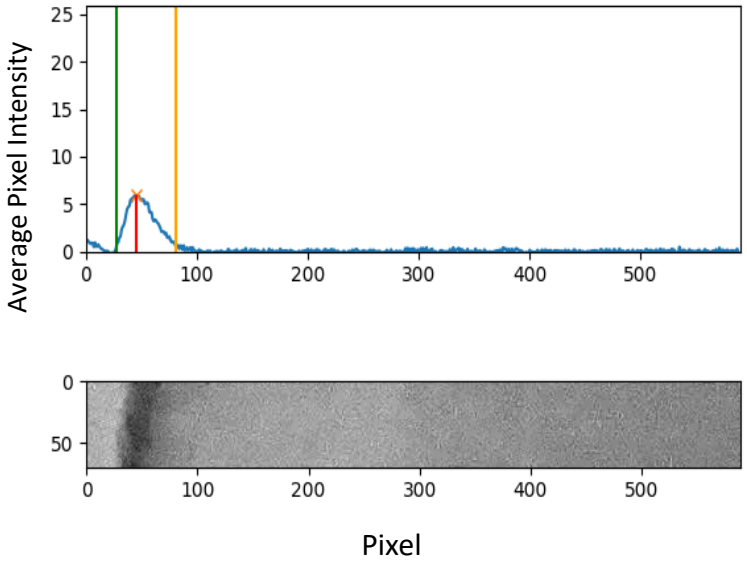

Figure 89: Image analysis of a low concentration runs from the DoE optimisation experiments. Peak integration 183, Peak height 6. Nanoparticles stuck at the base of strip, no peaks found at either the test or control line.

At the opposite extreme, where Tween and BSA concentration was maximised the nanoparticles flowed into the strip, but the high levels of blocking stopped any interactions taking place (Figure 90).

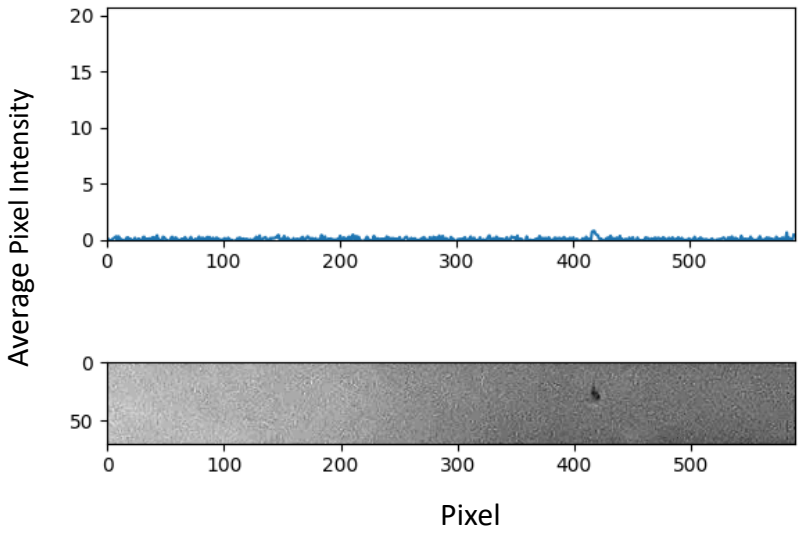

Figure 90: Image analysis of a high concentration run from the DoE optimisation here, Tween + BSA 10% no peaks found at either the test or control lines. A minor mark on the strip is in the region of the control line but is most likely due to deformation of the nitrocellulose membrane during handling, which can restrict nanoparticle flow.

As the contour plot (Figure 88) shows there was a strong effect from the addition of more BSA to the running buffer while the binding interaction was generally highly resistant to the addition of more Tween. The optimal running buffer conditions were 10% Tween and 0.2% BSA.

Au@BBSA Streptavidin Capture

To validate the binding behaviour of Au@Streptavidin in a lateral flow assay positive control particles were required and biotinylated BSA (BBSA) was used to synthesise functional gold nanoparticles that would be captured by streptavidin (Figure 91). Au@BBSA was synthesised through straightforward addition of biotinylated BSA (Abcam 1 mg/mL in PBS) to Au@Citrate. While there was no noticeable change in the peak absorbance wavelength in UV-Vis spectroscopy there was a measurable shift in DLS and zeta potential measurements that suggested

functionalisation had occurred. The change in zeta-potential was similar as that seen in the synthesis of Au@Streptavidin.

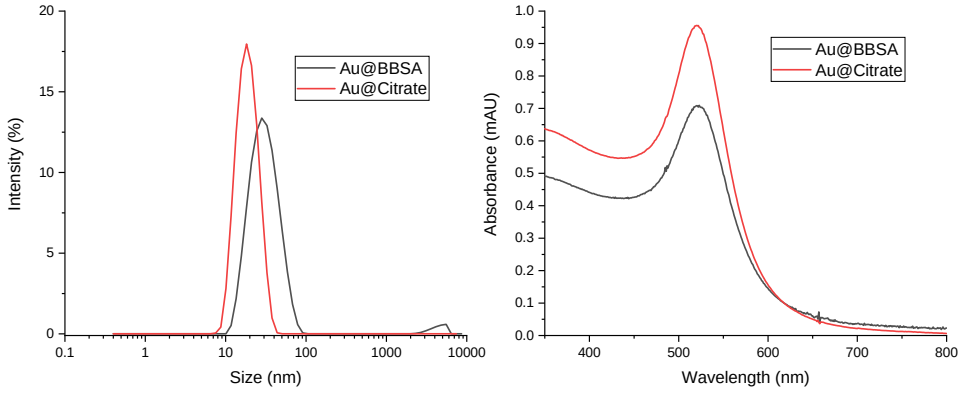

	λ_{max}	Z-Average DLS / nm	Intensity DLS / nm	PDI	Zeta Potential / mV	SD/ mV
Au@Citrate	521	23.9	21.2	0.14	-27.8	7.3
Au@BBSA	520	27.9	128	0.2	-11.0	14.9

Figure 91: Characterisation of Au@BBSA synthesis through DLS (left) and UV-Vis (right) post-purification.

To validate the use of streptavidin as the capture agent, a test line of streptavidin (1 mg/mL) was challenged with Au@BBSA (10 µL, 1 OD). The control line biotinylated BSA, acted as a negative control, where there should be no binding of the Au@BBSA (Figure 92).

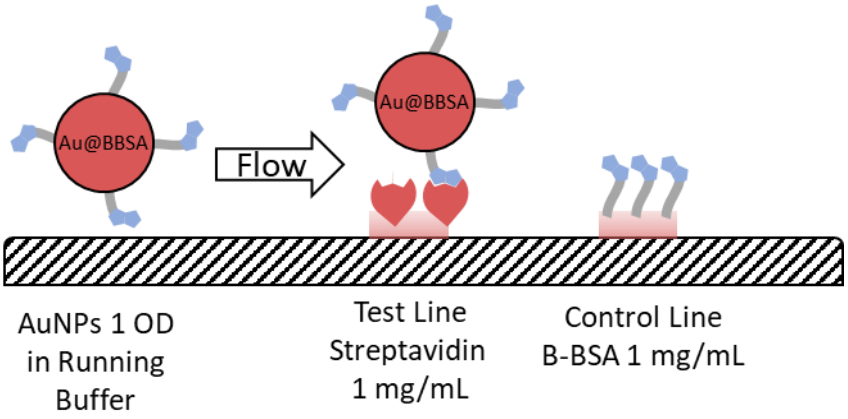

Figure 92: Illustration of the strip assay used to validate the binding of Au@BBSA to a Streptavidin test line in Flow.

Three running buffer conditions were trialled with Au@BBSA. Based on the earlier optimisation the surfactant was maintained as Tween 20 at 10% w/w. A negative control run with Au@Streptavidin was also performed to verify that there was no non-specific binding between Au@Streptavidin and the streptavidin test line (Figure 93).

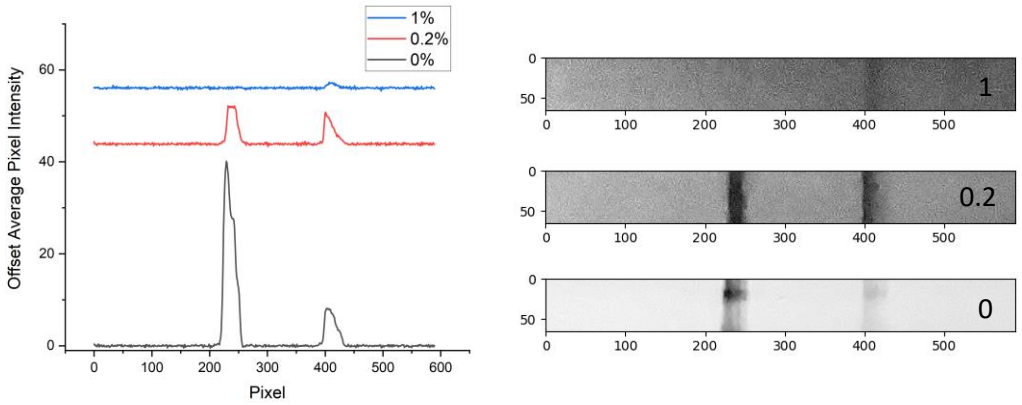

Figure 93: Image analysis of the control assay with Au@BBSA capture by streptavidin with running buffer BSA concentrations at 0, 0.2 and 1% and right associated strip images.

Increasing the percentage of BSA in the running buffer from 0 to 0.2% showed a large decrease in the test line signal with only a minor reduction in non-specific binding. Even at the highest percentage of BSA the non-specific binding was still present while the test line signal was entirely suppressed. These results showed that the Au@BBSA – Streptavidin interaction was more strongly suppressed by the addition of BSA than Au@Streptavidin– BBSA.

Au@Strep-**12** Conjugate Binding Control.

The next part of validating the binding of the particles in flow was to challenge the nanoparticles with **12** in the running buffer (Figure 94).

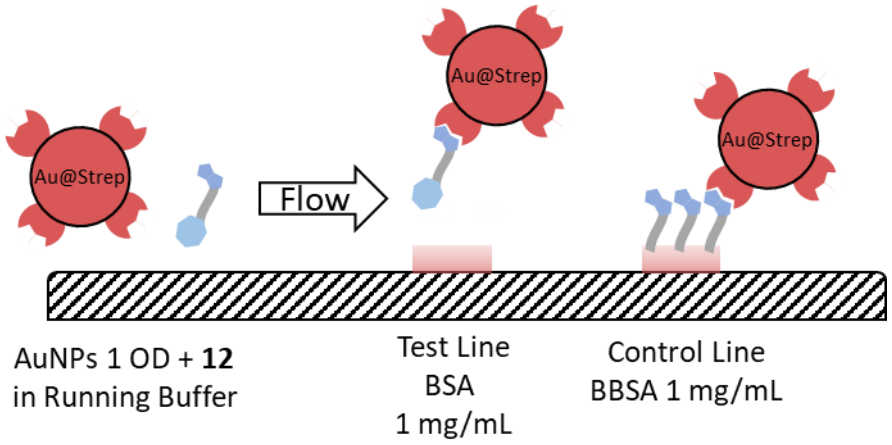

Figure 94: Illustration of strip design to test the non-specific binding of an Au@Streptavidin+**12** conjugate

12 (13, 1.3 and 0.13 µM) was used in conjunction with the standard running buffer of 10% Tween and 0.2% BSA and the Au@Streptavidin.

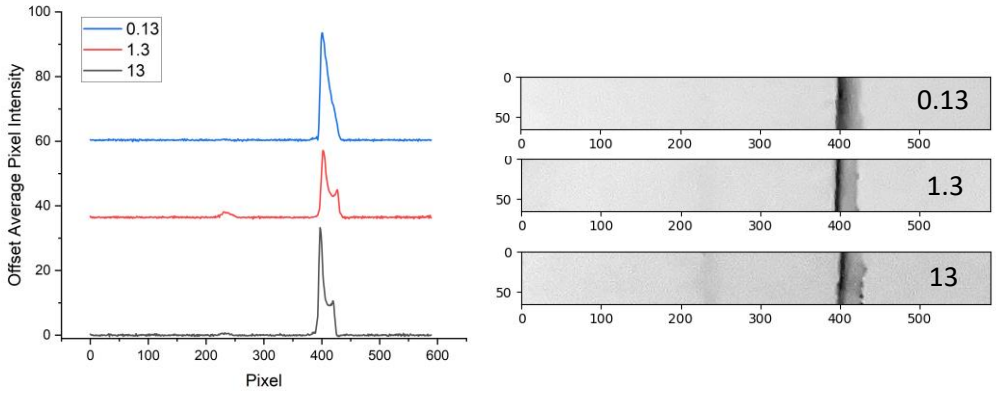

Figure 95: Image analysis of control assay with Au@Streptavidin with the addition of **12** at 13, 1.3 and 0.13 µM testing for non-specific binding with a BSA test line, and associated strip images (right).

As the concentration of **12** was decreased, there was an increase in the intensity of the control line and a minor peak of non-specific binding in the 'test line' (Figure 95). This is in line with the expected behaviour as **12** binds into the available streptavidin binding sites which act to block binding to the control line. There was a

slight peak at the test line in each strip but only at the highest concentration did this test line peak rise significantly above the background.

The reduction in the control line intensity was not enough to cause a problem with the identification and suggests that there was not complete saturation of the streptavidin binding sites. These control experiments validated the relevant binding pairs and bacteria testing was analysed next.

5.4.2 Bacteria Testing

To assess the efficacy of the assay components in the detection of bacteria in flow two assay design were used. The first assay design was a simplification of the full sandwich assay where *E. coli* was incubated with **12** under the conditions used in the previous labelling experiments, then washed to remove excess **12**, before being printed as the test line on the membrane (Figure 96).

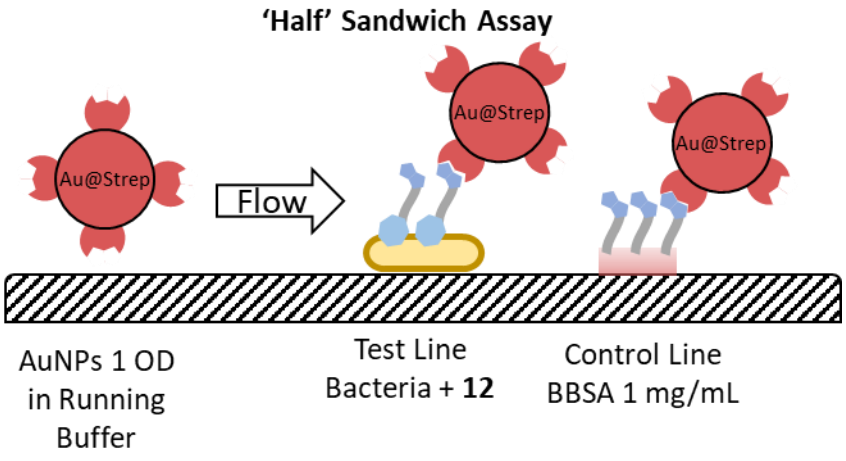

Figure 96: Illustration of a strip design for the capture of Au@Streptavidin with *E. coli*+**12** conjugates making up one half of a sandwich assay

This 'half sandwich' assay design essentially bypasses the capture step of the standard sandwich assay design. By fixing the bacteria to the test line position just

the binding of the nanoparticles to the bacteria can be isolated from the rest of the test's functions. This also serves as a platform to optimise some of the parameters for the bacteria detection assay.

Some limitations to this method were in the printing the test line with bacteria as the inkjet style spotting system required passing the solution through a small aperture. This limited the total concentration of bacteria solution possible to print (≤ 1 OD) and combined with the relatively small print volume (0.63 µL), the total number of bacteria was low (≤ 10^4 bacteria per test line).

Half Sandwich Assays

Screening Polymyxin Concentration against E. coli

This was performed with a range of probe concentrations (1, 10, 100 µM) and across a range of bacteria concentrations (0.1, 0.5, 1 OD_{600}). Each set of runs was performed with an internal control of unlabelled bacteria printed.

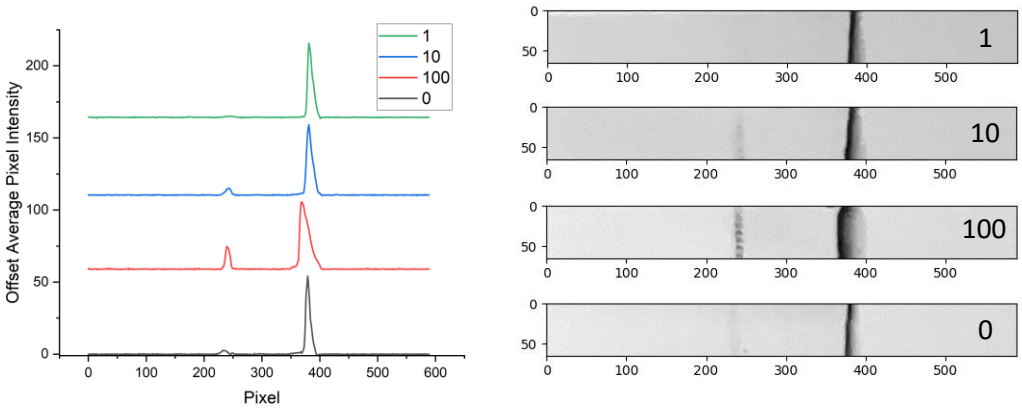

Figure 97: Image analysis of half sandwich assay with a test line printed with *E. coli* at 1 OD labelled with compound 12 at 100, 10, 1 and 0 µM, and right associated strip images.

Initial tests with the *E. coli* test line printed at 1 OD showed strong labelling at the highest concentration of **12** with a decrease in labelling as concentration was reduced (Figure 97). There appeared to be a proportion of non-specific binding in the control experiment (0 µM), but this was absent in other experiments with lower concentrations of **12**. Reducing the concentration of the printed *E. coli* down to 0.5 OD showed a similar trend (Figure 98).

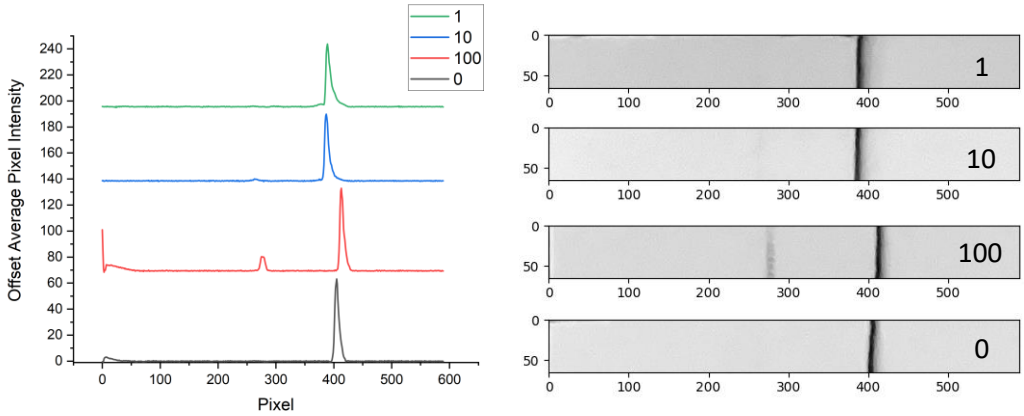

Figure 98: Image analysis of half sandwich assay with a test line printed with *E. coli* at 0.5 OD labelled with **12** at 100, 10, 1 and 0 µM, and right associated strip images. Note the artefacts at <50 pixels in the 100 µM and 0 µM runs are from a slight misalignment of the strips in the holder.

Reducing the *E. coli* concentration down to 0.1 OD showed complete loss of signal at the test line for both the labelled and unlabelled bacteria (Figure 99).

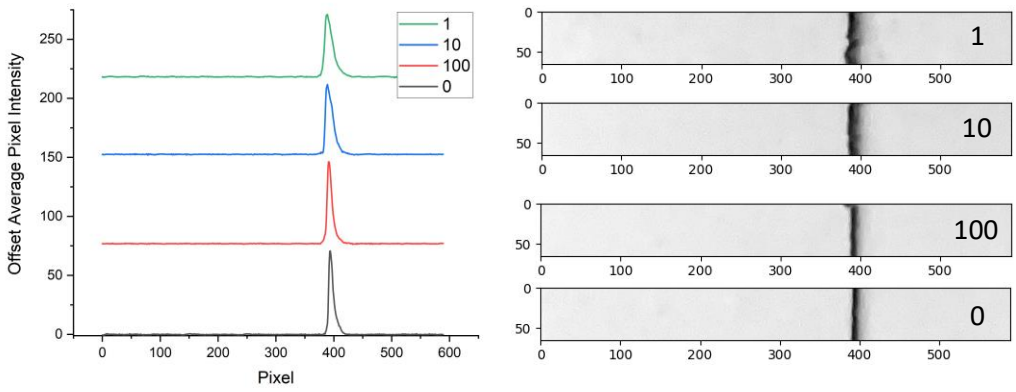

Figure 99: Image analysis of half sandwich assay with a test line printed with *E. coli* at 0.1 OD labelled with **12** at 100, 10, 1 and 0 µM, and right associated strip images.

The disappearance of binding in the unlabelled strip would suggest that the binding might have been tied to printed *E. coli* concentration (reduction from 10^4 to 10^3 bacteria per test line). Looking across the strips with 100 µM (Figure 100) there was a 27 % decrease in peak integration when bacteria concentration was halved from 1 OD to 0.5 OD, below 0.1 OD this fell below detection limits.

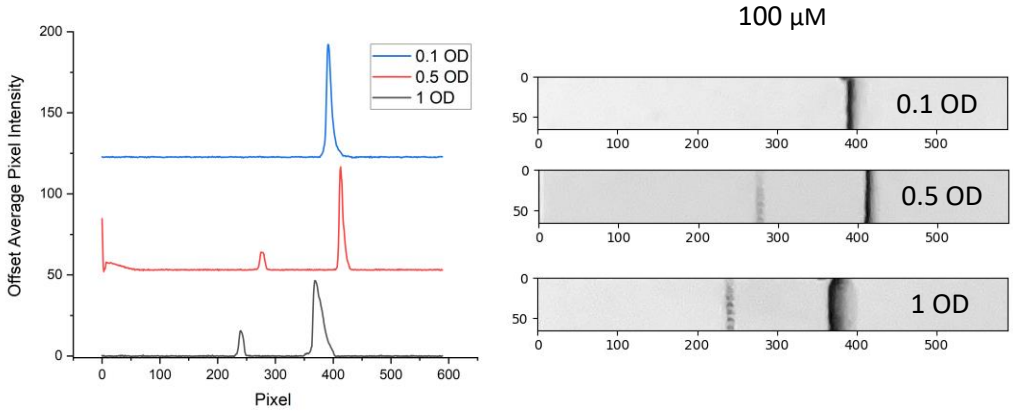

Figure 100: A comparison of half sandwich assays where *E. coli* was labelled with **12** at 100 µM across 1, 0.5 and 0.1 OD bacteria concentrations and right: associated strips.

This suggests that the limit of detection of the assay as designed is between 1 and 0.1 OD which is in the range of 10^7-10^9 CFU/mL which is significantly above all other

available bacteria detecting lateral flow tests. However, there must be a consideration for the low volume of bacteria solutions used in the generation of these assays. The total volume of bacteria solution deposited on the test lines was 0.63 µL per strip (approximately 10^4 - 10^3 bacteria for 1 OD - 0.1 OD solutions) compared to the total volume used in commercial lateral flow tests (approximately 100 µL) with capture in flow.

Full Sandwich Assays

Pre-labelled E. coli

Here, *E. coli* was pre-labelled with **12** before being added to the running buffer along with Au@Streptavidin. The combined mixture was then allowed to run through the strip before being imaged.

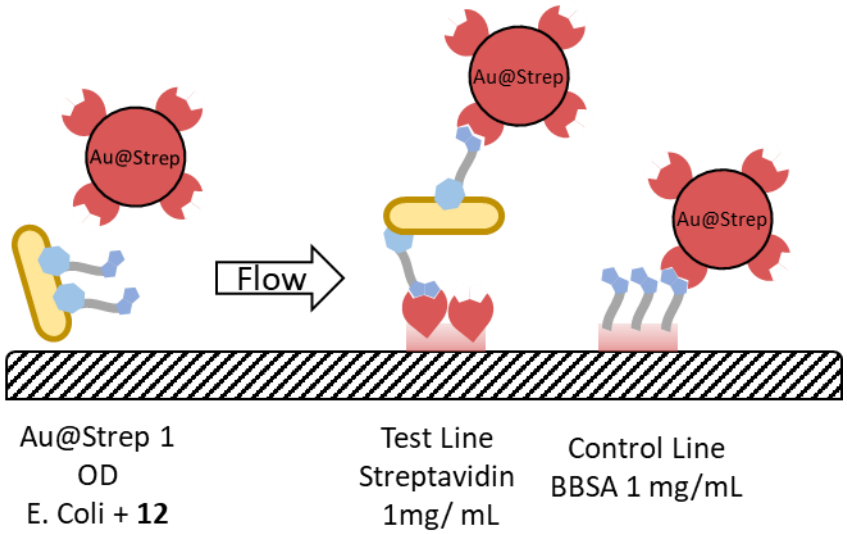

Figure 101: Illustration of the full sandwich assay design used where E coli labelled with 12 and Au@Streptavidin are flowed through the strip to be captured on the test line loaded with streptavidin.

With zero incubation time (Figure 102) there was no binding seen at 1 µM labelling but at 10 µM a faint test line was seen.

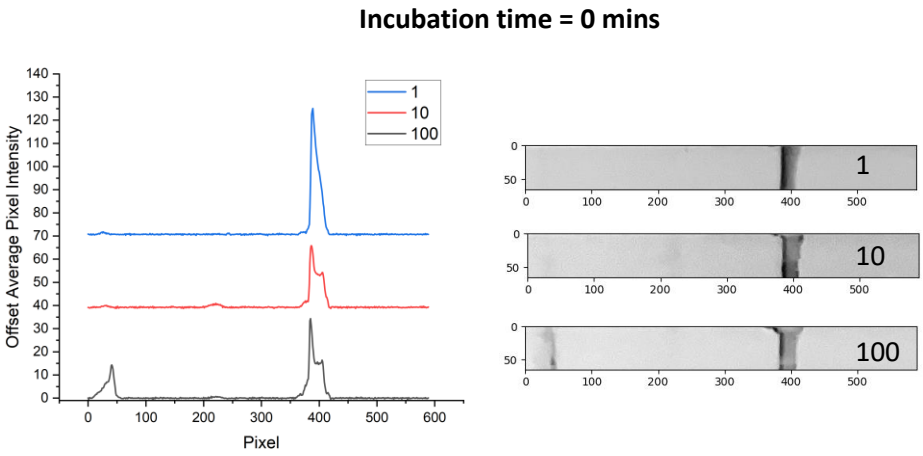

Figure 102: Image analysis of the full sandwich assay run with pre-labelled *E. coli* (1 OD, 100, 10, 1 µM) and tested with Au@Streptavidin (1 OD, 10 µL) with no incubation time before running, and associated strips.

For the highest concentration run a large degree of binding was seen where the test strip was immersed into the test solution, presumably the bacteria were not flowing into the strip. The higher incubation time showed an increase in both signal at the test line at 100 and 10 µM along with capture of nanoparticles at the immersed end of the strip.

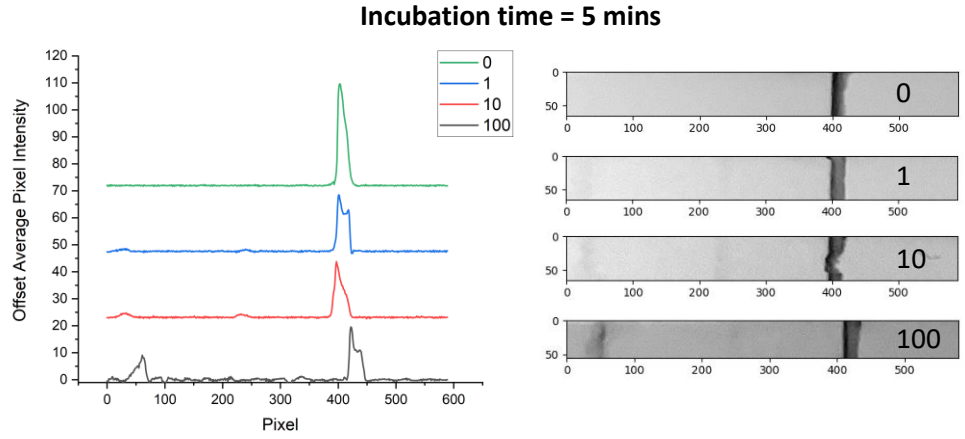

Figure 103: Image analysis of the full sandwich assay run with pre-labelled *E. coli* (1 OD, 100, 10, 1 µM) and tested with Au@Streptavidin (1 OD, 10 µL) with a five-minute incubation time before running, and associated strips

The pixel intensity at the test lines was only barely above baseline so was not identified as a peak through the image analysis but were apparent from the greyscale images. These two tests (Figure 102 and 103) suggested that there was *in situ* labelling of the *E. coli* with the Au@Streptavidin and that the labelling was broadly insensitive to incubation time. However, the capture of nanoparticles at the immersed end of the strip was consistent across both incubation times.

The capture of AuNPs at the bottom of the test strip due to Au@Streptavidin labelling the bacteria but the bacteria not flowing through the strip. The effect of increasing the percentage of BSA in the running buffer was briefly revisited (Figure 104).

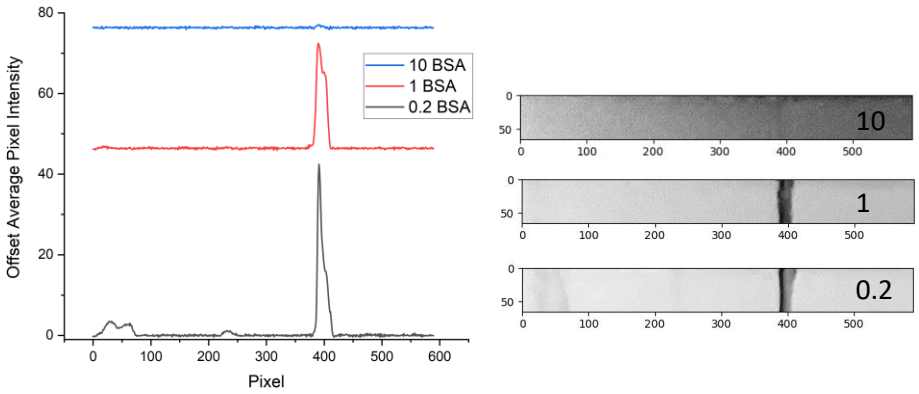

Figure 104: Image analysis of full sandwich assay where pre-labelled *E. coli* (1 OD, 100 µM) was run with Au@Streptavidin (1 OD, 10 µL) with altered running buffer (10% Tween and BSA (0.2%, 1%, 10%)) and associated strips.

The resulting strips from the higher percentage of BSA (Figure 104) showed results consistent with the initial running buffer optimisation experiment. An alternative method for identifying the cause of the nanoparticle capture was to increase the number of bacteria added to the assay by increasing the volume of *E. coli* added to the test at 1 OD (Figure 105).

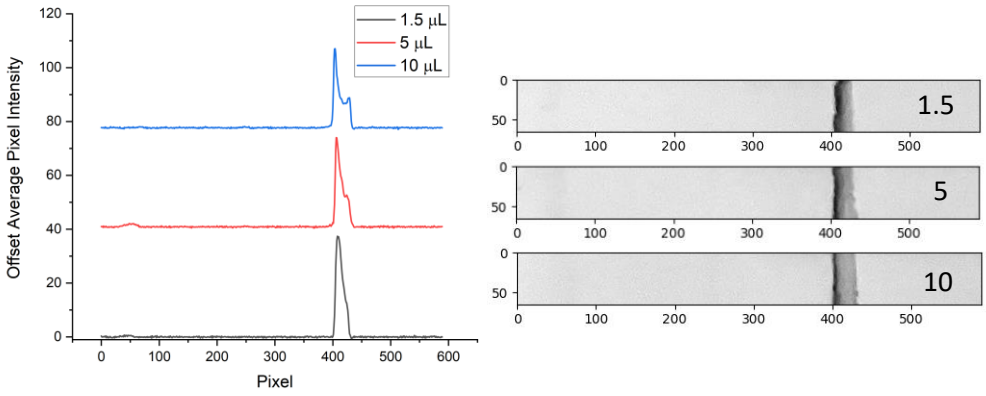

Figure 105: Image analysis of full sandwich assay where pre-labelled *E. coli* (1 OD, 100 µM) was added at increasing volumes (1.5, 5 and 10 µL) then run with Au@Streptavidin (10 µL) and associated strips.

The result appeared to be a loss of binding at both the base of the assay and on the test line. This result suggests that the issue with the assay design was an inability for the bacteria to flow through the nitrocellulose membrane. This would cause the nanoparticles bound to the bacteria to be trapped in the running solution and concentrate at the base of the strip. The higher loading of the bacteria increases the trapping of nanoparticles.

Screening Nitrocellulose membrane pore size

To investigate this issue the assay was remade with a range of nitrocellulose membrane pore sizes using Merck Hi-Flow™ HFC135, 120, 90 and, 75 membranes (these manufacturer labels denote average speed of flow measured in seconds over 4 cm on a 10 mm wide membrane, with the higher numbered membranes having smaller pore sizes). The test and control lines were printed under the same conditions and the assays used *E. coli* labelled with **12** (100 µM) and washed (Figure 106).

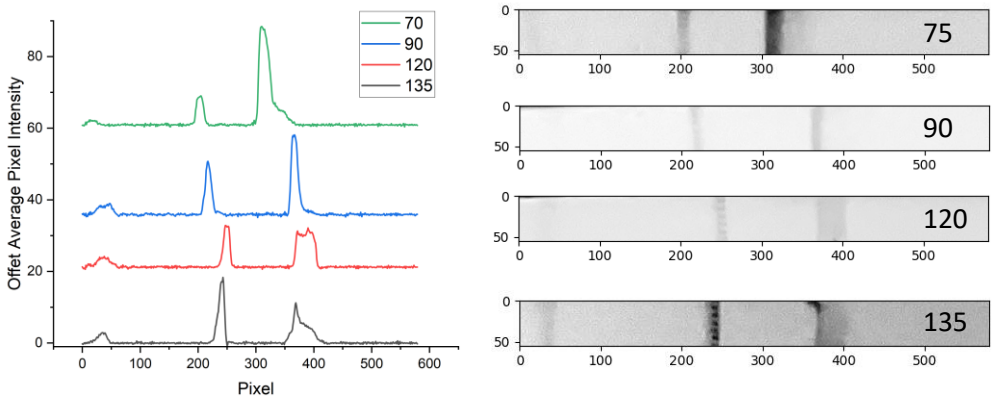

Figure 106: Image analysis of full sandwich assay run with *E. coli* (2 OD, 1.5 µL) with Au@Streptavidin (1 OD, 10 µL) in the standard running buffer with associated (right) strips. Nitrocellulose membrane varied from 135 (smaller pores) to 75 (larger pores). All membranes were printed with a test line of streptavidin (1 mg/mL) and a control line of BBSA (1 mg/mL) and dried overnight at 37 ºC.

The image analysis of the strips (Figure 106) showed detection of *E. coli* on all of the strips suggesting that the pore sizes cut of the Merck Hi-Flow™ HFC135 membranes allowed bacterial flow (unlike the Whatman membrane). Both by peak heights and integrations there is not a major difference at the test line across the 135-75 range (Figure 107).

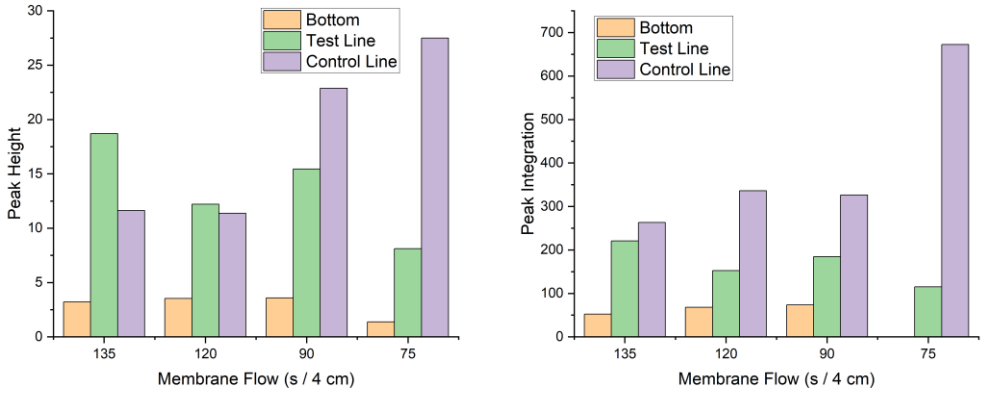

Figure 107: Peak analysis of nitrocellulose membrane variation experiment showing Peak Height (Left) and Peak integrations (Right) at the bottom of the strips, test and control lines. Bottom of strip peak in HFC75 membrane was not significantly above background.

This series of experiments has shown the development of a sandwich assay lateral flow test that can successfully detect *E. coli*. Based on this final experiment there was strong detection of approximately 3 x 10^5 bacteria (based on 1.5 µL, 2 OD *E. coli* added to the assays) and future development of this assay could explore the lower limit of detection. This would have to be paired with more optimisation studies to improve the flow of *E. coli* further as even with the change in nitrocellulose pore sizes there was still entrapment of bacteria at the bottom of the strip.

Additionally, as the test is further developed, the introduction of sample, conjugate and absorbent pads would have to be investigated. Each of these elements would improve the detection limits of this assay and make it more sensitive. An exploration of a wider range of bacteria species, including clinical samples and antibiotic resistant strains would be particularly relevant.

Conclusions & Future work

The result of this work has shown the development of a Gram-negative selective binding agent in compound **12** that allows for the application of a variety with Streptavidin based secondary binding assays. This secondary binding allowed for the labelling of *E. coli* selectively with both a fluorescent streptavidin and with gold nanoparticles functionalised with streptavidin. To implement these in a lateral flow test system was developed and it was shown that *E. coli* could be detected using nanoparticles flowing through the membrane. This resulted in a proof-of-concept lateral flow system that could detect *E. coli* using an antibiotic based binding agent showing that such an assay is possible to produce without antibodies or aptamers.

This opens a new path for the development of novel lateral flow tests which could be expanded on in two primary ways. The first is further development of the lateral flow assay reported in this thesis with additional exploration of each system (probe and nanoparticles) to improve sensitivity and streamline use by eliminating steps such as the pre-incubation of bacteria. The second would be to expand the range of binding agents to a wider variety of target analytes. The simplest path forward would be to look at other antibiotic based probes and substitute them into the described assay test system.

The relatively straightforward and robust binding system of a streptavidin-biotin pair system removed many of the complications and allows for the more rapid generation of future tests based on small molecules/antibiotics.

6 Experimental

Chapter 3

Materials and Methods

Chemicals used in this work were purchased from Sigma Aldrich, Merck, Acros, and Fluorochem. Commercially available reagents were used without further purification. NMR spectra were recorded at 298 K in deuterated solvents using Bruker AVA600 (600 MHz) or a Bruker AVA500 (^{1}H 500 MHz, ^{13}C 126 MHz) spectrometer. Chemical shifts are reported in ppm and are referenced to the residual non-deuterated solvent peak. Normal phase column chromatography was carried out on silica gel 60 (230–400 mesh). Analytical reverse-phase high-performance liquid chromatography (RP–HPLC) was performed on an Agilent 1100 system equipped with a Phenomenex Kinetex® 5 µm XB-C18 100 Å LC Column (50 × 4.6 mm) with a flow rate of 1 mL/min. A gradient of H_2O/CH_3CN (95/5) to H_2O/CH_3CN (5/95) with 0.1% HCOOH, over 6 min, holding at 95% CH_3CN for 3 min, followed by 1 minutes isocratic elution with detection at 254 nm and by evaporative light scattering.

Semi-preparative RP–HPLC was performed on an Agilent 1100 system equipped with a Zorbax Eclipse XDB-C18 reverse-phase column (250 mm × 10 mm, 5 µm) with a flow rate of 2 mL/min and eluting with a gradient of H_2O/CH_3CN (95/5) to H_2O/CH_3CN (5/95) with 0.1% HCOOH, over 20 min.

Electrospray ionization mass spectrometry (ESI–MS) analyses were carried out on an Agilent Technologies LC/MSD Series 1100 quadrupole mass spectrometer (QMS). High Resolution MS were performed on a Bruker microTOF focus II mass

spectrometer. Plate-reader measurements were performed on a Biotek Synergy HT multi-mode reader. Absorbance spectrometry was performed on an Agilent 8453 absorbance spectrometer.

Automated Column chromatography was performed on the Biotage® Isolera™ One Flash system. Microwave reactions were performed in a Biotage® Initiator+ microwave reactor.

Bacterial Cell Culture

Microbial cultures (Bacillus Subtilis (Ehrenberg) Cohn 6051 and Escherichia coli DH5α were grown from single colonies on agar plates and incubated overnight at 37 °C in nutrient media or Luria Bertani liquid medium (10 mL) respectively in a shaking incubator at 37 °C. The overnight cultures (late-log phase) were centrifuged at 6000 rpm for 3 minutes and the pellet washed (2x) into phosphate buffered saline (PBS) and adjusted to the required OD_{600} .

Confocal Fluorescence Microscopy

μ-Slide 15-well glass bottom confocal chambers (Ibidi) were coated with poly-D-lysine (50 μL, 0.1 mg mL^{-1} in PBS) for 20 minutes at 37 °C, after which the wells were washed with PBS. The prepared samples in the slide chambers were imaged on a Leica SP5 confocal microscope (excitation: 561 nm, 20%, HyD detector: 570–600 nm with gain 100, bright field PMT trans-detector with 200 gain). HCX PLAPO 100x oil immersion objective lens was used and zoom set to 2x. Fluorescence signal captured with Leica HyD detector. Digital acquisition of images was done using a Leica LAS-AF.

Concentration Optimisation and Off-target-labelling

Individual aliquots of 200 μL of bacteria culture (*E. coli / B. subtilis*) was prepared in PBS at a concentration of 0.5 OD_{600} in Eppendorf tubes and **12** was added to each to achieve final concentrations of 0-50 μM. The tubes were vortexed for 1 minute before placing in a shaking incubator set at 37 °C for 1 hour. After incubation the tubes were centrifuged (6000 rpm, 3 minutes), the supernatants were removed, and the pellets re-suspended in 200 μL of PBS by pipette aspiration. 2 μL of a 1 mg/mL stock solution of Streptavidin-555 (iFluor™ 555-streptavidin conjugate, Stratech 16989-AAT) was added to each tube and vortexed for 2 minutes before moving to a shaking incubator at 37 °C for 30 minutes. A final washing step (3 x 6000 rpm, 3 minutes, 200 μL PBS) removed unbound streptavidin before addition of a 50 μL aliquot to the poly-D-lysine coated slide chamber. The slide was incubated in a plate incubator at 37 °C for 30 minutes for the bacteria to attach to the surface. The excess solution was then removed and the slide was washed (2x) with PBS before drying and imaging.

Incubation Time Optimisation

1000 μL of bacteria culture (*E. coli / B. subtilis*) was prepared in PBS at a concentration of 0.5 OD_{600}. Compound **12** was added to a final concentration of 10 μM. At each time point, 200 μL of this mixture was removed and subjected to the same labelling protocol described in the concentration optimisation experiment (but with the incubation time with streptavidin being reduced from 30 to 5 minutes).

Microscopy Image Analysis

Quantitative analysis was based on the corrected total cell fluorescence method described by McCloy et al.[269] images were analysed by Image J (using the plug-in Fiji, National Institutes of Health). To perform this analysis, 15 bacteria distributed over the area of interest were selected and their fluorescence intensity measured. Background correction was done by finding an average background fluorescence intensity using 15 random spots without bacteria and subtracting this from each bacteria fluorescence intensity measurement. The background corrected bacteria fluorescence intensity was then averaged to provide a mean fluorescence intensity and to calculate standard deviations.

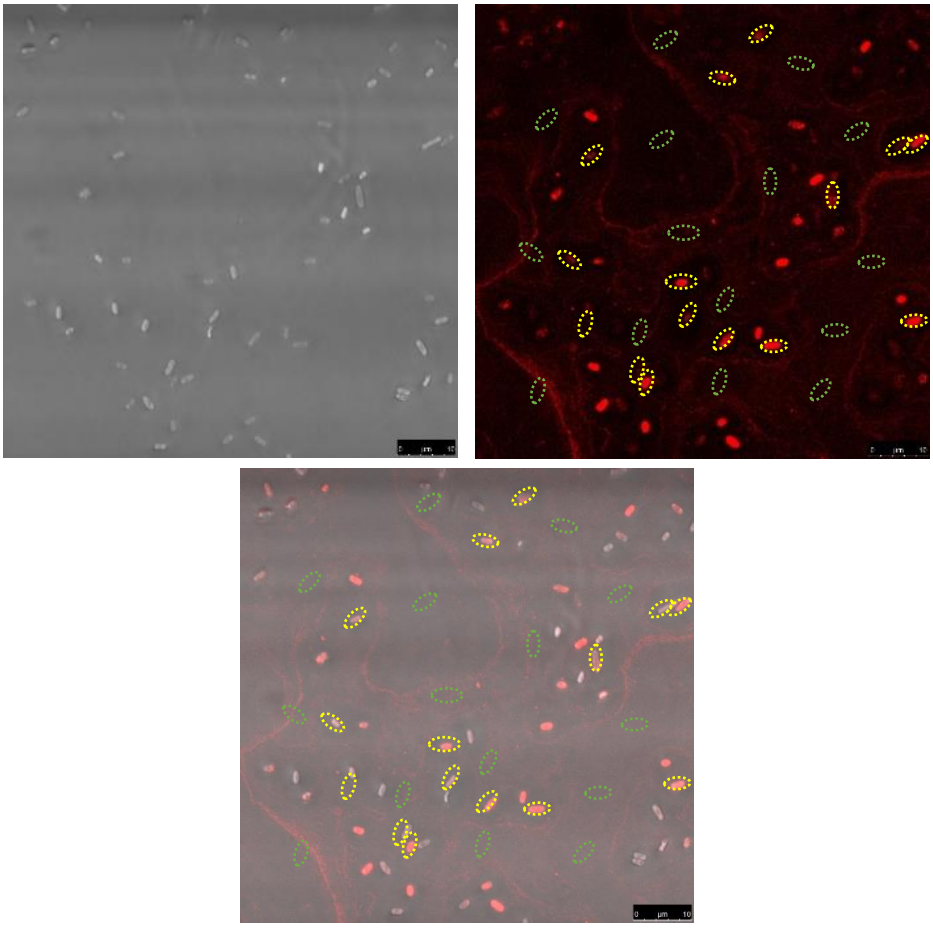

Figure 108: Example of analysis selection of 15 random bacteria (yellow) and 15 random positions of background (Green) that were used for ImageJ analysis. Images shown are the brightfield (left) and the fluorescence (right) on which the analysis was done. A merged image shows where bacteria were

non/weakly fluorescent were also included to make sure that selection was representative of the whole population.

HABA - Streptavidin Assay

HABA stock solution was prepared (10 mM in water) and adjusted to pH 9 with 1N NaOH prior to the experiment. Streptavidin (*Streptavidin from Streptomyces avidinii*, Sigma-Aldrich S4762) was assumed to be 100% pure 66kDa protein with 4 binding sites available and used as received.

Streptavidin was diluted to 0.5 mg/mL in PBS (485 µL, 7.6 µM) and saturated with HABA (15 µL, 10 mM) for 15 minutes to generate a HABA-Streptavidin complex 'test solution'. 45 µL (7.4 µM Streptavidin, 0.3 mM HABA) of this test solution was added into the well of a 96 well plate before the addition of Biotin or **9** (5 µL, 0.5 mM) and mixed via pipette aspiration (3x) before the absorbance spectra were measured on a plate reader.

2 Polymyxin Nonapeptide (PMBN)

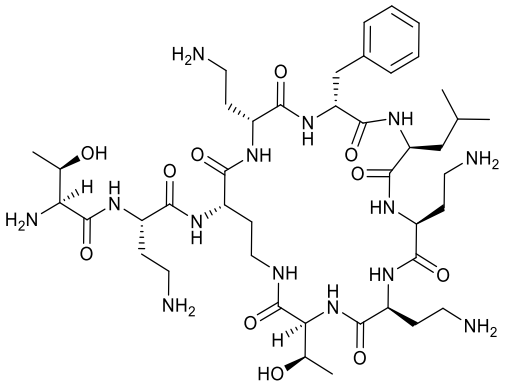

2

The synthetic procedure was performed as described in literature.[138] Thus, polymyxin B sulfate (10 g) and Papain (1.2 g) were added to deionized water (250 mL) and toluene (2 mL). The mixture was heated to 55 °C and stirred until both components were fully dissolved (10 minutes). The flask was loosely stoppered, and gently stirred at 55 °C overnight. The stirring was increased, and the temperature raised to 100 °C for 30 minutes to denature the papain which precipitated from the solution. This precipitate was removed by centrifugation followed by filtration through filter paper. The filtrate was concentrated in vacuo and lyophilised yielding a crude mixture of compound **2** (7.4 g) as an off-white powder which was used in the next step without further purification.

HPLC $t_{R\ (ELSD)}$ 0.71 min. LCMS (ESI+) calc. $C_{43}H_{74}N_{14}O_{11}$ m/z = 962.6, found m/z = 963.2 $[M+H]^+$.

3 PMBN-Boc$_4$

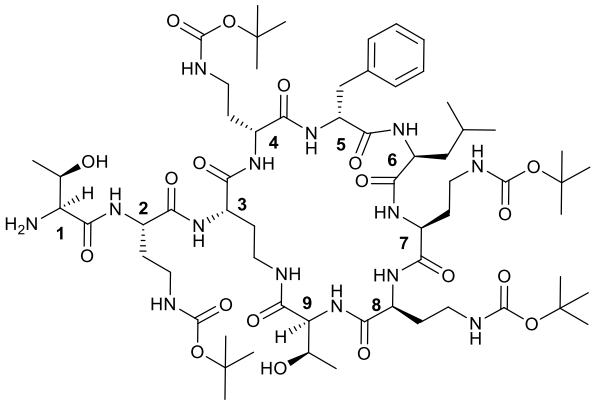

Optimised Method

Compound **2** (10 g, 7.8 mmol, 1.0 equiv.) was dissolved in a mixture of H_2O:Dioxane:Et_3N (150 mL, 1:1:1, 0.05 M) and a solution of 2-(Boc-oxyimino)-2-phenylacetonitrile (7.7g, 31 mmol, 4.0 equiv.) in dioxane (3.5 mL) was added at 24 °C. Conversion was monitored by RP-HPLC and additional aliquots of Boc-ON (0.2 g 0.77, 0.10 equiv) were added until <1% under protected material remained. Solvents were removed under reduced pressure and the crude residue was dissolved in methanol (30 mL), then filtered. The methanolic solution was added to an excess of cold diethyl ether (500 mL) and the precipitated PMBN–Boc$_4$ was isolated via filtration. Crude PMBN–Boc$_4$ was split into two equal batches and dry loaded onto silica (8 g). Then each batch was subjected to automatic flash column chromatography (silica gel, Biotage Sfär 100 g) using a gradient elution 2-10% DCM/MeOH (1% NH_3). Both batches were combined post purification to yield **3** as a beige powder (3.8 g, 37%)

HPLC $t_{R\ (ELSD)}$ 4.53 minutes LCMS (ESI+) calc. $C_{63}H_{106}N_{14}O_{19}$ m/z = 1362.8, found m/z = 1363.3 $[M+H]^+$.

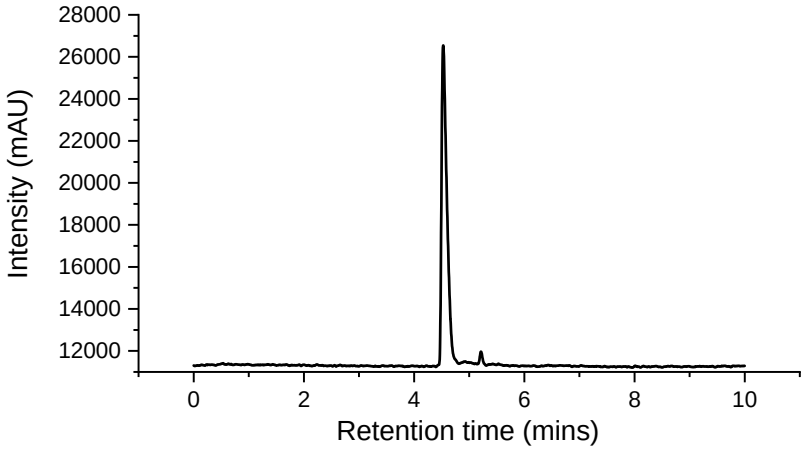

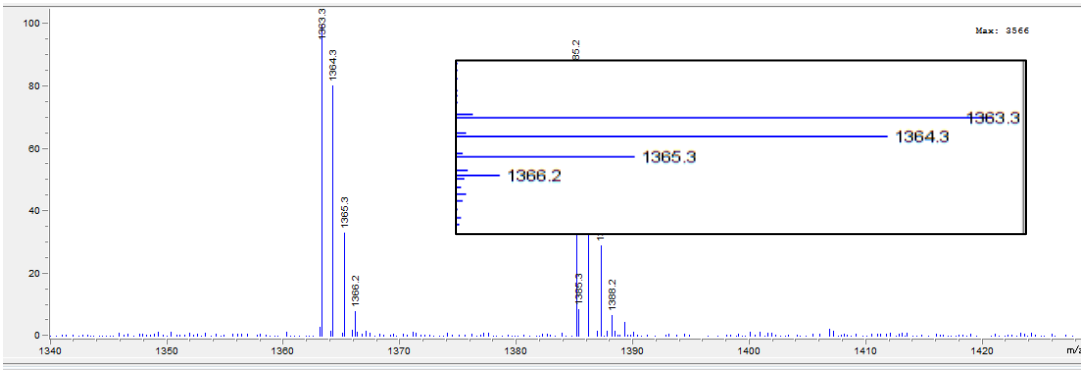

HPLC and mass spectrometry were the primary methods uses to determine compound identity and purity in line with other synthetic reports of PMBN-Boc$_4$.[182] Due to the highly overlapping nature of the amino acid protons in PMBN only a partial assignment of the NMR spectrum was performed. The key signal for the successful Boc protection was evident at 1.44 ppm. Partial assignments were based on literature studies on Polymyxin B.[270] For PMBN derivatives, comparative spectra are provided.

δ_H (500 MHz, Methanol-d_4) 7.32 – 7.20 (5 H, m, γ-Ph, 6-Phe), 4.55 (1 H, s), 4.46 – 4.38 (1 H, m), 4.35 (1 H, dd, *J* 10.2, 5.9), 4.31 – 4.23 (2 H, m), 4.16 – 4.05 (2 H, m), 4.03 (1 H, d, *J* 3.6), 3.59 – 3.49 (1 H, m), 3.35 (1 H, s), 3.29 – 3.19 (2 H, m), 3.19 – 2.91 (7 H, m), 2.22 – 2.12 (1 H, m), 2.12 – 1.95 (4 H, m), 1.94 – 1.70 (5 H, m), 1.44 (36 H, s, CH_3 Boc), 1.39 – 1.25 (2 H, m), 1.22 (3 H, d, *J* 6.4, CH3 2-Thr), 1.20 (3 H,

d, *J* 6.4, CH_3 9-Thr), 0.93 – 0.83 (2 H, m CH_2 6-Leu), 0.72 (3 H, s, CH_3 6-Leu), 0.69 – 0.62 (3 H, m, CH_3 6-Leu).

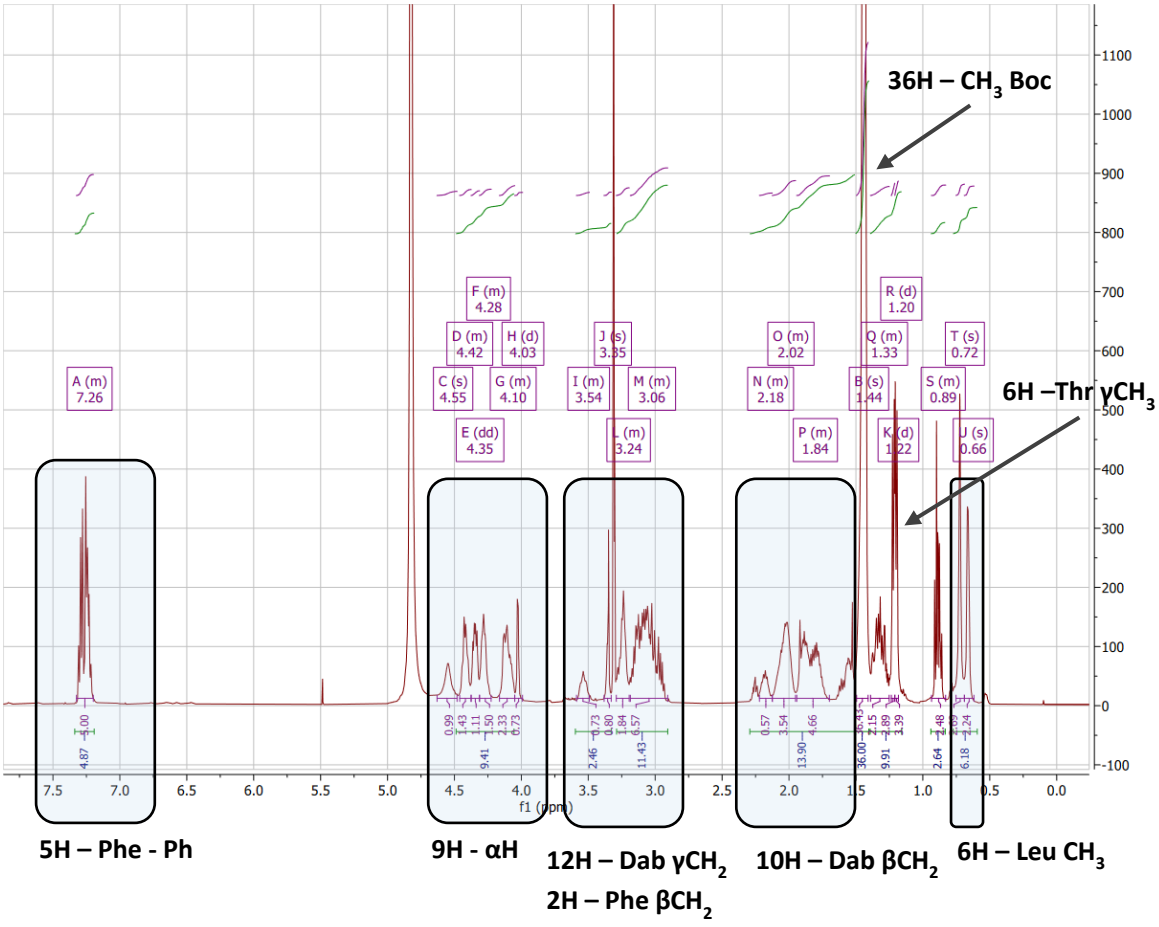

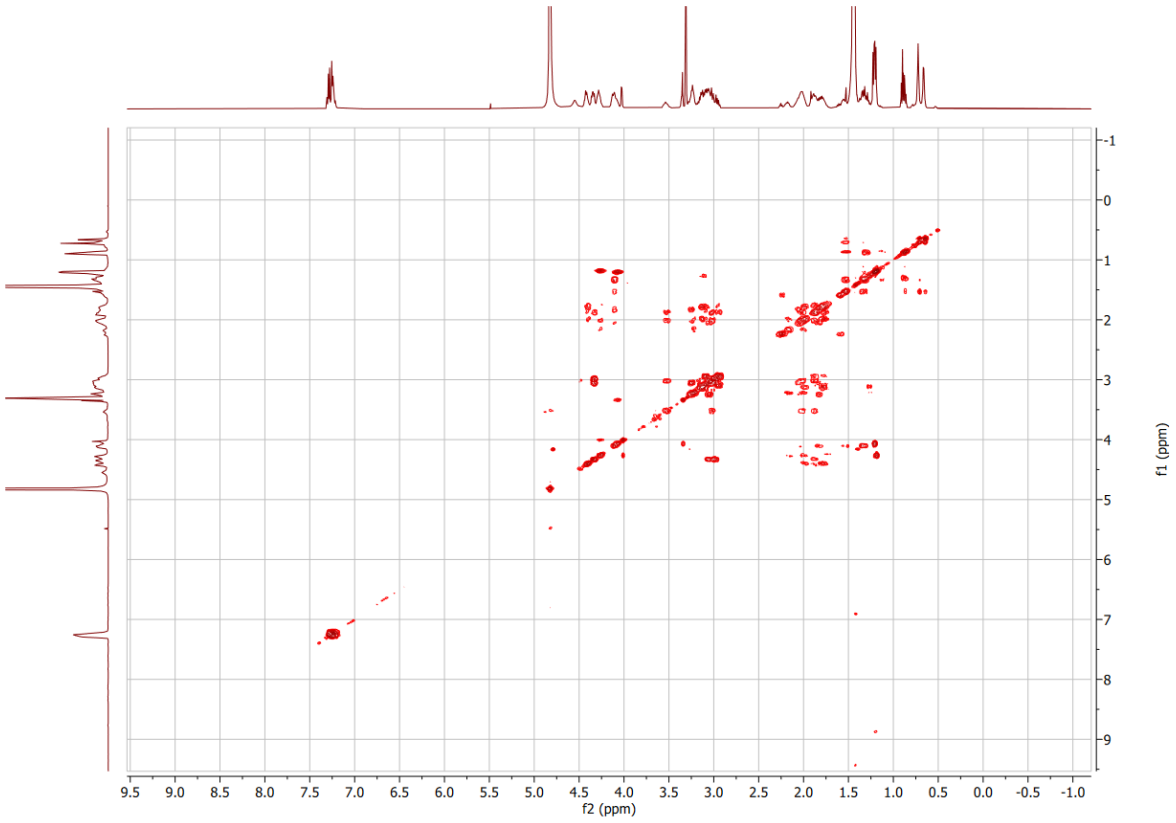

PMBN-Boc4 Synthesis Optimisation Experiments

Literature Method[182]

This method was used prior to the optimisation experiments and was used in early purification experiments (Section 3.2, Tables 1,2 Purifications A-K,)

Compound **2** (1.0 g, 0.8 mmol, 1.0 equiv.) was dissolved in a mixture of H_2O:Dioxane:Et_3N (15 mL, 1:1:1, 0.05 M) and a solution of 2-(Boc-oxyimino)-2-phenylacetonitrile (0.9 g, 3.6 mmol, 5 eq) in dioxane (3 mL) was added. The solution was stirred for 20 minutes at room temperature before being quenched with methanolic ammonia (4.0 M solution, 10 mL). Solvents were removed under reduced

pressure. The crude solid was re-dissolved in methanol and precipitated in cold Diethyl Ether (50 mL), collected and dried yielding the crude **3** product. The resulting crude was purified by chromatography on a silica gel column.

Boc-ON / Boc_2O time-dosed addition method

Compound **2** (1.0 g, 0.8 mmol, 1.0 equiv.) was dissolved in a mixture of H_2O:Dioxane:Et_3N (15 mL, 1:1:1, 0.05 M) and held at 24±1 °C. To this, a solution of 2-(Boc-oxyimino)-2-phenylacetonitrile (1.3 g, 5.3 mmol, 6 equiv.) in dioxane (4 mL), or Di-*tert*-butyl dicarbonate (1.1g, 5 mmol, 6 equiv.) in Dioxane (4.5 mL) was added to the reaction via syringe pump over the course of 4 hours. Every 30 minutes a 100 µL aliquot was taken from the reaction mixture and was subjected to a mini-work up (quenched with methanolic ammonia (4.0 M solution, 500 µL), evaporated to dryness then re-dissolved in 200 µL methanol before precipitation with cold Diethyl Ether (500 µL). The collected precipitate was dissolved in 300 µL of 1:1 H_2O:Acetonitrile). RP-HPLC / LCMS monitoring was performed with the standard elution method using a 30 µL injection. Once the dosing of respective Boc-reagent was complete, the reaction was left stirring overnight with an ‘overnight’ aliquot taken 12 hours after dosing was finished.

Identification of PMBN-Boc$_X$

LCMS was used to identify each of the peaks seen in HPLC analysis. Peak masses were matched to the corresponding PMBN-Boc$_X$ species however the exact structural isomers present were not individually characterised.

PMBN-Boc$_1$

LCMS 3.0 – 3.3 minutes (ESI+) calc. $C_{48}H_{82}N_{14}O_{13}$ m/z = 1063.3, found m/z = 1063.5 $[M]^+$.

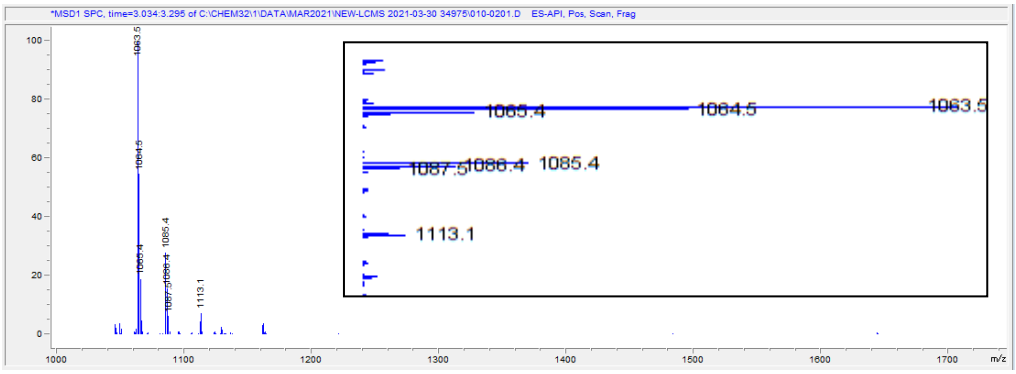

PMBN-Boc$_2$

LCMS 3.5 – 3.8 minutes (ESI+) calc. $C_{53}H_{90}N_{14}O_{15}$ m/z = 1163.4, found m/z = 1163.5 [M+].

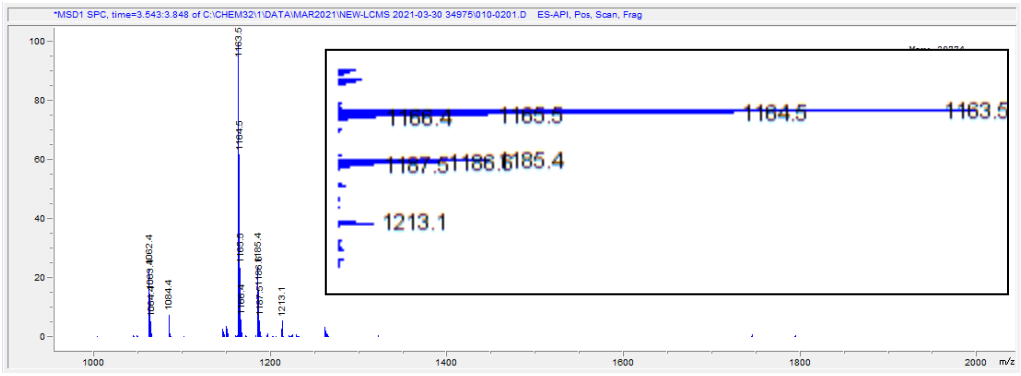

PMBN-Boc$_3$

LCMS 4.1 – 4.3 minutes (ESI+) calc. $C_{58}H_{98}N_{14}O_{17}$ m/z = 1263.5, found m/z = 1263.8 $[M]^+$.

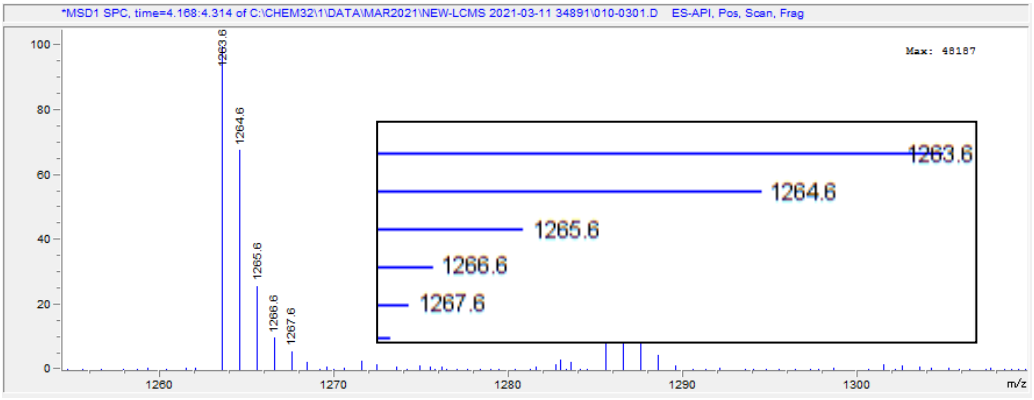

PMBN-Boc$_5$

LCMS 6.3 – 6.8 minutes (ESI+) calc. $C_{68}H_{114}N_{14}O_{21}$ m/z = 1463.7, found m/z = 1463.7 $[M]^+$.

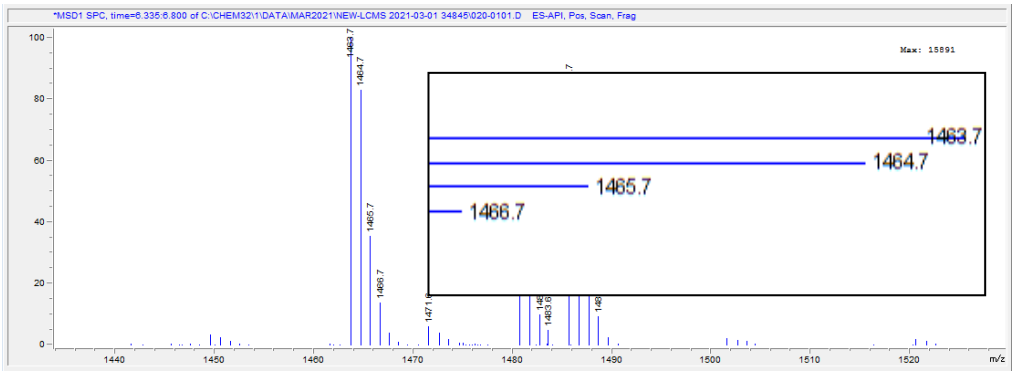

CF2

LCMS 5.7 – 5.9 minutes (ESI+) calc. $C_{18}H_{34}N_2O_5$ m/z = 358.5, found m/z = 357.3 [M-H]

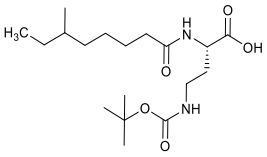

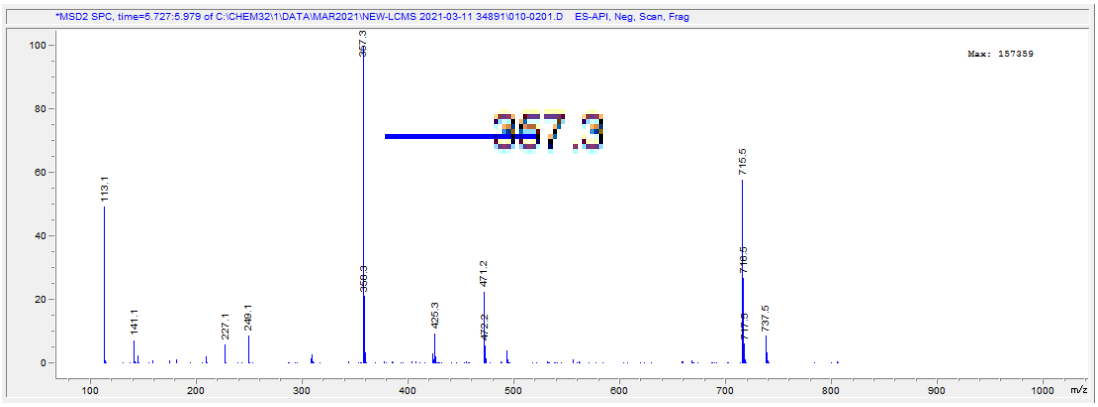

CF1

LCMS 5.4 – 5.6 minutes (ESI+) calc. $C_{17}H_{32}N_2O_5$ m/z = 344.5, found m/z = 343.3 [M-H]

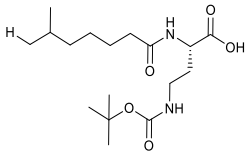

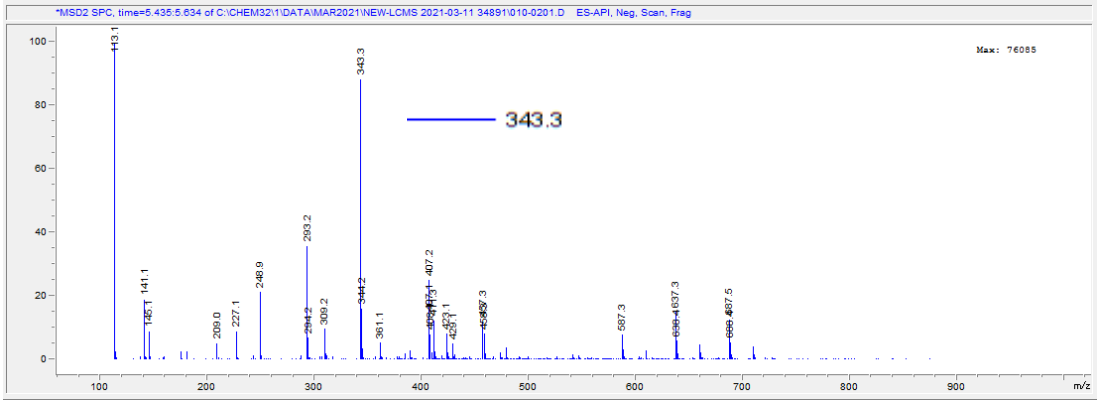

PMBN-Conjugate Synthesis

4 (3R)-*N*-hydroxysuccinimidyl liponate

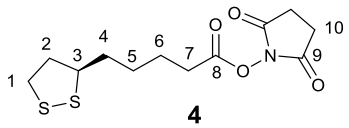

4

The synthetic procedure was performed as described in literature.[184] To a solution of (R)-(+)-α-Lipoic acid (0.995 g, 4.82 mmol, 1.0 equiv.) in acetonitrile (75 mL), *N*-hydroxysuccinimide (0.790 g, 6.89 mmol, 1.4 equiv.) and 1-ethyl-3-(3-dimethylaminopropyl)carbodiimide hydrochloride (1.22 g, 6.36 mmol, 1.3 equiv.) were added and the reaction was stirred overnight at 20 °C. The solvent was evaporated under reduced pressure and the residue was dissolved in dichloromethane (100 mL). The organic phase was washed with a saturated solution of $NaHCO_3$ (100 mL) and with brine (100 mL), dried over Na_2SO_4, filtered and evaporated under reduced pressure to give compound **2** as a yellow solid (1.09 g, 74%).

HPLC $t_{R\ (ELSD)}$ 5.36 minutes LCMS (ESI+) calc. $C_{12}H_{17}NO_4S_2$ m/z = 303.39 found m/z = 304.1 $[M+H]^+$.

^{1}H NMR (500 MHz, Chloroform-*d*) 3.62 – 3.54 (1 H, m, H_3), 3.22 – 3.08 (2 H, m, H_1), 2.83 (4 H, s, H_{10}), 2.63 (2 H, t, *J* = 7.4 Hz, H_7), 2.50 – 2.43 (1 H, m, H_{2a}), 1.97 – 1.88 (1 H, m, H_{2b}), 1.83 – 1.74 (2 H, m, H_6), 1.74 – 1.66 (2 H, m, H_5), 1.63 – 1.51 (2 H, m, H_4).

^{13}C NMR (126 MHz, Chloroform-*d*) δ 169.1, 168.4, 56.1, 40.2, 38.5, 34.4, 30.8, 28.3, 25.6, 24.4.

Analytical data were in accordance with the published literature. [184]

5 Lipoic acid-PMBN-Boc$_4$

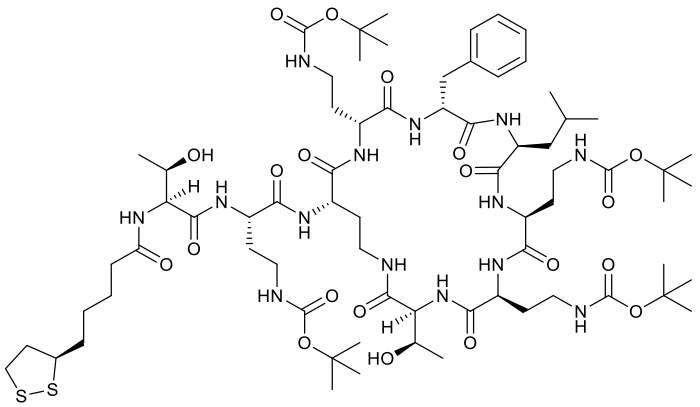

5

To a solution of **3** (117 mg, 0.085 mmol, 1 equiv.) in DMF (1.5 mL) was added **4** (20 mg, 0.094 mmol, 1.1 equiv.) and DIPEA (17 µL, 0.10 mmol, 1.2 equiv.). The reaction mixture was stirred at room temperature overnight and monitored via RP-HPLC until conversion stopped. Cold water (10 mL) was added to precipitate the crude product which was collected by filtration and purified by column chromatography (silica gel) eluting with DCM with MeOH (5%) yielding compound **11** (95 mg, 81%) as a beige solid.

HPLC $t_{R\ (ELSD)}$ 6.31 min. HRMS (ESI+) calc. $C_{71}H_{118}N_{14}O_{20}S_2$ m/z = 1551.8161 found m/z = 1551.8159 $[M+H]^+$.

δ_H (601 MHz, Methanol-d_4) 7.28 – 7.17 (5 H, m), 4.43 – 4.17 (8 H, m), 4.11 – 4.07 (2 H, m), 4.00 (1 H, d, *J* 3.5), 3.73 – 3.66 (1 H, m), 3.65 – 3.45 (3 H, m), 3.29 – 2.83 (7 H, m), 2.64 (5 H, s), 2.48 – 2.38 (1 H, m), 2.37 – 2.26 (2 H, m), 2.27 – 2.09 (1 H, m), 2.02 – 1.97 (3 H, m), 1.90 – 1.47 (8 H, m), 1.40 (36 H, s), 1.36 – 1.21 (7 H, m), 1.20 – 1.07 (6 H, m), 0.89 – 0.80 (2 H, m), 0.69 (3 H, s), 0.63 (3 H, d, *J* 5.2).

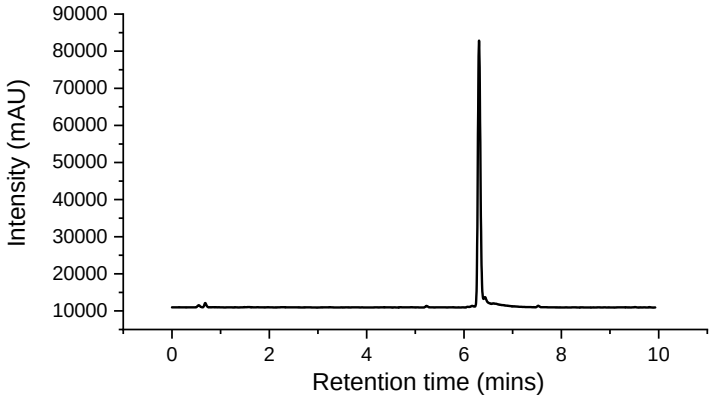
Intensity (mAU)
90000
80000
70000
60000
50000
40000
30000
20000
10000
0
2
4
6
8
10
Retention time (mins)

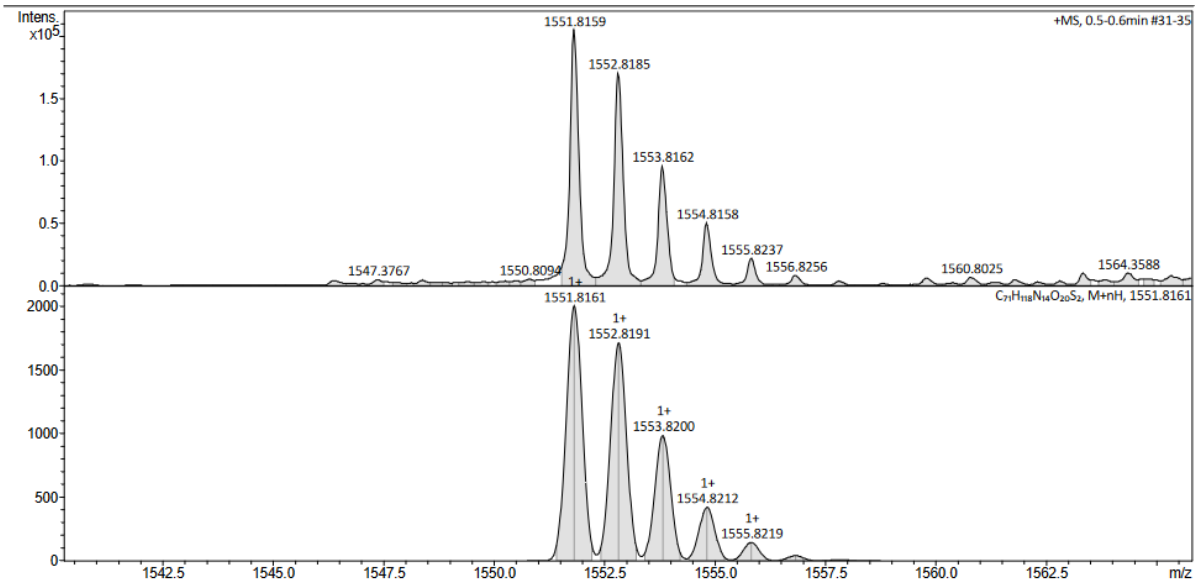
Intens.
x10^5
1.5
1.0
0.5
0.0
1551.8159
1552.8185
1553.8162
1554.8158
1555.8237
1556.8256
1547.3767
1550.8094
1560.8025
1564.3588
1+
+MS, 0.5-0.6min #31-35
1551.8161
C71H118N14O20S2, M+nH, 1551.8161
2000
1500
1000
500
0
1+
1552.8191
1+
1553.8200
1+
1554.8212
1+
1555.8219
1542.5
1545.0
1547.5
1550.0
1552.5
1555.0
1557.5
1560.0
1562.5
m/z

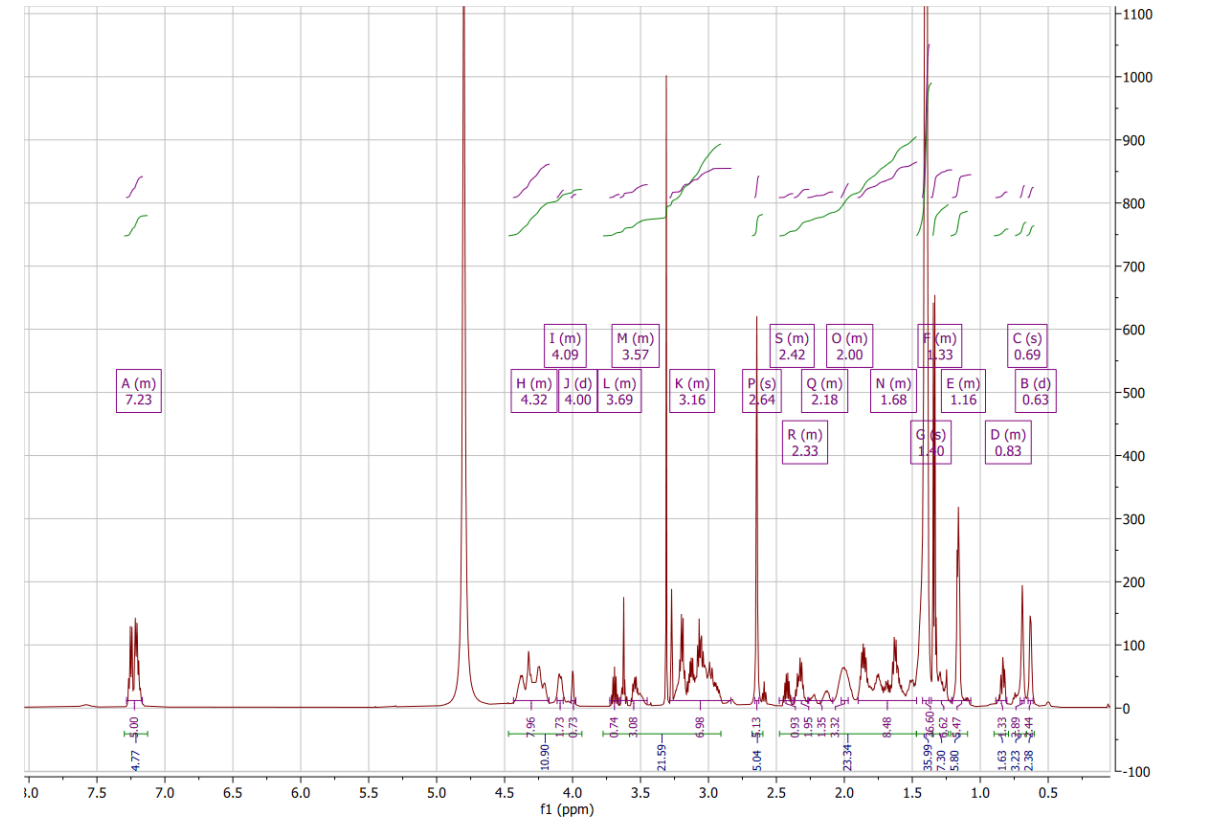
A (m) 7.23
I (m) 4.09
M (m) 3.57
H (m) 4.32
J (d) 4.00
L (m) 3.69
K (m) 3.16
P (s) 2.64
S (m) 2.42
O (m) 2.00
Q (m) 2.18
R (m) 2.33
N (m) 1.68
F (m) 1.33
E (m) 1.16
G (s) 1.00
C (s) 0.69
B (d) 0.63
D (m) 0.83
f1 (ppm)

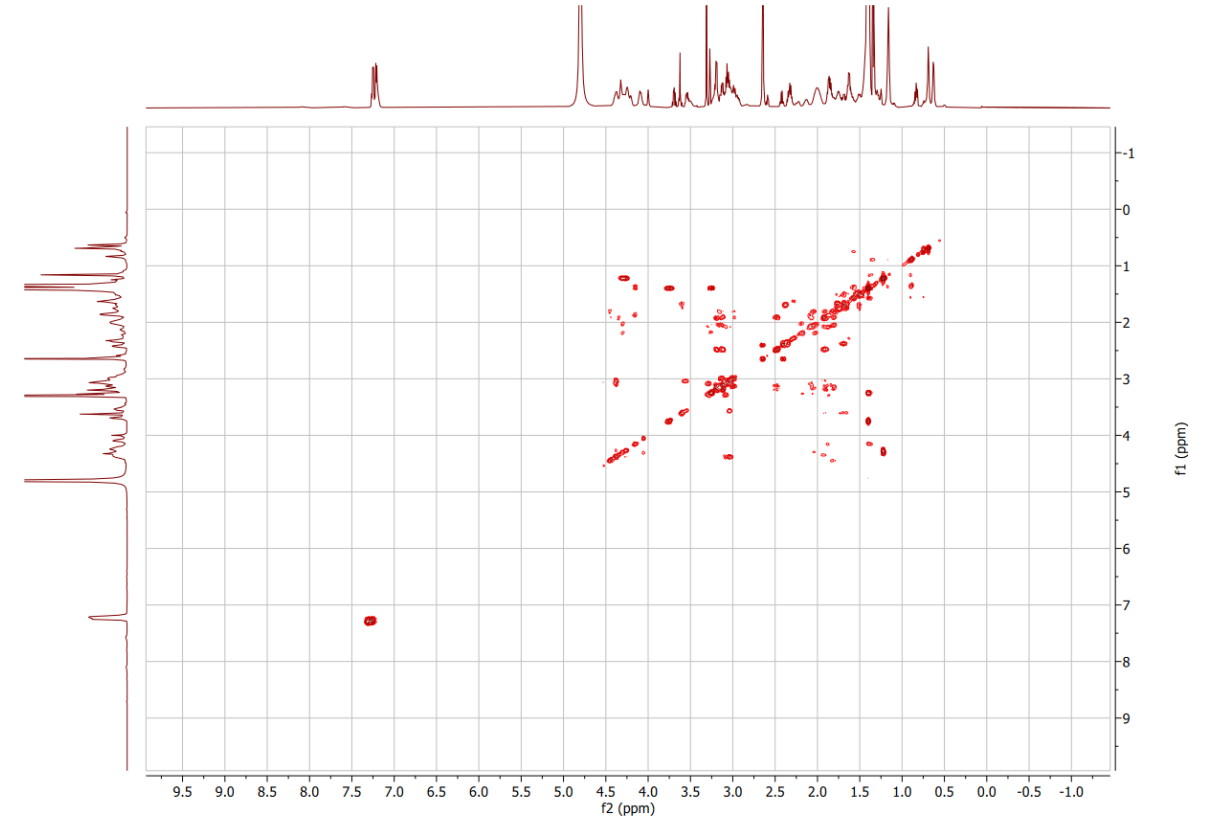
f2 (ppm)
f1 (ppm)

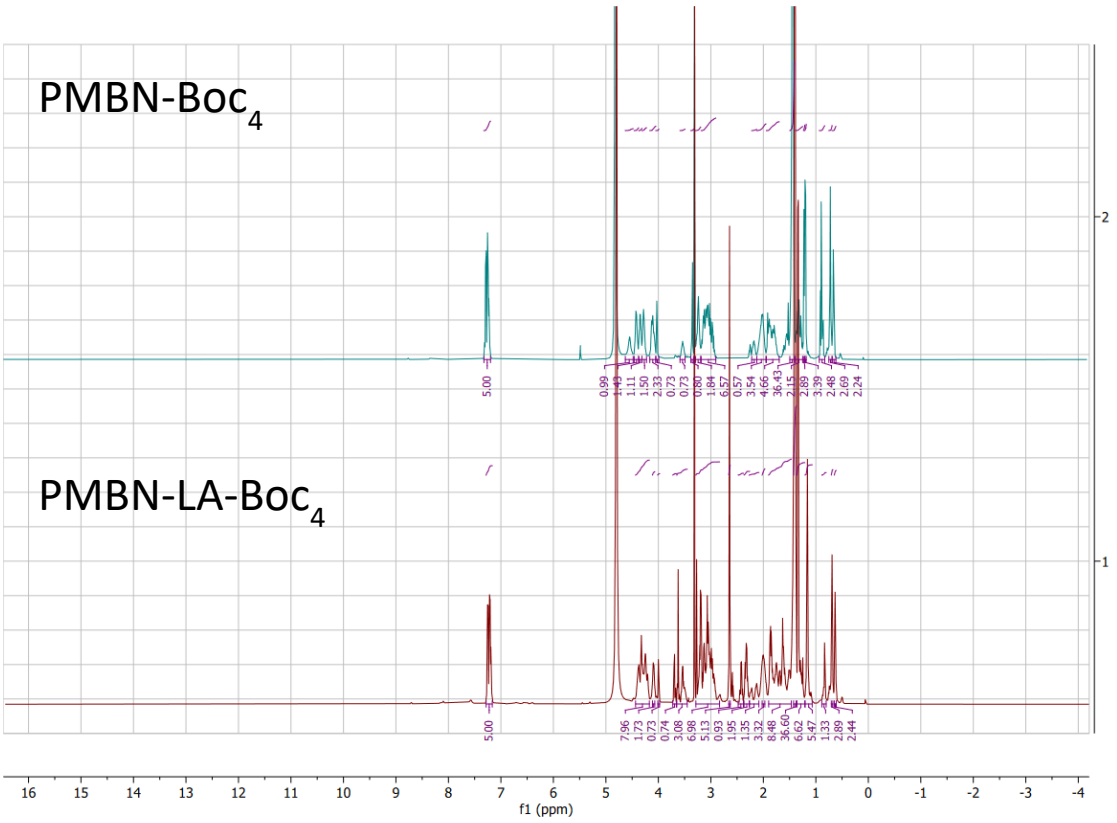
PMBN-Boc4
PMBN-LA-Boc4
f1 (ppm)

6 Lipoic Acid-PMBN

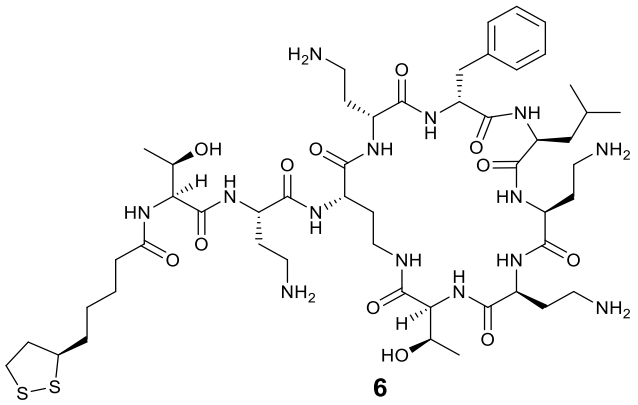

6

To compound **12** (94 mg, 0.59 mmol) in DCM (4 mL), was added of a 20% solution of TFA in DCM (10 mL). The mixture was stirred for 2 h before concentration under vacuum. The resulting oil was treated with water (2 mL) then lyophilised to yield compound **13** as a TFA salt (94 mg, 100%) as a white powder.

HPLC $t_{R\ (ELSD)}$ 10.96 minutes HRMS (ESI+) calc. $C_{51}H_{86}N_{14}O_{12}S_2$ m/z = 1151.6064, found m/z = 1151.6060 $[M+H]^+$.

δ_H (601 MHz, Deuterium Oxide) 7.37 – 7.18 (5 H, m), 4.55 (1 H, t, *J* 8.3), 4.46 – 4.41 (1 H, m), 4.32 – 4.10 (4 H, m), 3.68 – 3.62 (1 H, m), 3.33 – 2.99 (13 H, m), 2.96 (1 H, s), 2.84 – 2.79 (4 H, m), 2.73 (2 H, s), 2.67 – 1.67 (9 H, m), 1.63 – 1.55 (4 H, m), 1.48 – 1.34 (4 H, m), 1.30 – 1.26 (1 H, m), 1.25 – 1.20 (1 H, m), 1.20 – 1.13 (6 H, m), 0.84 (1 H, s), 0.73 (3 H, d, *J* 6.6), 0.66 (3 H, d, *J* 6.5).

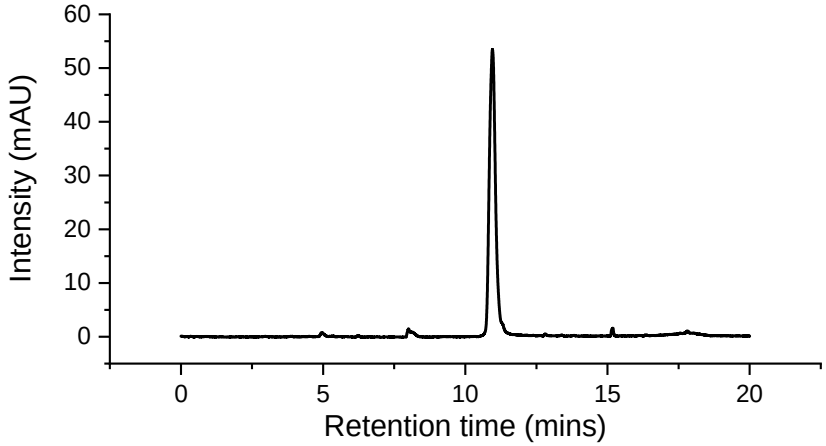
Intensity (mAU)
Retention time (mins)

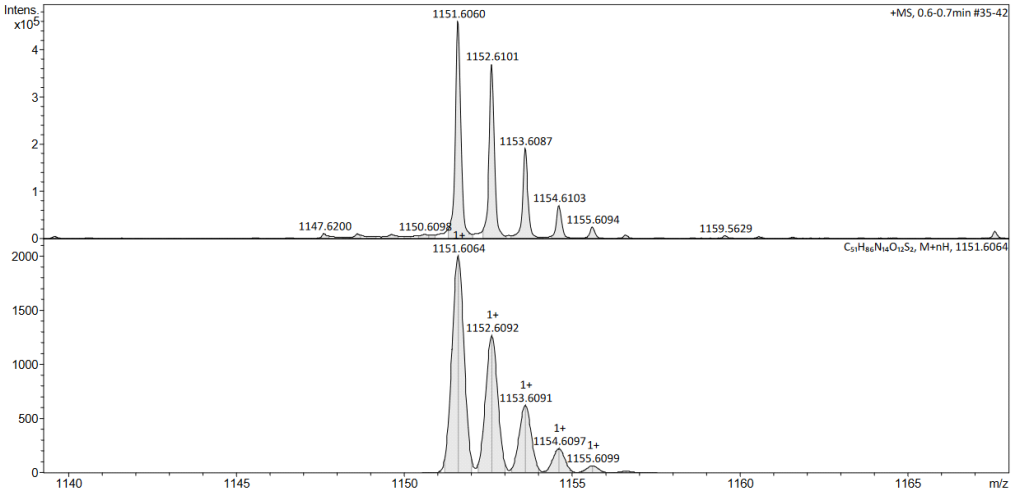
Intens.
x10^5
1151.6060
1152.6101
1153.6087
1154.6103
1155.6094
1147.6200
1150.6098
1159.5629
+MS, 0.6-0.7min #35-42
1+
1151.6064
C51H86N14O12S2, M+nH, 1151.6064
1+
1152.6092
1+
1153.6091
1+
1154.6097
1+
1155.6099
m/z

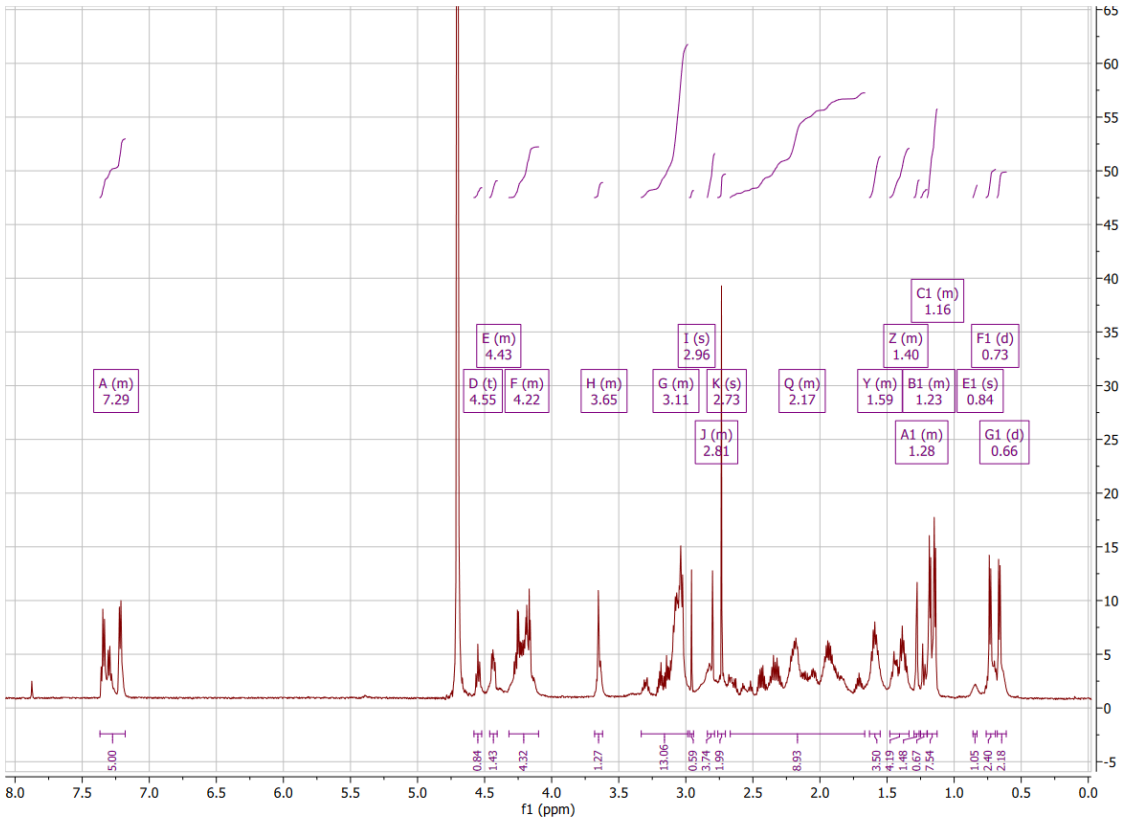
A (m) 7.29
E (m) 4.43
D (t) 4.55
F (m) 4.22
H (m) 3.65
I (s) 2.96
G (m) 3.11
K (s) 2.73
J (m) 2.81
Q (m) 2.17
C1 (m) 1.16
Z (m) 1.40
Y (m) 1.59
B1 (m) 1.23
A1 (m) 1.28
F1 (d) 0.73
E1 (s) 0.84
G1 (d) 0.66
f1 (ppm)

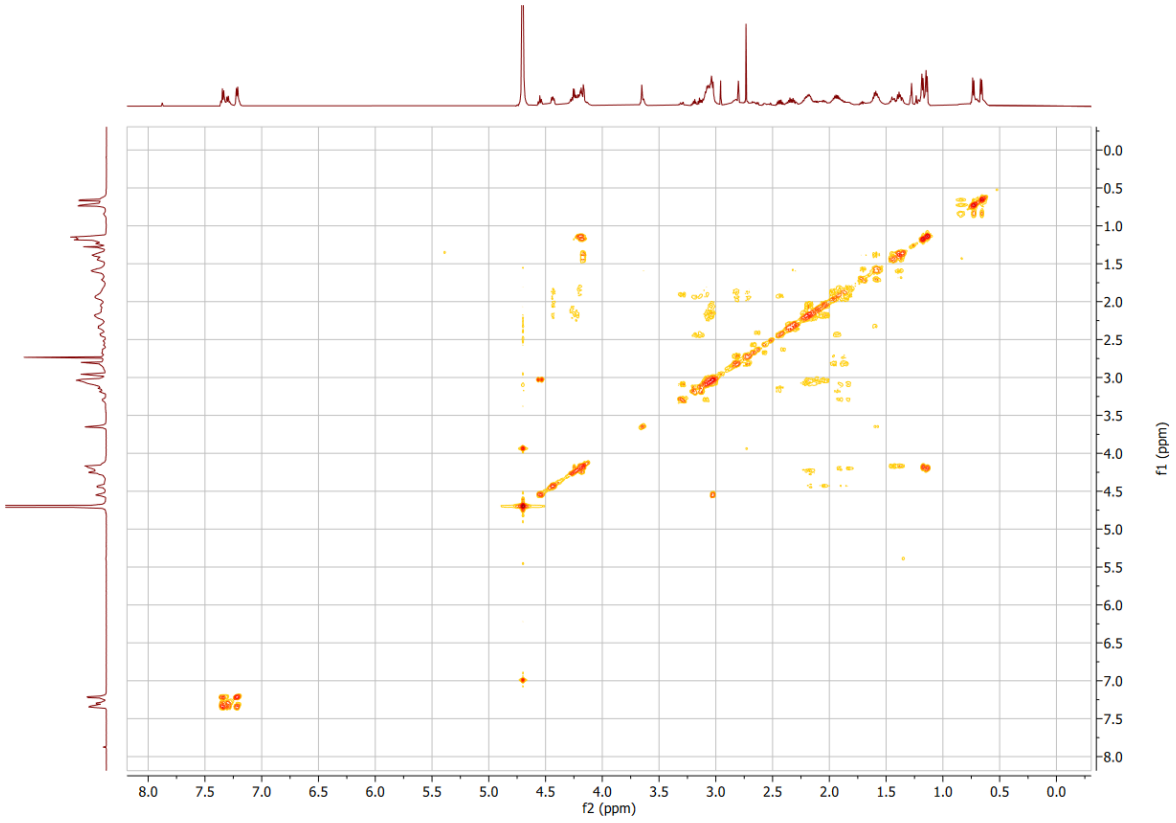
f2 (ppm)
f1 (ppm)

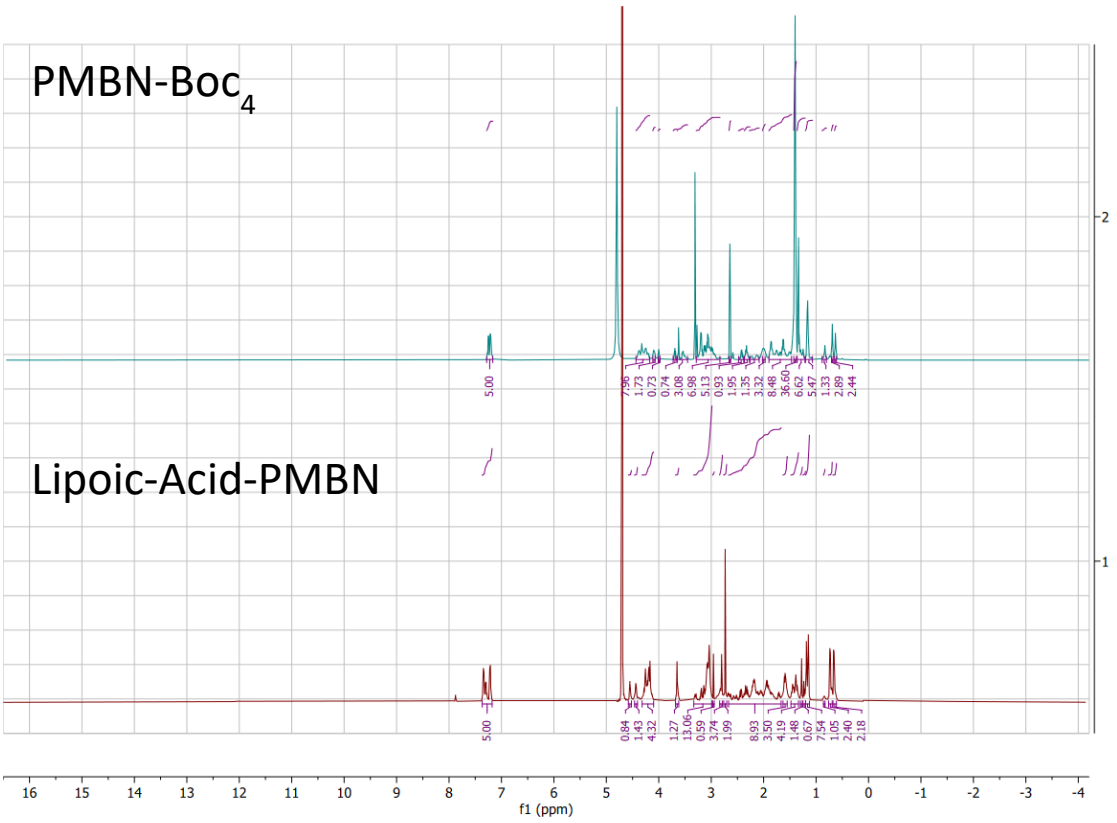
PMBN-Boc4
Lipoic-Acid-PMBN
f1 (ppm)

8 Biotin-PMBN-Boc$_4$

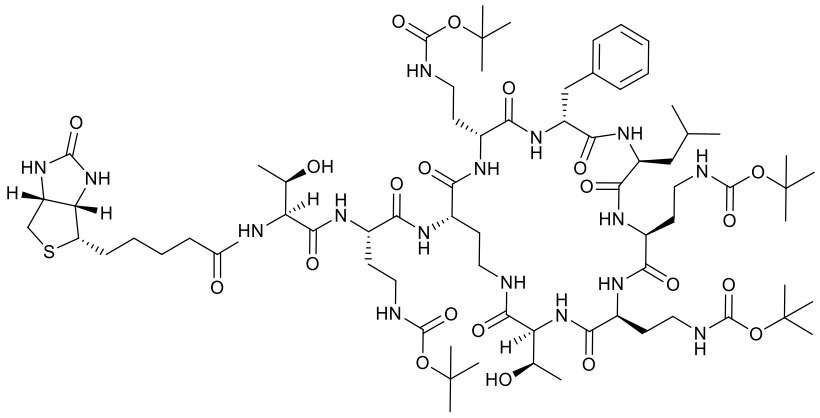

8

(+)-Biotin *N*-hydroxysuccinimide ester (**7**) (20 mg, 0.055 mmol, 1.5 equiv.) and Et_3N (5 µL, 0.040 mmol, 1.1 equiv.) were dissolved in DMF (3 mL) and stirred for 1 min. PMBN-Boc$_4$ (50 mg, 0.036 mmol, 1.0 equiv.) was added and the reaction mixture was stirred at room temperature overnight. The reaction solvent was removed in vacuo and the resulting solid was subjected to silica gel column chromatography (DCM/MeOH) yielding **8** as an off white solid (32 mg, 55%)

HPLC $t_{R\ (ELSD)}$ 5.50 minutes HRMS (ESI+) calc. $C_{73}H_{121}N_{16}O_{21}S_1$ m/z = 1590.8686, found m/z = 1590.8677 $[M+H]^+$.

δ_H (500 MHz, Methanol-d_4) 7.33 – 7.21 (5 H, m), 4.52 – 4.47 (1 H, m), 4.46 – 4.29 (4 H, m), 4.29 – 4.23 (1 H, m), 4.17 – 4.10 (2 H, m), 4.04 (1 H, d, *J* 3.4), 3.29 – 3.20 (1 H, m), 3.17 – 2.89 (6 H, m), 2.75 – 2.61 (2 H, m), 2.44 – 2.32 (2 H, m), 2.20 – 1.96 (3 H, m), 1.96 – 1.52 (7 H, m), 1.46 – 1.43 (36 H, m), 1.37 – 1.27 (3 H, m), 1.23 – 1.17 (6 H, m), 0.97 – 0.81 (2 H, m), 0.72 (3 H, s), 0.66 (3 H, s).

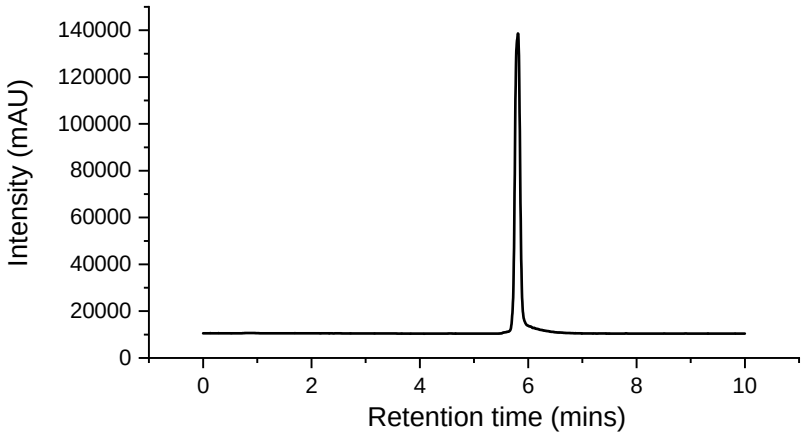
Intensity (mAU)
140000
120000
100000
80000
60000
40000
20000
0
0
2
4
6
8
10
Retention time (mins)

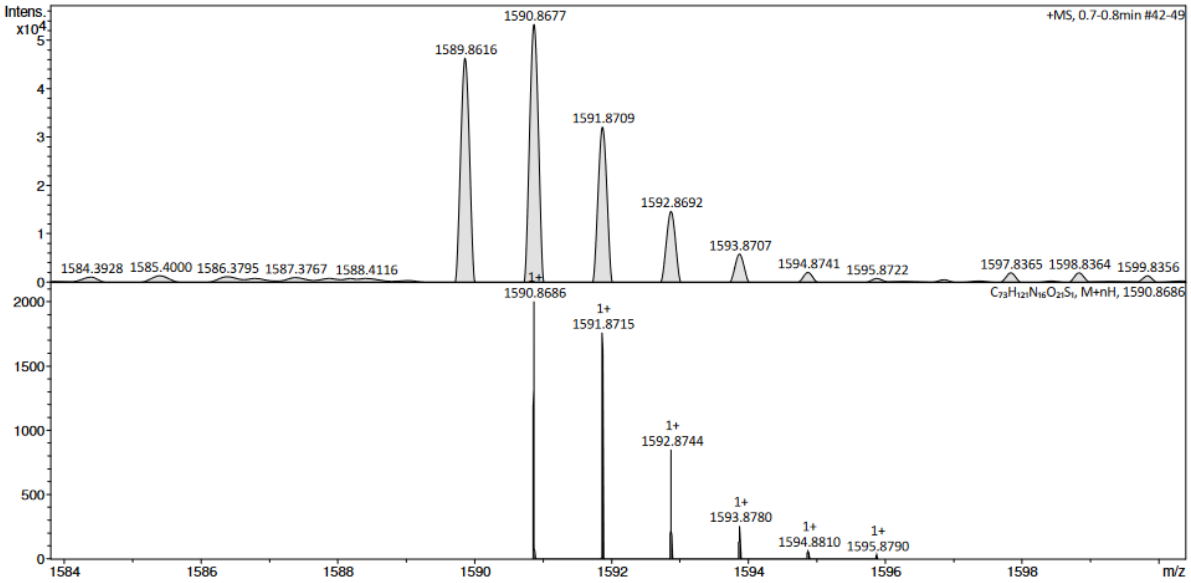
Intens.
x10^4
+MS, 0.7-0.8min #42-49
1590.8677
1589.8616
1591.8709
1592.8692
1593.8707
1594.8741
1595.8722
1584.3928
1585.4000
1586.3795
1587.3767
1588.4116
1597.8365
1598.8364
1599.8356
1+
1590.8686
C73H121N16O21S11, M+nH, 1590.8686
1+
1591.8715
1+
1592.8744
1+
1593.8780
1+
1594.8810
1+
1595.8790
m/z

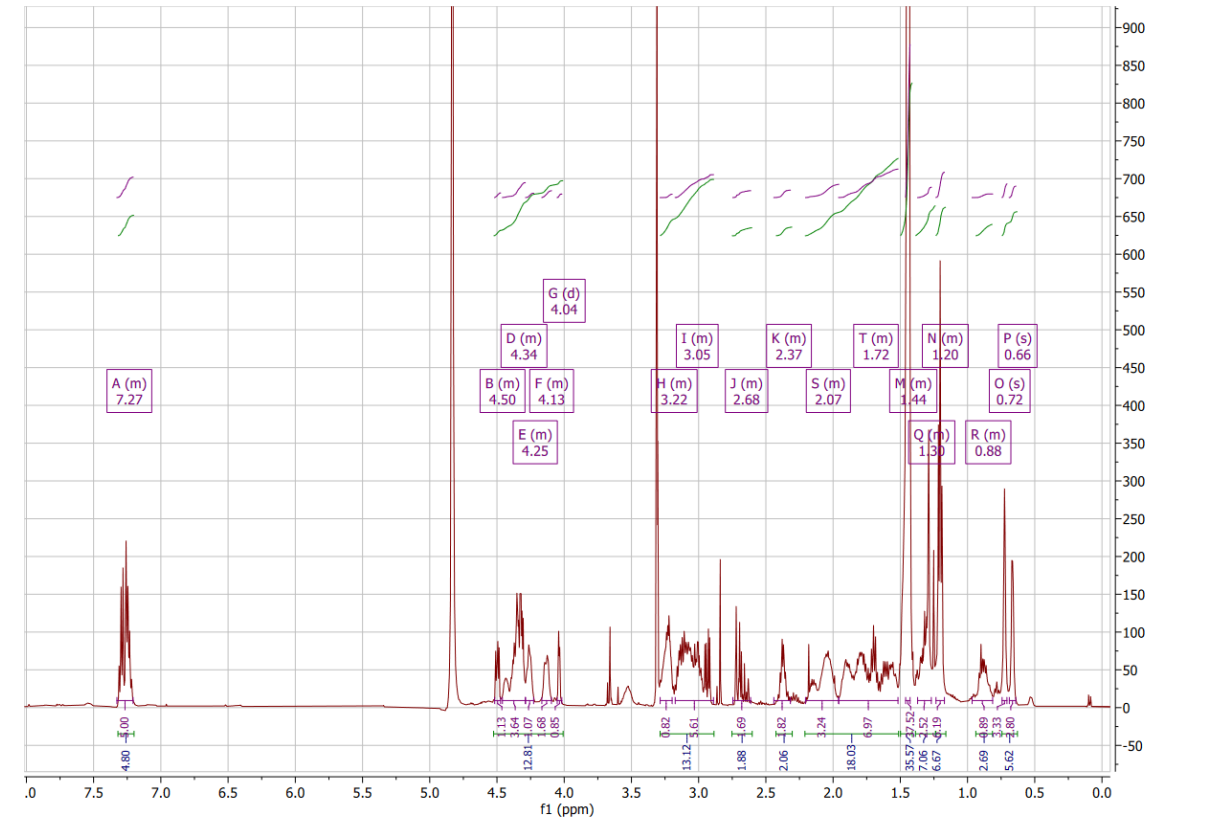
A (m)
7.27
B (m)
4.50
D (m)
4.34
E (m)
4.25
F (m)
4.13
G (d)
4.04
H (m)
3.22
I (m)
3.05
J (m)
2.68
K (m)
2.37
S (m)
2.07
T (m)
1.72
M (m)
1.44
N (m)
1.20
Q (m)
1.30
R (m)
0.88
O (s)
0.72
P (s)
0.66
f1 (ppm)

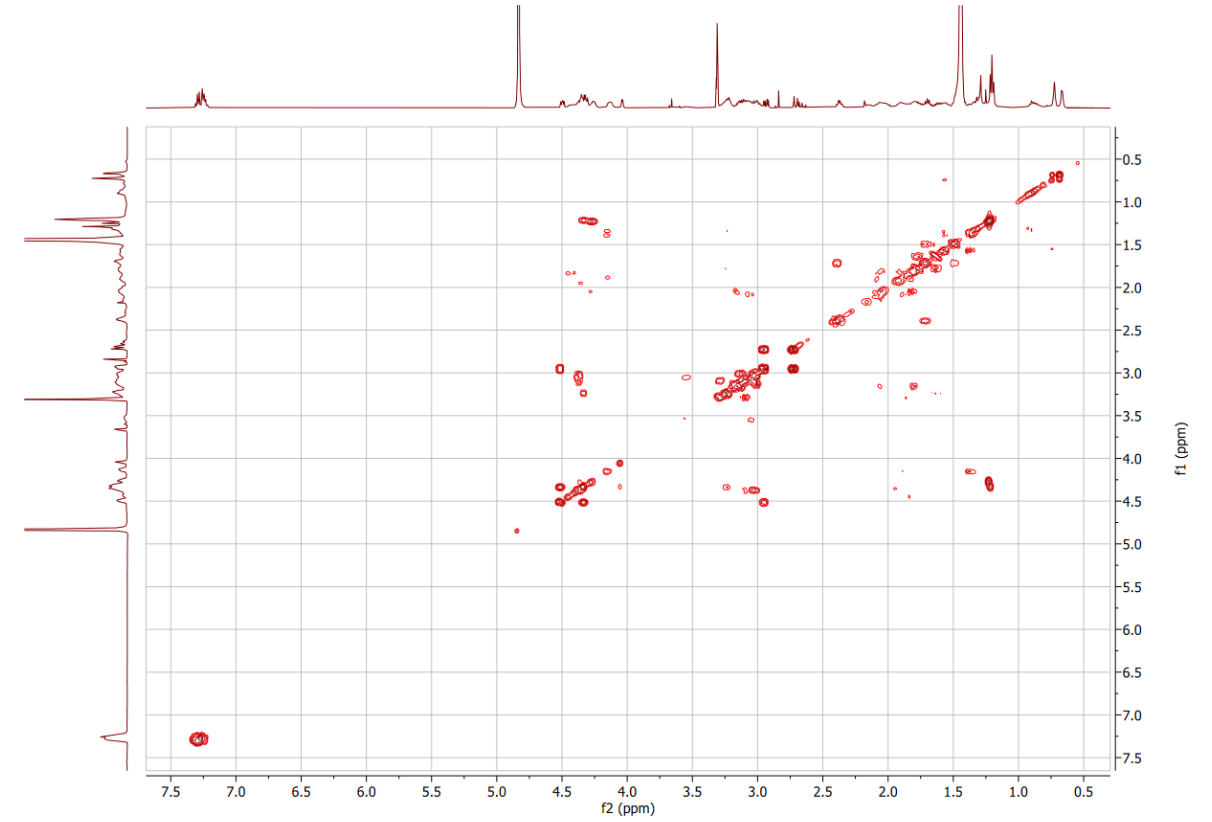
f2 (ppm)
f1 (ppm)

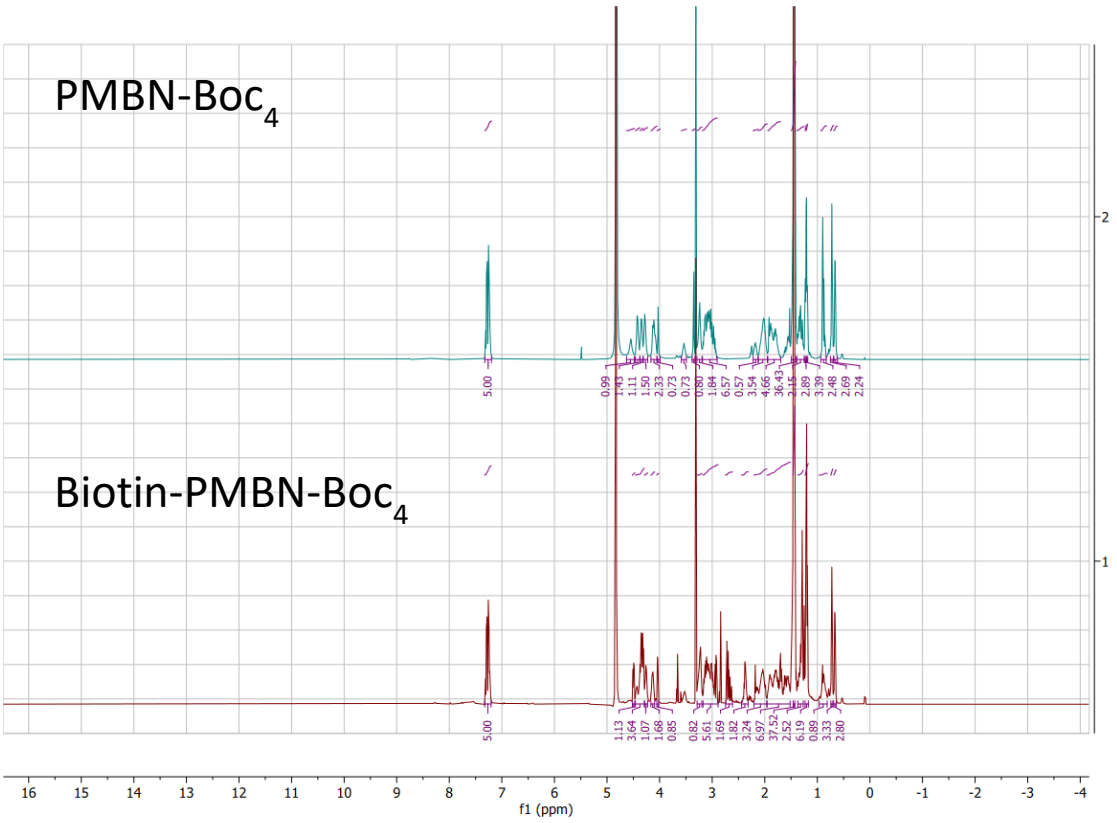
PMBN-Boc4
Biotin-PMBN-Boc4
f1 (ppm)

9 Biotin-PMBN

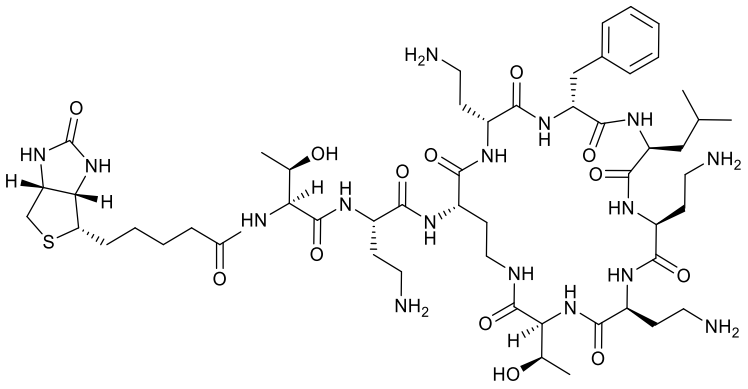

9

HCl in Diethyl Ether (2M) (5 mL) was added to **8** (32 mg, 0.020 mmol) and the reaction was stirred for 4 h. After complete deprotection of the Boc groups was observed through monitoring (RP-HPLC), excess HCl and solvent were removed through evaporation in vacuo yielding the final product as the HCl salt (26 mg 100%).

HPLC $t_{R\ (ELSD)}$ 10.05 minutes HRMS (ESI+) calc. $C_{53}H_{88}N_{16}O_{13}S_1$ m/z = 1189.6510, found m/z = 1189.6503 $[M+H]^+$.

δ_H (601 MHz, Deuterium Oxide) 7.47 – 7.26 (5 H, m), 4.66 – 4.58 (2 H, m), 4.58 – 4.50 (2 H, m), 4.48 – 4.43 (1 H, m), 4.37 – 4.25 (4 H, m), 4.27 – 4.20 (2 H, m), 3.43 – 3.33 (2 H, m), 3.26 – 3.07 (11 H, m), 3.05 – 3.00 (1 H, m), 3.00 – 2.92 (1 H, m), 2.91 – 2.85 (1 H, m), 2.83 – 2.74 (1 H, m), 2.49 – 2.35 (2 H, m), 2.35 – 2.18 (5 H, m), 2.18 – 2.06 (1 H, m), 2.05 – 1.96 (1 H, m), 1.80 – 1.58 (3 H, m), 1.54 – 1.39 (3 H, m), 1.32 – 1.17 (10 H, m), 0.78 (3 H, s), 0.73 – 0.68 (3 H, m).

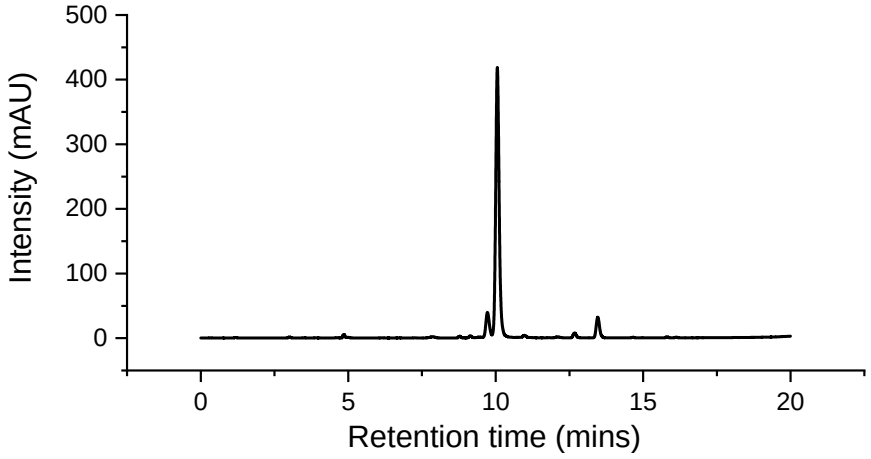
Intensity (mAU)
500
400
300
200
100
0
0
5
10
15
20
Retention time (mins)

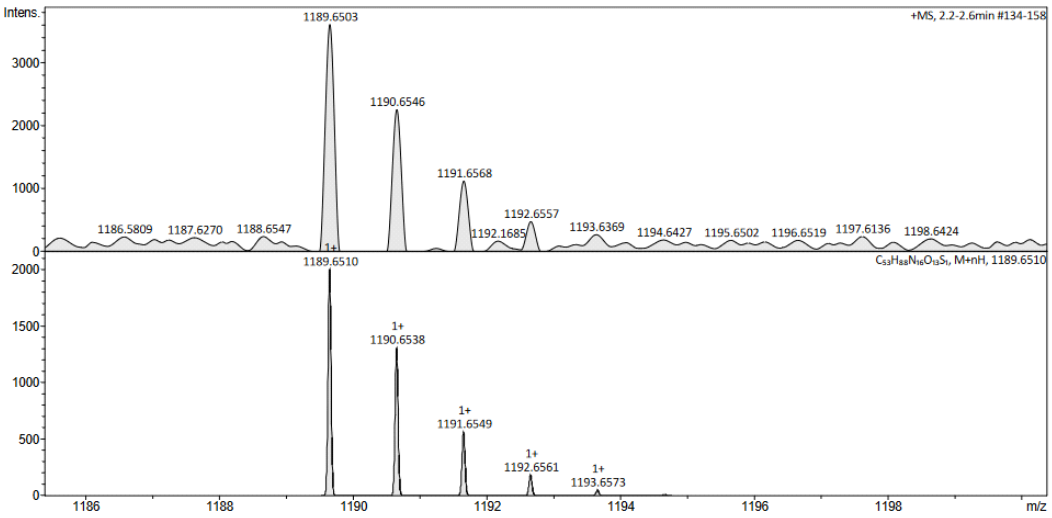
Intens.
+MS, 2.2-2.6min #134-158
1189.6503
1190.6546
1191.6568
1192.6557
1186.5809
1187.6270
1188.6547
1192.1685
1193.6369
1194.6427
1195.6502
1196.6519
1197.6136
1198.6424
1+
1189.6510
C53H88N16O13S2, M+nH, 1189.6510
1+
1190.6538
1+
1191.6549
1+
1192.6561
1+
1193.6573
m/z

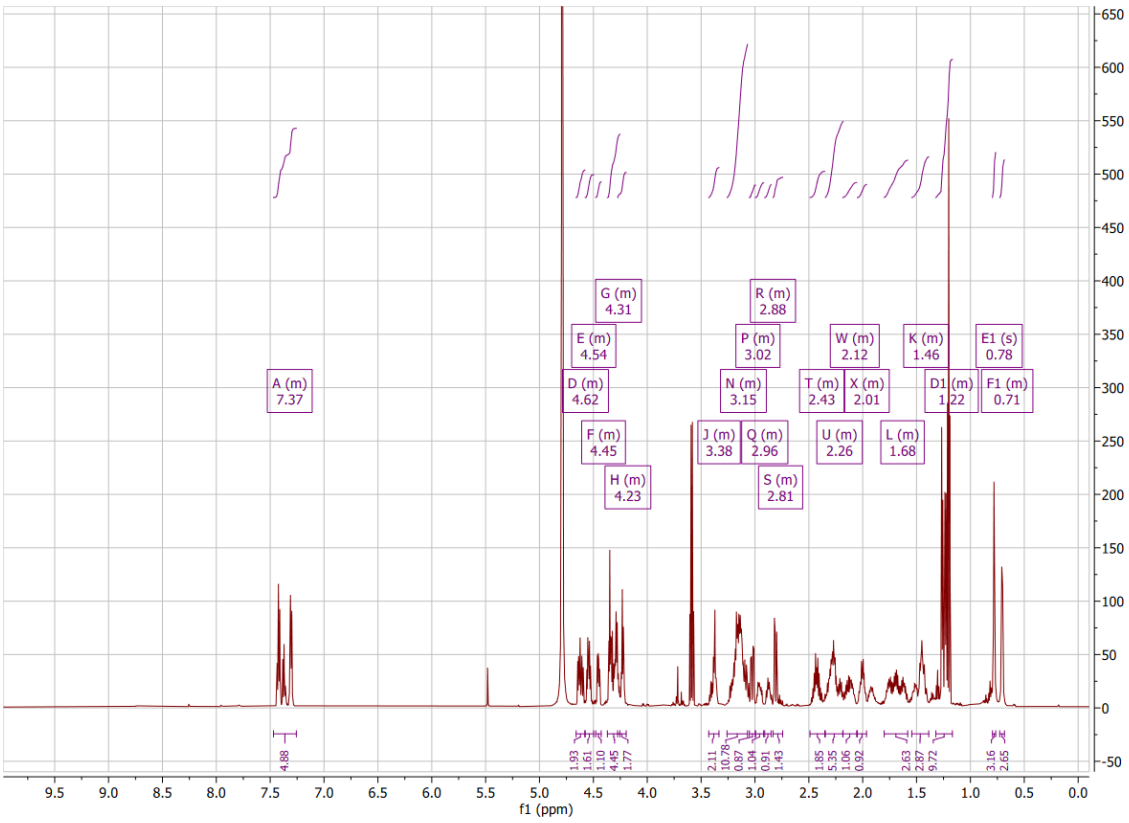
A (m) 7.37
G (m) 4.31
E (m) 4.54
D (m) 4.62
F (m) 4.45
H (m) 4.23
R (m) 2.88
P (m) 3.02
N (m) 3.15
J (m) 3.38
Q (m) 2.96
S (m) 2.81
W (m) 2.12
T (m) 2.43
X (m) 2.01
U (m) 2.26
K (m) 1.46
L (m) 1.68
D1 (m) 1.22
E1 (s) 0.78
F1 (m) 0.71
f1 (ppm)

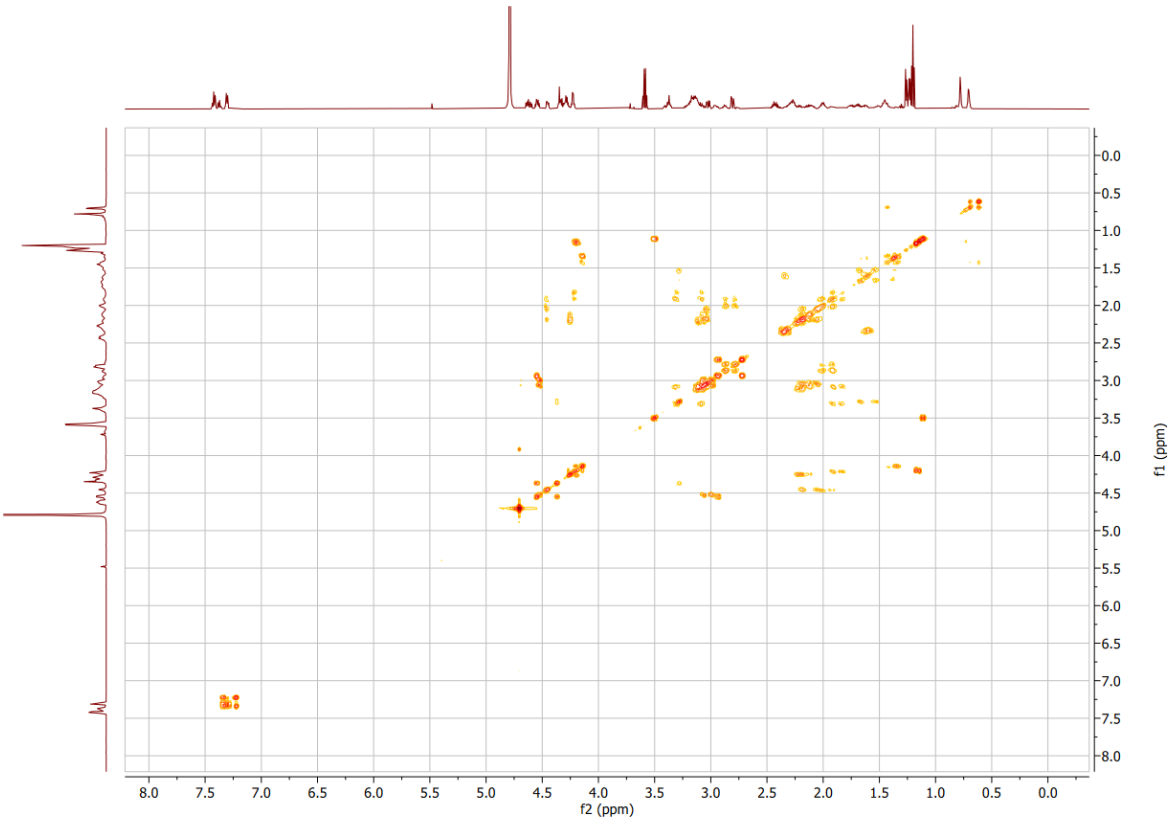
f2 (ppm)
f1 (ppm)

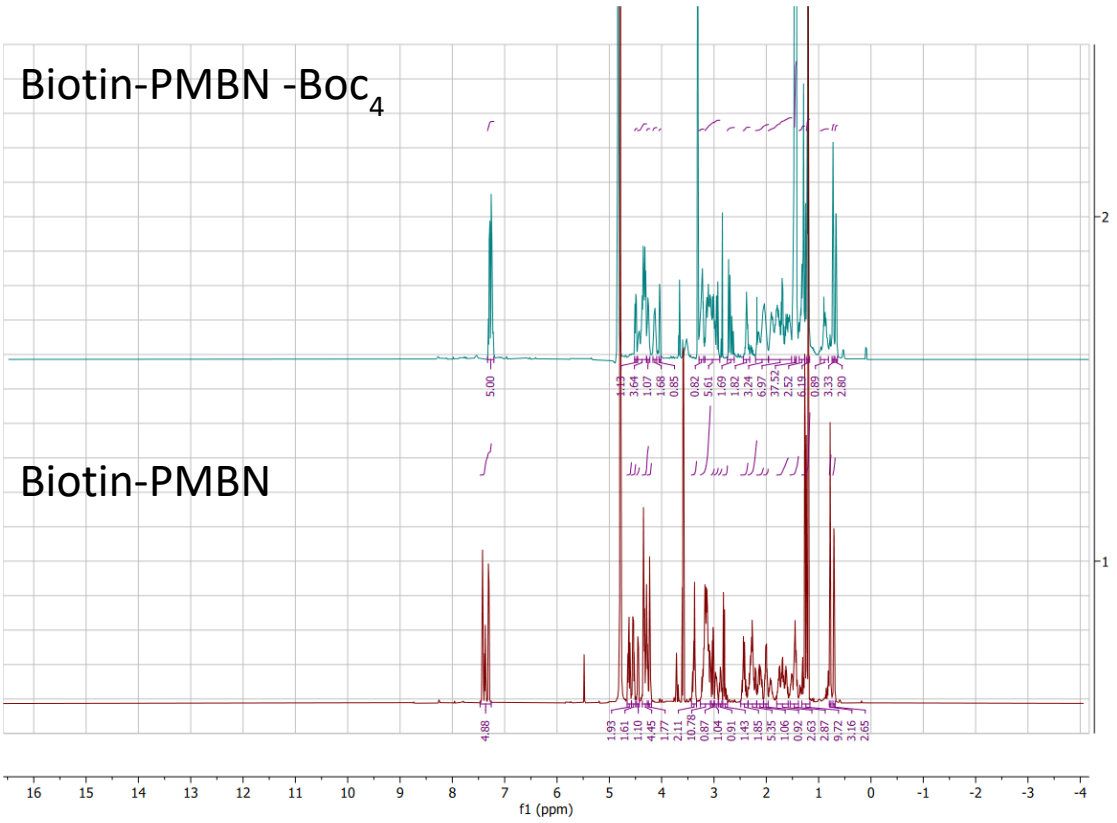

12 Biotin-Ahx-PMBN

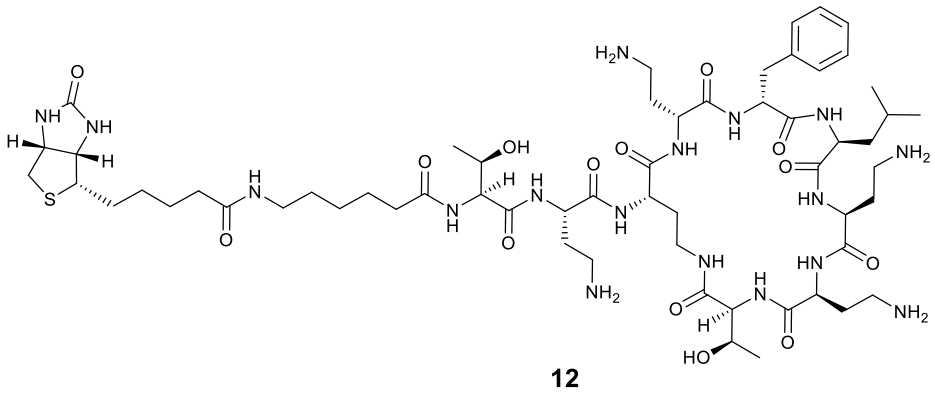

12

N-(+)-Biotinyl-6-aminohexanoic acid (0.11mmol, 40mg, 1.5 equiv.), HSPyU (0.15 mmol. 45 mg, 2.0 equiv.) and PMBN-Boc$_4$ (0.073 mmol 100 mg, 1 equiv.) were added to a sealable microwave reaction vial along with DIPEA (0.22 mmol, 40 µL, 3 equiv.) and DMF (10 mL). The vial was sealed and microwave heated to 80 °C for a series of 3 × 1 hour cycles (the reaction was monitored in between cycles by TLC

(DCM/MeOH). The crude reaction mixture was precipitated with water and the product was collected by filtration. To this crude filtrate was added HCl in Diethyl Ether (2M) (5 mL) and the reaction was stirred for 4 h. After complete deprotection of the Boc groups was observed through monitoring (RP-HPLC), excess HCl and solvent were removed through evaporation in vacuo before purification by RP-HPLC. HPLC fractions were collected and lyophilised yielding a white powder of **12** as the formate salt (11 mg, 10%)

HPLC $t_{R\ (ELSD)}$ 2.27 minutes HRMS (ESI+) calc. m/z = $C_{59}H_{100}N_{17}O_{14}S_1$ = 1302.7351, Found m/z = 1302.7373$[M+H]^+$.

δ_H (601 MHz, Deuterium Oxide) 7.49 – 7.22 (5 H, m), 4.74 – 4.71 (9 H, m), 4.67 – 4.61 (1 H, m), 4.55 – 4.49 (2 H, m), 4.48 – 4.40 (1 H, m), 4.38 – 4.22 (5 H, m), 3.43 – 3.34 (2 H, m), 3.23 – 3.07 (12 H, m), 3.06 – 3.00 (1 H, m), 2.97 – 2.87 (1 H, m), 2.84 – 2.77 (2 H, m), 2.54 – 1.86 (1 H, m), 1.80 – 1.50 (4 H, m), 1.50 – 1.41 (1 H, m), 1.41 – 1.33 (1 H, m), 1.26 (3 H, d, *J* 6.3), 1.23 (3 H, d, *J* 6.3), 0.87 – 0.79 (3 H,), (0.79 – 0.71 (3 H, m).

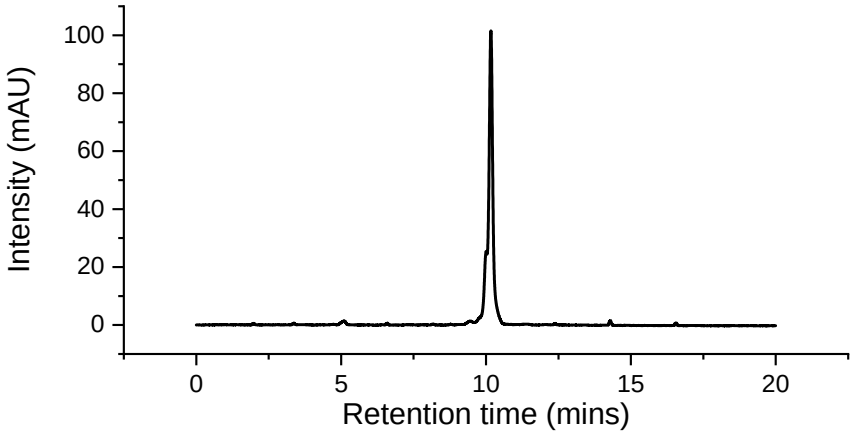
Intensity (mAU)
100
80
60
40
20
0
0
5
10
15
20
Retention time (mins)

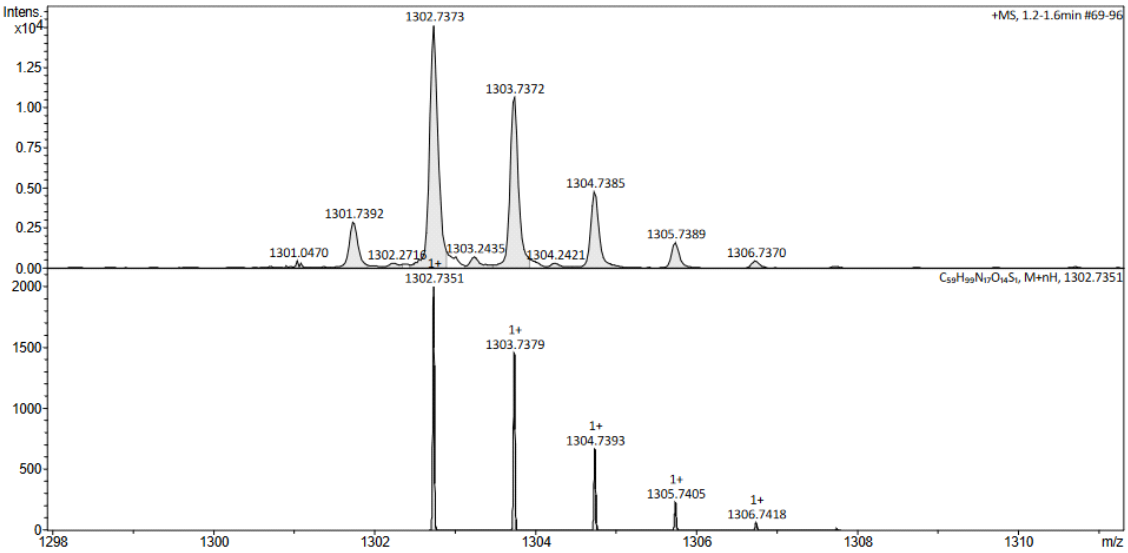
Intens.
x10^4
1.25
1.00
0.75
0.50
0.25
0.00
1302.7373
+MS, 1.2-1.6min #69-96
1303.7372
1304.7385
1301.7392
1305.7389
1301.0470
1302.2716
1303.2435
1304.2421
1306.7370
2000
1500
1000
500
0
1+
1302.7351
C59H99N17O14S2, M+nH, 1302.7351
1+
1303.7379
1+
1304.7393
1+
1305.7405
1+
1306.7418
1298
1300
1302
1304
1306
1308
1310
m/z

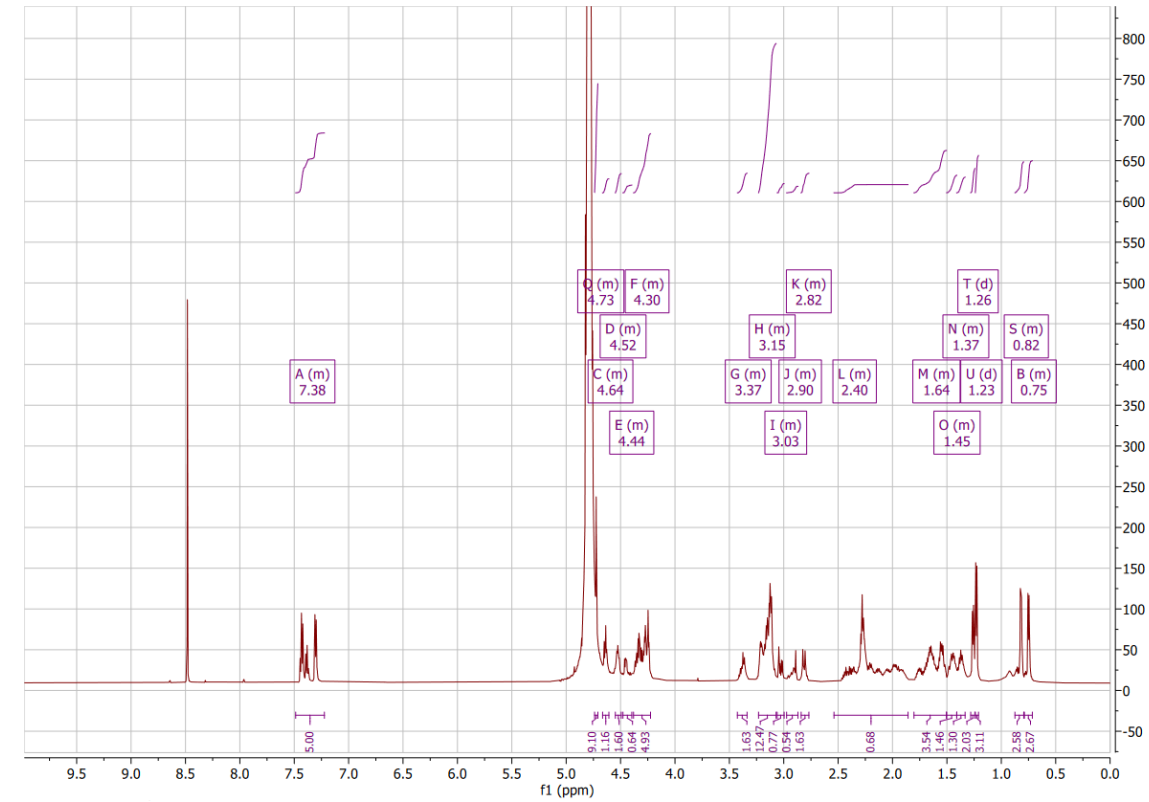
A (m) 7.38
Q (m) 4.73
F (m) 4.30
D (m) 4.52
C (m) 4.64
E (m) 4.44
K (m) 2.82
H (m) 3.15
G (m) 3.37
J (m) 2.90
L (m) 2.40
I (m) 3.03
T (d) 1.26
N (m) 1.37
S (m) 0.82
M (m) 1.64
U (d) 1.23
B (m) 0.75
O (m) 1.45
f1 (ppm)

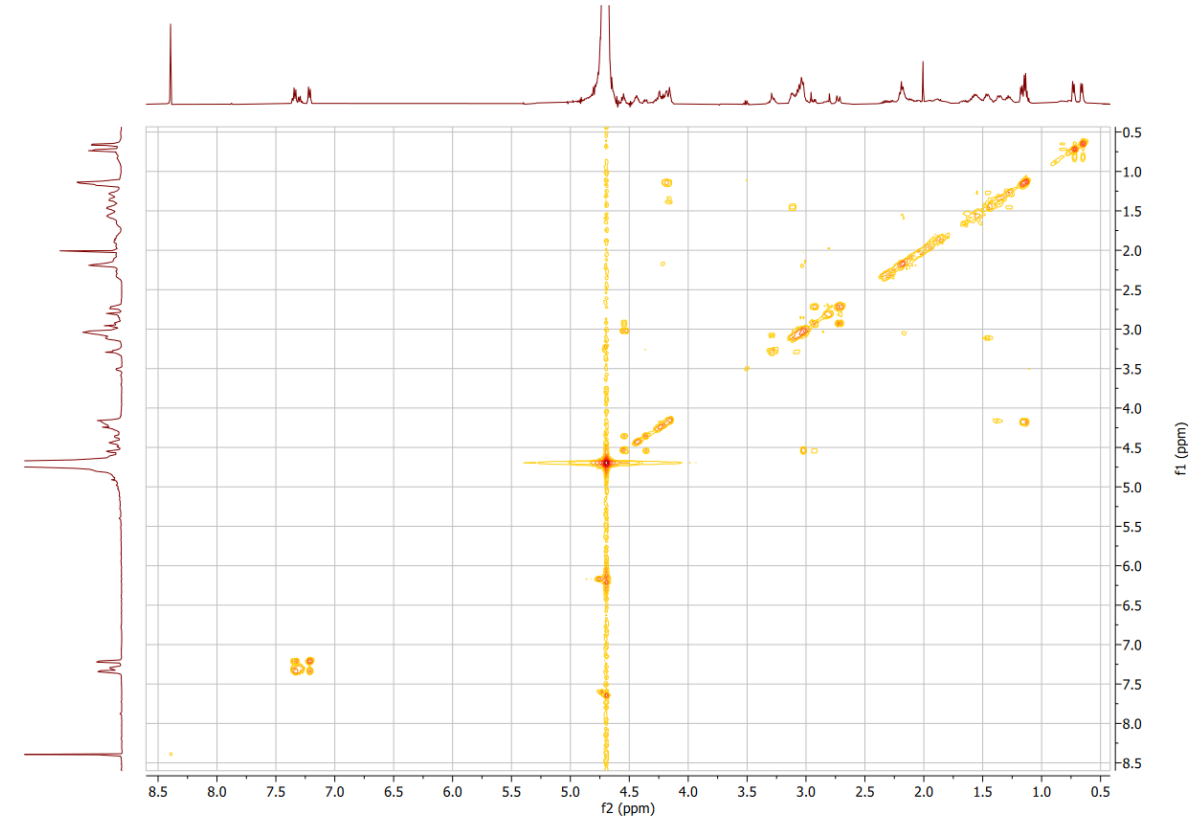
f2 (ppm)
f1 (ppm)

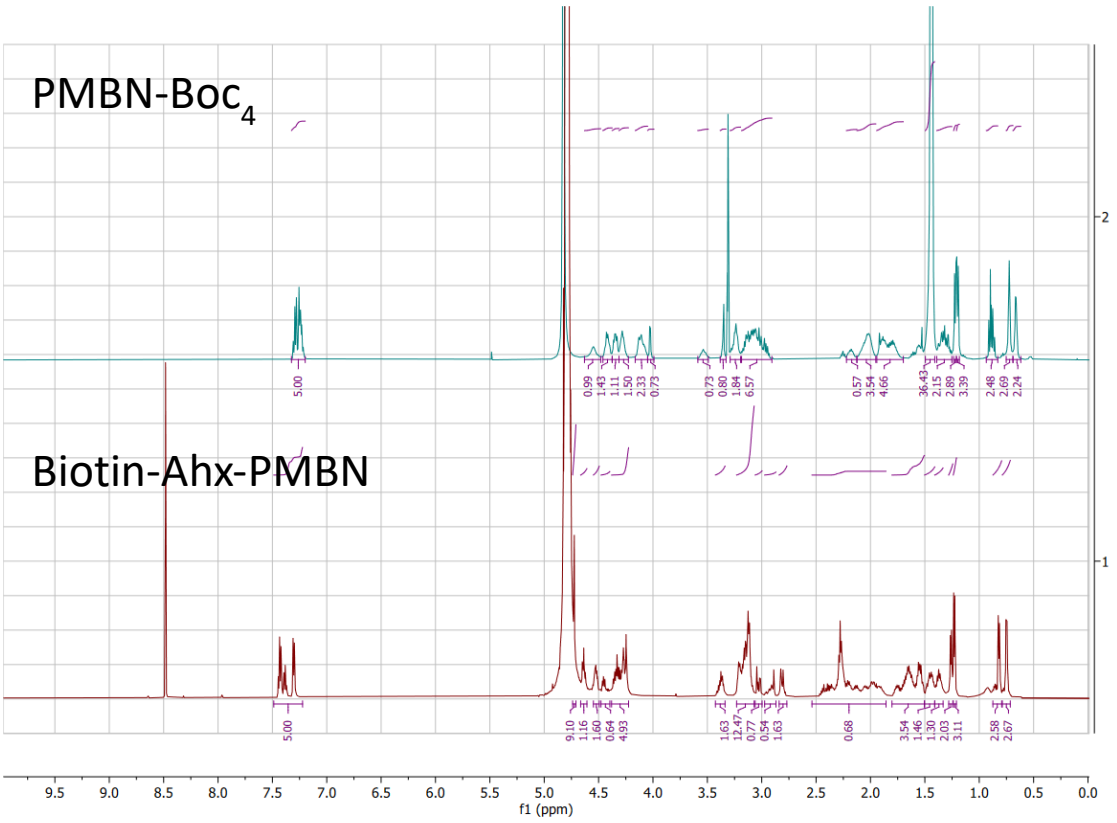
PMBN-Boc4
Biotin-Ahx-PMBN
f1 (ppm)

Chapter 4

Instruments

Transmission Electron Microscope (TEM) imaging was conducted on a JEOL JEM-1400 Plus using TAAB 3.05 mm copper grids (200 mesh, formvar/carbon support film) and representative images were processed using Image J. All DLS and Zeta potential measurements were performed using a Malvern Analytical Zetasizer Nano ZS with a 633 nm laser. Accurate pH measurements were performed with the Mettler Toledo FiveGo pH meter F2 calibrated with 3 buffer solutions (pH 4.01, 7.00, 9.21) immediately prior to use.

Characterisation of nanoparticles was performed with particle solutions suspended in ultrapure (18 MΩ) water unless otherwise specified.

DLS

Laser power was set to automatic adjustment to maintain signal count rate between 100 – 500 kcps. Runs used a minimum volume of 500 µL in a polystyrene 3 mL cuvette. Measurement position was fixed to the centre cell position of 4.65 mm.

Zeta Potential

A minimum volume of 800 µL in a folded capillary zeta cell (DTS1070 Malvern) was used. Measurement position was fixed to the centre cell position of 5.50 mm.

TEM

Bacterial cultures of *E. coli* and *B. subtilis* were prepared to 1.0 OD_{600} in PBS and 1000 µL of the washed culture solutions were incubated with **12** (10 µM) in an orbital shaker at 37^{o}C for 1 hour with a blank solution incubated with PBS under the

same conditions. Excess probe was removed via centrifugation (2 minutes, 6000 rcf). The bacterial pellet was resuspended in PBS (1000 µL) and a 180 µL aliquot removed for the addition of AuNP@streptavidin solution (10 OD, 20 µL) in a buffer solution (1x PBS, 0.2 % Tween 20 w/w, 0.2% BSA w/w), followed by vortexing and incubation for 5 minutes. The excess nanoparticles were removed by centrifugation (2 minutes, 6000 rcf) to selectively pellet the bacteria. The resulting labelled bacteria were washed once with ultrapure water before being readjusted to 1.0 OD_{600}, 10 µL of which was added to the copper grid. Bacteria solutions were left to sediment on the grids for 10 minutes before excess solution was removed with filter paper. Nanoparticle only solutions were left on the grids for 20 minutes as they were slower to sediment.

Gold nanoparticle Synthesis

All glassware used for nanoparticle synthesis reactions were cleaned with aqua regia prior to use.

Caution! Aqua regia is extremely corrosive and may result in explosion or skin burns if not handled with extreme caution.

Microwave Citrate Nanoparticle synthesis

To a solution of $HAuCl_4$ (200 µL, 25 mM) was added a solution of trisodium citrate dihydrate (300 µL, 34 mM) and the mixture was diluted to a final volume of 20 mL with water in a microwave vial and sealed. The reaction was heated to 100^{o}C and held for 10 minutes at temperature before being cooled back to room temperature. The nanoparticle solution was purified through centrifugation (10,000 rcf, 20

minutes) with replacement of the supernatant with a solution of trisodium citrate (1% w/w) three times. The solutions were stored at 4°C.

Frens Citrate Nanoparticle synthesis

A solution of $HAuCl_4$ (400 mL, 250 µM) was heated to boiling before a solution of trisodium citrate dihydrate (7.5 mL, 34 mM) was added. Heating and stirring was maintained as the colour changed through clear, grey, blue, purple and finally a deep red. Once the red stage was seen (approximately 6 minutes after the citrate addition) the solution was heated for an additional 5 minutes before the heating bath was removed and the solution allowed to cool to room temperature while stirring was maintained. The nanoparticles were purified through centrifugation (10,000 rcf, 20 minutes) and replacement of the supernatant with a solution of trisodium citrate (1% w/w) (three times). The solutions were stored at 4°C

Table 8: Analysis of Au@Citrate particles produced by the Frens and Microwave synthesis methods. Data for Frens method was averaged from 4 separate syntheses. Microwave method data averaged from 3 separate synthesise. The table summarises key characterisation data. *UV-Vis Size refers to diameter calculated using values from the absorbance spectra processed with equation 3

Nanoparticles	λ_{max}	UV-Vis Size	Intensity DLS / nm	PDI	Zeta / mV	SD / mV
Microwave	521	20.2	21.2	0.14	-27.8	7.32
Frens	519	16.7	22.4	0.12	-33.5	3.73

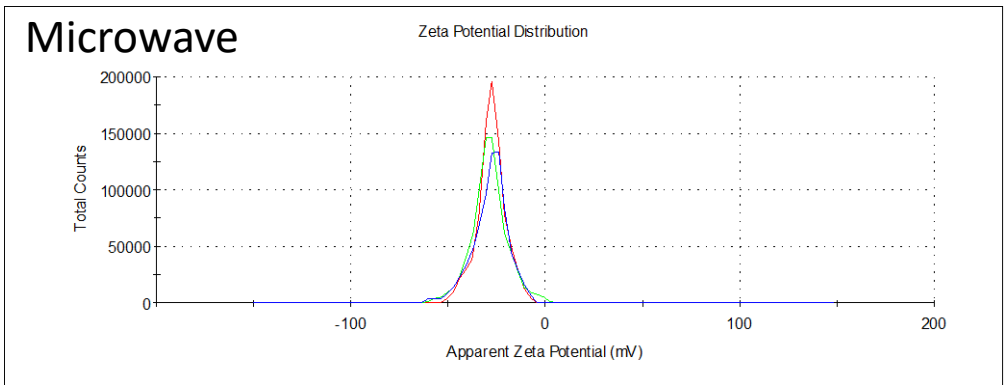

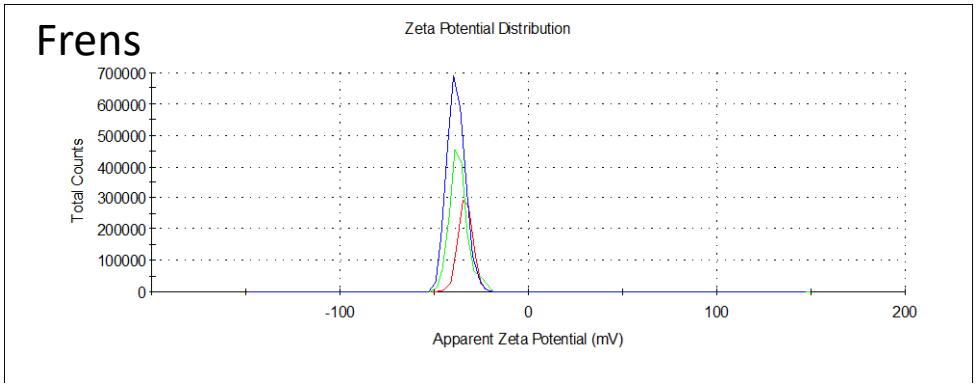

Figure 109: Zeta Potential distribution for Au@Citrate particles produced by the Microwave and Frens synthesis methods.

Au@Citrate ligand substitution

Compound **6** (0.03 mM stock in 18 MΩ ultrapure water) was added to Au@Citrate (1 mL, 1 OD, 1.68 nM calculated from UV) and mixed for 2 hours. Reactions were visually inspected for colour changes indicating aggregation. Solutions that had not aggregated were characterised with DLS / UV-vis measurements before purification. Stable solutions were taken forward to the purification step.

Purification was performed by centrifuge pelleting the nanoparticles (10,000 rpm, 10 minutes) and replacement of the supernatant with ultrapure water. Solutions of nanoparticles that did not freely redisperse on the addition of fresh solvent were sonicated for up to 10 minutes at room temperature.

Substitution reaction used Au@Citrate Particles ‘as synthesised’ with pH measured at 5.2 ± 0.3. **6** was added from stock solution with micropipette and the reaction was manually shaken to mix before placing the Eppendorf tubes on a rotator for mixing. Solutions were visually inspected after 2 hours and purified as described above.

Table 9: Aggregation results observed in the synthesis of Au@6 from the substitution of Au@Citrate used 'as synthesised' with 6.

		Aggregation	
Reaction	**6** / nM	Pre-purification	Post- Purification
A	1.8	-	-
B	18	-	-
C	45	-	-
D	84	-	+
E	168	+	+
F	1680	+	+

Follow up screening at higher pH was achieved through the addition of a pH adjustment step prior to the addition of **6.** A larger volume stock solution of Au@Citrate (20 mL, 1 OD) was adjusted to pH 11.2 (monitored with pH probe) with NaOH (0.2 M, 150 µL). This solution was separated into 1 mL aliquots in 1.5 mL

Table 10: Aggregation results observed in the synthesis of Au@6 from the substitution of Au@Citrate used after adjustment of solution pH to 11.2.

		Aggregation		
Reaction	**6** / nM	Pre-purification	Post- Purification	λ_{max}
G	84	-	+	520
H	168	-	+	525
I	1680	-	+	525
J	3360	+	+	561

After each purification step the pH of the solutions was monitored by universal indicator paper. On average the pH of the solution decreased from pH 11 to pH 9 after the first centrifugation step and further reduced to 7-8 after the second centrifugation step.

A repetition of this experiment with an alternative purification method was performed using MWCO centrifuge filters (Amicon® Ultra-4 Centrifugal Filter Unit, 10 kDa MWCO regenerated cellulose membrane). Samples were centrifuged (5000 rcf, 5 mins) with approximately 75% of the sample volume passing through the filter

which was replaced with water (18 MΩ). This procedure was repeated 4x to return the pH of the solution to the 7-8 range.

Au@Streptavidin

Synthesis procedure was adapted from literature[246]

Au@Citrate (1 mL, 1 OD, 1.68 nM) was adjusted to pH 10 with K_2CO_3 (100 µL, 100 µM) then concentrated to 200 µL via centrifugation. To this, Streptavidin (50 µL, 1 mg/ml) was added and the solution was stirred for 1 hour at room temperature before purification through centrifugation. The nanoparticle solution was redispersed in ultrapure water for analysis before 0.1x PBS and 0.01% BSA w/w was added for stable storage.

Table 11: Analysis of the synthesis of Au@Streptavidin from Au@Citrate showing the changes in characteristic properties over the course of the synthesis

Nanoparticles	λ_{max}	Intensity DLS / nm	PDI	Zeta / mV	SD
Au@Citrate	521	21.2	0.14	-27.8	7.32
Au@Streptavidin	529	99.8	0.21	-38.8	9.08
Au@Streptavidin post-purification	529	56.7	0.09	-18.8	17.2

Chapter 5

General method for producing strips:

An A4 nitrocellulose membrane was cut with a laser cutter (Mantech Pro Series 4060 120 W) to give a batch of strips collectively 126 mm wide by 85 mm long (2 x 28 individual strips) with each individual strip being 4.25 mm x 45 mm. The individual strips were held together as a batch with 0.5 mm tabs from the laser cutter.

The batched strips (2 x 28) were loaded onto the Polypico precise spotter and the test and control lines were printed across all the strips. The test line was positioned 1 cm from the bottom of the strips and the control line was positioned 0.5 mm above the test line. The lines were created through the sequential deposition of 15 nL drops spaced 0.3 mm apart across the width (in the x axis) which was then repeated 3x spaced 0.1 mm apart across the length (in the y axis). This yielded 14 spots per line in X and 3 lines per strip in Y (Figure 110) resulting in a 1 mm total width for the overall line. This results in 0.63 µL total volume printed for each test and control line per strip.

These dimensions were determined experimentally to account for the spreading of each spot after deposition.

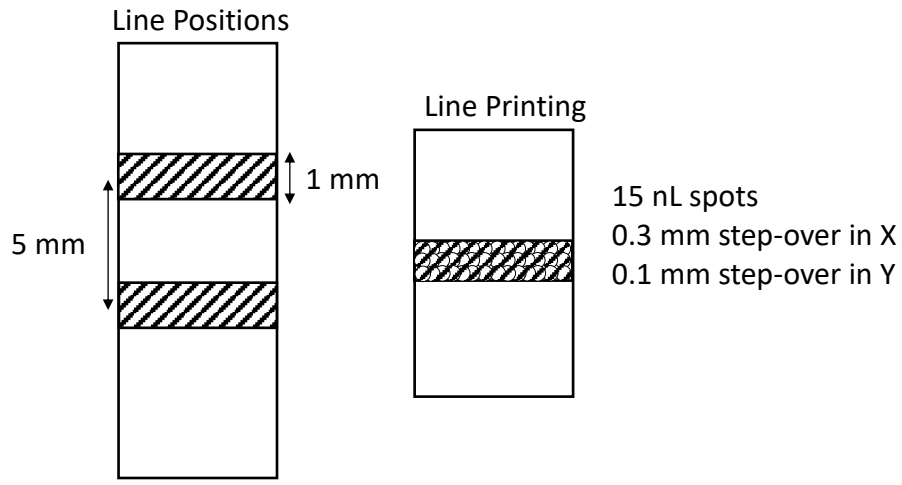

Figure 110: Diagram illustrating the positioning of the test and control lines printed on the nitrocellulose strips for lateral flow experiments. Line were made up of individual spots printed with the Polypico printer and the separation between the spots is listed.

After the combined strips were printed with both the test and control lines they were dried at 37ºC overnight in an oven. Individual strips were separated with a scalpel with cuts made to remove the tabs as close as possible to the edge of the strip without damaging the main area of flow.

General Method for running strips

The test nanoparticle solution was prepared in the running buffer and adjusted to 1 OD_{SPR} concentration as measured by UV-Vis spectroscopy. 10 µL of the nanoparticle solution was added into a well of a 96 well plate and the prepared strip was placed vertically into the well taking care to make sure it was that placed evenly to avoid the solution flowing faster down the left or right side.

Once the nanoparticle solution had flowed completely into the membrane, 10 µL of PBS was added to the well to act as a wash solution. Volumes of both the nanoparticle and wash solution were chosen to fit several priorities:

1. The nanoparticle solution had to be of sufficient volume to flow into the region of both the test and control line.
2. The wash solution had to be of sufficient volume to completely clear the test and control line of unbound nanoparticles.
3. The total volume of the combination of nanoparticle solution and wash solution fit within the total bed volume of the membrane.

Once both the nanoparticle and wash solutions had finished flowing through the strip, the strip was removed from the 96 well plate and placed on the strip carrier and allowed to dry at room temperature. This was to ensure a high contrast, consistent white background for the imaging of the strips. After all the strips of a particular experiment were dry the imaging of the strips was performed.

Control experiments

A nitrocellulose membrane (Whatman FF170 HP, 4.5 mm x 42.5 mm) was printed with a test line (BSA 1 mg/mL in 1x PBS) and control line (Biotinylated BSA abcam 286862, 1 mg/mL in 1x PBS). Au@Streptavidin (10 µL, 1 OD) was prepared in a running buffer solution with Tween 20 and BSA prior to adding to the strips.

Design of Experiments

A 2 factor, 4 level full factorial design of experiments was planned with Minitab 20 and run in randomised order. Tween and BSA solutions were prepared with a total volume of 5 µL to which 5 µL of 2 OD Au@Streptavidin in PBS was added to achieve a final volume of 10 µL of nanoparticle solution at 1 OD and the required percentage of Tween and BSA.

Table 12: DoE parameters used for the optimisation of the running buffer and the Line intensity values measured from the experiments.

StdOrder	RunOrder	Tween 20 %	BSA %	Line Intensity Pixel Values (BBSA-BSA)
12	1	1	10	0
14	2	10	0.1	219
13	3	10	0.01	180
10	4	1	0.1	148
2	5	0.01	0.1	90
9	6	1	0.01	113
11	7	1	1	0
16	8	10	10	0
1	9	0.01	0.01	0
8	10	0.1	10	0
5	11	0.1	0.01	86
15	12	10	1	182
7	13	0.1	1	37
6	14	0.1	0.1	131
3	15	0.01	1	0
4	16	0.01	10	0

The outcome of the strips was calculated as the integration of the BBSA peak minus the integration of the BSA line. Where there were peaks arising from non-specific binding to the nitrocellulose directly (e.g. <1 cm up the strip) this was also ‘removed’ from the BBSA integration.

Biotinylated BSA control

Au@BBSA

Biotinylated Bovine Serum Albumin (Biotin-LC-BSA) (3 biotin/BSA) (ab286862) (50 µL, 1 mg/ mL in PBS) was added to Au@Citrate (1 mL, 1 OD, 1.68 nM) and mixed for 2 hours. Solution was purified with centrifugation and the supernatant was replaced with ultrapure water for analysis, volumes maintained at 1 mL.

Table 13: Analysis of Au@BBSA synthesised from the substitution reaction with Au@Citrate

Nanoparticles	λ_{max}	Z-Average DLS / nm	Intensity DLS / nm	PDI	Zeta Potential / mV	SD/ mV
Au@Citrate	521	23.9	21.20	0.14	-27.8	7.32
Au@BBSA	520	27.9	127.6	0.2	-11	14.9

Au@BBSA were concentrated to 2 OD and was treated with running buffer test solutions (10% Tween 20, then BSA at 0%, 0.2% and 1% respectively) in a 1:1 ratio for a final volume of 10 µL.

The solutions were vortexed for 30 seconds and allowed to stand for 2 hours before use. The nanoparticles were run on a strip printed with Streptavidin (1mg/mL) as a test line using standard conditions and a control line of BBSA (1mg/mL) at standard conditions. Each solution was followed with a 10 µL PBS wash before imaging. The negative Au@Streptavidin test was performed using the standard running buffer and a PBS wash against the same strips.

Table 14: Image analysis (Both Integrations and Heights) of Au@BBSA control experiments showing capture on a streptavidin test line with different amounts of blocking BSA in the running buffer.

	Peak Integrations		
Line	BSA 0 %	BSA 0.2 %	BSA 1 %
Test	825	170	0
Control	189	121	0

	Peak Heights		
Line	BSA 0 %	BSA 0.2 %	BSA 1 %
Test	41	8	0
Control	9	7	1

Screening Polymyxin Concentration Control

1.5 µL of **12** was added from three different stock solutions at 100 µM 10 µM and 1 µM concentrations. To this was added Au@Streptavidin (10 µL, 1 OD, running buffer) and the combined solutions were pipette aspirated 3 times to mix. The solutions were left for 2 minutes before being run on the strip. Final concentrations of **12** therefore 13 1.3 and 0.13 µM respectively.

This test was run on a nitrocellulose membrane printed with a 'Test line' of BSA (1 mg/mL) and a control line of BBSA (1 mg/mL) printed under standard conditions.

Table 15: Peak analysis of Au@Strep+**12** conjugate non-specific binding against BSA test line showing Integrations and Heights at the test and control lines.

	Peak Integrations		
Line	100 / µM	10 / µM	1 / µM
Test	28	0	0
Control	358	462	601

	Peak Heights		
Line	100 / µM	10 / µM	1 / µM
Test	2	0	0
Control	21	34	34

'Half' Sandwich Assay Design

Screening Polymyxin Concentration against E. coli

E. coli was grown in overnight culture and washed into PBS (1000 µL) before being adjusted to 1 OD. This was split into four (200 µL) corresponding to the 4 concentrations (100, 10, 1, 0 µM) of **12** and incubated for 1 hour before washing.

Bacteria were then diluted down with PBS to the required concentration (1, 0.5, 0.1 OD). These solutions were then loaded into the print cartridge and printed in the test

line position under standard conditions (i.e 0.63 µL printed per test line). The strips were then dried for 2 hours at 37 ^{o}C before being run with the addition of Au@Streptavidin (10 µL, 1 OD) in the running buffer.

Table 16: Peak analysis of half sandwich assay with a test line printed with *E. coli* at 1/0.5/0.1 OD labelled with compound **12** showing Peak integrations and Peak Heights at the test and control lines.

		Peak Integrations			
Line	Bacteria Concentration / OD	100 / µM	10 / µM	1 / µM	0 / µM
Test	1	144	53	0	32
Control	1	902	596	545	521
Test	0.5	105	0	0	47
Control	0.5	542	506	558	573
Test	0.1	0	0	0	0
Control	0.1	784	925	924	744

		Peak Heights			
Line	Bacteria Concentration / OD	100 / µM	10 / µM	1 / µM	0 / µM
Test	1	16	5	0	3
Control	1	47	49	52	55
Test	0.5	11	0	0	4
Control	0.5	64	52	49	64
Test	0.1	0	0	0	0
Control	0.1	70	60	53	71

‘Full’ Sandwich Assay Design

E. coli in Flow

This test was run on a nitrocellulose membrane printed with a ‘Test line’ of Streptavidin (1 mg/mL) and a control line of BBSA (1 mg/mL) printed under standard conditions.

E. coli was grown in overnight culture and washed with PBS (1000 µL) before being adjusted to 2 OD. This was split into four aliquots (200 uL) corresponding to the 4 concentrations (100, 10, 1, 0 µM) of **12** and incubated with the probe for 1 hour before washing via centrifugation. The labelled *E. coli* (1.5 µL) was added to the Au@Streptavidin solution (10 µL, 1 OD) in the running buffer (10% Tween 0.2% BSA) and pipette aspirated 3x to mix. The combined solution was incubated for either 0 minutes (i.e the nitrocellulose test strip was added immediately post mixing) or 5 minutes at room temperature.

Table 17: Peak analysis of the full sandwich assay run with pre-labelled *E. coli* (1 OD, 100, 10, 1 µM) and tested with Au@Streptavidin (1 OD 10 µL) with no incubation time showing Peak integrations and Peak Heights at the test and control lines. * Test line peak measured at the base of the strip. ** Test line measured at standard position

		Peak Integration			
Incubation time / mins	Line	100 / µM	10 / µM	1 / µM	0 / µM
0	Test	221*	28**	0	-
	Control	557	507	819	-
5	Test	153*	0	0	0
	Control	387	350	378	593

		Peak Heights			
Incubation time / mins	Line	100 / µM	10 / µM	1 / µM	0 / µM
0	Test	16	2	0	-
	Control	37	29	55	-
5	Test	9	0	0	0
	Control	24	21	22	38

Screening Higher E. coli Volumes

This experiment was then repeated with *E. coli* volume screened at 1.5, 5 and 10 µL

	Peak Integration		
Line	1.5 / µL	5 / µL	10 / µL
Test	0	0	0
Control	582	502	463

	Peak Heights		
Line	1.5 / µL	5 / µL	10 / µL
Test	0	0	0
Control	39	35	31

Screening Increased Blocking for *E. coli* in Flow

Experiment was performed as per the above '*E. coli* in Flow' experiments.

E. coli was labelled with **12** at 100 µM and changes were made to the running buffer. Three strips were run with BSA at 0.2, 1 and, 10%, with Tween 20 held at 10% through all strips.

Table 18: Peak Analysis of full sandwich assay where pre-labelled *E. coli* (1 OD, 100 µM) was run with Au@Streptavidin (10 µL) with altered running buffer with 10% Tween and BSA (0.2%, 1%, 10%) showing Peak integrations (Int) and Peak Heights (Heights) at the test and control lines.

	Peak Integration		
Line	0.2 / %	1 / %	10 / %
Test	137*	0	0
Control	528	457	0

	Peak Heights		
Line	0.2 / %	1 / %	10 / %
Test	4	0	0
Control	42	26	0

Nitrocellulose pore size variation

This test was run on nitrocellulose membranes (Merck Hi-Flow™ Plus 30.5 cm x 25 cm) with different pore sizes (HFC135, HFC120, HFC90, HFC75) cut to the same dimensions (45 mm x 45 mm). These were printed with a 'Test line' of Streptavidin (1 mg/mL) and a control line of BBSA (1 mg/mL) printed under standard conditions.

E. coli was grown in overnight culture and washed into PBS before being adjusted to 2 OD. The *E. coli* was labelled with **12** (100 µM) and 1.5 µL was added to the well of a 96 well plate along with Au@Streptavidin solution (1 OD, 15 µL) in the running buffer (10% Tween 0.2% BSA) and pipette aspirated 3x to mix. This solution was run through the strip.

Table 19: Image analysis of E. coli detection seen at the test and control lines along with the bottom of the strips (<0.5 cm up the strip). 4 Nitrocellulose membranes were tested under the same conditions. Both peak heights and integrations were analysed.

	Peak Integration			
Line	HFC135	HFC120	HFC90	HFC75
Bottom	3	4	4	1
Test	19	12	15	8
Control	12	11	23	27

	Peak Heights			
Line	HFC135	HFC120	HFC90	HFC75
Bottom	52	68	73	0
Test	221	153	185	115
Control	263	336	326	673

7 References

1 A. Fleming, *Br. J. Exp. Pathol.*, 1929, **10**, 226–236.
2 N. Kardos and A. L. Demain, *Appl. Microbiol. Biotechnol.*, 2011, **92**, 677–687.
3 W. A. Adedeji, *Ann. Ib. Postgrad. Med.*, 2016, **14**, 56–57.
4 Global Health Estimates, https://www.who.int/data/gho/data/themes/mortality-and-global-health-estimates, (accessed 24 July 2023).
5 D. Mabey, R. W. Peeling, A. Ustianowski and M. D. Perkins, *Nat. Rev. Microbiol.*, 2004, **2**, 231–240.
6 M. Urdea, L. A. Penny, S. S. Olmsted, M. Y. Giovanni, P. Kaspar, A. Shepherd, P. Wilson, C. A. Dahl, S. Buchsbaum, G. Moeller and D. C. Hay Burgess, *Nature*, 2006, **444**, 73–79.
7 K. S. Ikuta, L. R. Swetschinski, G. Robles Aguilar, F. Sharara, T. Mestrovic, A. P. Gray, N. Davis Weaver, E. E. Wool, C. Han, A. Gershberg Hayoon, S. I. Hay, C. Dolecek, B. Sartorius, C. J. L. Murray and M. Naghavi, *The Lancet*, 2022, **400**, 2221–2248.
8 J. Davies and D. Davies, *Microbiol. Mol. Biol. Rev.*, 2010, **74**, 417–433.
9 A. Chokshi, Z. Sifri, D. Cennimo and H. Horng, *J. Glob. Infect. Dis.*, 2019, **11**, 36–42.
10 J. O'Neill, *Tackling drug-resistant infections globally: final report and recommendations*, Government of the United Kingdom, 2016.
11 Antimicrobial resistance, https://www.who.int/news-room/fact-sheets/detail/antimicrobial-resistance, (accessed 22 July 2023).
12 C. J. L. Murray, K. S. Ikuta, F. Sharara, L. Swetschinski, G. R. Aguilar, A. Gray, C. Han, C. Bisignano, P. Rao, E. Wool, S. C. Johnson, A. J. Browne, M. G. Chipeta, F. Fell, S. Hackett, G. Haines-Woodhouse, B. H. K. Hamadani, E. A. P. Kumaran, B. McManigal, A. D. Lopez, A. Stergachis, C. Moore, C. Dolecek and M. Naghavi, *The Lancet*, 2022, **399**, 629–655.
13 R. Kelly and S. C. Davies, *Med. J. Aust.*, 2017, **207**, 371–373.
14 S. van der Pol, D. E. M. C. Jansen, A. W. van der Velden, C. C. Butler, T. J. M. Verheij, A. W. Friedrich, M. J. Postma and A. D. I. van Asselt, *PharmacoEconomics*, 2022, **40**, 823–833.
15 B. Malik and S. Bhattacharyya, *Sci. Rep.*, 2019, **9**, 9788.
16 B. K. English and A. H. Gaur, in *Hot Topics in Infection and Immunity in Children VI*, eds. A. Finn, N. Curtis and A. J. Pollard, Springer, New York, NY, 2010, pp. 73–82.
17 B. Carey and B. Cryan, *Ir. Med. J.*, 2003, **96**, 43–4, 46.
18 J.-C. Lagier, S. Edouard, I. Pagnier, O. Mediannikov, M. Drancourt and D. Raoult, *Clin. Microbiol. Rev.*, 2015, **28**, 208–236.
19 L. Váradi, J. L. Luo, D. E. Hibbs, J. D. Perry, R. J. Anderson, S. Orenga and P. W. Groundwater, *Chem. Soc. Rev.*, 2017, **46**, 4818–4832.
20 M. Bonnet, J. C. Lagier, D. Raoult and S. Khelaifia, *New Microbes New Infect.*, 2020, **34**, 100622.
21 K. Syal, M. Mo, H. Yu, R. Iriya, W. Jing, S. Guodong, S. Wang, T. E. Grys, S. E. Haydel and N. Tao, *Theranostics*, 2017, **7**, 1795–1805.
22 J. D. Perry, *Clin. Microbiol. Rev.*, 2017, **30**, 449–479.
23 F. Joanny, S. J. Löhr, T. Engleitner, B. Lell and B. Mordmüller, *Malar. J.*, 2014, **13**, 234.
24 T. L. Pitt and M. R. Barer, *Med. Microbiol.*, 2012, 24–38.

25 D. P. Breakwell, R. B. Moyes and J. Reynolds, *Curr. Protoc. Microbiol.*, 2009, **15**, A.3I.1-A.3I.4.
26 I. J. Strumpf, A. Y. Tsang, M. A. Schork and J. G. Weg, *Am. Rev. Respir. Dis.*, 1976, **114**, 971–976.
27 R. Kalich, G. Bennert, T. Fiedler, M. Kubin, MezenskyL, M. Turzova and H. Ulber, *J. Hyg. Epidemiol. Microbiol. Immunol.*, 1979, **23**, 307–317.
28 T. Hamouda, A. Y. Shih and J. R. Baker, *Lett. Appl. Microbiol.*, 2002, **34**, 86–90.
29 J. N. Harris, P. B. New and P. M. Martin, *Soil Biol. Biochem.*, 2006, **38**, 1521–1526.
30 S. A. Berger, B. Bogokowsky and C. Block, *J. Clin. Microbiol.*, 1990, **28**, 1066–1067.
31 J. J. Tarrand and D. H. Gröschel, *J. Clin. Microbiol.*, 1982, **16**, 772–774.
32 R. M. Atlas and J. W. Synder, in *Manual of Clinical Microbiology*, John Wiley & Sons, Ltd, 2011, pp. 272–303.
33 K. S. Park, *Biosens. Bioelectron.*, 2018, **102**, 179–188.
34 G. A. R. Y. Suaifan, S. Alhogail and M. Zourob, *Biosens. Bioelectron.*, 2017, **90**, 230–237.
35 About CKS | CKS | NICE, https://cks.nice.org.uk/about/, (accessed 25 July 2023).
36 S. T. Williams and F. L. Davies, *Microbiology*, 1965, **38**, 251–261.
37 J. D. Perry, K. Asir, D. Halimi, S. Orenga, J. Dale, M. Payne, R. Carlton, J. Evans and F. K. Gould, *J. Clin. Microbiol.*, 2010, **48**, 3852–3858.
38 D. A. Enoch and S. H. Aliyu, *CMAJ Can. Med. Assoc. J.*, 2012, **184**, 17–18.
39 T. D. Wilkins and D. M. Lyerly, *J. Clin. Microbiol.*, 2003, **41**, 531–534.
40 S. Ramírez-Guízar, H. Sykes, J. D. Perry, E. C. Schwalbe, S. P. Stanforth, Ma. C. I. Perez-Perez and J. R. Dean, *J. Chromatogr. A*, 2017, **1501**, 79–88.
41 J. R. Porter, *Bacteriol. Rev.*, 1976, **40**, 260–269.
42 R. M. Trüeb, in *Hair in Infectious Disease: Recognition, Treatment, and Prevention*, eds. R. M. Trüeb, H. Dutra Rezende and M. F. R. Gavazzoni Dias, Springer International Publishing, Cham, 2023, pp. 1–17.
43 R. Coico, *Curr. Protoc. Microbiol.*, 2006, **00**, A.3C.1-A.3C.2.
44 K. P. Smith, A. D. Kang and J. E. Kirby, *J. Clin. Microbiol.*, 2018, **56**, 10.1128/jcm.01521-17.
45 G. A. O'Toole, *J. Bacteriol.*, 2016, **198**, 3128–3128.
46 B. Mills, M. Bradley and K. Dhaliwal, *Clin. Transl. Imaging*, 2016, **4**, 163–174.
47 R. Piña, A. I. Santos-Díaz, E. Orta-Salazar, A. R. Aguilar-Vazquez, C. A. Mantellero, I. Acosta-Galeana, A. Estrada-Mondragon, M. Prior-Gonzalez, J. I. Martinez-Cruz and A. Rosas-Arellano, *Int. J. Mol. Sci.*, 2022, **23**, 1426.
48 K. Shah and R. Weissleder, *NeuroRx*, 2005, **2**, 215–225.
49 H. Li, Q. Yao, W. Sun, K. Shao, Y. Lu, J. Chung, D. Kim, J. Fan, S. Long, J. Du, Y. Li, J. Wang, J. Yoon and X. Peng, *J. Am. Chem. Soc.*, 2020, **142**, 6381–6389.
50 A. Baibek, M. Üçüncü, B. Short, G. Ramage, A. Lilienkampf and M. Bradley, *Chem. Commun.*, 2021, **57**, 1899–1902.
51 C. D. Doern and S. M. Butler-Wu, *J. Mol. Diagn.*, 2016, **18**, 789–802.
52 Michael. Karas, Doris. Bachmann and Franz. Hillenkamp, *Anal. Chem.*, 1985, **57**, 2935–2939.
53 R. D. Holland, J. G. Wilkes, F. Rafii, J. B. Sutherland, C. C. Persons, K. J. Voorhees and J. O. Lay, *Rapid Commun. Mass Spectrom. RCM*, 1996, **10**, 1227–1232.

54 J. O. Lay Jr, *Mass Spectrom. Rev.*, 2001, **20**, 172–194.
55 T. R. Sandrin, J. E. Goldstein and S. Schumaker, *Mass Spectrom. Rev.*, 2013, **32**, 188–217.
56 S. K. P. Lau, B. S. F. Tang, J. L. L. Teng, T.-M. Chan, S. O. T. Curreem, R. Y. Y. Fan, R. H. Y. Ng, J. F. W. Chan, K.-Y. Yuen and P. C. Y. Woo, *J. Clin. Pathol.*, 2014, **67**, 361–366.
57 L. Ferreira, F. Sánchez-Juanes, M. González-Ávila, D. Cembrero-Fuciños, A. Herrero-Hernández, J. M. González-Buitrago and J. L. Muñoz-Bellido, *J. Clin. Microbiol.*, 2010, **48**, 2110–2115.
58 M. Reil, M. Erhard, E. J. Kuijper, M. Kist, H. Zaiss, W. Witte, H. Gruber and S. Borgmann, *Eur. J. Clin. Microbiol. Infect. Dis.*, 2011, **30**, 1431–1436.
59 S. Ambardar, R. Gupta, D. Trakroo, R. Lal and J. Vakhlu, *Indian J. Microbiol.*, 2016, **56**, 394–404.
60 S. Moorthie, C. J. Mattocks and C. F. Wright, *HUGO J.*, 2011, **5**, 1–12.
61 D. Mendes Silva and L. Domingues, *Ecotoxicol. Environ. Saf.*, 2015, **113**, 400–411.
62 M. Mitsuhashi, *J. Clin. Lab. Anal.*, 1996, **10**, 285–293.
63 H. Zhu, H. Zhang, Y. Xu, S. Laššáková, M. Korabečná and P. Neužil, *BioTechniques*, 2020, **69**, 317–325.
64 P. Rådström, A. Bäckman, N. Qian, P. Kragsbjerg, C. Påhlson and P. Olcén, *J. Clin. Microbiol.*, 1994, **32**, 2738–2744.
65 M. Yengui, R. Trabelsi, L. Khannous, N. E. Mathlouthi, M. Adnan, A. J. Siddiqui, E. Noumi, M. Snoussi and R. Gdoura, *BioMed Res. Int.*, 2022, **2022**, e8612933.
66 J. Aslanzadeh, *Ann. Clin. Lab. Sci.*, 2004, **34**, 389–396.
67 T. Demeke and G. R. Jenkins, *Anal. Bioanal. Chem.*, 2010, **396**, 1977–1990.
68 U. B. Schaad, *Infection*, 1983, **11**, S87–S89.
69 P. Kralik and M. Ricchi, *Front. Microbiol.*
70 C. Agrimonti, B. Bottari, M. L. S. Sardaro and N. Marmiroli, *Crit. Rev. Food Sci. Nutr.*, 2019, **59**, 423–442.
71 S. Pabinger, S. Rödiger, A. Kriegner, K. Vierlinger and A. Weinhäusel, *Biomol. Detect. Quantif.*, 2014, **1**, 23–33.
72 E. A. Ottesen, J. W. Hong, S. R. Quake and J. R. Leadbetter, *Science*, 2006, **314**, 1464–1467.
73 R. Pal, M. Yang, R. Lin, B. N. Johnson, N. Srivastava, S. Z. Razzacki, K. J. Chomistek, D. C. Heldsinger, R. M. Haque, V. M. Ugaz, P. K. Thwar, Z. Chen, K. Alfano, M. B. Yim, M. Krishnan, A. O. Fuller, R. G. Larson, D. T. Burke and M. A. Burns, *Lab. Chip*, 2005, **5**, 1024–1032.
74 M. U. Kopp, A. J. de Mello and A. Manz, *Science*, 1998, **280**, 1046–1048.
75 S. Park, Y. Zhang, S. Lin, T.-H. Wang and S. Yang, *Biotechnol. Adv.*, 2011, **29**, 830–839.
76 S. Singh, A. Numan and S. Cinti, *Anal. Chem.*, 2022, **94**, 26–40.
77 T. Shu, H. Hunter, Z. Zhou, Y. Sun, X. Cheng, J. Ma, L. Su, X. Zhang and M. J. Serpe, *Anal. Methods*, 2021, **13**, 5418–5435.
78 H. Kettler, K. White, S. J. Hawkes and U. B. S. P. for R. and T. in T. Diseases, *Mapping the landscape of diagnostics for sexually transmitted infections : key findings and recommendations*, World Health Organization, 2004.
79 J. M. Hong, H. Lee, N. V. Menon, C. T. Lim, L. P. Lee and C. W. M. Ong, *Sci. Transl. Med.*, 2022, **14**, eabj4124.

80 S. T. Abdurrahman, N. Emenyonu, O. J. Obasanya, L. Lawson, R. Dacombe, M. Muhammad, O. Oladimeji and L. E. Cuevas, *Pan Afr. Med. J.*, 2014, **18**, 277.
81 P. J. Garcia, P. You, G. Fridley, D. Mabey and R. Peeling, *Lancet Glob. Health*, 2015, **3**, e257–e258.
82 J. R. Choi, *Front. Chem.*, 2020, **8**, 1–9.
83 M. Rezaei, S. Razavi Bazaz, S. Zhand, N. Sayyadi, D. Jin, M. P. Stewart and M. Ebrahimi Warkiani, *Diagnostics*, 2021, **11**, 9.
84 Q. Song, X. Sun, Z. Dai, Y. Gao, X. Gong, B. Zhou, J. Wu and W. Wen, *Lab. Chip*, 2021, **21**, 1634–1660.
85 M. K. Haleyur Giri Setty and I. K. Hewlett, *AIDS Res. Treat.*, 2014, **2014**, e497046.
86 R. McNerney and P. Daley, *Nat. Rev. Microbiol.*, 2011, **9**, 204–213.
87 S. E. McBirney, D. Chen, A. Scholtz, H. Ameri and A. M. Armani, *ACS Sens.*, 2018, **3**, 1264–1270.
88 M. Marks and D. C. Mabey, *Expert Rev. Mol. Diagn.*, 2017, **17**, 321–325.
89 Point of Care Tests, https://www.who.int/teams/sexual-and-reproductive-health-and-research-(srh)/areas-of-work/sexual-health/sexually-transmitted-infections/point-of-care-tests, (accessed 24 July 2023).
90 S. Sharma, J. Zapatero-Rodríguez, P. Estrela and R. O'Kennedy, *Biosensors*, 2015, **5**, 577–601.
91 S. Rosen, in *Lateral Flow Immunoassay*, eds. R. Wong and H. Tse, Humana Press, Totowa, NJ, 2009, pp. 1–15.
92 E. B. Bahadır and M. K. Sezgintürk, *TrAC Trends Anal. Chem.*, 2016, **82**, 286–306.
93 A. K. Yetisen, M. S. Akram and C. R. Lowe, *Lab. Chip*, 2013, **13**, 2210–2251.
94 B. Ngom, Y. Guo, X. Wang and D. Bi, *Anal. Bioanal. Chem.*, 2010, **397**, 1113–1135.
95 D. Xu, X. Huang, J. Guo and X. Ma, *Biosens. Bioelectron.*, 2018, **110**, 78–88.
96 F. Di Nardo, E. Alladio, C. Baggiani, S. Cavalera, C. Giovannoli, G. Spano and L. Anfossi, *Talanta*, 2019, **192**, 288–294.
97 IVD Lateral Flow - Sample, Conjugate and Absorbent Pad Basics, https://www.sigmaaldrich.com/technical-documents/articles/ivd-immunoassay/lateral-flow/pads-chemistries-selections-specifications-and-conjugates.html, (accessed 28 April 2020).
98 S. Oehler, R. Alex and A. Barker, *Anal. Biochem.*, 1999, **268**, 330–336.
99 M. Sajid, A.-N. Kawde and M. Daud, *J. Saudi Chem. Soc.*, 2015, **19**, 689–705.
100 nanoComposix, Sample and Absorbent Pad Selection for Lateral Flow Assays, https://nanocomposix.com/pages/sample-and-absorbent-pad-selection-for-lateral-flow-assays, (accessed 22 April 2020).
101 J. Park, *Sensors*, 2022, **22**, 7398.
102 S. Bazsefidpar, E. Serrano-Pertierra, G. Gutiérrez, A. S. Calvo, M. Matos and M. C. Blanco-López, *Microchim. Acta*, 2023, **190**, 264.
103 A. E. Urusov, A. V. Zherdev and B. B. Dzantiev, *Biosensors*, 2019, **9**, 89.
104 E. Eltzov, S. Guttel, A. Low Yuen Kei, P. D. Sinawang, R. E. Ionescu and R. S. Marks, *Electroanalysis*, 2015, **27**, 2116–2130.
105 Y. Jung, Y. Heo, J. J. Lee, A. Deering and E. Bae, *J. Microbiol. Methods*, 2020, **168**, 105800.
106 V. K. Rajendran, P. Bakthavathsalam, P. L. Bergquist and A. Sunna, *Sens. Actuators B Chem.*, 2019, **298**, 126849.
107 D. Wild, in *The Immunoassay Handbook*, Elsevier, 2013, pp. 7–10.

108 E. Frohnmeyer, N. Tuschel, T. Sitz, C. Hermann, G. T. Dahl, F. Schulz, A. J. Baeumner and M. Fischer, *Analyst*, 2019, **144**, 1840–1849.
109 C. Y. Yu, G. Y. Ang, A. L. Chua, E. H. Tan, S. Y. Lee, G. Falero-Diaz, O. Otero, I. Rodríguez, F. Reyes, A. Acosta, M. E. Sarmiento, S. Ghosh, T. Ramamurthy, C. Yean Yean, P. Lalitha and M. Ravichandran, *J. Microbiol. Methods*, 2011, **86**, 277–282.
110 C. Davies, in *The Immunoassay Handbook*, Elsevier, 2013, pp. 661–672.
111 S. K. Vashist and J. H. T. Luong, in *Handbook of Immunoassay Technologies*, Elsevier, 2018, pp. 81–95.
112 X. Cui, Q.-R. Xiong, Y.-H. Xiong, S. Shan and W.-H. Lai, *Chin. J. Anal. Chem.*, 2013, **41**, 1812–1816.
113 H.-L. Hsu, C.-C. Chuang, C.-C. Liang, D.-J. Chiao, H.-L. Wu, Y.-P. Wu, F.-P. Lin and R.-H. Shyu, *BMC Infect. Dis.*, 2018, **18**, 402.
114 N. Ariffin, N. A. Yusof, J. Abdullah, S. F. Abd Rahman, N. H. Ahmad Raston, N. Kusnin and S. Suraiya, *J. Sens.*, 2020, **2020**, e1365983.
115 Y. Zhao, H. Wang, P. Zhang, C. Sun, X. Wang, X. Wang, R. Yang, C. Wang and L. Zhou, *Sci. Rep.*, 2016, **6**, 21342.
116 C. Huang, T. Wen, F.-J. Shi, X.-Y. Zeng and Y.-J. Jiao, *ACS Omega*, 2020, **5**, 12550–12556.
117 S. Maher, M. Kamel, Z. Demerdash, H. El Baz, O. Sayyouh, A. Saad, N. Ali, F. Salah and S. Atta, *Sci. Rep.*, 2023, **13**, 10643.
118 J. E. Pinto Torres, J. Goossens, J. Ding, Z. Li, S. Lu, D. Vertommen, P. Naniima, R. Chen, S. Muyldermans, Y. G.-J. Sterckx and S. Magez, *Sci. Rep.*, 2018, **8**, 9019.
119 S. C. B. Gopinath, *Anal. Bioanal. Chem.*, 2007, **387**, 171–182.
120 M. Darmostuk, S. Rimpelova, H. Gbelcova and T. Ruml, *Biotechnol. Adv.*, 2015, **33**, 1141–1161.
121 M. Bauer, M. Strom, D. S. Hammond and S. Shigdar, *Molecules*, 2019, **24**, 4377.
122 L. Huang, S. Tian, W. Zhao, K. Liu, X. Ma and J. Guo, *Biosens. Bioelectron.*, 2021, **186**, 113279.
123 M. Majdinasab, M. Badea and J. L. Marty, *Pharmaceuticals*, 2022, **15**, 90.
124 S. Ellipilli, H. Wang, W.-J. Lee, D. Shu and P. Guo, *Nanomedicine Nanotechnol. Biol. Med.*, 2022, **45**, 102590.
125 C. Lu, X. Gao, Y. Chen, J. Ren and C. Liu, *Anal. Lett.*, 2020, **53**, 646–659.
126 E. A. Bayer and M. Wilchek, in *Methods in Enzymology*, Elsevier, 1990, vol. 184, pp. 174–187.
127 J. G. Bruno, *Pathogens*, 2014, **3**, 341–355.
128 S. Smiley, M. DeRosa and B. Blais, *J. Nucleic Acids*, 2013, **2013**, e936542.
129 Tools and resources | Sore throat (acute), https://www.nice.org.uk/guidance/ng84/resources/, (accessed 5 December 2023).
130 Y.-L. Sun, C.-M. Kuo, C.-L. Lu and C.-S. Lin, *J. Food Saf.*, 2021, **41**, e12867.
131 W. Wu, S. Zhao, Y. Mao, Z. Fang, X. Lu and L. Zeng, *Anal. Chim. Acta*, 2015, **861**, 62–68.
132 C. Song, J. Liu, J. Li and Q. Liu, *Biosens. Bioelectron.*, 2016, **85**, 734–739.
133 M. Kohlberger and G. Gadermaier, *Biotechnol. Appl. Biochem.*, 2022, **69**, 1771–1792.
134 A. Chen and S. Yang, *Biosens. Bioelectron.*, 2015, **71**, 230–242.
135 R.-M. Lu, Y.-C. Hwang, I.-J. Liu, C.-C. Lee, H.-Z. Tsai, H.-J. Li and H.-C. Wu, *J. Biomed. Sci.*, 2020, **27**, 1.

136 A. Alanio and S. Bretagne, *Med. Mycol.*, 2017, **55**, 56–62.
137 R. Souvenir, J. Buhler, G. Stormo and W. Zhang, in *PCR Primer Design*, ed. A. Yuryev, Humana Press, Totowa, NJ, 2007, pp. 245–267.
138 A. R. Akram, S. V. Chankeshwara, E. Scholefield, T. Aslam, N. McDonald, A. Megia-Fernandez, A. Marshall, B. Mills, N. Avlonitis, T. H. Craven, A. M. Smyth, D. S. Collie, C. Gray, N. Hirani, A. T. Hill, J. R. Govan, T. Walsh, C. Haslett, M. Bradley and K. Dhaliwal, *Sci. Transl. Med.*, 2018, **10**, eaal0033.
139 M. Ucuncu, B. Mills, S. Duncan, M. Staderini, K. Dhaliwal and M. Bradley, *Chem. Commun.*, 2020, **56**, 3757–3760.
140 T. Velkov, P. E. Thompson, M. A. K. Azad, K. D. Roberts and P. J. Bergen, in *Polymyxin Antibiotics: From Laboratory Bench to Bedside*, eds. J. Li, R. L. Nation and K. S. Kaye, Springer International Publishing, Cham, 2019, pp. 15–36.
141 K. Hayashi and T. Suzuki, *Bull. Inst. Chem. Res. Kyoto Univ.*, 1965, **43**, 259–277.
142 T. Velkov, K. D. Roberts, P. E. Thompson and J. Li, *Future Med. Chem.*, 2016, **8**, 1017–1025.
143 M. E. Falagas and I. A. Bliziotis, *Int. J. Antimicrob. Agents*, 2007, **29**, 630–636.
144 Z. Li and T. Velkov, in *Polymyxin Antibiotics: From Laboratory Bench to Bedside*, eds. J. Li, R. L. Nation and K. S. Kaye, Springer International Publishing, Cham, 2019, pp. 37–54.
145 T. Mogi, Y. Murase, M. Mori, K. Shiomi, S. Ōmura, M. P. Paranagama and K. Kita, *J. Biochem. (Tokyo)*, 2009, **146**, 491–499.
146 T. Velkov, P. E. Thompson, R. L. Nation and J. Li, *J. Med. Chem.*, 2010, **53**, 1898–1916.
147 S. Bhattacharjya, S. A. David, V. I. Mathan and P. Balaram, *Biopolymers*, 1997, **41**, 251–265.
148 A. K. Duwe, C. A. Rupar, G. B. Horsman and S. I. Vas, *Antimicrob. Agents Chemother.*, 1986, **30**, 340–341.
149 M. Vaara, *Microbiol. Rev.*, 1992, **56**, 395–411.
150 H. Tsubery, I. Ofek, S. Cohen and M. Fridkin, *J. Med. Chem.*, 2000, **43**, 3085–3092.
151 M. A. K. Azad, R. L. Nation, T. Velkov and J. Li, in *Polymyxin Antibiotics: From Laboratory Bench to Bedside*, eds. J. Li, R. L. Nation and K. S. Kaye, Springer International Publishing, Cham, 2019, pp. 305–319.
152 P. Brown, *J. Antibiot. (Tokyo)*, 9.
153 A. Gallardo-Godoy, C. Muldoon, B. Becker, A. G. Elliott, L. H. Lash, J. X. Huang, M. S. Butler, R. Pelingon, A. M. Kavanagh, S. Ramu, W. Phetsang, M. A. T. Blaskovich and M. A. Cooper, *J. Med. Chem.*, 2016, **59**, 1068–1077.
154 J. Li, D. Guan, F. Chen, W. Shi, L. Lan and W. Huang, *J. Med. Chem.*, 2021, **64**, 5746–5765.
155 P. R. G. Schindler and M. Teuber, *Antimicrob. Agents Chemother.*, 1975, **8**, 95–104.
156 Z. Z. Deris, J. D. Swarbrick, K. D. Roberts, M. A. K. Azad, J. Akter, Andrew. S. Horne, R. L. Nation, K. L. Rogers, P. E. Thompson, T. Velkov and J. Li, *Bioconjug. Chem.*, 2014, **25**, 750–760.
157 B. Yun, K. D. Roberts, P. E. Thompson, R. L. Nation, T. Velkov and J. Li, *Sensors*, 2017, **17**, 2598.
158 P. Sarker, J. Shepherd, K. Swindells, I. Douglas, S. MacNeil, L. Swanson and S. Rimmer, *Biomacromolecules*, 2011, **12**, 1–5.

159 H. Shoji, *Ther. Apher. Dial.*, 2003, **7**, 108–114.
160 C. S. Bell, R. Mejías, S. E. Miller, J. M. Greer, M. S. McClain, T. L. Cover and T. D. Giorgio, *ACS Appl. Mater. Interfaces*, 2017, **9**, 26719–26730.
161 P. J. Tighe, R. R. Ryder, I. Todd and L. C. Fairclough, *PROTEOMICS – Clin. Appl.*, 2015, **9**, 406–422.
162 S. Zhang, R. Geryak, J. Geldmeier, S. Kim and V. V. Tsukruk, *Chem. Rev.*, 2017, **117**, 12942–13038.
163 N. M. Green, *Biochem. J.*, 1963, **89**, 585–591.
164 X. Duan, Y. Li, N. K. Rajan, D. A. Routenberg, Y. Modis and M. A. Reed, *Nat. Nanotechnol.*, 2012, **7**, 401–407.
165 M. Srisa-Art, E. C. Dyson, A. J. deMello and J. B. Edel, *Anal. Chem.*, 2008, **80**, 7063–7067.
166 J. R. Wayment and J. M. Harris, *Anal. Chem.*, 2009, **81**, 336–342.
167 F. Rusmini, Z. Zhong and J. Feijen, *Biomacromolecules*, 2007, **8**, 1775–1789.
168 O. H. Laitinen, V. P. Hytönen, H. R. Nordlund and M. S. Kulomaa, *Cell. Mol. Life Sci. CMLS*, 2006, **63**, 2992–3017.
169 A. Kroetsch, B. Chin, V. Nguyen, J. Gao and S. Park, *Appl. Microbiol. Biotechnol.*, 2018, **102**, 10079–10089.
170 O. Azzaroni, M. Mir and W. Knoll, *J. Phys. Chem. B*, 2007, **111**, 13499–13503.
171 N.-P. Huang, J. Vörös, S. M. De Paul, M. Textor and N. D. Spencer, *Langmuir*, 2002, **18**, 220–230.
172 V. H. Pérez-Luna, M. J. O'Brien, K. A. Opperman, P. D. Hampton, G. P. López, L. A. Klumb and P. S. Stayton, *J. Am. Chem. Soc.*, 1999, **121**, 6469–6478.
173 X. Zhao, X. He, W. Li, Y. Liu, L. Yang and J. Wang, *Afr J Microbiol Res*, 2010, **4**, 663–670.
174 I.-H. Cho, A. Bhunia and J. Irudayaraj, *Int. J. Food Microbiol.*, 2015, **206**, 60–66.
175 A. Holmberg, A. Blomstergren, O. Nord, M. Lukacs, J. Lundeberg and M. Uhlén, *Electrophoresis*, 2005, **26**, 501–510.
176 K. J. Hamblett, B. B. Kegley, D. K. Hamlin, M.-K. Chyan, D. E. Hyre, O. W. Press, D. S. Wilbur and P. S. Stayton, *Bioconjug. Chem.*, 2002, **13**, 588–598.
177 A. Anastasiadis, C. J. Morton, G. H. Talbo, R. E. Koeppe and F. Separovic, *Int. J. Pept. Res. Ther.*, 2006, **12**, 243–252.
178 A. Rosenthal, S. Rauch, K.-J. Eichhorn, M. Stamm and P. Uhlmann, *Colloids Surf. B Biointerfaces*, 2018, **171**, 351–357.
179 R. L. Danner, K. A. Joiner, M. Rubin, W. H. Patterson, N. Johnson, K. M. Ayers and J. E. Parrillo, *Antimicrob. Agents Chemother.*, 1989, **33**, 1428–1434.
180 G. Lowe, *Philos. Trans. R. Soc. Lond. B Biol. Sci.*, 1997, **257**, 237–248.
181 M. Itoh, D. Hagiwara and T. Kamiya, *Tetrahedron Lett.*, 1975, **16**, 4393–4394.
182 H. O'Dowd, B. Kim, P. Margolis, W. Wang, C. Wu, S. L. Lopez and J. Blais, *Tetrahedron Lett.*, 2007, **48**, 2003–2005.
183 C. J. Slingerland, C. M. J. Wesseling, P. Innocenti, K. G. C. Westphal, R. Masereeuw and N. I. Martin, *J. Med. Chem.*, 2022, **65**, 15878–15892.
184 J. K. Molloy, C. Lincheneau, M. M. Karimdjy, F. Agnese, L. Mattera, C. Gateau, P. Reiss, D. Imbert and M. Mazzanti, *Chem. Commun.*, 2016, **52**, 4577–4580.
185 K. Sikora, M. Jaśkiewicz, D. Neubauer, D. Migoń and W. Kamysz, *Pharmaceuticals*, 2020, **13**, 442.
186 N. M. Green, *Biochem. J.*, 1965, **94**, 23C-24C.
187 P. Strzelczyk, D. Plażuk, J. Zakrzewski and G. Bujacz, *Molecules*, 2016, **21**, 1270.

188 R. F. Delgadillo, T. C. Mueser, K. Zaleta-Rivera, K. A. Carnes, J. González-Valdez and L. J. Parkhurst, *PLoS ONE*, 2019, **14**, e0204194.
189 In *Greene's Protective Groups in Organic Synthesis*, John Wiley & Sons, Ltd, 2006, pp. 696–926.
190 Q. Fu, L. Yuan, F. Cao, L. Zang and D. Ji, *Microchem. J.*, 2021, **171**, 106859.
191 S. Liao, W. Yue, S. Cai, Q. Tang, W. Lu, L. Huang, T. Qi and J. Liao, *Front. Pharmacol.*
192 G. Han, P. Ghosh and V. M. Rotello, *Nanomed.*, 2007, **2**, 113–123.
193 D. R. Bhumkar, H. M. Joshi, M. Sastry and V. B. Pokharkar, *Pharm. Res.*, 2007, **24**, 1415–1426.
194 M.-E. Kyriazi, D. Giust, A. H. El-Sagheer, P. M. Lackie, O. L. Muskens, T. Brown and A. G. Kanaras, *ACS Nano*, 2018, **12**, 3333–3340.
195 J. D. Gibson, B. P. Khanal and E. R. Zubarev, *J. Am. Chem. Soc.*, 2007, **129**, 11653–11661.
196 V. Amendola, R. Pilot, M. Frasconi, O. M. Maragò and M. A. Iatì, *J. Phys. Condens. Matter*, 2017, **29**, 203002.
197 U. Kreibig and M. Vollmer, *Optical Properties of Metal Clusters*, Springer, Berlin, Heidelberg, 1995, vol. 25.
198 M. H. Tu, T. Sun and K. T. V. Grattan, *Sens. Actuators B Chem.*, 2012, **164**, 43–53.
199 S. E. Lohse and C. J. Murphy, *Chem. Mater.*, 2013, **25**, 1250–1261.
200 S. Link and M. A. El-Sayed, *J. Phys. Chem. B*, 1999, **103**, 8410–8426.
201 X. Li, K. Tamada, A. Baba, W. Knoll and M. Hara, *J. Phys. Chem. B*, 2006, **110**, 15755–15762.
202 N. Ajdari, C. Vyas, S. L. Bogan, B. A. Lwaleed and B. G. Cousins, *Nanomedicine Nanotechnol. Biol. Med.*, 2017, **13**, 1531–1542.
203 M. Brust, M. Walker, D. Bethell, D. J. Schiffrin and R. Whyman, *J. Chem. Soc. Chem. Commun.*, 1994, 801–802.
204 G. Pacchioni, *Nat. Rev. Mater.*, 2019, **4**, 226–226.
205 K. Mahato, S. Nagpal, M. A. Shah, A. Srivastava, P. K. Maurya, S. Roy, A. Jaiswal, R. Singh and P. Chandra, *3 Biotech*, 2019, **9**, 57.
206 M. S. Inkpen, Z.-F. Liu, H. Li, L. M. Campos, J. B. Neaton and L. Venkataraman, *Nat. Chem.*, 2019, **11**, 351–358.
207 J. P. Oliveira, A. R. Prado, W. J. Keijok, P. W. P. Antunes, E. R. Yapuchura and M. C. C. Guimarães, *Sci. Rep.*, 2019, **9**, 13859.
208 J. Turkevich, P. C. Stevenson and J. Hillier, *Discuss. Faraday Soc.*, 1951, **11**, 55–75.
209 G. Frens, *Nat. Phys. Sci.*, 1973, **241**, 20–22.
210 C. Daruich De Souza, B. Ribeiro Nogueira and M. E. C. M. Rostelato, *J. Alloys Compd.*, 2019, **798**, 714–740.
211 M. Wuithschick, A. Birnbaum, S. Witte, M. Sztucki, U. Vainio, N. Pinna, K. Rademann, F. Emmerling, R. Kraehnert and J. Polte, *ACS Nano*, 2015, **9**, 7052–7071.
212 J. Polte, *CrystEngComm*, 2015, **17**, 6809–6830.
213 J. Polte, T. T. Ahner, F. Delissen, S. Sokolov, F. Emmerling, A. F. Thünemann and R. Kraehnert, *J. Am. Chem. Soc.*, 2010, **132**, 1296–1301.
214 J. Dong, P. L. Carpinone, G. Pyrgiotakis, P. Demokritou and B. M. Moudgil, *KONA Powder Part. J.*, 2020, **37**, 224–232.
215 M. S. Bakshi, *Langmuir*, 2009, **25**, 12697–12705.
216 C. Ziegler and A. Eychmüller, *J. Phys. Chem. C*, 2011, **115**, 4502–4506.

217 W. Haiss, N. T. K. Thanh, J. Aveyard and D. G. Fernig, *Anal. Chem.*, 2007, **79**, 4215–4221.
218 M. A. Dobrovolskaia, B. W. Neun, S. Man, X. Ye, M. Hansen, A. K. Patri, R. M. Crist and S. E. McNeil, *Nanomedicine Nanotechnol. Biol. Med.*, 2014, **10**, 1453–1463.
219 H. Hinterwirth, S. K. Wiedmer, M. Moilanen, A. Lehner, G. Allmaier, T. Waitz, W. Lindner and M. Lämmerhofer, *J. Sep. Sci.*, 2013, **36**, 2952–2961.
220 S. Bhattacharjee, *J. Controlled Release*, 2016, **235**, 337–351.
221 P. Rademeyer, D. Carugo, J. Yu Lee and E. Stride, *Lab. Chip*, 2015, **15**, 417–428.
222 B. N. Khlebtsov and N. G. Khlebtsov, *Colloid J.*, 2011, **73**, 118–127.
223 J. Doak, R. K. Gupta, K. Manivannan, K. Ghosh and P. K. Kahol, *Phys. E Low-Dimens. Syst. Nanostructures*, 2010, **42**, 1605–1609.
224 T. Zheng, S. Bott and Q. Huo, *ACS Appl. Mater. Interfaces*, 2016, **8**, 21585–21594.
225 R. Erni, M. D. Rossell, C. Kisielowski and U. Dahmen, *Phys. Rev. Lett.*, 2009, **102**, 096101.
226 S. Zhang and C. Wang, *Methods Protoc.*, 2023, **6**, 63.
227 F. Caputo, J. Clogston, L. Calzolai, M. Rösslein and A. Prina-Mello, *J. Controlled Release*, 2019, **299**, 31–43.
228 A. M. Keene and K. M. Tyner, *J. Nanoparticle Res.*, 2011, **13**, 3465–3481.
229 C.-C. Huang and H.-T. Chang, *Chem. Commun.*, 2007, 1215–1217.
230 Y.-W. Lin, C.-C. Huang and H.-T. Chang, *Analyst*, 2011, **136**, 863–871.
231 K.-M. Song, M. Cho, H. Jo, K. Min, S. H. Jeon, T. Kim, M. S. Han, J. K. Ku and C. Ban, *Anal. Biochem.*, 2011, **415**, 175–181.
232 S. K. Ghosh and T. Pal, *Chem. Rev.*, 2007, **107**, 4797–4862.
233 A. Heuer-Jungemann, N. Feliu, I. Bakaimi, M. Hamaly, A. Alkilany, I. Chakraborty, A. Masood, M. F. Casula, A. Kostopoulou, E. Oh, K. Susumu, M. H. Stewart, I. L. Medintz, E. Stratakis, W. J. Parak and A. G. Kanaras, *Chem. Rev.*, 2019, **119**, 4819–4880.
234 T. Kim, C.-H. Lee, S.-W. Joo and K. Lee, *J. Colloid Interface Sci.*, 2008, **318**, 238–243.
235 T. Mohamed, S. Matou-Nasri, A. Farooq, D. Whitehead and M. Azzawi, *Int. J. Nanomedicine*, 2017, **12**, 8813–8830.
236 P. Khullar, V. Singh, A. Mahal, P. N. Dave, S. Thakur, G. Kaur, J. Singh, S. Singh Kamboj and M. Singh Bakshi, *J. Phys. Chem. C*, 2012, **116**, 8834–8843.
237 H. Kang, J. T. Buchman, R. S. Rodriguez, H. L. Ring, J. He, K. C. Bantz and C. L. Haynes, *Chem. Rev.*, 2019, **119**, 664–699.
238 E. Harrison, J. A. Coulter and D. Dixon, *Nanomed.*, 2016, **11**, 851–865.
239 Z. Lee, K.-J. Jeon, A. Dato, R. Erni, T. J. Richardson, M. Frenklach and V. Radmilovic, *Nano Lett.*, 2009, **9**, 3365–3369.
240 J. Liu and Y. Lu, *Nat. Protoc.*, 2006, **1**, 246–252.
241 M. A. Shaker and M. I. Shaaban, *Int. J. Pharm.*, 2017, **525**, 71–84.
242 A. Bard, R. Rondon, D. T. Marquez, A. E. Lanterna and J. C. Scaiano, *Photochem. Photobiol.*, 2018, **94**, 1109–1115.
243 D.-H. Tsai, F. W. DelRio, R. I. MacCuspie, T. J. Cho, M. R. Zachariah and V. A. Hackley, *Langmuir*, 2010, **26**, 10325–10333.
244 V. Amendola and M. Meneghetti, *J. Phys. Chem. C*, 2009, **113**, 4277–4285.
245 I. Ojea-Jiménez and V. Puntes, *J. Am. Chem. Soc.*, 2009, **131**, 13320–13327.
246 R. D'Agata, P. Palladino and G. Spoto, *Beilstein J. Nanotechnol.*, 2017, **8**, 1–11.

247 G. A. Posthuma-Trumpie, J. Korf and A. van Amerongen, *Anal. Bioanal. Chem.*, 2008, **392**, 1215–1223.
248 M. A. Mansfield, in *Lateral Flow Immunoassay*, eds. R. Wong and H. Tse, Humana Press, Totowa, NJ, 2009, pp. 1–19.
249 M. A. Mansfield, in *Drugs of Abuse: Body Fluid Testing*, eds. R. C. Wong and H. Y. Tse, Humana Press, Totowa, NJ, 2005, pp. 71–85.
250 M. L. Yahaya, N. D. Zakaria, R. Noordin and K. A. Razak, *Mater. Today Proc.*, 2019, **17**, 878–883.
251 A. L. Ahmad, S. C. Low and S. R. Abd. Shukor, *Scr. Mater.*, 2007, **57**, 743–746.
252 R. Tang, N. Alam, M. Li, M. Xie and Y. Ni, *Carbohydr. Polym.*, 2021, **268**, 118259.
253 A. H. Iles, P. J. W. He, I. N. Katis, P. Horak, R. W. Eason and C. L. Sones, *Talanta*, 2022, **248**, 123579.
254 C. Carrell, A. Kava, M. Nguyen, R. Menger, Z. Munshi, Z. Call, M. Nussbaum and C. Henry, *Microelectron. Eng.*, 2019, **206**, 45–54.
255 A. Jain and K. Cheng, *J. Controlled Release*, 2017, **245**, 27–40.
256 A. J. Baeumner, J. Pretz and S. Fang, *Anal. Chem.*, 2004, **76**, 888–894.
257 J. H. T. Luong and S. K. Vashist, *ACS Omega*, 2020, **5**, 10–18.
258 L. G. Lee, E. S. Nordman, M. D. Johnson and M. F. Oldham, *Biosensors*, 2013, **3**, 360–373.
259 E. M. Linares, L. T. Kubota, J. Michaelis and S. Thalhammer, *J. Immunol. Methods*, 2012, **375**, 264–270.
260 C. Parolo, A. Sena-Torralba, J. F. Bergua, E. Calucho, C. Fuentes-Chust, L. Hu, L. Rivas, R. Álvarez-Diduk, E. P. Nguyen, S. Cinti, D. Quesada-González and A. Merkoçi, *Nat. Protoc.*, 2020, **15**, 3788–3816.
261 P. Chun, in *Lateral Flow Immunoassay*, eds. R. Wong and H. Tse, Humana Press, Totowa, NJ, 2009, pp. 1–19.
262 K. Faulstich, R. Gruler, M. Eberhard, D. Lentzsch and K. Haberstroh, in *Lateral Flow Immunoassay*, eds. R. Wong and H. Tse, Humana Press, Totowa, NJ, 2009, pp. 1–27.
263 B. Ngom, Y. Guo, X. Wang and D. Bi, *Anal. Bioanal. Chem.*, 2010, **397**, 1113–1135.
264 M. Mahmoud, C. Ruppert, S. Rentschler, S. Laufer and H.-P. Deigner, *Sens. Actuators B Chem.*, 2021, **333**, 129246.
265 S.-J. Baek, A. Park, Y.-J. Ahn and J. Choo, *Analyst*, 2014, **140**, 250–257.
266 R. J. Tallarida and R. B. Murray, in *Manual of Pharmacologic Calculations: With Computer Programs*, eds. R. J. Tallarida and R. B. Murray, Springer, New York, NY, 1987, pp. 77–81.
267 H. V. Hsieh, J. L. Dantzler and B. H. Weigl, *Diagnostics*, 2017, **7**, 29.
268 S. M. Spinola and J. G. Cannon, *J. Immunol. Methods*, 1985, **81**, 161–165.
269 R. A. McCloy, S. Rogers, C. E. Caldon, T. Lorca, A. Castro and A. Burgess, *Cell Cycle*, 2014, **13**, 1400–1412.
270 J. Mares, S. Kumaran, M. Gobbo and O. Zerbe, *J. Biol. Chem.*, 2009, **284**, 11498–11506.

8 Appendix

```
import numpy as np
from numpy import trapz
import cv2
import matplotlib.pyplot as plt
import os
from tkinter import Tk
from tkinter.filedialog import askdirectory
import csv
from scipy.signal import find_peaks, peak_widths, peak_prominences
from scipy.integrate import simpson
import pandas as pd



filepath = ''
filename = ''
#Sourced from https://stackoverflow.com/questions/29156532/python-baseline-correction-library citing
https://pubs.rsc.org/en/content/articlelanding/2015/AN/C4AN01061B#!divAbstract
from scipy import sparse
from scipy.sparse import linalg
from numpy.linalg import norm



def baseline_arPLS(y, ratio=1e-6, lam=100, niter=10, full_output=False):
    L = len(y)

    diag = np.ones(L - 2)
    D = sparse.spdiags([diag, -2*diag, diag], [0, -1, -2], L, L - 2)

    H = lam * D.dot(D.T)  # The transposes are flipped w.r.t the Algorithm on pg. 252

    w = np.ones(L)
```

```
W = sparse.spdiags(w, 0, L, L)

crit = 1
count = 0

while crit > ratio:
    z = linalg.spsolve(W + H, W * y)
    d = y - z
    dn = d[d < 0]

    m = np.mean(dn)
    s = np.std(dn)

    w_new = 1 / (1 + np.exp(2 * (d - (2*s - m))/s))

    crit = norm(w_new - w) / norm(w)

    w = w_new
    W.setdiag(w)  # Do not create a new matrix, just update diagonal values

    count += 1

    if count > niter:
        print('Maximum number of iterations exceeded')
        break

if full_output:
    info = {'num_iter': count, 'stop_criterion': crit}
    return z, d, info
else:
    return z
```

```
def getpeaks(iteration,raw_signal,strip):
    global filename
    global filepath
        #peak finding troughs by inverse peak detection with prominence and with a width limit
    #flipping signal from negative to positive peaks and adding a -20 shift to account for baseline i.e 235 rather than 255
    #signal = np.array([235 - x for x in signal])


# remove the baseline (change lam and niter to alter)
    baseline, signal, info = baseline_arPLS(-raw_signal, lam=1e4, niter=10, full_output=True)
    peaks,_= find_peaks(signal, prominence=2, width=[1,60])

    #Save signals as a pandas dataframe
    signal_dataframe = pd.DataFrame(signal, columns=['Pixel Intensity'])
    signal_dataframe.to_csv(f'{filepath}/{filename.split('.')[0]}_strips/test_{iteration}.csv')

    #trying to extract information about the peak that it has picked
    prominences,left_bases,right_bases = peak_prominences(signal, peaks)
    contour_heights = signal[peaks] - prominences



    ### Calculate area of peaks
    ## First, check for number of peaks, raise correct error messages

    #if len(peaks) == 0: raise Exception('No peaks found')
    #if len(peaks) <= 2: raise Exception('Fewer than 2 peaks found')

    ## Initialize arrays

    left_edges = []
    right_edges = []
```

```
    areas = []

    ## Iterate for every peak
    # Find left and right edges of each peak
    # Then integrate between left and right edge of the signal to 0 (the baseline)

    for peak in peaks:
        left_edge = 0
        for i in range (peak, 0 , -1):
            if signal[i] < 0.5:
                left_edge = i
                break
        left_edges.append(left_edge)
        right_edge = 0
        for i in range (peak, len(signal) , 1):
            if signal[i] < 0.5:
                right_edge = i
                break
        right_edges.append(right_edge)

        if left_edges[-1] == right_edges[-1]:
            areas.append(0)
        else:
            areas.append(simpson(signal[left_edges[-1]:right_edges[-1]], dx=1))

        ## Debug output for areas

        print(f'\nPeak: {peak}\tAmplitude: {signal[peak]}\nLeft Edge: {left_edges[-1]}\tRight
Edge: {right_edges[-1]}\nArea: {areas[-1]}\n')

#
    ## Save results to a dataframe using Pandas
    Test_results = {'Peak': peaks, 'Left Edge': left_edges, 'Right Edge': right_edges, 'Area':
areas}
```

```
    print(Test_results)
    sig_int_dataframe = pd.DataFrame(Test_results)

    #
    ## Save dataframe to csv

sig_int_dataframe.to_csv(f'{filepath}/{filename.split('.')[0]}_strips/results_{iteration}.csv')
    fig,(ax1,ax2) = plt.subplots(nrows=2, ncols=1)
    ax1.plot(signal)
    #set axis limits for top graph
    ax1.set_xlim([0,590])
    ax1.set_ylim([0,max(signal+20)])
    ax1.plot(peaks,signal[peaks],'x')
    ax1.vlines(x=(left_edges), ymin=0, ymax=50, color='green')
    ax1.vlines(x=(right_edges), ymin=0, ymax=50, color='orange')
    ax1.vlines(x=peaks, ymin=contour_heights, ymax=signal[peaks], color='red')
    ax2.imshow(strip, cmap='binary_r')
    #create variant that displays the full colour version
    #plt.show(block=False)

    #Always save the file into a new folder labelled with the image name in the directory that
it was found
    return fig,prominences



def imgprocess():
    global filename
    global filepath

    img = cv2.imread(os.path.join(filepath, filename))
    gray_img = cv2.cvtColor(img, cv2.COLOR_BGR2GRAY)

    #iterate y by 305 for next strip 6 times for 7 strips
    strips = []
```

```
    for i in [x*307 for x in range(7)]:
        strips.append(gray_img[725+i:790+i, 760:1350])
    #print(strips)



    try:
        os.mkdir(os.path.join(filepath, filename.split('.')[0]+'_strips'))
    except FileExistsError:
        pass

    prominences = []
    for i,strip in enumerate(strips):
        stripaverage = np.average(strip, axis=0)
        fig,prominence = getpeaks(i,stripaverage,strip)
        fig.savefig(os.path.join(filepath, filename.split('.')[0]+f'_strips/strip_{i+1}'))
        prominences.append(prominence)
    with open(os.path.join(filepath, filename.split('.')[0]+f'_strips/strips.csv'),'w') as file:
        writer = csv.writer(file)
        writer.writerows(prominences)
    #np strip array data
    #with open(os.path.join(filepath, filename.split('.')[0]+f'_strips/strips2.csv'),'w') as file2:
        #np.savetxt(file, strips, delimiter=',')

    #Turn this on if you want the pictures to stay open after running
    #input()



def main():
    global filename
    global filepath
    #Get image

        #Ask for Folder path
    directorypath = askdirectory(title='Select Folder') # shows dialog box and return the path
```

```
    for root, subdirs, files in os.walk(directorypath):
        for file in files:
            if os.path.splitext(file)[1].lower() in ('.jpg', '.jpeg') and ‘experiment’ in file.lower():
                target_file = os.path.join(root, file)
                print(target_file)
                filepath = root
                filename = file
                imgprocess()
        #from folder path find all images below that
        #pass each of those images into the program
        #If the folder contains subfolders also search those for jpgs

if __name__ == ‘__main__’:
    main()
```